Transition Metal-Free Oxygen Activation by Ammonium Based Ionic Liquids for Selective Oxidation Reactions: Experimental and Theoretical Studies

Thesis Submitted for the Degree of
Doctor of Philosophy
In the Faculty of Science
Jadavpur University

BY

KRISHNENDU KHAMARU

CSIR-Indian Institute of Chemical Biology
Structural Biology & Bioinformatics Division
Organic & Medicinal Chemistry Division
4, Raja S.C. Mallick Road, Jadavpur, Kolkata-700032

Declaration by the Author

I hereby declare that the work presented in this thesis, entitled '**Transition Metal-Free Oxygen Activation by Ammonium Based Ionic Liquids for Selective Oxidation Reactions: Experimental and Theoretical Studies**' was carried out at CSIR-Indian Institute of Chemical Biology, Kolkata, India. I confirm that I have written this thesis completely on my own, using my own research work, under the supervision of Dr. Nakul C. Maiti, Senior Principal Scientist, Structural Biology and Bioinformatics Division, and Dr. Biswadip Banerji, Chief Scientist, Organic & Medicinal Chemistry Division.

I have duly acknowledged all the sources of information used in this thesis. Part of this thesis has been published in the Journal of the American Chemical Society. This thesis has not been submitted for any degree to any other University/Institute.

Krishnendu Khamaru

Krishnendu Khamaru
UGC Fellow
CSIR-Indian Institute of Chemical Biology

सी.एस.आई.आर–भारतीय रासायनिक जीवविज्ञान संस्थान
वैज्ञानिक तथा औद्योगिक अनुसंधान परिषद की एक इकाई
4, राजा एस. सी. मल्लिक रोड, कोलकाता - 700 032, भारत
CSIR - INDIAN INSTITUTE OF CHEMICAL BIOLOGY
A Unit of Council of Scientific & Industrial Research
4, Raja S. C. Mullick Road, Jadavpur, Kolkata-700 032, India

CERTIFICATE FROM THE SUPERVISORS

This is to certify that the work presented in the thesis entitled **'Transition Metal-Free Oxygen Activation by Ammonium-Based Ionic Liquids for Selective Oxidation Reactions: Experimental and Theoretical Studies'**, submitted by **Krishnendu Khamaru**, who registered his name on **05.09.2018** [**Reg. No. SCHEM1114718** and **Index No. 147/18/Chem./26**] for the award of a Ph.D. (Science) degree by Jadavpur University, is entirely based on his own work under the supervision of **Dr. Nakul C. Maiti, Senior Principal Scientist** and **Dr. Biswadip Banerji, Chief Scientist, CSIR-IICB**. Furthermore, we confirm that neither this thesis nor any part of it has been submitted for any degree, diploma, or other academic award elsewhere before.

Nakul Chandra Maiti

Dr. Nakul C. Maiti

डॉ. नकुल चंद्र माईति / Dr. Nakul C. Maiti
वरिष्ठ प्रधान वैज्ञानिक / Senior Principal Scientist
संरचनात्मक जीवविज्ञान और जैवसूचना प्रभाग
Structural Biology & Bioinformatics Division
सीएसआईआर-भारतीय रासायनिक जीवविज्ञान संस्थान
CSIR-Indian Institute of Chemical Biology
(भारत सरकार / Govt. of India)
कोलकाता - 700 032 / Kolkata - 700 032

Biswadip Banerji 22/5/24

Dr. Biswadip Banerji

डॉ. बिश्वदीप बनर्जी / Dr. Biswadip Banerji
PhD (IIT-Kanpur), M. Sc (Cal)
प्रधान वैज्ञानिक / Chief Scientist
आर्गेनिक एवं औषधीय रसायन प्रभाग
Organic & Medicinal Chemistry Division
सीएसआईआर-भारतीय रासायनिक जीवविज्ञान संस्थान
CSIR-Indian Institute of Chemical Biology
(भारत सरकार / Govt. of India)
कोलकाता 700 032 / Kolkata - 700 032

Phone : 2499-5700 (Pilot No. / EPABX No.) ● Website : www.iicb.res.in ● Telegram : LIVINGCELL
Fax : 91-33-2473-5197 (Dir) ● 91-33-2473-5368 (Dir) ● Fax : 91-33-2414-9475 (A.O.) ● 91-33-2429-8490 (A.O.)
91-33-2483-1983 (F&AO) ● 91-33-2483-1982 (SPO)

DEDICATED TO

MY BELOVED WIFE, FAMILY, AND

RESPECTED SUPERVIOSRS

Thanks giving....

Finally, the challenging seven years have come to an end, and I find myself on the final stretch towards earning that extra title to my name. Above all, because this trip was difficult and full of intense adrenaline rushes, it has taught me incredible patience. There were countless nights when I returned home demoralized, burdened by frustration. Yet, among these challenges, every small success brought immense joy to my heart and made me energetic to work hard and solve unsolved problems in chemistry.

The journey began with an aspiration to contribute to science, no matter how modestly, while others around me provided encouragement and support. And now, as I take a seat to begin the enormous effort of distilling everything I have done in order to obtain the highest degree in education, I understand that my primary responsibility is to thank everyone who has contributed to this trip.

I extend my deepest gratitude to my supervisor, Dr. Nakul C. Maiti, who has been a guiding light throughout my Ph.D. journey since its beginning. Over the span of more than five years, his unwavering support, both in words of inspiration and encouragement during challenging times, has been a source of strength, propelling me forward on the path to success. Dr. Maiti's steadfast belief in my abilities has been a driving force behind my pursuit of the highest educational degree, transforming what once seemed like a distant dream into a tangible reality. I consider myself immensely fortunate to have had the opportunity to work under Dr. Maiti's guidance. His mentorship has not only provided me with a solid foundation but has also afforded me the freedom to explore my research interests with full autonomy. Dr. Maiti's expertise in the field has served as a beacon of inspiration, fuelling my passion for innovative research and pushing me to delve deeper into the realms of experimental organic synthesis. As I reflect on the culmination of my Ph.D. journey, I am filled with profound satisfaction, knowing that Dr. Maiti's contributions have played an integral role in shaping the outcome of my research. Dr. Maiti's dedication and support have been instrumental in my academic and personal growth and I am truly appreciative of his efforts throughout my Ph.D. journey. Finally, I am grateful for his foresight in facilitating a collaborative environment, allowing me to benefit from the joint supervision of Dr. Biswadip Banerji, whose expertise has further enriched my academic experience.

Thanks giving....

I am immensely grateful to my other supervisor, Dr. Biswadip Banerji, who became my primary supervisor two years into my PhD journey. When some scientists declined to take me on, Dr. Banerji generously offered me the opportunity to work in his lab. This opened the door for me to delve into experimental organic chemistry and benefit from his vast knowledge and expertise in the field. From the very first day in Dr. Banerji's lab, I never felt that he was merely a joint supervisor; rather, I perceived him as my primary mentor, alongside Dr. Nakul C. Maiti. I am deeply thankful of his exceptional support and guidance. It is also important to note Dr. Banerji's affection and dedication to my research, despite facing health challenges. After spending one year in Dr. Banerji's lab, he was admitted for a critical operation. Despite his condition, he remained deeply invested in my research, even long discussion during his hospitalization. His unwavering dedication truly speaks volumes about his commitment. I am sincerely thankful for his invaluable contribution to my publications, including his assistance in correcting manuscripts into the late night. Furthermore, I am filled with emotion as I reflect on Dr. Banerji's lab and the extraordinary experiences it has afforded me. His support has extended beyond my Ph.D fellowship, as he entrusted me with a project for financial assistance. I am deeply grateful for his mentorship and the countless lessons I have learnt under his guidance.

Another individual who has been my pillar of strength during this monumental task is my wife, ***Jayanti****. You have been a friend, philosopher, and guide to me. I am thankful for your patience when I have shared all my hardships. My Ph.D. journey would not have been as manageable without your assistance. I want to express my gratitude to my wife,* ***Jayanti Dhara****, for enduring my frustrations and providing consistent psychological and financial support. She played a crucial role in absorbing all my frustrations like a sponge and fostering positivity within me. Additionally, your immense faith in me has propelled me to where I am today. Thank you for being my rock.*

Thanks giving....

*I want to thank my parents, for always being there for me during my studies. Their love, help, and trust in me kept me going. **Maa** and **Baba**, your encouragement, talks late into the night, and belief in me helped me a lot during my Ph.D. journey. Your support and sacrifices gave me the strength to do my best in my studies. I'm really thankful for your unconditional love and support, which helped me through the good times and the tough ones. This thesis is not just about my hard work but also about your dedication and sacrifices. Thank you, **Maa** and **Baba**, for being my rocks, and for teaching me to keep going no matter what. I'll always be grateful for your love and trust in me.*

It wouldn't have been easy to carry on with my work peacefully if my in-laws hadn't been so supportive. My new family joined me halfway through my Ph.D. journey, and they have been compassionate in all my endeavors. I am thankful to my new parents and the entire family.

I am deeply grateful to all my current (Esha, Banadipa, Ananya, Kaushik, Abhyuday, Vijay, Arpan, Asikul) and former colleagues (Lopamudra, Kaushik, Animesh da, Sandip da, Satadru da, Suvankar da, Saswati, Leena) in both of my labs. Without each of you, life would have been considerably more difficult. Our endless discussions about career prospects often ended in laughter, providing much-needed relief from the seriousness of our work. I want to give special mention to a few colleagues who have been particularly impactful. Firstly, I would like to express my gratitude to Debabrata (Debu ji), whose exceptional work ethic served as an inspiration for my unique scientific research. I am truly thankful to Subhankar (Kochi) for his active assistance on my project. His extensive knowledge of chemistry, as well as our frequent discussions, significantly contributed to the success of our project. Subhankar holds a special place as we shared similar academic backgrounds, having attended the same undergraduate and postgraduate institutions, and now working together in the same Ph.D. lab. Next, I express my gratitude to Arindam (Ari) for his unwavering support, project discussion and encouragement. Anupam (Anu) deserves special thanks for being my companion during late-night lab sessions. His efforts to bring food and prepare coffee for me enabled me to work throughout the night effectively. I am thankful to Rajdip and Mrinmoy for their support and inspiration in my research endeavors. Lastly, I appreciate Shubham for our

Thanks giving....

meaningful discussions about life. Each of you has played a significant role in my journey, and I am profoundly thankful for your contributions to my research and personal growth.

I'd like to thank two exceptional seniors from my past (CSIR-CSMCRI) and present (CSIR-IICB) labs, Dr. Rabindranath Lo and Dr. Uttam Pal. I learned a lot from them, witnessing their unwavering dedication to scientific research. They are truly committed to advancing knowledge in their respective fields. I am particularly grateful to Dr. Rabindranath Lo for teaching me about DFT and for his outstanding contributions to our prestigious journal. Additionally, I extend my thanks to Dr. Uttam Pal, who has devoted his life to science. I appreciate Dr. Uttam Pal's systematic contributions to our journal.

I am thankful to my institute, the CSIR Indian Institute of Chemical Biology, for giving me the space to carry on with my research work. I extend my gratitude to the current director, Prof. Vibha Tandon, and the previous both directors, Prof. Samit Chattopadhyay and Prof. Arun Bandyopadhyay, for allowing me to be a part of this institute. I extend my heartfelt gratitude to all the administrative staff of the institute for their valuable assistance during the official work. I am thankful to the staff of central instrumentation facilities: Mr.G. Karmakar and Dr. E. Padmanaban for NMR facilities; Mr. Sandip Chowdhury and Mr. Soumik Laha; Khan Da for mass facilities; Mr. Sandip Kundu for X-ray crytal facilities; and Tarak Da for lyophilization.

My list of acknowledgements would be incomplete without my doctoral committee members, HOD of Chemistry, Jadavpur University, and my subject expert, Prof. Snehasikta Swarnakar. I am really grateful for their patience, valuable time, and intellectual questions to clarify my subject concept.

I would also like to acknowledge in advance the professors who will review my Ph.D. thesis. I'd like to thank both reviewers for their valuable time in reviewing my thesis.

Krishnendu Khamaru

Krishnendu Khamaru

UGC Fellow

CSIR-Indian Institute of Chemical Biology

GENERAL REMARKS

- ^{1}H NMR and ^{13}C NMR were calculated on a Bruker DPX 300 MHz and Bruker DRX 600 MHz NMR instrument. Generally, DMSO-d_6, $CDCl_3$ and MeOD have been used for NMR sample solution preparation. Chemical shifts (δ) were expressed in parts per million (ppm), using tetramethylsilane (δ = 0.00) as the reference compound. The standard abbreviations s, d, t, q, m, and J refer to singlet, doublet, triplet, quartet, multiplet, and the coupling constant respectively. ESI mass spectral analysis was performed using LCQ-ORBITRAP-XL instrument. EI mass spectral analysis was performed using High Resolution Mass Spectrometer JEOL Japan.
- Analytical thin layer chromatography (TLC) was obtained via standard Merck TLC silica gel 60 F254 aluminium sheets. Visualization of the spots on TLC plate was achieved through exposure to UV light, iodine vapour, etc. Progress of the reaction was monitored via TLC checking. Moisture sensitive reactions were carried out using standard syringe-septum techniques. Column chromatography was performed using silica gel of 60-120 or 100-200 mesh. For column chromatography, ethylacetate:hexane and methanol:dichloromethane solvent partners were used as eluent. All reagents and solvents were purified and dried by conventional protocol. All evaporation of solvents was done under reduced pressure in Heidolph Rotary Evaporator of Cat. No: P/N Hei-VAP Value/G3: 560-01300-001. Peroxide test kit (cat no: 1.10337, colorimetric, 100-1000 mg/L (H_2O_2), MQuant) was purchased from Sigma-Aldrich.

LIST OF ABBREVIATIONS

NMR:	Nuclear Magnetic Resonance
MHz	Megahertz
ppm:	parts per million
ESI:	Electron Spray Ionization
HRMS:	High-Resolution Mass Spectrometry
EI:	Electron Ionization
UV:	Ultraviolet
TLC:	Thin Layer Chromatography
R_f:	Retention factor
DFT:	Density Functional Theory
MO:	Molecular Orbital
pDOS:	Partial Density of State
ATP:	Adenosine triphosphate
NADPH:	Nicotinamide adenine dinucleotide phosphate
VBT:	Valence Bond Theory
VB:	Valence Bond
GVB:	Generalized Valence Bond
OS:	Open-shell
CS:	Closed-shell
TNT:	Trinitrotoluene
FAD:	Flavin adenine dinucleotide
ORR:	Oxygen reduction reaction
ROS:	Reactive oxygen species
EDC.HCl:	(3-Dimethylamino-propyl)-ethyl-carbodiimide Hydrochloride
HOBT:	Hydroxybenzotriazole
DIPEA:	N,N-Diisopropylethylamine
HATU:	1-[Bis(dimethylamino)methylene]-1H-1,2,3-triazolo[4,5-b]pyridinium 3-oxide hexafluorophosphate
^{t}Bu:	tert-butyl
ACN:	Acetonitrile
DCM:	Dichloromethane
TCCA:	Trichloroisocyanuric acid
NMP:	N-Methylpyrrolidone
IL:	Ionic liquid
VOC:	Volatile organic compound

TBHP:	Tert-Butyl hydroperoxide
DBN:	1,5-Diazabicyclo[4.3.0]non-5-ene
DMF:	Dimethylformamide
Triton B	Trimethylbenzylammonium hydroxide
TMAOH:	Tetramethyl ammonium hydroxide
TBAOH:	TetraButyl ammonium hydroxide
TBAB:	Tetrabutyl Ammonium Bromide
Boc:	tert-butoxycarbonyl
^{o}C:	Temperature in degrees centigrade
DDQ:	2,3-Dichloro-5,6-dicyano-p-benzoquinone
IBX:	2-Iodoxybenzoic acid
RB:	Round Bottom
hr:	hour
mmol:	millimole
min:	minute
gm:	gram
mg:	milligram
mM:	millimolar
μM:	micromolar
μL:	microliters
mL:	milliliters
K:	temperature in Kelvin
kcal:	kilocalorie
DMSO:	Dimethyl sulfoxide
TEA:	Triethylamine
ICP-AES:	Inductively Coupled Plasma Atomic Emission Spectroscopy
ICP:	Inductively Coupled Plasma
Dl:	Detection limit
Eq:	equivalent
MD:	Molecular Dynamics
OPLS:	optimized potentials for liquid simulations
NVT:	Canonical ensemble
NPT:	Isothermal-isobaric ensemble
RESPA:	Reference System Propagator Algorithm
PME:	Particle Mesh Ewald
B3LYP:	Becke, 3-parameter, Lee–Yang–Par
IRC:	Intrinsic Reaction Coordinate
MECP:	Minimum Energy Crossing Point
HAT:	Hydrogen Atom Transfer

PES:	Potential Energy Surface
MCSCF	Multiconfigurational Self-Consistent Field
AP:	Antisymmetric Projection
PCET:	Proton Coupled Electron Transfer
BDE:	Bond Dissociation Energy
DLPNO:	Domain-based Local Pair Natural Orbital
GEDT:	Global Electron Density Transfer
TS:	Transition State
FMO:	Frontier Molecular Orbitals
DOS:	Density of States

Publications

1. ***Metal-Free Activation of Molecular Oxygen by Quaternary Ammonium-Based Ionic Liquid:A Detail Mechanistic Study***, Krishnendu Khamaru, Uttam Pal, Subhankar Shee, Rabindranath Lo, Kaushik Seal, Prasanta Ghosh, Nakul Chandra Maiti*, Biswadip Banerji*, **J. Am. Chem. Soc.** ***2024, 146, 10, 6912–6925*.**

2. ***NMR and vibrational spectroscopic studies on the structure and self-assembly of Two de novo dipeptides in methanol,*** Leena Majumder, Kaushik Bera, Krishnendu Khamaru, Uttam Pal, Nakul C.Maiti, Biswadip Banerji***, Journal of Molecular Structure,*** ***Volume 1266, 15 October 2022, 133455.***

3. ***Synthesis of N-Fused Triazole–Piperazine–Quinazolinones via One-Pot Tandem Click Reaction and Cross-Dehydrogenative Coupling,*** Ravuri Srinath, Arindam Manna, Subhankar Shee, Vijay Babu Pathi, Krishnendu Khamaru, Nakul Chandra Maiti Biswadip Banerji*, **Org. Lett.** ***2021, 23, 24, 9365–9370.***

4. ***Cu-Catalyzed Direct Diversification of 2-(2-Bromophenyl)quinazolin-4(3H)-ones through Orthogonal Reactivity Modulation,*** Satadru Chatterjee, Ravuri Srinath, Suvankar Bera, Krishnendu Khamaru, Afifa Rahman, Biswadip Banerji*, **Org. Lett.** ***2019, 21, 22, 9028–9032*.**

5. ***Sensing of Iron(III) Ion via Modulation of Redox Potential on Biliverdin Protected Silver Nanosurface,*** Mritunjoy Maity, Kaushik Bera, Uttam Pal, Krishnendu Khamaru, Nakul C Maiti*, **ACS Applied Nano Materials,** ***2018, 1(11), 6099-6111*.**

JACS
JOURNAL OF THE AMERICAN CHEMICAL SOCIETY
pubs.acs.org/JACS
Article

Metal-Free Activation of Molecular Oxygen by Quaternary Ammonium-Based Ionic Liquid: A Detail Mechanistic Study

Krishnendu Khamaru, Uttam Pal,[⊥] Subhankar Shee,[⊥] Rabindranath Lo, Kaushik Seal, Prasanta Ghosh, Nakul Chandra Maiti,* and Biswadip Banerji*

Cite This: J. Am. Chem. Soc. 2024, 146, 6912−6925
Read Online

ABSTRACT: Most oxidation processes in common organic synthesis and chemical biology require transition metal catalysts or metalloenzymes. Herein, we report a detailed mechanistic study of a metal-free oxygen (O_2) activation protocol on benzylamine/alcohols using simple quaternary alkylammonium-based ionic liquids to produce products such as amide, aldehyde, imine, and in some cases, even aromatized products. NMR and various control experiments established the product formation and reaction mechanism, which involved the conversion of molecular oxygen into a hydroperoxyl radical via a proton-coupled electron transfer process. Detection of hydrogen peroxide in the reaction medium using colorimetric analysis supported the proposed mechanism of oxygen activation. Furthermore, first-principles calculations using density functional theory (DFT) revealed that reaction coordinates and transition state spin densities have a unique spin conversion of triplet oxygen leading to formation of singlet products via a minimum energy crossing point. In addition to DFT, domain-based local pair natural orbital coupled cluster, (DLPNO−CCSD(T)), and complete active space self-consistent field, CASSCF(20,14) methods complemented the above findings. Partial density of states analysis showed stabilization of π^* orbital of oxygen in the presence of ionic liquid, making it susceptible to hydrogen abstraction in a mild, metal-free condition. Inductively coupled plasma atomic emission spectroscopic (ICP-AES) analysis of reactant and ionic liquids clearly showed the absence of any significant transition metal contamination. The current results described the origin of O_2 activation within the context of molecular orbital (MO) theory and opened up a new avenue for the use of ionic liquids as inexpensive, multifunctional and high-performance alternative to metal-based catalysts for O_2 activation.

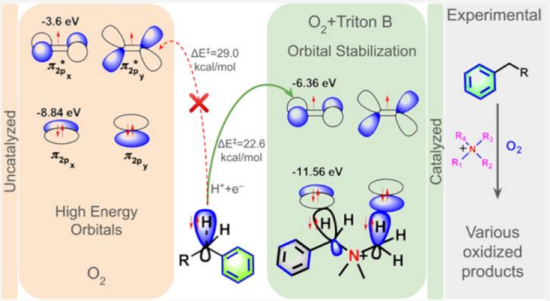

INTRODUCTION

The sole abundant paramagnetic molecule in our environment is dioxygen (O_2), which has a triplet ground state. In reality, this triplet O_2 diradical accounts for 20.94% of the total gases in the atmosphere of earth and is critical for the survival of life. However, questions may arise why oxygen is so "stable" in the earth's atmosphere.[1] The resonance stabilization of triplet •O=O• diradical renders it kinetically inactive for hydrogen atom abstraction, which may be the reason why O_2 is so abundant in the earth's atmosphere.[1] Then, another pertinent question may arise about the mechanism, as to how living organism utilizes oxygen in their body to run so many biochemical reactions. However, nature has created a family of enzymes in biological systems that contain transition metals such as iron,[2,3] copper,[4] and manganese,[5] which facilitate activation of triplet ground-state oxygen. Even in the absence of any transition metal, oxygen can react at high temperature. Thus, paper catches fire when it reaches 232 °C.[1] The most crucial oxidative step for oxygen in various types of oxygen-based oxidative reactions in biology or chemistry is the hydrogen atom abstraction process.[4] In chemistry, hydrogen atom abstraction by triplet O_2 from HOOH was reported to have an energy barrier of about 37 kcal/mol, whereas hydrogen atom abstraction from H_2 gas encounters an even larger barrier of 60.7 kcal/mol.[1,6] From a thermodynamic point of view, the reactions that produce water or hydrogen peroxide are exothermic by at least −30 kcal/mol and therefore be defined as spontaneous processes.[6] Nevertheless, these reactions are kinetically very slow. Thus, the interactions of O_2/H_2 or O_2 with organic molecules and living matter are persistent or "kinetically stable" and exist for a sufficiently long time at ambient conditions. Astonishingly high barriers prevent oxygen from reacting with C−H bonds in any organic molecule.[1,6] O_2 is

Received: December 18, 2023
Revised: February 3, 2024
Accepted: February 6, 2024
Published: February 29, 2024

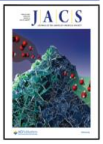

https://doi.org/10.1021/jacs.3c14366
J. Am. Chem. Soc. 2024, 146, 6912−6925

Journal of Molecular Structure 1266 (2022) 133455

Contents lists available at ScienceDirect

Journal of Molecular Structure

journal homepage: www.elsevier.com/locate/molstr

NMR and vibrational spectroscopic studies on the structure and self-assembly of Two *de novo* dipeptides in methanol

Leena Majumder[a], Kaushik Bera[b], Krishnendu Khamaru[b], Uttam Pal[b], Nakul C. Maiti[b,*], Biswadip Banerji[a,*]

[a] Division of Organic and Medicinal Chemistry, Division of Structural Biology and Bioinformatics, Organic and Medicinal Chemistry Division, Indian Institute of Chemical Biology, CSIR – Council of Scientific and Industrial Research, Academy of Scientific and Innovative Research (AcSIR) 4, Raja S, C, Mullick Road, Kolkata, West Bengal 700032, India

[b] Structural Biology and Bioinformatics Division, Indian Institute of Chemical Biology, Council of Scientific and Industrial Research, India

ARTICLE INFO

Article history:
Received 14 December 2021
Revised 30 May 2022
Accepted 5 June 2022
Available online 6 June 2022

Key words:
Dipeptide
NMR
FT-IR
Raman
Thioflavin T
Assembly formation

ABSTRACT

Short peptides are known to form self-organized nano-architectures useful for advanced biomedical applications. Both hydrogen-bonding and hydrophobic interactions play a pivotal role in molecular assembly, including self-assembly of proteins and peptides. In the current investigation, we reported the synthesis, self-assembly pattern and physicochemical properties of two *de novo* dipeptides: *N*-Boc-(O-benzyl)-tyro-(dimethyl)-glutamate and *N*-Boc-(O-benzyl)-glu-(O-benzyl)-tyrosine-methyl ester, abbreviated as P1 and P2, respectively. These two peptides produced different morphological features under similar conditions due to the presence of a small twist in their molecular structures. In methanol, P1 gave rise to a unique fibrillar network whereas P2 self-assembled into oligomers of 20-30 nm diameters. The UV-Vis, FT-IR and Raman spectra were recorded using experimental methods and compared with the computational spectra obtained by density functional method (B3LYP/6-31G(d)). The electronic absorption spectra of both P1 and P2 measured in methanol showed broad absorption peaks in the UV region with an absorption maximum at ~ 273 nm. FT-IR and Raman spectra of both the dipeptides in solid state showed amide I vibration bands at ~1650 cm^{-1} indicating a similar conformation state of the peptide bonds. However, H/D exchange ^1H NMR measurements confirmed that the amide NH of P1 was strongly involved in H-bond formation compared to P2 amide NH and rapid H/D exchange occurred upon addition of D_2O in the solution. Thioflavin T (ThT) fluorescence assay measurement suggested that incubation of P1 in methanol at room temperature produced fibrillar aggregates enriched with compact ß-sheet conformation. Formation of such ordered structure also caused a blue shift in the amide-carbonyl Raman frequency of the peptide to ~1657 cm^{-1}. P1 fibrils further showed gel formation behaviour in 1:1 methanol/water mixture. The minimum gelation concentration (MGC) of the dipeptide was found to be 0.5% w/v and the calculated gelation temperature (T_{gel}) of the corresponding MGC was 67°C. On the other hand, the amide carbonyl stretching vibration of P2 appeared at ~1650 cm^{-1} in the Raman spectra and it was not significantly altered in its oligomeric state (produced in methanol).Moreover, no significant enhancement of ThT fluorescence intensity of P2 indicating absence of compact ß-sheet conformation of the peptide. The P2 oligomers also showed no gel like phase transformation in methanol/water mixtures.

1. Introduction

Short synthetic peptides provide a potential building block for *in vitro* fabrication of higher ordered structures ranging from nano to supramolecular architectures [14,23,37,40,53], which has various applications as in bio-interface engineering, biosensor design and therapeutics [17,20,21,26,34,36,38,45,48,49]. Due to their biocompatibility, biodegradability and some resemblance with protein,

Abbreviations: P1, *N*-Boc-(O-benzyl)-tyro-(di-methyl)-glutamate; P2, *N*-Boc-(O-benzyl)-glu-(O-benzyl)-tyrosine-methyl ester; BOC, Tert-butoxycarbonyl (protecting group); DMF, N, N-dimethylformamide; DMSO, Dimethyl sulfoxide; UV-Vis, Ultraviolet-visible; FT-IR, Fourier Transform Infrared; Powder XRD, Powder X-Ray Diffraction; NMR, Nuclear magnetic resonance; AFM, Atomic force microscopy; ThT, Thioflavin T; K_{app}, Apparent rate constant value; DFT, Density functional theory; MGC, Minimum gelation concentration; exp, Experimental; theo, Calculated/ theoretical; h, Hour; min, Minute.

* Corresponding authors.
E-mail addresses: ncmaiti@iicb.res.in (N.C. Maiti), biswadip@iicb.res.in (B. Banerji).

https://doi.org/10.1016/j.molstruc.2022.133455
0022-2860/

OL | Organic Letters

pubs.acs.org/OrgLett Letter

Synthesis of N-Fused Triazole–Piperazine–Quinazolinones via One-Pot Tandem Click Reaction and Cross-Dehydrogenative Coupling

Ravuri Srinath, Arindam Manna, Subhankar Shee, Vijay Babu Pathi, Saswati Ghosh, Krishnendu Khamaru, Nakul Chandra Maiti, and Biswadip Banerji*

Cite This: *Org. Lett.* 2021, 23, 9365–9370 Read Online

ACCESS | Metrics & More | Article Recommendations | Supporting Information

ABSTRACT: Herein, a one-pot protocol to synthesize tetracyclic triazole–piperazine–quinazolinone-fused N-heterocyclic scaffolds is reported. In this strategy, a tandem approach of two highly efficient synthetic reactions, click and cross-dehydrogentive coupling reactions, with high atom economy were employed to obtain the target N-fused scaffolds. Being highly functional group tolerable, this method has broad substrate scope. Interestingly, some of these derivatives showed strong white solid-state fluorescence.

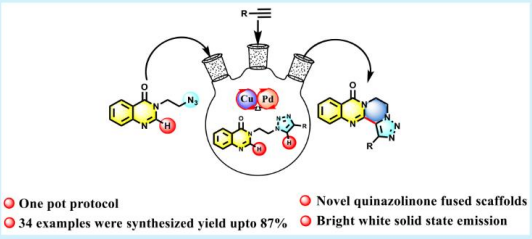

Nature is a tremendous source of many natural products, which contain many medicinally important N-fused heterocycles as their core moiety and are often responsible for their biological efficacies.[1] Synthesis of these fused heterocycles by various transition-metal-catalyzed approaches in the laboratory is always a challenging task for synthetic organic chemists worldwide. It is interesting to note that most of the time, these molecules possess potential therapeutic applications along with high luminescence properties due to high electronic conjugations because of their extended π-aromatic frameworks.[2a−c] In an ongoing project in our laboratory on the synthesis and efficacy studies of natural-product-inspired hybrid molecules, we were interested to synthesize a library of N-fused heterocyclic molecules, which may be useful as potential therapeutic agents. In the present design strategy, we incorporated quinazolinone, pyrazine, and triazole heterocyclic moieties, which individually have very good reported therapeutic efficacies (Figure 1). In recent times, transition-metal-catalyzed cross-dehydrogenative coupling (CDC) approaches have emerged as the most versatile and atom-economical procedures for C−C bond formations.[3] Furthermore, no use of prefunctionalized substrates and very clean conversions[4] are major advantages of the CDC reaction by various transition metals such as Ru,[5] Rh,[6] and Pd.[7] In addition to that, there are several synthetic methods which utilize palladium-catalyzed intermolecular C−H bond functionalization to synthesize fused quinazolinones.[8] On the other hand, Cu-catalyzed click chemistry is well-known for the synthesis of 1,2,3-triazoles through 1,3-dipolar cycloaddition. The triazole moiety has potential applications in many biochemical as well as drug discovery studies.[9] For the past few years, our group was engaged in developing simple protocols to access novel N-fused polyheterocycles by utilizing C−H activation strategies.[10]

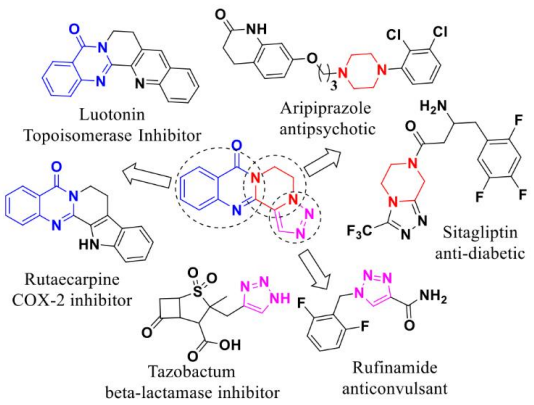

Figure 1. Some of the important drugs containing quinazolinone, piperazine, and triazole moieties.

In the present work, we report a one-pot protocol to synthesize a tetracyclic triazolodihydropyrazine-fused quinazolinone framework via the click reaction followed by palladium-catalyzed oxidative intramolecular cross-dehydrogenative coupling from 3-(2-azidoethyl)quinazolin-4(3*H*)-one (**1a**). Typi-

Received: October 11, 2021
Published: November 21, 2021

https://doi.org/10.1021/acs.orglett.1c03435
Org. Lett. 2021, 23, 9365–9370

OL | Organic Letters

Letter

Cite This: Org. Lett. 2019, 21, 9028−9032

pubs.acs.org/OrgLett

Cu-Catalyzed Direct Diversification of 2-(2-Bromophenyl)quinazolin-4(3*H*)-ones through Orthogonal Reactivity Modulation

Satadru Chatterjee,[‖,†] Ravuri Srinath,[‖,‡] Suvankar Bera,[†] Krishnendu Khamaru,[†] Afifa Rahman,[‡] and Biswadip Banerji*[,†,§]

[†]Organic and Medicinal Chemistry Division, CSIR-Indian Institute of Chemical Biology, Raja S. C. Mullick Road, Kolkata-700032, India

[‡]National Institute of Pharmaceutical Education and Research (NIPER-Kolkata), Chunilal Bhawan, Maniktala, Kolkata-700054, India

[§]Academy of Scientific and Innovative Research (AcSIR), (CSIR-IICB), 4 Raja S. C. Mullick Road, Kolkata-700032, India

Supporting Information

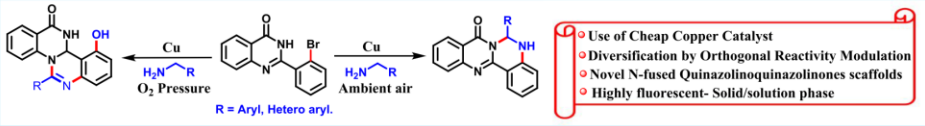

ABSTRACT: A modular strategy to obtain three different products from a single substrate was developed. The present methodology unveils new step-economical and cost-efficient routes to access diverse fused quinazolinoquinazolinone derivatives which are not prevalent in literature. Owing to the importance of quinazolinones in therapeutics, quick access to the arena of these scaffolds could be a valuable addition to the scientific domain of heterocyclic chemistry.

Quinazolinones belong to a privileged class of N-heterocycles due to their great abundance in several natural products and pharmaceuticals which exhibit a wide range of biological activities, including anti-inflammatory, antitubercular, antiviral, and anticancer activities, etc. (Figure 1).[1] Due to the extensive biological significance of the quinazolinone moiety, the development of new synthetic methods for the construction of quinazolinone based molecular scaffolds draws considerable attention. Furthermore, synthesis of a new molecular scaffold containing a quinazolinone nucleus by a short and efficient synthetic route is in high demand for various kinds of interests, especially for the therapeutic targets in the pharmaceutical sectors worldwide.

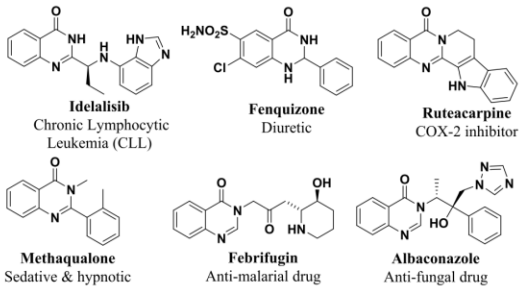

Figure 1. Some quinazolinone-based drugs and natural products.

In the past few decades, transition metal catalyzed direct C−H bond functionalization has emerged as a powerful tool to construct new carbon−carbon (C−C) and C−heteroatom (C−X) bonds for the synthesis of structurally complex natural or unnatural compounds.[2] This C−H functionalization strategy provides direct access and delivers more atom-economical routes in the synthesis of complex structures as compared to the traditional synthetic protocols, and this technique also opens up the scope for the late stage derivatization of bioactive molecules.[3] Hence, use of different transition metal catalysts in C−H functionalization reactions received the spotlight over the past few years. However, the majority of the C−H bond functionalization strategies depend on the use of different noble metals, for example, palladium,[4] rhodium,[5] etc. However, the scope is still limited due to the expensive scale-up procedure of these techniques. In contrast to these highly expensive metal catalysts, cheap copper catalysts may be widely utilized to functionalize specific C−H bonds in large scale and thus copper catalyzed C−H functionalization reactions have gained much focus with critical progression.[6]

In spite of the fact that a number of methodologies involving synthesis of quinazoline fused structures have been accomplished,[7] most of these methods suffer from the major drawback of using expensive metal catalysts. Thus, a straightforward, efficient strategy for the synthesis of quinazolinone fused polyheterocycles is still a challenging

Received: September 27, 2019
Published: November 4, 2019

DOI: 10.1021/acs.orglett.9b03428
Org. Lett. 2019, 21, 9028−9032

ACS APPLIED NANO MATERIALS
Cite This: ACS Appl. Nano Mater. 2018, 1, 6099−6111
Article
www.acsanm.org

Sensing of Iron(III) Ion via Modulation of Redox Potential on Biliverdin Protected Silver Nanosurface

Mritunjoy Maity,[†,∥] Kaushik Bera,[∥] Uttam Pal,[‡] Krishnendu Khamaru, and Nakul C. Maiti*

Structural Biology and Bioinformatics Division, CSIR—Indian Institute of Chemical Biology, 4- Raja S. C. Mullick Road, Kolkata 700032, India

Supporting Information

ABSTRACT: Silver nanoparticle shows distinctive electrochemical properties, and it has a wide range of applications in most areas of science and technology. In the current work we reported the synthesis of biliverdin protected silver nanosurface (Ag-BV) that could sense Fe(III) ion via reduction despite of their unfavorable reduction potential in aqueous medium. The addition of Fe(III) to the Ag-BV suspension resulted an initial red shift in its surface plasmon resonance (SPR) band (420−450 nm) and a color change from straw yellow to deep brown due to the agglomeration of the nanoparticles. Subsequently a redox reaction caused the disappearance of the deep brown color and a significant blue shift occurred in its SPR band (up to 410 nm). The analysis further suggested that the aromatic π system of biliverdin (BV) on the Ag-BV nanosurface could make an electron carrier bridge that favors the transfer of an electron from atomic silver to an empty d orbital of Fe(III) ion. The reduction of Fe(III) ion resulted in oxidation of silver nanoparticles and loss of the nanostructure, which were evidenced in transmission electron microscopy analysis. Further investigation revealed that the partial charge on the iron center was ∼+1.16 in the Fe(II)−biliverdin complex compared to ∼+1.26 in the Fe(III)−biliverdin complex, suggesting a shift of electron density to the metal ion center. Thus, the biliverdin coated silver nanoparticle could be useful as a specific metal ion detector and a redox modulator for an Fe(III)/Fe(II) aqueous system. This might be the first report of its kind as the sensing mechanism involves an exceptional redox type phenomenon instead of mere coagulation of the nanoparticles in the presence of specific ions and produces a different color as an indicator for the ion detection.

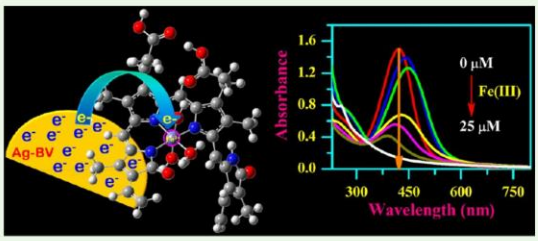

KEYWORDS: *silver nanoparticle, biliverdin, heavy metal, sensing, surface plasmon resonance, reduction potential, iron*

INTRODUCTION

Nanoparticles are of great scientific interest as they bridge the gap between bulk materials and atomic or molecular structures.[1] Among various metal nanoparticles, silver nanoparticle (AgNP) is one of the most promising one due to its wide range of applications in optoelectronics, renewable energy, and many other active fields of science and technology.[2−4] Therefore, serious efforts are made to make silver nanosurfaces of different shapes and sizes. In addition, surface modification of nanoparticles are often carried out to modulate both the physical and chemical aspects of silver atoms on the naosurfaces. One of the most important characteristics of AgNPs is their localized surface plasmon resonance (SPR). The SPR band of silver nanoparticles is caused by the collective oscillations of conduction electrons excited by light and is manifested by an absorption band around 400 nm.[5,6] The absorption wavelengths depend on the size, shape, and refractive index of the surrounding environment of the dispersed nanoparticles.[7−10] The shift of the SPR band also depends on the pH of the nanosuspension and the presence of different types of heavy metal ions.[11] Therefore, any changes in their surface structure and aggregation, the medium's refractive index, and the presence of other ions may affect the absorption band position and color of the nanoparticle dispersion.[8] Based on these plasmon resonance properties, several colorimetric sensor methods are developed.[12−14] The SPR is also used as an important descriptor to realize the chemistry within and around the metal nanosurfaces.[12,15,16] The colorimetric sensors provide a platform through the immediate color change in the presence of analyte and are highly demanding due to their simplicity, rapidity, high sensitivity, and ease of measurement. There are several methods for the detection of Fe(III), Hg(II), and Pb(II) based on chromophores or fluorophores, organic compounds, and polymers.[17−20] Shyamal et al. synthesized an anthracene based fluorescent probe, which exhibited Hg(II)-selective "on−off" type fluorescence switching via ground state complexation.[21] Zhao et al. prepared a thiocarbazone derivative based selective fluorescent sensor which underwent desulfurization reaction in the presence of Hg(II) ions.[22] Madhu et al. developed a benzimidazole substituted BODIPY sensor for the

Received: July 27, 2018
Accepted: October 4, 2018
Published: October 4, 2018

DOI: 10.1021/acsanm.8b01311
ACS Appl. Nano Mater. 2018, 1, 6099−6111

CONTENTS

Page No.

Chapter 1: A Concise Overview of Oxygen: Stability and Reactivity 1

1. Introduction..... 2-30

Chapter 2: Transition Metal-Free Molecular Oxygen Activation by Ionic Liquid for Selective Oxidation Reactions 31

2.1 Introduction..... 32-40

2.2 Result and Discussion..... 41-63

2.3 Conclusion 63-64

2.4 Characterization of Spectral Data **.....** 65-114

Chapter 3: Oxygen Activation by Ionic Liquid: A Detail Mechanistic Study.....115

3.1 Introduction..... 116-120

3.2 Methods..... 120-123

3.3 Result and Discussion..... 123-153

3.4 Conclusion 153-154

3.5 References..... 155-166

Summary

Developing mild, cost-effective, and selective oxidation methods to convert low-cost and valuable hydrocarbons into useful oxidative compounds is still a major challenge in organic synthesis. In organic chemistry and chemical biology, transition metal catalysts, or metalloenzymes, are typically required for most oxidation reactions. Among various oxidation strategies, the use of dioxygen (O_2) is acknowledged as a highly effective reagent.

This thesis explores the detailed study of the transition metal-free oxygen (O_2) activation process using ionic liquids for selective oxidation reactions. This thesis shows an efficient, cost-effective, and green protocol to transform hydrocarbons (benzylamine and alcohols) into useful oxidized compounds that are oxygenated (amide) and non-oxygenated (aldehyde, imine, and aromatic heterocycle). These compounds can be used as fine chemicals or as building blocks for chemical synthesis in the lab or in industry. This thesis's research describes first-principles calculations using Density Functional Theory (DFT), revealing that the various reaction coordinates and transition state spin densities demonstrate a unique spin conversion of triplet oxygen to singlet products via a minimum energy crossing point, without the assistance of transition metal ions. It talks about how quaternary alkylammonium-based ionic liquids make the π^* orbital of oxygen more stable, which makes it succeptable for hydrogen atom transfer from desired organic molecule in a mild, metal-free condition. This research elucidates the mechanism of O_2 activation using molecular orbital (MO) theory. The partial density of states (pDOS) calculations suggests a new approach for O_2 activation using quaternary alkylammonium-based ionic liquids instead of metal-based catalysts.

The thesis, entitled "**Transition Metal-Free Oxygen Activation by Ammonium-Based Ionic Liquids for Selective Oxidation Reactions: Experimental and Theoretical Studies**," is structured into three chapters:

- **Chapter 1** discusses the chemistry of the oxygen molecule and its reactivity in the presence of a transition metal catalyst.
- **Chapter 2** describes the efficient strategy for oxygen activation using quaternary alkylammonium-based ionic liquids, leading to the synthesis of valuable oxidized compounds from benzylamines and alcohols.
- **Chapter 3** presents a detailed mechanistic study of oxygen activation using quaternary alkylammonium-based ionic liquids.

Chapter 1

A Concise Overview of Oxygen: Stability and Reactivity

This chapter provides a concise overview of the chemistry of oxygen molecules, focusing on their stability and reactivity. It explores the unique characteristics of dioxygen, such as its triplet diradical ground state, through molecular orbital theory explanations. Despite its simplicity, oxygen stands as a remarkable molecule, constituting a significant percentage of Earth's atmosphere. This chapter describes its stability, which is attributed to its high resonance energy and adherence to the spin selection rule, rendering it inert under normal conditions. In this chapter, the significance of transition metals in altering the spin multiplicity of oxygen, thus enabling reactions to proceed, is highlighted. It gives an outline of how transition metal complexes are promising candidates for regulated oxygen activation and diverse reactive moods with oxygen, facilitating the synthesis of diverse and structurally important molecules through selective oxidation reactions.

1. Introduction

1.1 Photosynthetic Oxygen Production:

Plants play a critical role in the synthesis of oxygen through a process called photosynthesis. The process by which plants, algae, and some microorganisms transform solar light energy into chemical energy is known as photosynthesis. During this process, plants take in carbon dioxide from the air and emit oxygen as a by-product.

Here is a short overview of photosynthesis:

1.1.1 Absorption of Light:

Sunlight absorbtion is the first stage of photosynthesis, a critical event where a variety of pigments work together to complete the complex process of utilizing solar energy. These include phycobilins (phycoerythrin, phycocyanin), carotenoids (carotenes, xantophylls, and carotenoic acid), chlorophylls (a, b, c, and d typical for various taxonomic groups), and phycobilins (phycoerythrin, phycocyanin). Each of them has a unique light absorption pattern over the radiation spectrum.[1] The pigments are located within the chloroplasts, which serve as the sites of photosynthesis in plant cells. In this process, some of these pigments serve as "auxiliary" pigments, receiving energy and transmitting it to the "main" pigments, which carry out the most crucial photosynthetic reactions.

1.1.2 Conversion of Light Energy:

During photosynthesis, solar energy is absorbed by light-harvesting complexes, which consist of chlorophyll "a", auxiliary pigments such as carotenoids, phycobilins, and chlorophyll "b". This absorbed energy then activates electrons inside the chlorophyll molecules. Through light-dependent reactions, these excited electrons enable the synthesis of ATP (adenosine triphosphate) and NADPH (nicotinamide adenine dinucleotide phosphate), resulting in the

formation of energy-rich molecules that are crucial for subsequent biological activities.[2]

1.1.3 Splitting of Water:

The oxidation of water (H_2O), known as the photolysis process, is driven by absorbed solar energy. In this process, water molecules (H_2O) are split into hydrogen ions (H^+), electrons (e^-), and oxygen (O_2) as part of the light-dependent reactions. As a by-product, the released oxygen diffuses into the atmosphere.[3]

1.1.4 Calvin Cycle (Light-Independent Reactions):

The Calvin cycle, sometimes referred to as the light-independent reactions or the dark reactions, uses the ATP and NADPH produced in the light-dependent reactions. As a result of a series of enzyme processes that incorporate CO_2 from the air, glucose ($C_6H_{12}O_6$) and oxygen is produced in this phase **(Figure 1)**.[4]

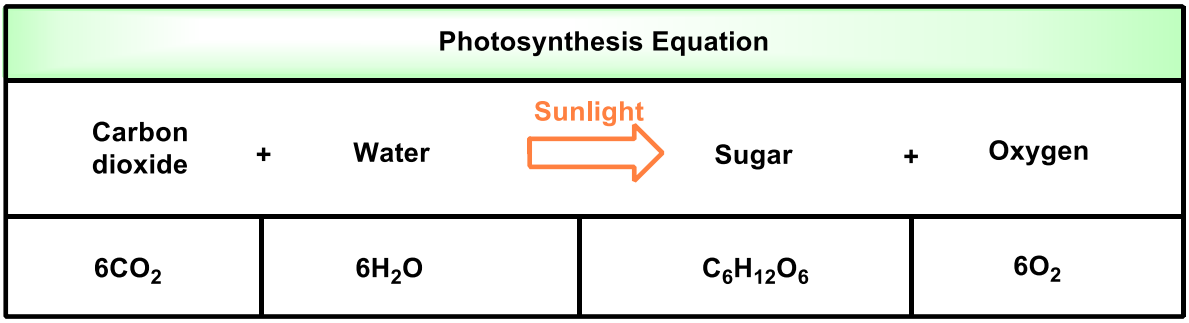

Figure 1. The process of photosynthesis is expressed by above equation, in which carbon dioxide and water combine to form sugar and oxygen, absorbing energy obtained through sunshine.

1.1.5 Oxygen Release:

As a by-product of the Calvin cycle, oxygen is produced. Through the stomata, it diffuses out of the plant and is discharged into the atmosphere.

Overall, a considerable amount of the oxygen produced by the Earth is due to plants. Through the process of photosynthesis, they contribute to the

equilibrium of atmospheric gases by absorbing carbon dioxide and releasing oxygen. For this reason, plants are frequently called as the "lungs of the Earth."

1.2 Discovery of Oxygen by the Scientific Community:

Even though the process of photosynthesis has been there since the beginning of time, nobody knew it even existed. This significant natural phenomenon wasn't just discovered by one scientist; rather, it was discovered by several scientists over more than 200 years. Belgian chemist, physiologist, and physician Jan Baptista van Helmont made some progress in understanding photosynthesis in the 1600s. Helmont conducted a 5-year experiment in which he placed a willow tree in a pot filled with soil and maintained it in a controlled environment. Over the five years, the willow tree was watered carefully. After completing his experiment, Helmont concluded that the tree's growth was not due to the soil but rather to the nutrients it had absorbed from the water. Helmont's conclusion was incorrect, but his experiment demonstrated that water is a factor in plant growth. Another scientist who contributed to the understanding of photosynthesis was Joseph Priestley. He was born in 1733 and later worked as a chemist, preacher, natural philosopher, teacher, and political theorist in addition to other professions. He conducted tests by lighting a candle and sealing a jar. Priestley observed that the flame vanished fast and that the air in the jar had been "injured". Similar experiments were conducted on mice, leading him to the conclusion that the mice had similarly caused harm to the atmosphere. Later, Priestley discovered that the air that the candle and the mice "injured" could be repaired by plants. Priestley's research findings were made public in 1774 with the publication of "Experiments and Observations of Different Kinds of Air, Volume I." Priestley's investigations demonstrated that air includes oxygen, even though he was unaware of this at the time.

Three chemists—an Englishman, a Swede, and a Frenchman—share credit for the discovery of oxygen. The first account of oxygen was written by Joseph

Priestley, who discovered it in 1774 by shining sunlight through mercuric oxide (HgO) and collecting the gas that resulted. He noticed that a candle burned brighter in it and that it was more comfortable to breathe in. Carl Wilhelm Scheele had discovered oxygen in June 1771, but Priestly was unaware of this. He had documented an account of his discovery but it wasn't published until 1777. Since French chemist Antoine-Laurent Lavoisier initially believed that oxygen was an acid maker since he was able to produce acids by burning phosphorus and sulfur and dissolving them in water, the name derives from the Greek words oxy for "acid" and genes for "forming." Both the English clergyman and chemist Joseph Priestly and the Swedish pharmacist and physicist Carl-Wilhelm Scheele independently discovered oxygen in the years 1771 and 1774, respectively. Since Priestly published first and Scheele's "Chemical Treatise on Air and Fire" didn't appear until 1777, Priestly is given credit for the discovery.[5]

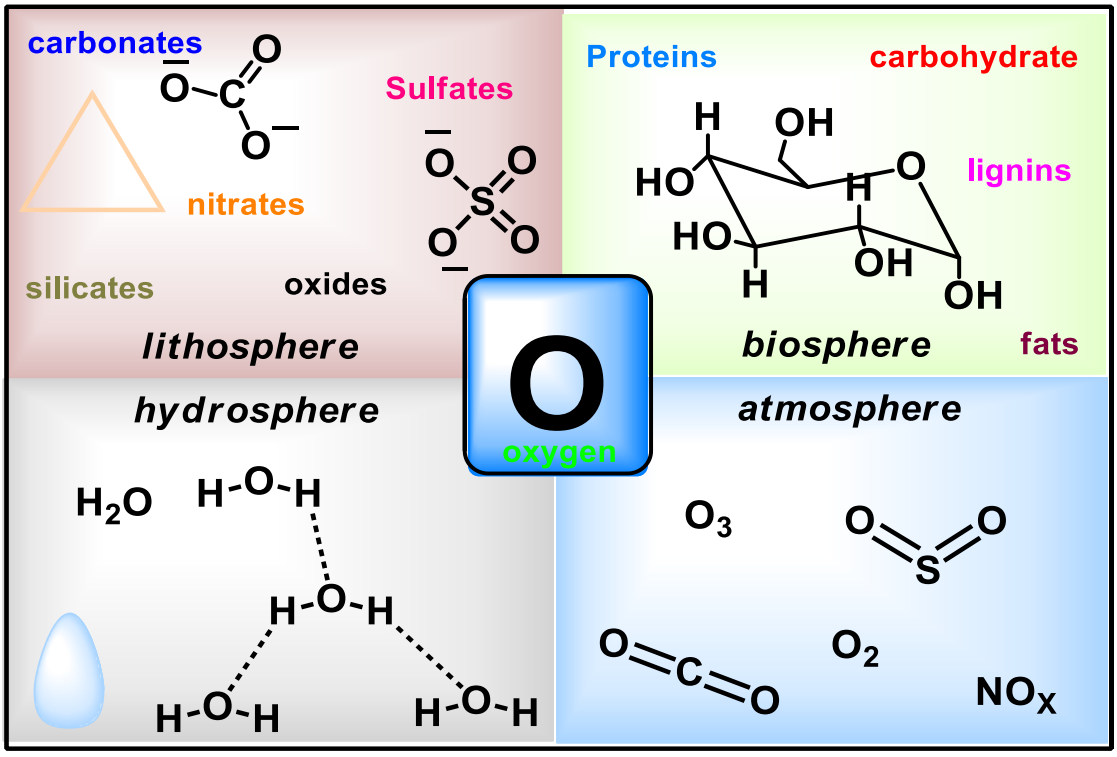

Figure 2. Existence of oxygen in the atmosphere, lithosphere, biosphere, and hydrosphere.

1.3 Electronic Structure of Oxygen:

So the plant created the most prevalent element by mass in the Earth's crust, hydrosphere, and biosphere is dioxygen O_2, which has the atomic number 8. Minerals (such as silicates, oxides, carbonates, sulfates, phosphates, and nitrates), water, and biomolecules (carbohydrates, lignin, proteins, and lipids) all include a significant amount of bonded oxygen (**Figure 2**).[6] All major elements of the world's biogeochemical cycles, including carbon, nitrogen, phosphorus, and sulfur, are oxygenated species.[7] Although each of these molecules undoubtedly holds considerable importance, ozone stands out as the most mobile and widely dispersed component of the oxygen family. There are various forms of elemental oxygen, the most significant of which is molecular dioxygen O_2 (here simply referred to as oxygen), which comprises 21% of the Earth's atmosphere.[8]

Due to its exceptional stability, it displays some attractive peculiar characteristics in terms of its magnetic behavior, energy transfer capabilities, chemical reactions toward different molecules, and existence in nature. The Lewis structure for the oxygen molecule O_2 is shown below.

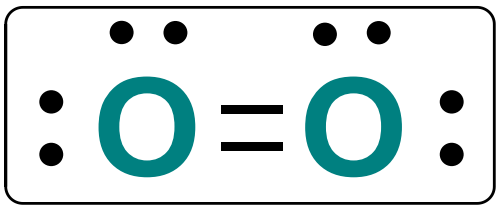

Figure 3. Lewis bond structure of dioxygen.

This electronic structure complies with every requirement of Lewis's theory. Every oxygen atom is surrounded by eight electrons, and in order to complete the octate configuration **(Figure 3)**, an O=O double bond is formed. This figure, however, conflicts with oxygen's magnetic properties. O_2 is not magnetic on its own, but it is drawn to magnetic fields. As a result, when liquid oxygen is

passed through a powerful magnet, it gathers between the magnet's poles and resists gravity. Paramagnetism, a type of attraction to a magnetic field, develops in molecules with unpaired electrons. The eminent English scientist and physicist Michael Faraday originally established that oxygen is paramagnetic, or attracted to a magnetic field, in the 1840s. The "molecular orbital theory" (also known as Hund-Mulliken theory after its creators), developed sixty years later by American chemist and physicist Robert Mulliken, explained for this property. Nevertheless, the Lewis structure of O_2 shows that every electron is coupled.

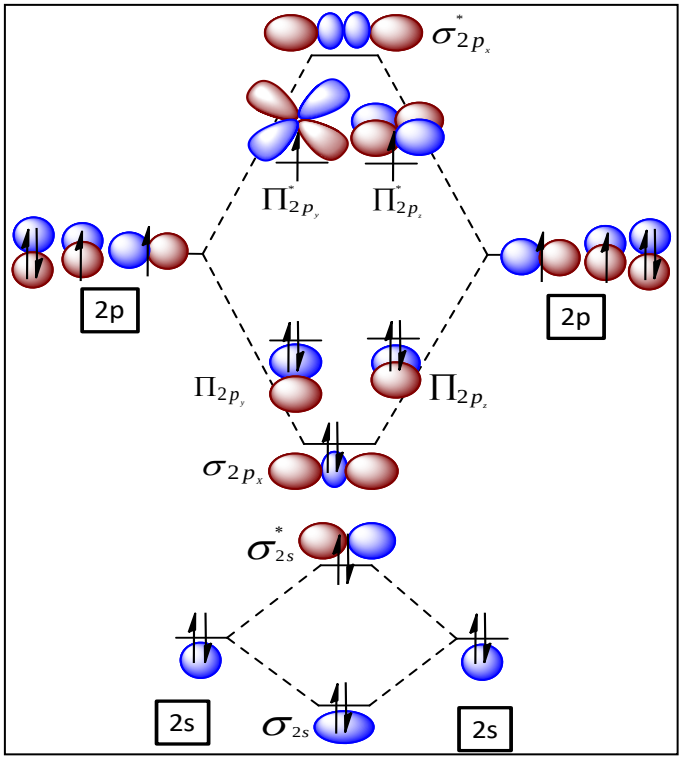

Figure 4. Molecular orbital diagram of dioxygen.

It was required to completely understand oxygen's electronic structure using molecular orbital theory to look into these peculiar characteristics of oxygen. The molecular orbitals of O_2 are filled with sixteen electrons by the Aufbau principle, which dictates that orbitals are filled starting from the lowest energy levels. The Pauli Exclusion Principle ensures that no two electrons can have the

same set of quantum numbers. As a result, six electrons are spread out between lower two π orbitals and higher two π* orbital, both of which are degenerate (see **Figure 4**). Following Hund's rule, the arrangement ensures that degenerate orbitals are filled with two electrons of the same spin before pairing them in a single orbital, thereby minimizing energy (see **Figure 4**).[9] The stable electronic configuration of oxygen gives rise to its diradical nature, paramagnetic characteristics, and triplet spin, despite the presence of several electronic states. A diradical is defined as a characteristic in which two electrons in a molecule (or atom) occupy two orbitals, Ψ_x and Ψ_y, that are either identical (degenerate) or nearly identical (pseudo-degenerate) in terms of energy levels.[9,10]

1.4 Various Electronic States of Oxygen:

The presence of degenerate orbitals is responsible for the distinctive triplet spin states observed in oxygen. Although a diradical can exist in multiple electronic states, it's crucial to examine the factors behind oxygen's preference for occupying particular degenerate orbitals. This section aims to provide a concise and lucid expression of the problem at hand. There are six distinct arrangements that allow for the allocation of two electrons among two orbitals **(Figure 5)**.

Configurations (a) and (b) are both called as singlets. These configurations are termed spin restricted closed-shell configurations and can be combined (±) to produce the symmetry-adapted two-configuration (TC) singlet states:

$$\psi_{S_{TC\pm}} = \frac{\left|\psi_x^{\alpha}(1)\psi_x^{\beta}(2)\right\rangle \pm \left|\psi_y^{\alpha}(1)\psi_y^{\beta}(2)\right\rangle}{\sqrt{2}} = \frac{\left|\psi_x^2\right\rangle \pm \left|\psi_y^2\right\rangle}{\sqrt{2}} \qquad \textbf{Equation 1}$$

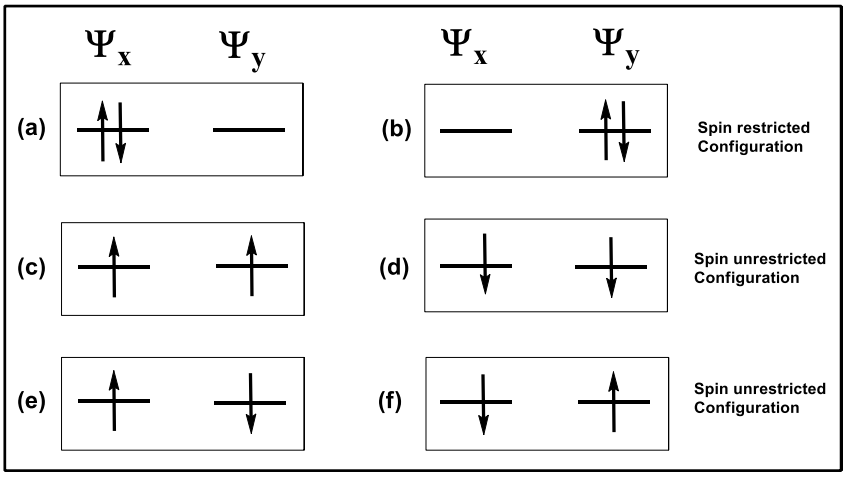

Figure 5. All Possible electronic configurations are considered, achieved by distributing two electrons across two degenerate orbitals labeled as Ψx and Ψy.

The Dirac ket represents a solitary Slater determinant. On the contrary, configurations (c) and (d) correspond to the M_S = ±1 components of a triplet (T):

$$\psi_{T_{+1}} = \left|\psi_x^{\alpha}(1)\psi_y^{\alpha}(2)\right\rangle \qquad \textbf{Equation 2}$$

$$\psi_{T_{-1}} = \left|\psi_x^{\beta}(1)\psi_y^{\beta}(2)\right\rangle \qquad \textbf{Equation 3}$$

The last two configurations, labeled as (e) and (f), represent mixed spin states. Rather, their linear combinations yield the M_S=0 triplet component (ψ_{T_0}) and the open-shell (OS) singlet ($\psi_{S_{os}}$):

$$\psi_{T_0} = \frac{\left|\psi_x^{\alpha}(1)\psi_y^{\beta}(2)\right\rangle + \left|\psi_x^{\beta}(1)\psi_y^{\alpha}(2)\right\rangle}{\sqrt{2}}$$

$$= \frac{[\psi_x(1)\,\psi_y(2) - \psi_y(1)\,\psi_x(2)\,][\alpha(1)\beta(2)+\alpha(2)\beta(1)]}{2} \qquad \textbf{Equation 4}$$

$$\psi_{S_{os}} = \frac{\left|\psi_x^{\alpha}(1)\psi_y^{\beta}(2)\right\rangle - \left|\psi_x^{\beta}(1)\psi_y^{\alpha}(2)\right\rangle}{\sqrt{2}}$$

$$= \frac{[\psi_x(1)\,\psi_y(2) + \psi_y(1)\,\psi_x(2)\,][\alpha(1)\beta(2)-\alpha(2)\beta(1)]}{2} \qquad \textbf{Equation 5}$$

Unrestricted wavefunctions allow different spatial distribution for electrons with α spins and β spins therefore can describe spin polarization. Spin polarization occurs due to exchange-correlations effects via the interactions of the electrons of the same spin as an unpaired electron in the open shell (e.g. radical) system. Unrestricted wavefunctions do not have the proper and well defined value of spin, i.e. are not eigenfunctions of $\widehat{S^2}$. They suffer from the spin contamination by states with higher spin. For example, open shell singlet states will be contaminated (have an admixture) of triplet, quintet etc.

In the absence of an external magnetic field, the three components of the triplet state are degenerate, and the spin-orbit coupling and the minor spin-dipole coupling between the unpaired electrons are not considered. The energy associated with this particular condition is followed according to **Equation 6**.

$E_T=h_x+h_y+J_{xy}-K_{xy}$ **Equation 6**

The values of h_x and h_y represent the individual energies of ψ_x and ψ_y orbitals, respectively. Additionally, J_{xy} and K_{xy} denote the corresponding Coulomb and exchange integrals.

For degenerate ψ_x and ψ_y, $h_x = h_y$. The antisymmetric spatial function in the triplet state essentially reduces the chance of both electrons being present at the same place at the same time. The interelectron interaction is decreased by a positive quantity denoted as K_{xy}.[11]

The energy associated with the singlet wave function $\psi_{S_{os}}$ reads

$E_{S_{OS}}=h_x+h_y+J_{xy}+K_{xy}$ **Equation 7**

Compare to the triplet state, the singlet state exhibits a symmetric spatial function that enhances the likelihood of both electrons occupying the same spatial area. Consequently, this leads to an increase in the singlet energy by the value of K_{xy}.

Equations 6 and **7** demonstrate that when the optimum molecular orbitals (MOs) for the triplet and open-shell singlet states are the same, the triplet state's energy decreases by $2K_{xy}$ compared to the open-shell singlet state. This reduction is due to Pauli repulsion, which hinders electrons with parallel spin proximity, reducing overall electrostatic repulsion energy. This phenomenon is fundamental to Hund's rule principles and can occur when there is a difference between MOs in singlet and triplet states.[9]

The energy associated with the pair of closed-shell singlet wave functions is provided by

$$E_{S_{TC\pm}} = h_x + h_y + \frac{J_{XX} + J_{YY}}{2} \pm K_{xy} \qquad \textbf{Equation 8}$$

According to **Equation 8**, the corresponding energy of the $\psi_{S_{TC-}}$ wave function is $2K_{xy}$ lower than that of the $\psi_{S_{TC+}}$ wave function. Subsequently, the difference in energy levels between the lower closed-shell singlet and the open-shell singlet is calculated by **Equation 9**.

$$E_{S_{OS}} - E_{S_{TC-}} = J_{xy} - \frac{J_{XX} + J_{YY}}{2} + 2K_{xy} \qquad \textbf{Equation 9}$$

It can be concluded that when two electrons occupy two degenerate orbitals, ψ_x and ψ_y, can be classified into two pairs. They form four states grouped into two pairs. Each pair shows a consistent spacing of $2K_{xy}$. **Equation 9** dictates how these pairs are arranged relative to each other, determining the final sequence of the spectroscopic states.

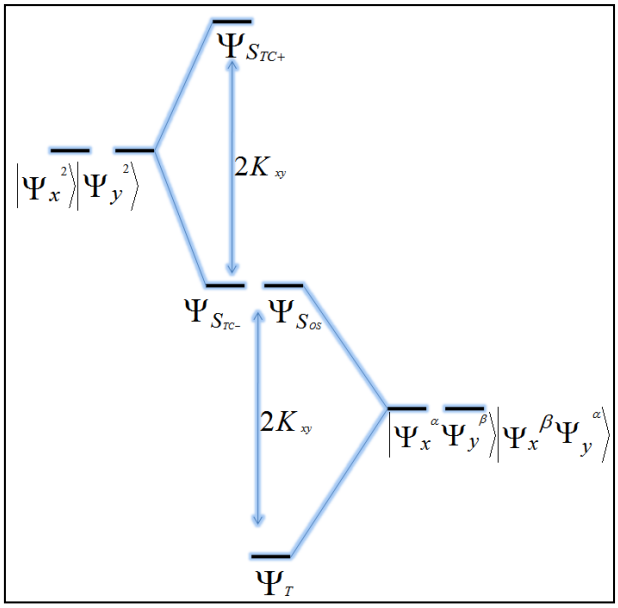

Figure 6. The relative energy levels of the four states formed by distributing two electrons across two orbitals. The spatial arrangement of these state pairs is dictated by **Equation 9**. The scenario depicted corresponds to a condition where the value on the right-hand side of the equation equals zero.

Molecular oxygen, denoted as O_2, exhibits three spectroscopic states, namely one triplet state and two singlet states. Specifically, the bottom closed-shell singlet state and the open-shell singlet state possess the same energy level, resulting in a degenerate singlet state. This degenerate singlet state corresponds to the middle panel seen in **Figure 6**.[12] It is worth noting that **Equation 9** reveals the presence of degeneracy between the wave function $\psi_{S_{OS}}$ and $\psi_{S_{TC-}}$

If $\frac{J_{xx}+J_{yy}}{2} = J_{xy} + 2K_{xy}$. This equality comes usually induced by symmetry.

In the context of $D_{\infty h}$ symmetry, the three spectroscopic term symbols representing the three low-lying states of O_2 are as follows: $^3\Sigma_{g-}$, $^1\Delta_g$, $^1\Sigma_{g+}$ states; The order of energy is depicted in **Figure 7**.

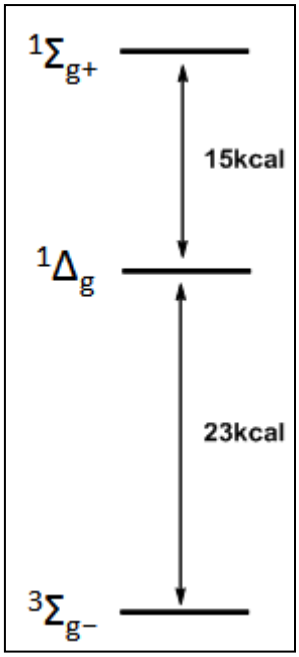

Figure 7. The energy ordering of the low-lying states of molecular oxygen (O_2). The state $^1\Delta_g$ is a double degenerate nature.

Valence bond theory (VBT) and molecular orbital theory analysis indicate that the $^1\Delta_g$ state is characterised by both an open-shell component and a closed-shell component.[13,14] In addition, the conclusion was further validated using point group analysis. **Figure 7** illustrates that the $^1\Delta_g$ representation in the $D_{\infty v}$ point group splits into two distinct irreducible representations in its point subgroup of C_{2v}. In this subgroup, the open-shell (OS) and closed-shell (CS) determinants correspond to A_2 and A_1 symmetries, respectively. Therefore, the configurations in the $^1\Delta_g$ state were formed by combining two open-shell determinants $\left|\psi_x^{\alpha}(1)\psi_y^{\beta}(2)\right\rangle + \left|\psi_x^{\beta}(1)\psi_y^{\alpha}(2)\right\rangle$ and two closed-shell determinants $\left|\psi_x^2\right\rangle - \left|\psi_y^2\right\rangle$ and the configuration of the $^1\Sigma_{g+}$ state was characterized as the combination of the two closed-shell determinants with the same sign. The $^1\Sigma_{g+}$ state is characterized by the wavefunction $\psi_{S_{TC+}}$ as seen in **Figures 6** and **7**.

The $^3\Sigma_{g-}$ of O_2 is roughly $2K_{xy}$ = 23 kcal/mol lower than that of the degenerate singlet state characterized as "open-shell" or "closed-shell" $^1\Delta_g$ and the second singlet $^1\Sigma_{g+}$ state, which is at a higher energy level, is approximately 38 kcal/mol above the ground state $^3\Sigma_{g-}$, were calculated by using absorption experiments.[15] The $^1\Sigma_{g+}$ state has a short lived and rapidly undergoes decay to the $^1\Delta_g$ state through a spin-allowed transition between the two singlet levels. But the transition from the $^1\Delta_g$ state to the $^3\Sigma_{g-}$ state is not allowed due to spin restrictions, and the duration of the $^1\Delta_g$ state is approximately 106 seconds. The $^1\Delta_g$ state has been identified as the metastable O_2 species, generally referred to as "singlet oxygen".

In the $^3\Sigma_{g-}$ electronic state of O_2, the presence of parallel spins among the electrons prevents their simultaneous occupation within specific spatial areas. While oxygen can be classified as a diradical based on the previous definition, it is important to emphasize the exceptional nature of its features. The remarkable stability of O_2 can be attributed mostly to its remarkable resonance stability, despite its diradical character.

1.5 Stability of Triplet Oxygen ($^3O_2$)

1.5.1 Resonance Stabilization of Oxygen:

Figure 8 shows the four resonance configurations are formed when six electrons, four with α-spin and two with β-spin, are placed in the four $2p_x$ and $2p_y$ π atomic orbitals in the triplet ground state oxygen molecule's. In each 2p-πAO, there's one α-spin electron. Meanwhile, the β-spin electron in each of the two perpendicular π systems spreads across the 2p-π atomic orbitals of both oxygen atoms.

Zwitterionic structures B and C show how the β-spin electrons spread across the two perpendicular π systems, similar to the second resonance structure for the peroxyl radical in **Figure 8b**. If resonance structures A, B, and C accurately represent the wave function of •OO•, it's expected that electron delocalization in

•OO• would provide a stability level akin to that observed in the two peroxyl radicals (**Figure 8**).

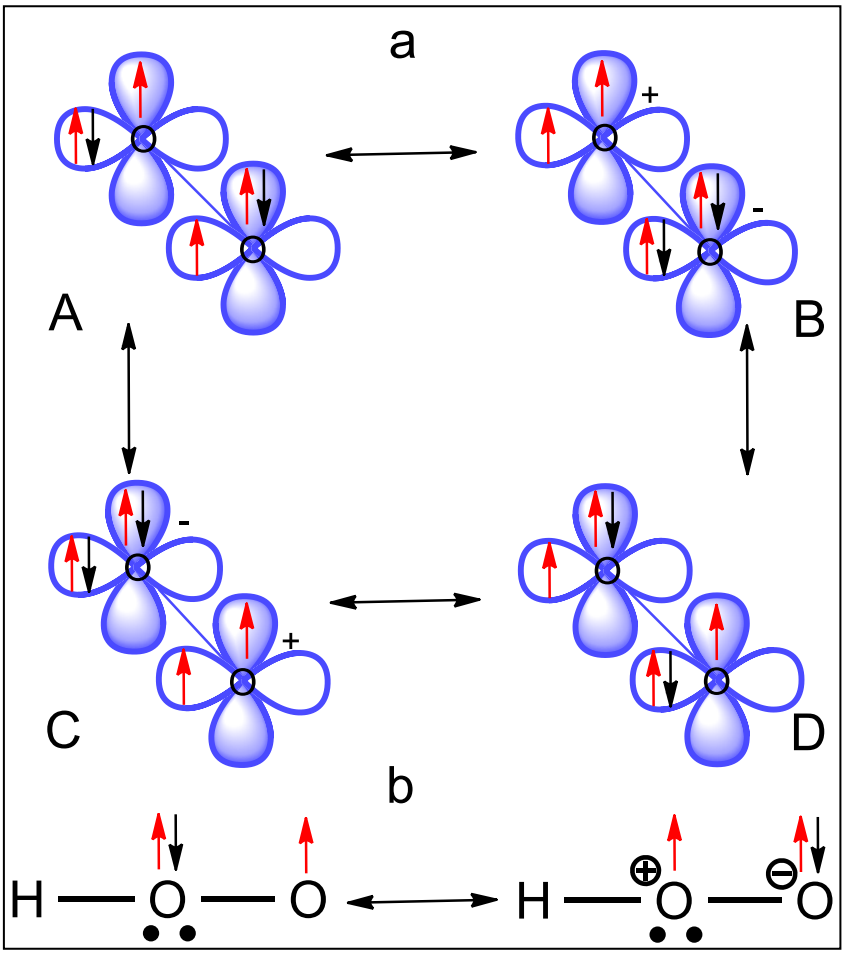

Figure 8. **(a)** The probable arrangements, labeled as A to D, depict how the two β-spin electrons are positioned within the two perpendicular π systems of the triplet •OO•. Meanwhile, the four α-spin electrons occupy the four 2p-π atomic orbitals. This results in delocalization solely among the β-spin electrons, as illustrated in resonance structures A to D. **(b)** Resonance stabilization of the hydroperoxyl radical through three-electron, two-center bonding. In this and following figures, α-spin electrons are represented in red, while β-spin electrons are depicted in black.

With two •OOH radicals as the reference, reaction **C** from **Table 1** would yield a resonance energy of 37–38 kcal/mol for •OO•. The delocalization energy of •OO• increases by 37-38 kcal/mol due to the contribution from resonance structure D in **Figure 8b**, surpassing the delocalization energy of two molecules

of •OOH. Structures A and D exhibit a lack of charge separation compared to resonance structures B and C. Therefore, resonance structures A and D in **Figure 8** are anticipated to be the main contributors to the wavefunction governing the behavior of electrons in the two perpendicular π systems. The bonding in O_2 shown in **Figure 8** is explained using valence bond (VB) theory. At first, it looks like it is not linked to the molecular orbital (MO) representation of the triplet state of the O_2 molecule. The connection between the valence bond (VB) and molecular orbital (MO) representations will be explained in the following section.[16]

1.5.2 Understanding the Thermodynamic Stability of the Triplet •OO• Diradical: A Valence Bond Approach

The VB hypothesis, similar to the MO theory, concludes that O_2 possesses a diradical character, exhibiting a triplet ground state.[17,18] The connection between MO theory and valence bond theory may be shown through the Generalized Valence Bond (GVB) theory, which was first developed by Goddard and colleagues.[19] How does the valence bond theory explain the 37-38 kcal/mol increase in stability due to electron delocalization in the triplet •OO• compared to two molecules of •OOH? The four structures seen in **Figure 8** are considered to be the primary resonance structures for the triplet •OO•. The VB computations performed by McWeeny are of particular academic interest,[20] found that the most favourable VB wave function is followed by **Equation 10**.

$$\Psi(VB)=0.59(A+D)-0.23(B+C) \qquad \textbf{Equation 10}$$

Non-zwitterionic structures A and D carry more weight in the overall wave function compared to zwitterionic structures B and C. This is because structures B and C involve the relocation of a single electron, while structures A and D involve the relocation of two electrons. The interaction between structures A and D with structures B and C results in more resonance energy than the

interaction between structures A and D alone.[21] The limited VB wave function has a higher energy than the optimized VB wave function.

Table 1. Reaction Enthalpies ΔH (298.15 K), in kcal/mol, calculated from Experimental Heats of Formation, $\Delta_f H°$ (298.15 K), and G4 Calculations ΔH (298.15 K)

		ΔH(298.15 K)	
Reaction label	Reaction	G4 value	ATcT value
A	•OH + H_2O_2 → H_2O + •OOH	−31.6	−31.0
B	•OH + •OOH → H_2O + •OO•	−69.0	−69.2
C	2•OOH → HOOH + •OO•	−37.4	−38.2
D	2•OH + HOOH → 2H_2O + •OO•	−100.6	−100.2

Harcourt studied the energy linked with the wave function in the valence bond framework, considering structures A-C and omitting structure D, to relate to an •OO• molecule. The energy difference between the incomplete VB wave function was 25.6 kcal/mol, which is 11-12 kcal/mol lower than the experimental and G4 enthalpies of reaction **C Table 1**. The delocalization energy in triplet •OO• is 37-38 kcal/mol higher than that in two molecules of •OOH. Harcourt compared the energy of the wave function in the valence bond model to the energy calculated for structure A, which lacks resonance stabilization. Su et al. found a lower energy of 102.6 kcal/mol for a valence bond wave function comprising structures A-D compared to structure A alone.

1.5.3 Resonance energy of Triplet Oxygen:

Summing reactions **A** and **B** in **Table 1** gives

2•OH+HOOH→2H_2O+•OO• **Equation 11**

The reaction labeled **D** in **Table 1** has an enthalpy of -100.6 kcal/mol, according to calculations using the G4 method. Moreover, experimental data gives a value of -100.2 kcal/mol for the enthalpy. This reaction releases a lot of heat because two unpaired electrons from two hydroxyl radicals join together to form a two-center, three-electron bond in an oxygen molecule. This makes the reaction very exothermic. So, **Equation 11** (also known as reaction **D** in **Table 1**) seems to describe well how the energy is spread out or shared within O_2. Using reaction **C** from **Table 1** instead of reaction **D** would yield a resonance energy of 37-38 kcal/mol for •OO•, with two •OOH radicals as the reference.

Reaction **A** shows that each •OOH radical has resonance stabilization energy of about 31−32 kcal/mol. The resonance stabilization energy of •OO•, which is 100 kcal/mol, includes the combined effects of the stabilization provided by each of the two three-electron bonds in this diradical. There's extra stabilization because both three-electron bonds are in the same molecule at the same time. The **Equation 11** (reaction **D** of **Table 1**) as a reliable indicator of the resonance stabilization of the oxygen molecule implies that the resonance energy of triplet •OO•, at 100 kcal/mol, is roughly three times greater than Kistiakowski's reported value of 36.5 kcal/mol for the resonance energy of benzene concerning the double bonds present in three molecules of cyclohexene.[22] The presence of high resonance energy renders oxygen molecule unreactive, or kinetically inert, in the absence of any catalyst.

1.5.4 Spin Rule Violation of Oxygen:

Due to its significant resonance energy, triplet oxygen exhibits a lack of reactivity towards a wide range of chemical entities, without a catalyst. The triplet ground state of molecular oxygen consists two unpaired electrons exhibiting parallel spins, resulting in the spectroscopic term $^3\Sigma_{g^-}$.[23] The involvement of triplet oxygen in oxidation processes in organic substrates, including oxygen insertion into hydrocarbon structures and oxidative

dehydrogenation, is a significant process. Organic substrates, such as hydrocarbons, alcohols, ketones, and acids, exhibit closed-shell electronic structures in their ground state, resulting in a singlet spin state. When a chemical reaction occurs between reactants (triplet oxygen and singlet organic molecule) with different spin states and the formation of products exclusively in the singlet state is prohibited, this is in accordance with Wigner's spin selection rule.[24] To provide a comprehensive understanding of this crucial process, let us examine the general oxidation process of a hydrocarbon, namely an alkane (R-H), is reacted with ground state oxygen, O_2 ($^3\Sigma_{g-}$), leading to formation of a ketone (K=O) and water (as seen in **Equation 14** and **Table 2**).

$R\text{-}H+O_2\ (^3\Sigma_{g-}) \rightarrow K{=}O+H_2O$ **Equation 12 Table 2**

It is necessary for the transition state $[R\text{-}H\cdots O_2]^{\ddagger}$ to possess a total spin $S_{RH\cdots O2\ddagger}$ dictated by the spin selection rules. This total spin can be achieved by either an algebraic combination of $S_{R\text{-}H}$ and $S_{3_{O_2}}$ (representing the reagents) or through $S_{K=O}$ and S_{H2O} (representing the products), with a minimum shared sum. The angular momenta are combined vectorially, and in the given reaction, the spins of the reactants are denoted as $S_{R\text{-}H} = 0$ and $S_{3_{O_2}} = 1$.

These spins are combined to get a total spin of $S_{Reactants} = 1$. While the singlet products $S_{K=O} = 0$ and $S_{H2O} = 0$ may only result in a sum of $S_{Products} = 0$. The reaction is prohibited by spin due to the inequality between the spin states ($S_{Reactants} \neq S_{Products}$) of the reactants and products.

1.6 Natural Oxidative Process using Atmospheric Oxygen:

At normal conditions, atmospheric oxygen is a colorless, odorless gas; nevertheless, it has a blueish color when it is liquid (b.p.: 183 °C) or solid (m.p.: 218 °C).[7] Although triplet oxygen exhibits kinetic persistence in its interactions with the majority of molecules, it becomes very reactive when it interacts with other radicals. Under the same reaction conditions where the more reactive

peroxyl radicals ROO* readily engage in such H atom transfer (HAT), triplet oxygen does not readily extract hydrogen atoms to produce HOO*. This is due to the exceptionally high resonance stabilization energy of $^3O_2$, which influences strong bonds and is already accounted for by the valence bond (VB) and molecular orbital theories.[16] Because of its diradical nature, oxygen reacts with almost everything on Earth's surface, releasing energy that favors the reaction process. High activation barriers, however, greatly slow down its reactivity, meaning it typically reacts slowly despite its high bond energy.

Table 2. In the following table, a general reaction is depicted. A typical organic compound with the molecular formula R-H is considered as the substrate, reacting with triplet ground state oxygen to yield singlet R=O and water via a transition state. In this specific case, when the number of reactants with spin ($S_{Reactants}$) equals 1 and the number of products with spin ($S_{Products}$) equals 0, the only feasible combination is $1 \neq 0$. Consequently, the reaction is restricted due to spin rule violation.

	Reactants	**Transition state**	**Products**
	R-H + O_2 ($^3\Sigma_{g^-}$) **Equation 12**	R-H···O_2‡ **Equation 13**	K=O + H_2O **Equation 14**
Spin	$S_{R\text{-}H} = 0$ $S_{O_2} = 1$	Requires: $\lvert S_{R\text{-}H} \pm S_{O_2} \rvert = \lvert S_{K=O} \pm S_{H2O} \rvert$	$S_{K=O}=0$ $S_{H2O} = 0$
Multiplicity of spin 2S + 1	1 3		1 1
Spin state	Singlet Triplet		Singlet Singlet

The hydrogen balloon won't explode until there is activation energy in the form of a spark. Likewise, paper doesn't spontaneously catch fire in the air until it reaches a temperature of roughly 230°C. Organic substances burn through several exothermic radical processes.[25,26] Due to their extremely high surface

area, fine dispersion of flammable substances in O_2/air (such as flour, coal dust, organic solvent vapors, etc.) can result in explosive combinations. The blazing splint test, employed in school laboratories to detect oxygen (or other oxidizing gases), makes use of the fact that flames burn more intensely in pure oxygen than in air. Even larger reactivities are seen in liquid oxygen; for instance, trinitrotoluene (TNT) and liquid oxygen together produce an explosive.[6] When handled with liquid $^3O_2$, several relatively common compounds, such as auto gasoline or other hydrocarbons, transform into extremely potent explosives.[27]

Throughout millions of years, photosynthesis has oxidized water, resulting in the oxygen that makes up the Earth's atmosphere. The continuous supply of oxygen is directly necessary for all higher living forms on earth. Adenosine triphosphate (ATP), the cellular "energy currency" that powers numerous processes in living cells, is produced during the aerobic respiration process as a result of the reduction of $^3O_2$ to water, which is a crucial stage in the process. The transfer of oxygen into the cells of virtually all vertebrates occurs via the reversible binding to the iron-containing protein hemoglobin[28] in red blood cells (**Figure 9**), which is a closely analogous interaction of oxygen with an iron atom.[29] Additionally, oxygen plays a crucial role in a variety of enzyme-catalyzed biosynthetic pathways that change molecules for energy and heat release, digestion, detoxification, signaling pathways, and other processes. $^3O_2$ is used by oxidases, monooxygenases, and dioxygenases as an oxidant and a source for adding one or two oxygen atoms to proteins. Enzymatic hydroxylations and epoxidations are among the most common oxidative mechanisms.[30,31] The function of $^3O_2$ in the blinking of fireflies is a particularly unique application (**Figure 9**). The dioxetane intermediate, an unstable four-membered ring, is formed when the enzyme luciferase catalyzes the interaction between molecular oxygen and luciferin. Oxyluciferin is produced when CO_2 is eliminated in a thermally excited condition. The emission of a photon occurs

simultaneously with the transition into the ground state. The firefly therefore sparkles. Similar oxygen-dependent bioluminescence mechanisms are also present in bacteria, algae, jellyfish, and squids, among other organisms.[32] Another real-world example of redox reactions is the process of corrosion. Some of the oxygen molecules in water oxidize iron (or the metal) when they come into touch with metal, like an iron door.

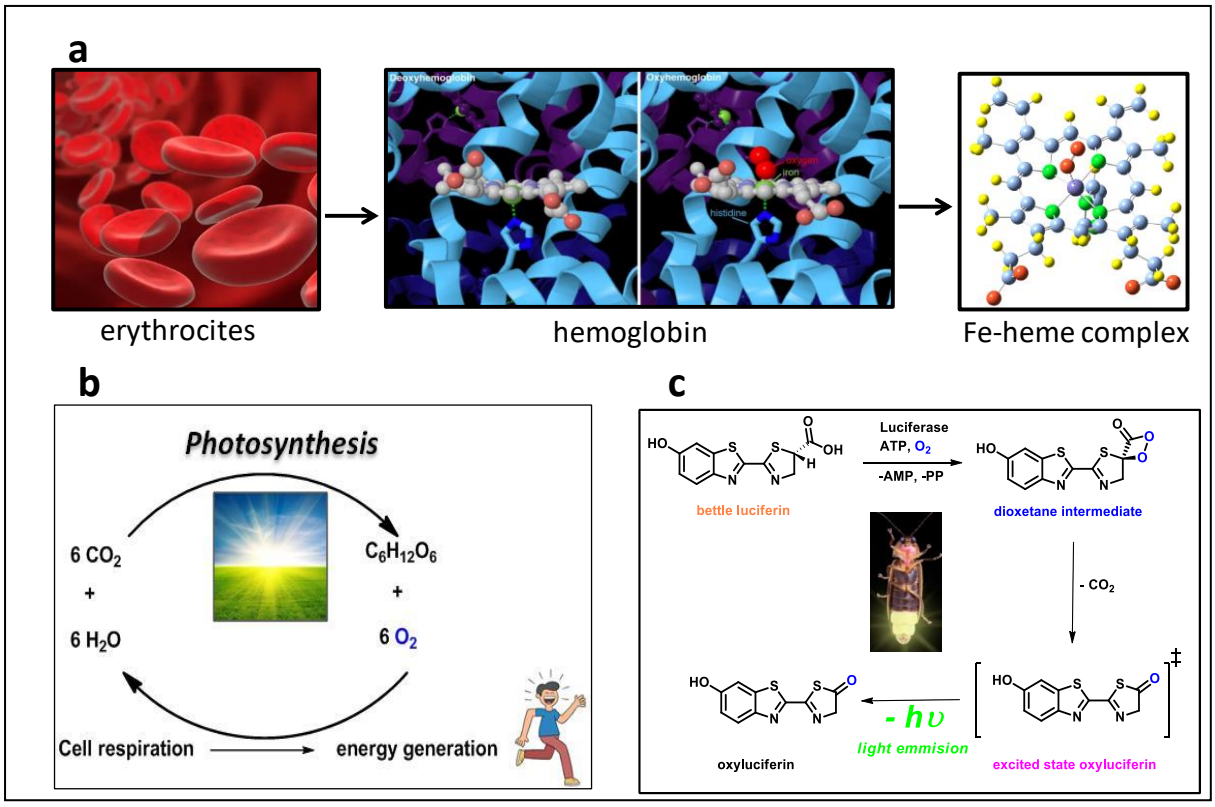

Figure 9. The figure illustrates multiple reaction routes involving oxygen.

Furthermore, carbon, hydrogen, and oxygen make up the bulk of all biological things in nature. Any living thing that dies causes its organic components to begin interacting with oxygen.

The involvement of diradical oxygen molecules is significant in autoxidation reactions,[33] as well as combustion processes. These reactions can yield a range of compounds, often exhibiting non-selective branching or oxidation states.[34] The oxidation of organic substrates by ground-state molecular oxygen O_2 ($^3\Sigma_{g^-}$)

occurs at an exceptionally slow rate when catalysts are absent.[35] This suggests that the presence of a catalyst is necessary for rapid oxidation processes, including oxygen activation, in addition to modifying the oxygen's multiplicity of spin to facilitate the reaction. In order to bind and activate oxygen, a metal must have the appropriate spin, despite the fact that spin selection principles are typically regarded as a possible explanation for low catalyst reactivity.

1.7 Transition Metal Catalyzed Oxygen Activation Pathways

1.7.1 Oxygen Activation by a Metal:

In consideration of these properties, different strategies are applied to activate oxygen in order to modify its spin state and control the resulting reactivity of activated oxygen species. Usually, spin selection restrictions can be avoided by activating paramagnetic ground state oxygen with another paramagnetic center, which is a transition metal M in the appropriate oxidation state n.[36,37] When triplet oxygen encounters a reaction with a transition metal M^n, which donates one electron to oxygen in its triplet state, it forms the oxygen superoxide $O_2^{\bullet-}$ (or O_2^-).[38]

$$M^n + \bullet OO\bullet \rightarrow M^{n+1} - O_2^{\bullet-} \qquad \textbf{Equation 15}$$

The initial metal center M^n must be paramagnetic, or possess unpaired electrons, for the metal to be in an appropriate oxidation state. This allows for reactions with O_2 ($^3\Sigma_{g-}$). The most often employed transition metals in catalysis are $Mo^{3+,5+}$, $Fe^{2+,3+}$, $Co^{2+,\ 3+}$, $Ni^{1+,\ 2+,\ 3+}$, $Mn^{2+,\ 3+,\ 4+}$ and Cu^{2+}.[39] Once the superoxide radical ($M^{n+1} - O_2^{\bullet-}$) is formed, a range of metal-oxygen species, including metal peroxo monomer ($M^{n+2} - O_2^{2-}$) and metal peroxide dimer species ($M^{n+1} - O_2^{2-} - M^{n+1}$), often referred to as η-peroxo and μ-peroxo complexes, can be generated (**Scheme 1**).[40] These η-peroxo and μ-peroxo complexes form as reactive intermediates when metals like Mo or V catalyze the oxidation of alkanes in the presence of oxygen donors[41,42], as well as the epoxidation of alkenes by W, Cr,

and Mo.[43] The peroxo species can subsequently go forward into two oxo-metal (M^{n+2}=O) centers or a single dioxo-metal center (M^{n+4}=O_2) (**Scheme 1**).[44]

In the last stage of both methods, four electrons are donated to molecular oxygen by a process called a metal-centered oxygen transfer reaction (**Scheme 2)**. This happens regardless of whether the metal forms two oxo units or a single dioxo species as a result of the oxygen addition.[45] A possible pathway for the following metals: Os, Ru, Ti, V, Cr, Ir, Mn, Ta, Nb, Mo, and W.[46,47] Thus, a process of metal-induced electron transfers can activate ground-state triplet oxygen, resulting in the formation of oxide, superoxide, peroxide, species.

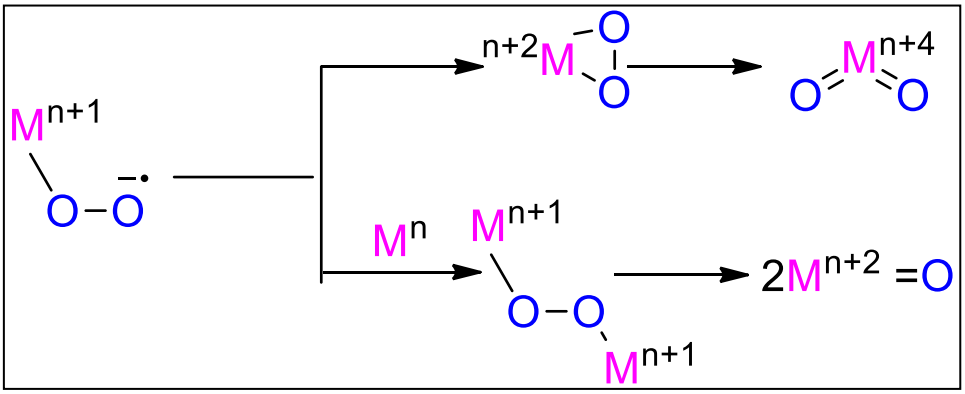

Scheme 1. This scheme illustrates the reaction of a transition metal M^n, with oxygen, leading to the initial formation of a superoxo species ($M^{n+1}-O_2^{\bullet-}$). This species can further proceed through η-superoxo and μ-peroxo complexes, ultimately resulting in either a single metal dioxo species (M^{n+4}=O_2) or two metal oxo species (M^{n+2}=O).

The formation of singlet oxygen by irradiation of the photocatalyst, followed by inter-system crossing, as well as the dissociation of molecular oxygen into atomic oxygen, are other ways that activation can take place without the transfer of electrons.

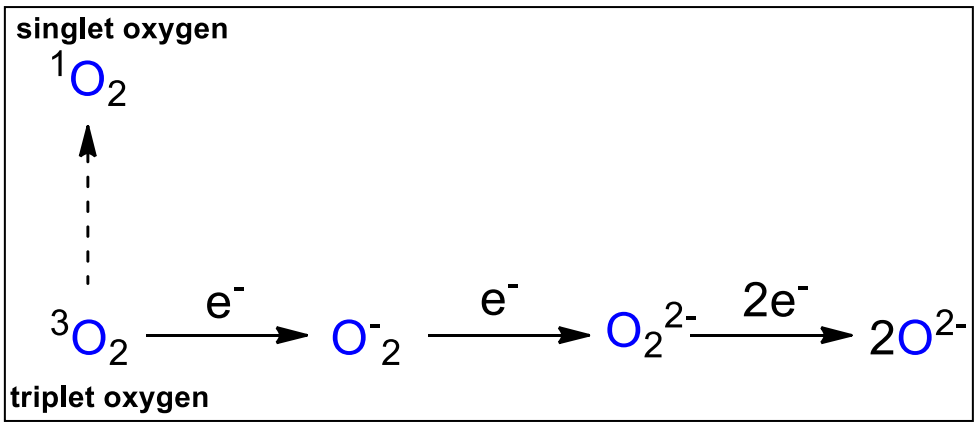

Scheme 2. This scheme outlines molecular oxygen reduction pathways based on the number of electrons involved. Through successive electron transfers, ground-state triplet oxygen can be activated to form superoxide, peroxide, and oxide species. Alternatively, singlet oxygen formation can occur via irradiation and inter-system crossing without requiring electron transfer.

However, η-peroxo species don't always need to develop into oxo-metal species; they can alternatively be reactive species on their own. For example, in the Sharpless process for alkenes[48] epoxidation, one of the initial molecular oxygen atoms finds itself in the oxidation product, while the other oxygen atom forms a single oxo-metal species (**Scheme 3**).[49]

Among these metal-oxygen species, scientists and studies often focus the most on metal superoxo complexes ($M^{n+1} - O_2^{\bullet-}$) and metal oxo species ($M^{n+2}=O$).[50] Recently, there has been a lot of interest in metal-superoxo species for fine chemical applications, as Fe^{III}-superoxo or Cu^{II}-superoxo intermediates are believed to be crucial in oxygenation processes by non-heme iron enzymes. In mild conditions, these superoxo complexes may oxidize industrially important substrates like cyclohexene and cyclooctene to produce allylic oxidation products (**Figure 10**).

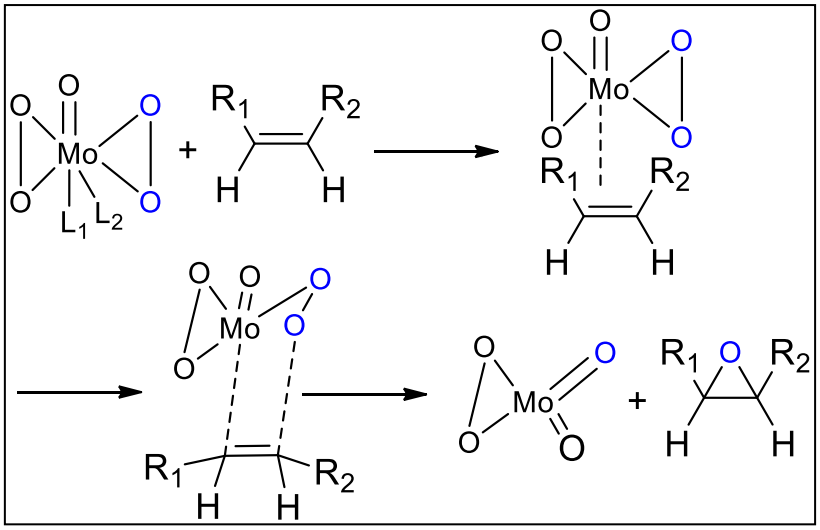

Scheme 3. In the Sharpless mechanism, alkenes undergo epoxidation. The molybdenum peroxo complex $MoO(O_2)L1L2$, where L1 is hexamethylphosphoramide (HMPA) and L2 is water, facilitates this reaction. Through the addition of one oxygen atom to the substrate and simultaneous formation of an oxo-metal species, the η-peroxo reagent induces the epoxidation of the alkene.

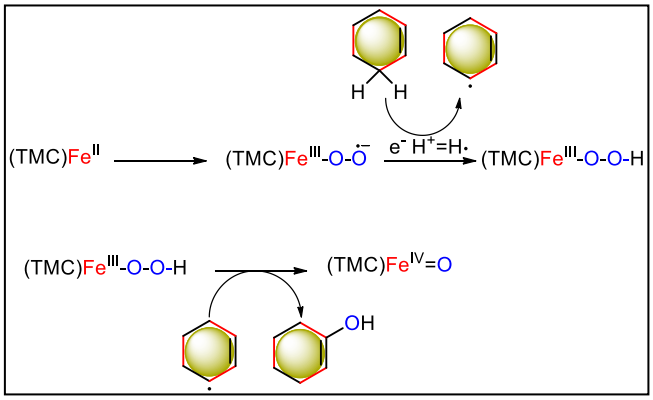

Figure 10. This figure depicts the production of superoxide (TMC)-$Fe^{II}(O_2^-)$ and oxygen activation by the (TMC)-Fe^{II} complex. The resulting metal hydroperoxide species, (TMC)-Fe^{III}-OOH, plays a role in the conversion of cyclohexene to cyclohexenol. The term TMC refers to Tetramethyl-1,4,8,11-tetraazacyclotetradecane.

1.7.2 Heterolytic Oxygen Activation Mechanisms:

One notable characteristic of heterolytic oxygen activation is that it proceeds without the need of free radicals as intermediaries. A metal center with a high oxidation state, like M^{n+2}, oxidizes the organic substrate in a two-electron process. This makes the substrate oxidized and the metal center reduced to the oxidation state of M^{n}. Then, using an electron transfer mediator[51], which may be another metal or, better yet, oxygen (as in the Mars and van Krevelen process), the reduced form of the metal is reoxidized to M^{n+2}. The Wacker oxidation process for oxidizing alkenes to aldehydes is one of the most known examples of this pathway that emphasizes the metal's oxidation/reduction cycle as well as the function of the electron transfer mediator.[52] The active catalyst in the system is $PdCl_2$. Pd^{II} reduces to Pd^{0} after oxidizing an alkene to an aldehyde. However, because molecular oxygen is notoriously bad at reoxidizing Pd^{0} to Pd^{II}, the reoxidation is accomplished via a Cu^{II}/Cu^{I} pair (**Scheme 4a**).

The substrate-selective redox catalyst in this model is $PdCl_2$, and the electron transfer mediator is $CuCl_2$. Roger A. Sheldon et al. intentionally avoid the requirement for a co-catalyst in the above mentioned procedure. Instead of using $PdCl_2$, they synthesized a bathophenanthroline ligand and incorporated it into a Pd metal to produce a modified Pd catalyst. Consequently, a water-soluble palladium (II)-bathophenanthroline complex was formed. This complex reacts with alcohols, converting Pd(II) into Pd(0) and alcohols into aldehydes. In the above procedure, $CuCl_2$ assists in the reoxidation of the Pd(0) complex back to its initial state, Pd (II) (**Scheme 4a**). Notably, the modified palladium(0) complex is capable of forming the modified palladium (II)-bathophenanthroline complex (**Scheme 4b**) solely using oxygen, without the need for an additional metal.[53]

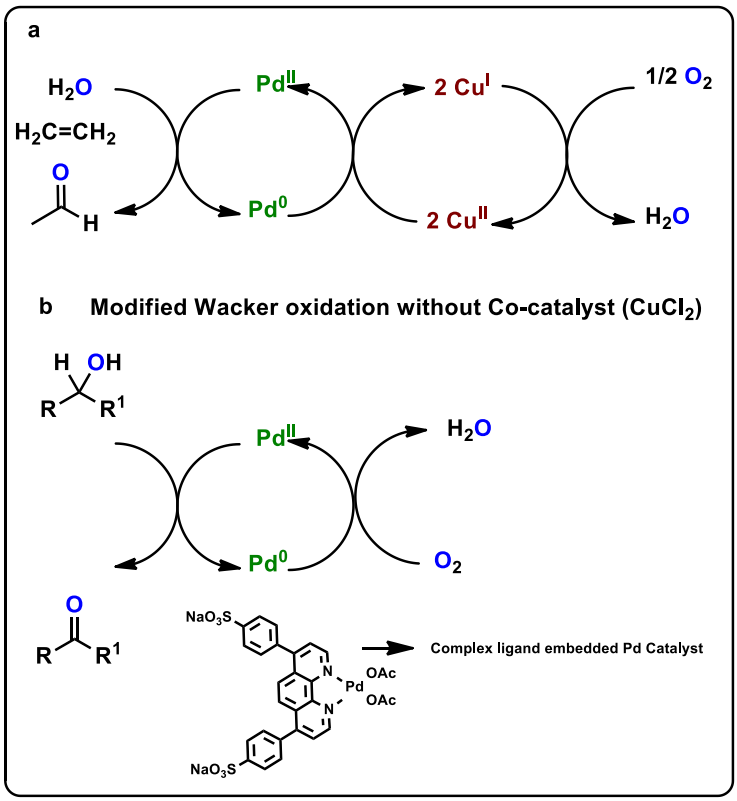

Scheme 4. In the Wacker method, ethylene is transformed into acetaldehyde. The primary metal responsible for substrate oxidation is Pd^0/Pd^{II}, with Cu^I/Cu^{II} serving as an electron transfer mediator, facilitating the reoxidation of Pd^0 to Pd^{II}.

Another class of enzymes known as monooxygenases is thought to exhibit the heterolytic process.[54,55] When monooxygenases are active, oxygen is transferred from a metal center that is highly oxidized to the substrate. Common metal centers are Fe or Cu and a co-factor like flavin can be used to transport electrons (**Scheme 5**).[56,57]

In this chemical process, a reduced flavin molecule undergoes electron loss, subsequently transferred to triplet oxygen, generating a radical pair. This resulting diradical species undergoes spin flipping, leading to the formation of flavin hydroperoxide (**Scheme 5**).

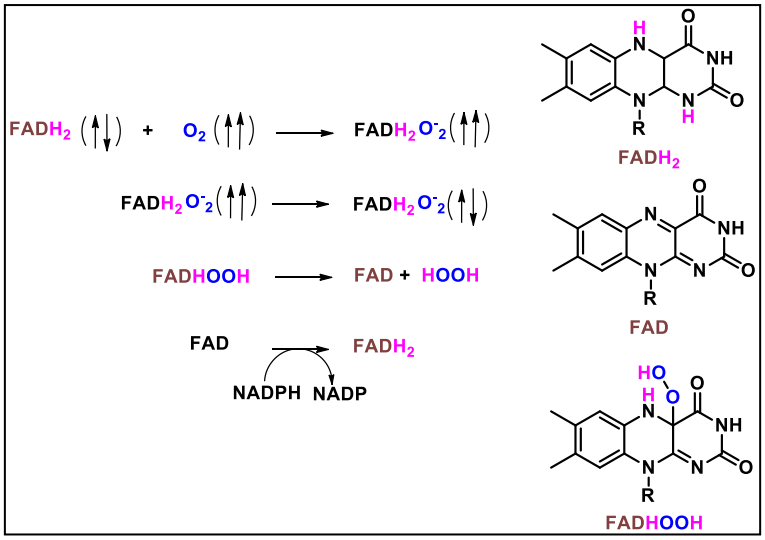

Scheme 5. Reaction of Reduced flavin (FADH2) with Oxygen. After interacting with oxygen, spin inversion causes the creation of a superoxide species, which is immediately followed by an unstable hydroperoxide intermediate (FADHOOH). FADHOOH carries out the oxygen transfer to an organic substrate as well as the production of flavin in oxidized form (FAD). NADPH is used in the catalytic cycle stoichiometrically and acts as a reductant for flavin regeneration.

While the final intermediate is unstable in an aqueous solution, it undergoes heterolytic dissociation to yield H_2O_2 and oxidized flavin. To restore the cofactor to its original reduced state, a reducing agent such as NADPH (nicotinamide adenine dinucleotide phosphate) is typically employed in conjunction with flavin-based enzymes. Upon oxygen rebinding, the catalytic cycle can start again.[58] A great example of this mechanism, important in industries, is seen in the Baeyer-Villiger oxidation. It converts cyclohexanone to ε-caprolactone using acinetobacter that carries flavin (See **Figure 11**).

Although it may appear contradictory, a reducing agent is required to carry out the above oxidation reaction in the same way that the active metal center is in a reduced state at the start of the cycle rather than an oxidized one (as in the Mars and van Krevelen mechanism or the Wacker process).

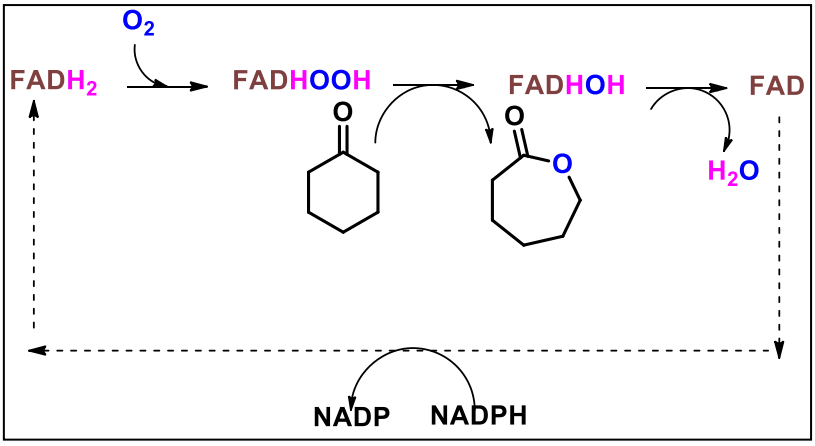

Figure 11. The Baeyer-Villinger reaction transforms cyclohexanone into ε-caprolactone using an acinetobacter with flavin. After flavin (FADH2) activates oxygen, cyclohexanone acquires one oxygen atom from the intermediate FADHOOH. The oxidized flavin (FAD) is subsequently reduced using a stoichiometric amount of NADP.

It has not yet been able to recreate these systems on a wide scale because the reducing agent NADPH is used stoichiometrically. Transition metals as well as flavin also promote extremely elegant and very selective oxidation reactions using oxygen in nature.

Chapter 2

Transition Metal-Free Molecular Oxygen Activation by Ionic Liquid for Selective Oxidation Reactions

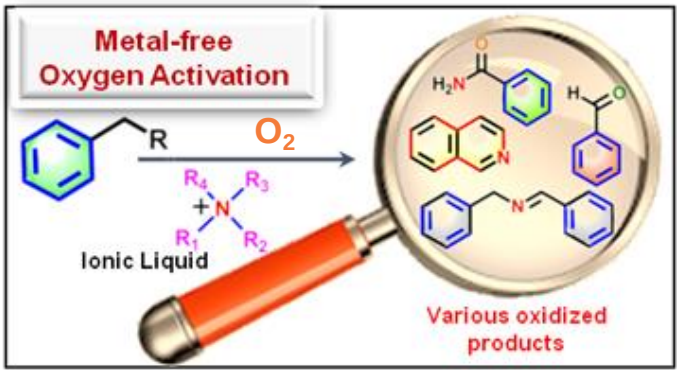

This chapter presents an efficient strategy for oxygen activation, leading to the synthesis of valuable oxidized compounds from readily available organic compounds. It demonstrates the optimization of oxygen activation conditions using Triton B ionic liquid and benzylamine as an oxidizing compound. The chapter explores the application of the O_2 activation protocol in benzylamine/alcohols oxidation reactions employing simple quaternary amine-based ionic liquids. Various oxidation products, including amide, aldehyde, imine, and aromatized products, are produced under these optimized conditions. Moreover, the chapter provides insights into the reaction mechanism through ^1H NMR analysis and various control experiments, elucidating the conversion of molecular oxygen into a hydroperoxyl radical via a proton-coupled electron transfer process. The detection of hydrogen peroxide in the reaction medium using colorimetric analysis supports the proposed mechanism of oxygen activation.

2.1 Introduction

Oxidation is a fundamentally important chemical conversion in organic chemistry. In recent years, there has been a significant increase in interest in the synthesis of valuable oxidative products through the mild and selective oxidation of readily available and inexpensive hydrocarbons. This attention arises from the desire to transform these hydrocarbons into valuable oxygenated products, serving as versatile building blocks or fine chemicals in both laboratory and industrial chemical synthesis.[59] To function properly, a selective oxidation approach requires a large number of basic variables to work together in a synergistic manner. These include oxidants, catalysts, raw materials, solvents, and the right reaction mechanisms and conditions.[60] Because of its complexity, there is a lot of potential for development in terms of designing diverse oxidation methods from different angles in order to meet the requirements of a state-of-the-art reaction. In recent times, this domain has witnessed numerous innovative scientific breakthroughs, driven by an increasing awareness of environmental issues. The focus was on minimizing the use of toxic chemicals, reducing energy consumption, and curbing waste production.

However, there is a clear need for improvement in oxidation methodologies to address environmental and economic concerns.[61,62] Among the different oxidation methods, the utilization of di-oxygen has been recognized as a highly effective protocol, supported by natural processes.[63,64] The replacement of conventional stoichiometric oxidants[65] such as chromium(VI) oxide, permanganates, and selenium dioxide, by molecular oxygen,[66–69] is considered one of the attractive protocols in terms of environment and economic aspects. The participation of molecular oxygen in reactions has positive impacts on a "green" process, improving sustainability, promoting environmental friendliness, and enhancing economic appeal.[70]

Molecular dioxygen is the sole abundantly paramagnetic molecule in our environment, which has a triplet ground state. In fact, this triplet O_2 diradical makes up 20.94% of all the gases in earth's atmosphere and is very important for life.[16] For this reason, oxygen could be considered a "stable" molecule in earth's atmosphere despite its diradical nature. The 100 kcal/mol resonance energy provides stabilization of triplet ·O=O· diradical, renders it kinetically inactive for hydrogen atom abstraction, and can be considered one of the reasons why O_2 is so abundant in the earth's atmosphere.[16] Despite the literature's recognition of molecular oxygen as a promising oxidant, the Wigner spin conservation rule[71] limits its direct use due to its triplet spin, particularly in the selective oxidation of singlet oxidizing compounds, which necessitates activation steps.[60] Over the past few decades, there has been significant progress in the development of superior catalysts for the activation of oxygen and the production of reactive oxygen species **(Figure 12)**.[72–75]

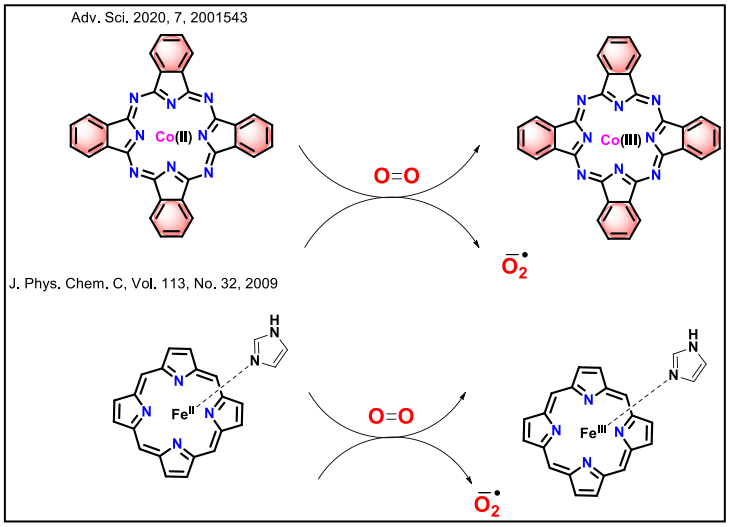

Figure 12. Transition metal-catalyzed oxygen activation leading to the generation of reactive oxygen species.

As a result, oxygen reduction reactions (ORR) have been a focus of research for a long time. Reactive oxygen species (ROS) are promising green oxidants[76,77] and numerous efficient strategies for producing ROS have been reported.

Transition-metal salts,[63,78] N-hydroxyphthalimide,[79,80] enzymatic catalysts,[81,82] biomimetic catalysts,[83,84] dye-related catalysts,[85,86] halogen-based catalysts,[87,88] and so on are examples of homogeneous catalysts, whereas heterogeneous catalysts include graphitic carbon nitrides (g-C_3N_4),[89] hetero atoms doped graphenes,[90] graphene sheet/polymeric carbon nitride nanocomposites (GSCNs),[91] carbon nanotubes (CNTs),[92] and mesoporous carbon nitrides.[93] In many oxidation processes involving molecular oxygen, metal-free organocatalytic methods have attracted considerable interest in recent years.[94] Compared to metallic or organometallic catalysis, these oxidation techniques have demonstrated remarkable performance and other undeniable benefits in green chemistry from a long-term perspective.[95] There are many ways that O_2 can be reduced, such as through electrochemical reactions, the breakdown of peroxide, chemical reactions, photochemical reactions, photocatalytic reactions, and one-electron reduction reactions involving singlet oxygen.[96] Most metal-based catalytic systems and photocatalytic procedure suffer from low availability, high noble metal prices, high purification costs, high product and waste disposal costs, and despite their high efficiency.[97] Therefore, the development of low-cost metal-free catalysts with comparable or even superior efficacy is both desirable and difficult.[98]

Following a thorough review of the relevant literature, the current studies focus on the activation of molecular oxygen and the conversion of O_2 into reactive oxygen species (ROS). These reactive oxygen species (ROS) play a crucial role in various transformations, such as converting amines to amides, alcohols to aldehydes, and inducing the aromatization of saturated systems.[94,99]

Amides are a very important group of chemicals in both chemistry and biology. They are used as building blocks for peptides and proteins, to boost the smell of things, as anti-blocking agents, ink pigments, detergents, and lubricants **(Figure 13)**.[100,101]

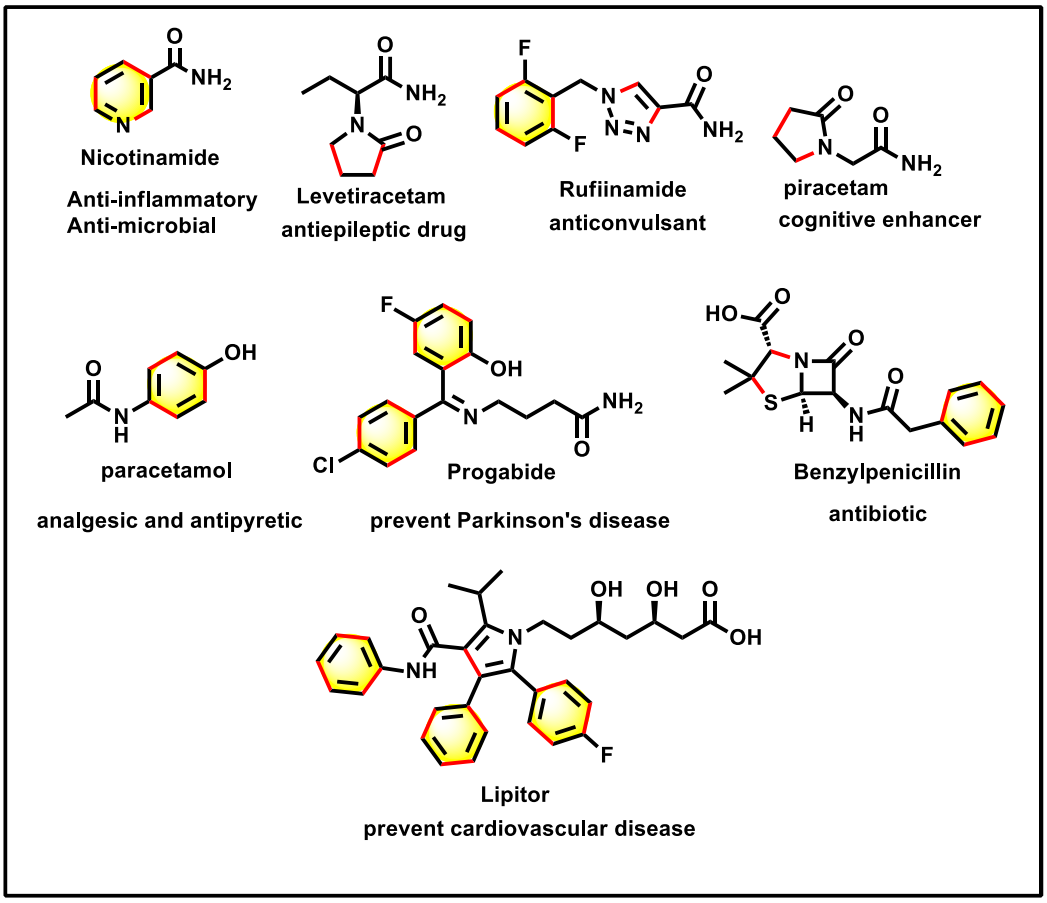

Figure 13. Some selected drug molecules containing prominent amide bond.

The synthesis of amides primarily depends on the use of carboxylic acids as the main substrates. The direct condensation of carboxylic acids with amines is a very efficient method that is recommended due to its ability to produce water as the only by-product. However, this approach requires high temperatures without the use of catalysts, additives, or coupling reagents to overcome the energy barrier caused by simultaneous acid-base reactions, which often leads to the undesired formation of ammonium carboxylate salts. The use of coupling reagents facilitates the activation of carboxylic acids by converting the -OH group into a good leaving group prior to treatment with the amine to synthesis amide **(Scheme 6)**.[102–105] Despite some disadvantages of coupling reagents, such as their expensive nature and the formation of hazardous stoichiometric by-products, couplings continue to be widely used in both academia and industry.

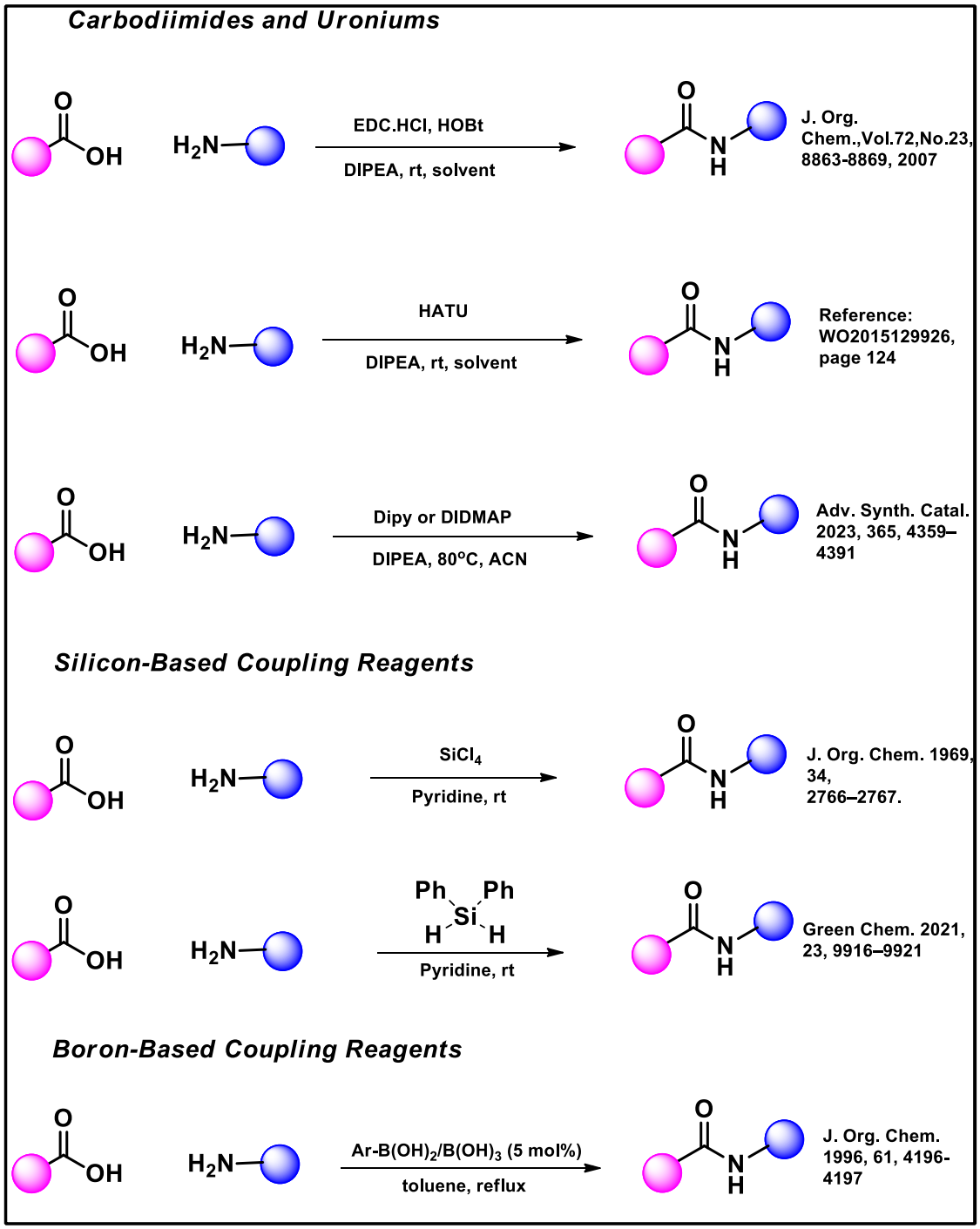

Scheme 6. Synthesis of amide molecules from carboxylic acid derivatives via various coupling reactions.

Different suitable organic compounds are also considered as efficient carboxylic acid surrogates in amide formation, including nitrile, acid chlorides, anhydrides, and esters **(Scheme 7)**. Alternatively, acid-catalyzed rearrangements of ketoximes have produced amides.[106] Hydration of nitriles[107,108] and the

Beckmann rearrangement have proven beneficial in the production of industrial chemicals on a large scale. However, these procedures require stoichiometric quantities of toxic or hazardous reagents and generate a substantial amount of waste compounds or by-products. In the past ten years, chemists have made significant efforts to develop environmentally benign processes. In this context, the development of new methodologies for amide bond formation represents a significant challenge for the chemical industry and academic research groups.

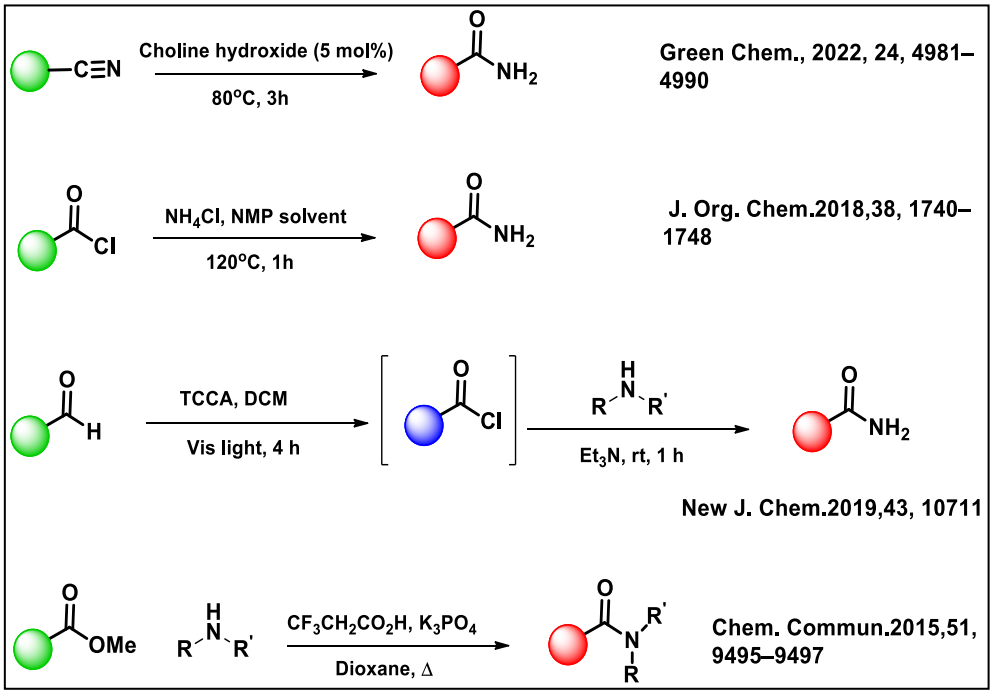

Scheme 7. Synthesis of amide molecules from various starting materials.

Therefore, it is highly desirable to develop novel and environmentally friendly methods for amide synthesis. Recent amide synthesis techniques have centered on the direct oxidation of primary/secondary/tertiary amines to the corresponding amides **(Scheme 8)**.[109–112] Most reported methods require expensive metal complexes or stoichiometric oxidants, including iodine, RuO_4, ^tBuOOH, iodobenzene, and $PhCO_3{}^tBu$ **(Scheme 8)**.[100,113–116] In recent times, in contrast to transition-metal catalysts, metal-free approaches have been utilized

to synthesize secondary or tertiary benzamide products utilizing the concept of singlet oxygen generation induced by photocatalysts **(Scheme 8)**.[117] Recently, the synthesis of primary benzamide has been achieved using organic ionic liquids, with nitrile and primary benzylamine as the key components.[118,119]
Unlike transition-metal catalysts, metal-free methods that use oxygen to change amines to amides are environmentally friendly and long-lasting. This is because oxygen from air is a great source for oxidative transformations, is found in large amounts in nature, and produces water or hydrogen peroxide as a by-product. Nevertheless, conventional methods often yield significant amounts of toxic chemicals as by-products. Therefore, there is a pressing need to develop efficient procedures for amide synthesis that minimize the wasteful use of stoichiometric reagents and acidic or basic media, posing a challenging task in modern organic synthesis.[120–122] In general, oxygenating the methylene groups of amines to the corresponding amides is extremely difficult.[123]

In the present study, ionic liquids (ILS) were used to activate molecular oxygen. Ionic liquids are very important in environmental and green chemistry. They are known for not evaporating, being thermally stable, not exploding, having a high polarity, mixing with water at different temperatures, being tensile in almost any way, and being very easy to dissolve.[124–126] As a result, ILs have attracted a lot of interest and are acknowledged as sustainable alternatives to catalysts and volatile organic solvents.[127] The ability of ILs to replace traditional industrial solvents, which are frequently volatile organic compounds (VOCs), is a major factor in their development. Using relatively non-volatile ionic liquids instead of traditional volatile solvents could potentially mitigate atmospheric pollution resulting from VOC emissions.[127] Hence, the development of novel ionic liquids (ILs)-mediated aerobic cascade catalysis reactions involving the activation of molecular oxygen under mild conditions is exceptionally attractive.

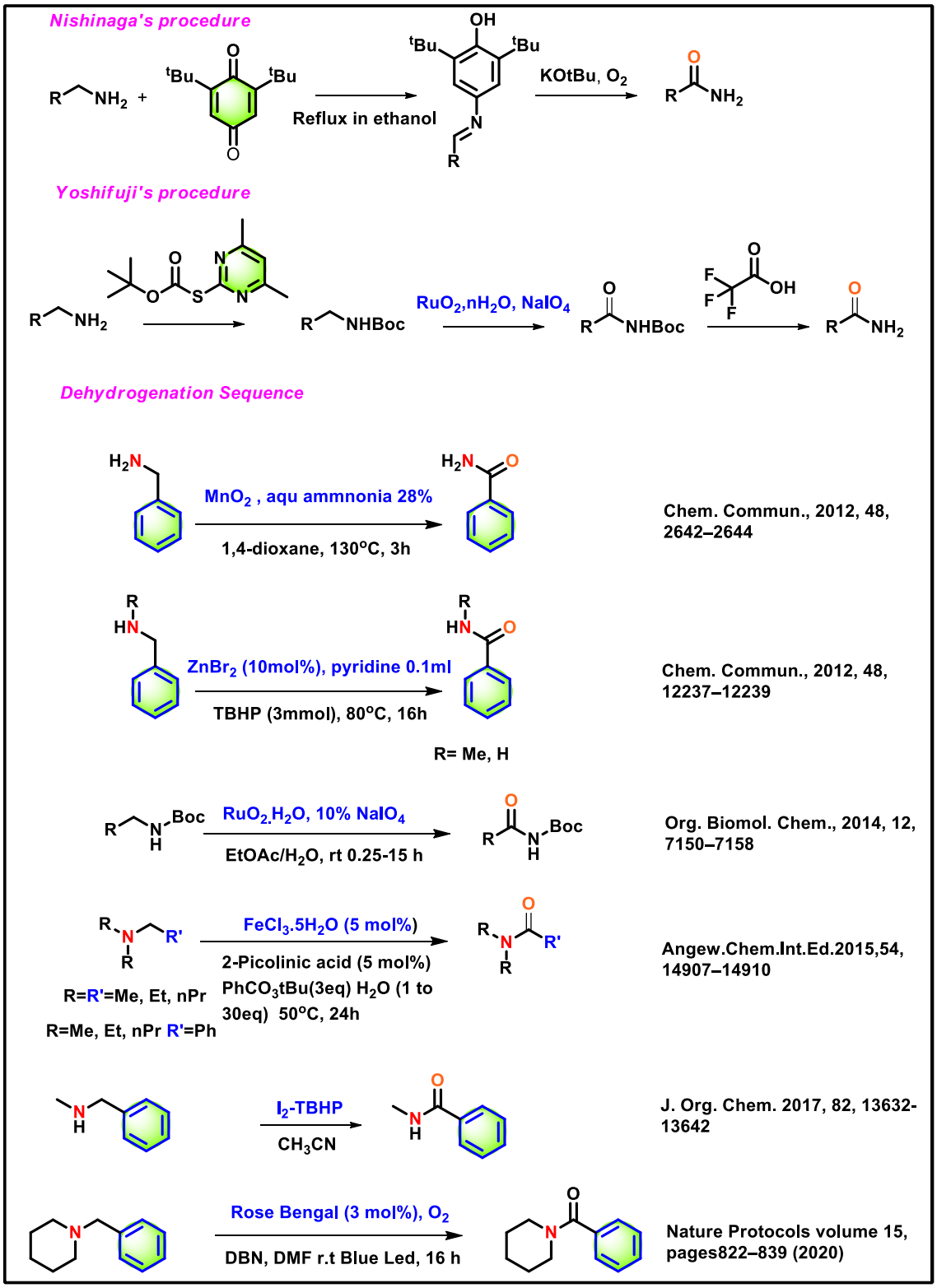

Scheme 8. Synthesis of amide derivatives from corresponding amine molecules.

Oxygen activation by ionic liquids and its application to the synthesis of benzylamine oxidation -NH_2 functionalized benzylic position was used as a

hydrogen atom donor (C-H bond dissociation energy is approximately 90 kcal/mol) in order to activate oxygen by ionic liquids.[128,129] This research will open up new avenues for general oxidation chemistry using natural oxygen and synthetic organic chemistry to convert low-cost hydrocarbons into oxidative value-added products.[130–132] This investigation will also aid in the future development of a metal-free selective oxidation route for expensive, valuable organic compounds.

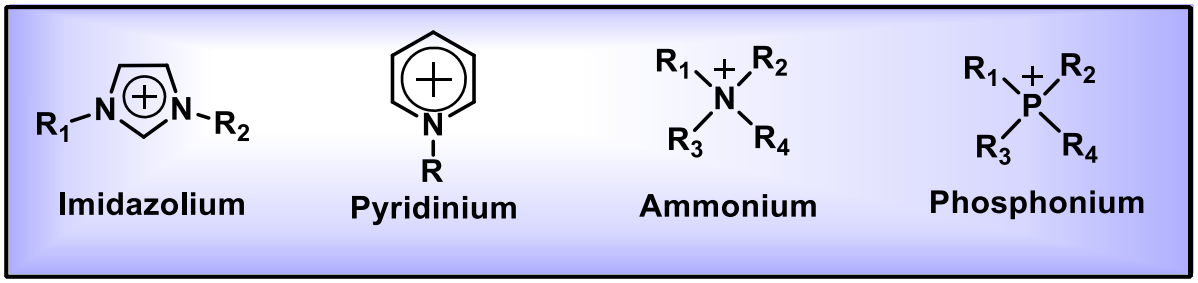

Scheme 9. Diffrent types of ionic liquids.

In the literature, various types of ionic liquids are documented, such as imidazolium-based, pyridinium-based, ammonium-based, and phosphonium-based ionic liquids **(Scheme 9)**. Among these, quaternary alkyl ammonium-based ionic liquids stand out as a versatile class increasingly utilized across diverse fields due to their unique properties.[124] These compounds, characterized by organic cations with four alkyl groups attached to a central nitrogen atom, offer tunable physicochemical properties, enabling customization of viscosity, polarity, and solubility for specific applications like catalysis, separation processes, and electrochemistry. Despite their potential properties, quaternary alkylammonium-based ionic liquids have not been explored for oxygen activation. These ILs offer a cost-effective solution as they serve multiple purposes, acting as oxygen activators, solvents, and bases simultaneously. By eliminating the need for transition metal catalysts, external bases, and extra solvents, they not only reduce chemical exposure but also enhance the eco-friendliness of the process.[94,99,133,134]

2.2 Results and Discussion

2.2.1 Stability Measurement of Triton B using ^{1}H NMR Studies:

Before going for optimization studies of oxygen activation using quaternary alkylammonium-based ionic liquids, there was a specific focus on assessing the stability of ionic liquids. This indicates a preliminary step in the experimental optimization process to ensure the thermal stability of the ionic liquid before further optimization efforts were undertaken. The thermal stability measurement could involve evaluating the ionic liquid's resistance to degradation over heating conditions, changes in physical properties, or potential side reactions. This careful assessment was crucial to establishing a robust foundation for subsequent optimization studies in an experimental context.

The structurally crucial quaternary alkylammonium-based ionic liquid, Triton B (40% w/w in methanol), was selected for thermal stability assessment using ^{1}H NMR. The assessment considered both temperature and time variables. To a solution of Triton B was heated in a properly sealed 5-ml round-bottom flask under four different conditions. After following experimental periods, mesitylene served as the ^{1}H NMR reference compound, mixed with Triton B in MeOD solvent at a 1:1 ratio for analysis. The quaternary methyl groups within Triton B were identified as its most sensitive part of Triton B molecule. Their ^{1}H NMR peak ratio was compared to that of standard mesitylene. Analysis under Condition 1 (70°C, 4 hours) revealed a degradation of only 4.7% of Triton B over the specified time (**Figure 14A**). Similarly, under Condition 2 (70°C, 12 hours), Triton B degradation was observed to be only 7.4% over the 12-hour duration (**Figure 14B)**. Notably, heating Triton B at 90°C for 4 hours resulted in approximately 19.53% degradation within the same timeframe (**Figure 14C)**. Based on stability studies of Triton B using ^{1}H NMR experiments, it is concluded that Condition 1 (70°C for 4 hours) optimizes both the stability and reactivity of Triton B.

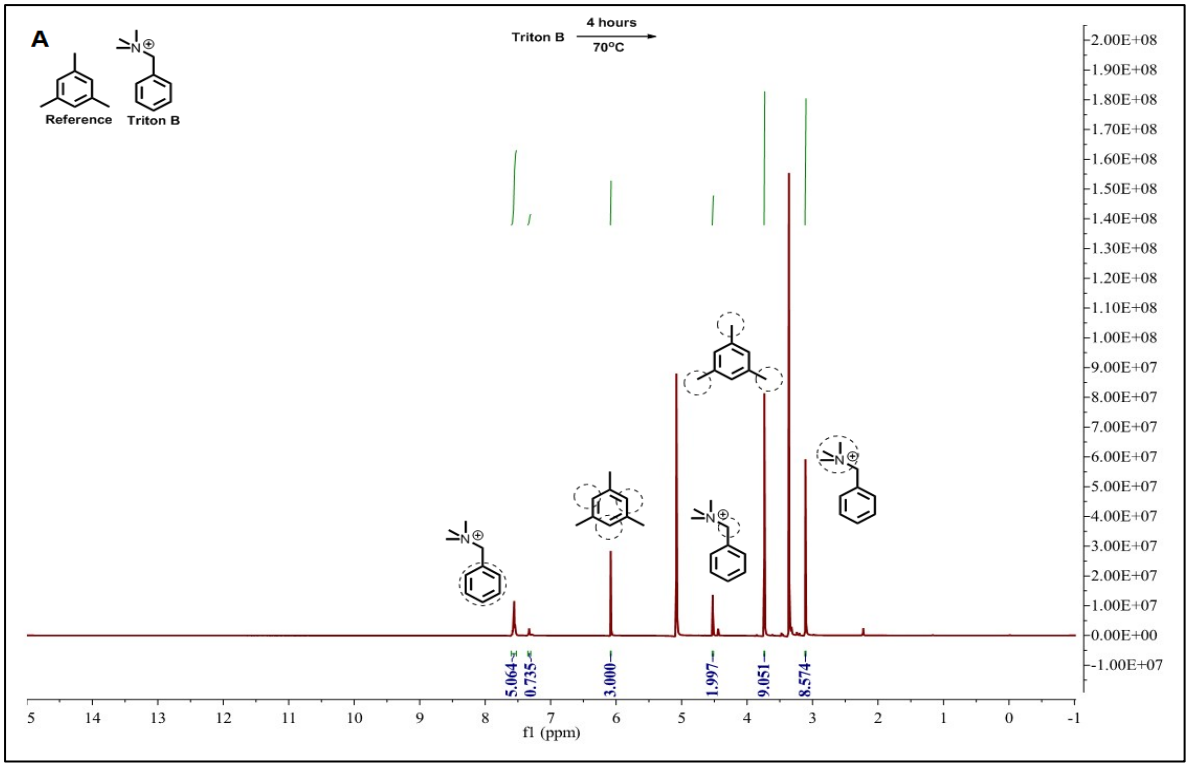
A
Reference
Triton B
Triton B
4 hours
70°C
5.064
0.735
3.000
1.997
9.051
8.574
f1 (ppm)

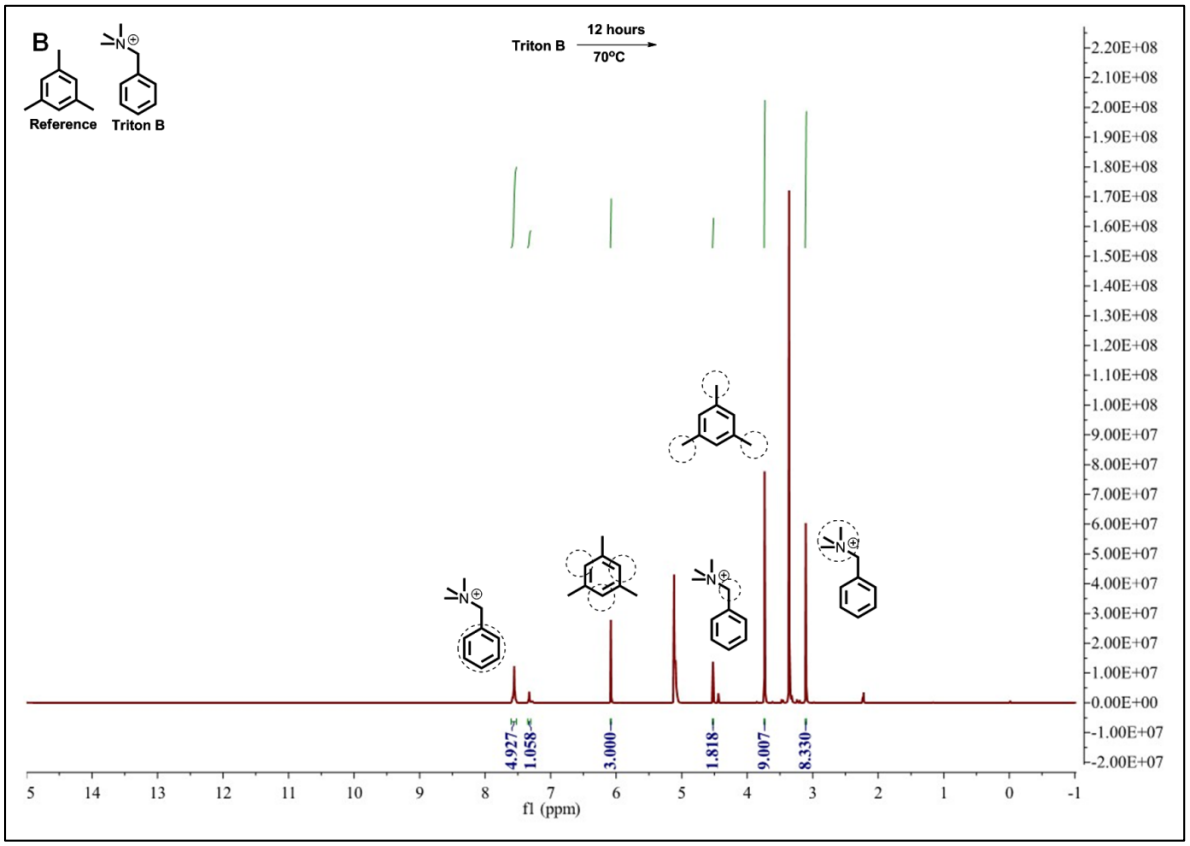
B
Reference
Triton B
Triton B
12 hours
70°C
4.927
1.058
3.000
1.818
9.007
8.330
f1 (ppm)

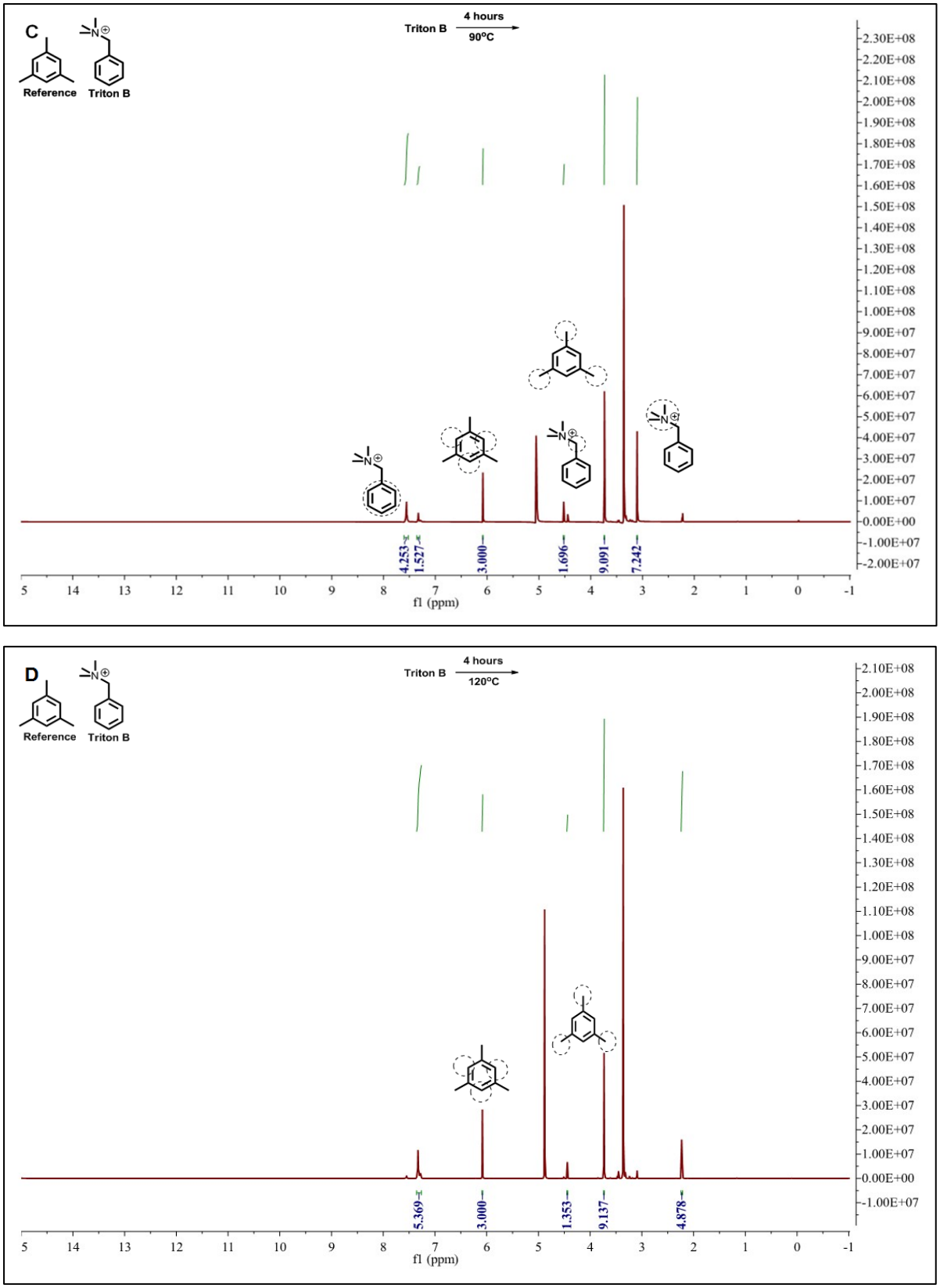

Figure 14. (A) represents ^{1}H NMR of Triton B at 70°C for 4 hours. **(B)** represents ^{1}H NMR of Triton B at 70°C for 12 hours. **(C)** represents ^{1}H NMR of Trion B at 90°C for 4 hours. (D) represents ^{1}H NMR of Triton B at 120°C for 4 hours.

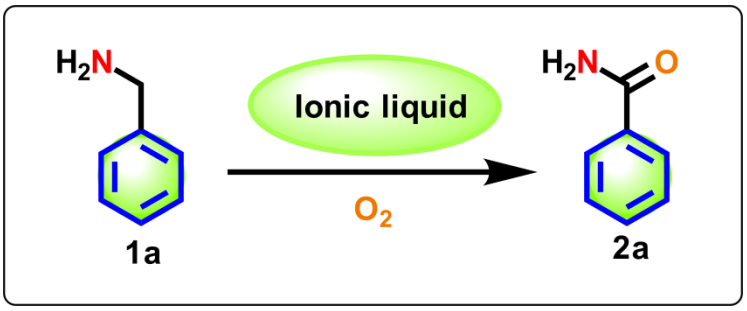

Scheme 10. General scheme for benzylamine oxidation using ionic liquid.

2.2.2 Reaction Optimization:

In the present study, different types of quaternary alkylammonium-based ionic liquids were used for oxygen activation, followed by the oxidation of benzylamine to obtain the oxidizing product (benzamide) **(Scheme 10)**. The activation of molecular oxygen and the subsequent oxidation of benzylamine were successfully achieved using these ionic liquids (**Table 3**). In order to get the best reaction conditions, optimization experiments were carried out by routine screening of various quaternary alkylammonium-based ionic liquids, adjusting temperature, and adding additives and solvents (**Table 3**). In a 5 ml round bottom flask (RB) with an oxygen balloon at 70°C for 12 hours, benzylamine (**1a**) was involved in oxidative amidation with Triton B in methanol (0.1 eq and 0.25 eq, respectively, **entries 1** and **3**), yielded 49% and 60% of the oxidative product (**2a**), respectively. Moreover, the reaction time was monitored using TLC. It was observed that when the reaction was carried out at 70°C for 4 hours, a better yield was obtained compared to the 12-hour reaction time (**entry 2** and **entry 4**). This observation was further corroborated by performing above ^{1}H NMR experiments.

Table 3. Optimization of oxygen activation followed by oxidative product yield[a]

Sl No	IL	Equiv	Solvent	T°C	O_2/ Air	Time	Isolated Yield (2a)
1	Triton B (40% w/w methanol)	0.10	Neat	70°C	O_2	12hr	49%
2	Triton B (40% w/w methanol)	0.10	Neat	70°C	O_2	4hr	55%
3	Triton B (40% w/w methanol)	0.25	Neat	70°C	O_2	12hr	60%
4	Triton B (40% w/w methanol)	0.25	Neat	70°C	O_2	4hr	68%
5	Triton B (40% w/w methanol)	0.50	Neat	70°C	O_2	4hr	76%
6	Triton B (40% w/w methanol)	0.75	Neat	70°C	O_2	4hr	81%
7	**Triton B (40% w/w methanol)**	**1**	**Neat**	**70°C**	**O_2**	**4hr**	**90%**
8	Triton B (40% w/w methanol)	1	Neat	70°C	Air	4hr	48%
9	TMAH (25% w/w methanol)	1	Neat	70°C	O_2	4hr	82%
10	Triton B (40% w/w methanol)	1	Neat	90°C	O_2	4hr	75%
11	Triton B (40% w/w methanol)	1	Neat	120°C	O_2	4hr	51%
12	Triton B (40% w/w water)	1	Neat	70°C	O_2	4hr	59%
13	Triton B (40% w/w methanol)	1	0.25 ml MeOH	70°C	O_2	4hr	72%
14	Triton B (40% w/w methanol)	1	0.5 ml MeOH	70°C	O_2	4hr	51%
15	Triton B (40% w/w methanol)	1	1 ml MeOH	70°C	O_2	4hr	26%
16	Triton B (40% w/w methanol)	1	2 ml MeOH	70°C	O_2	4hr	0%
17	TBAOH (10% w/w methanol)	1	Neat	70°C	O_2	4hr	0%

[a]**Reaction conditions.** Ionic liquid (1 eq with respect to the cation) and benzylamine (1 eq) were heated at the appropriate temperature under an oxygen/open atmosphere. Triton B (40%), trimethylbenzylammonium hydroxide; TMAH, tetramethylammonium hydroxide; TBAOH, tetrabutylammonium hydroxide.

It revealed that Triton B degraded more over the course of 12 hours at 70°C than 4 hours, indicating that temperature and time parameter for the present reaction is best for Triton B stability and reactivity (**Figure 14**). An increase in Triton B equivalence resulted in a corresponding improvement in product yields. As a result, the amount of Triton B increased from 0.50 to 1 eq (**entry 5-7**) in order to achieve an optimized yield of 90% (**entry 7 Table 3**) of the intended product. Moreover, when the same reaction was carried out in open air, **2a** was obtained in only 48% yield (**entry 8 Table 3**). The low yield of product suggested that positive oxygen pressure was necessary to produce a good yield of oxidizing product. When benzylamine (**1a**) was performed with another quaternary alkylammonium-based ionic liquid, TMAH (25 percent w/w methanol) under optimized conditions, an 82% oxidizing product (**entry 9 Table 3**) was obtained. A thorough examination of the experimental entries in **Table 3** revealed several interesting insights worth mentioning here. Using 1 eq Triton B in water produced compound **2a** with a 59% yield at 70°C for 4 hours (**entry 12**). The yield of the oxidizing product was gradually decreased (**entries** from **13** to **16**) with the addition of an external MeOH solvent (from 6 eq to 49 eq) to the reaction mixture under the optimized conditions. No reaction ensued (0% yield) when a substantial amount of MeOH (49 eq) was mixed with the reaction mixture. Similarly, when tetrabutylammonium hydroxide (10% w/w methanol) was employed under the same conditions, no desired product was obtained as expected (**entry 17 Table 3**).

2.2.3 Substrate Scope:

Under the optimized conditions, the broad substrate scope and viability of this one-pot technique were assessed by employing various benzylamine derivatives and benzyl ammonium chloride (HCl salt of benzylamine). Gratifyingly, this process yielded the corresponding oxidized amides in moderate to good yields (**Figure 15**). Successfully implementing this method on a set of nineteen (19)

different derivatives (**1a–s**) of benzylamine is shown in **Figure 15**. Interestingly, para-substituted derivatives of benzylamines, encompassing both electron-donating and electron-withdrawing groups, produced better yields. Heterocycles containing primary amines such as pyridin-2-ylmethanamine (**1b**), furan-2-ylmethanamine (**1c**), and piperolylamine (**1e**) were also subjected to the standard condition, resulting in the formation of the corresponding heteroamides (**2b**, **2c**, and **2e**) with moderate-to-good yields.

2.2.4 Scope of Secondary Benzylamine Oxidation:

To examine the impact of the one-pot oxidation methodology on secondary benzylamine substrates, the substrate scope was expanded from primary benzylamine to include secondary benzylamine. In addition, N-Bocbenzylamine (**3a**) was subjected to the optimized reaction condition. Only benzamide (**2a**) under an oxygen environment and benzylamine (**1a**) under a nitrogen environment were obtained as major products. To the best of the knowledge, only a few studies have been published on the Boc-deprotection of amines using an ionic liquid under benign conditions.[135,136] Dibenzylamine (**3b**) and N-benzylbenzamide (**3c**) were also treated under optimized conditions, but no desirable product was observed. This unexpected result may be attributed to steric hindrance around the nitrogen atom. The optimized conditions were applied to the less hindered cyclic secondary benzylamines **3d** and **3e** to determine whether the steric effect was a major factor (**Figure 16**) in the case of **3b** and **3c** secondary benzylamines. As expected, dehydrogenated amines (β-carboline and isoquinoline) were produced in good to moderate yields.

Oxidative dehydrogenation reactions of saturated heterocycles are widely employed for the synthesis of heteroarenes. These heteroarenes, in turn, are commonly utilized in the development of drug candidates, natural goods, and manufactured materials.[137,138] These reactions were frequently mediated by either a stoichiometric oxidant, such as DDQ,[139] IBX,[140] sulfur,[141] or SeO_2[142], or

a catalytic amount of a transition metal (e.g., Cu, Rh, Au, or Pt) in the presence of oxygen.[143,144]

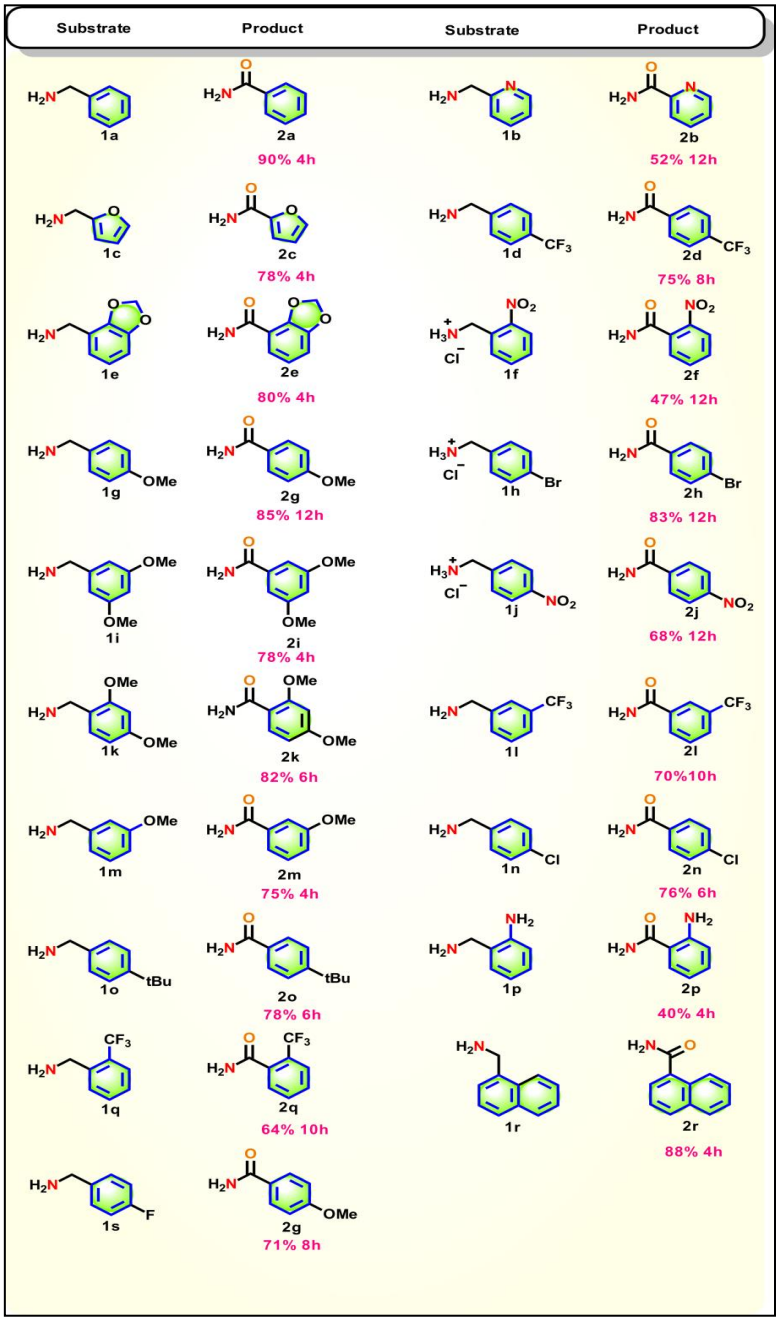

Figure 15. Scope of the Benzylamine oxidation using optimized conditions. All reactions used 1 mmol of benzylamine derivatives, 1 mmol of Triton B (40 w/w in methanol, 454 µl), 70°C, and an O_2 atmosphere; isolated yields.

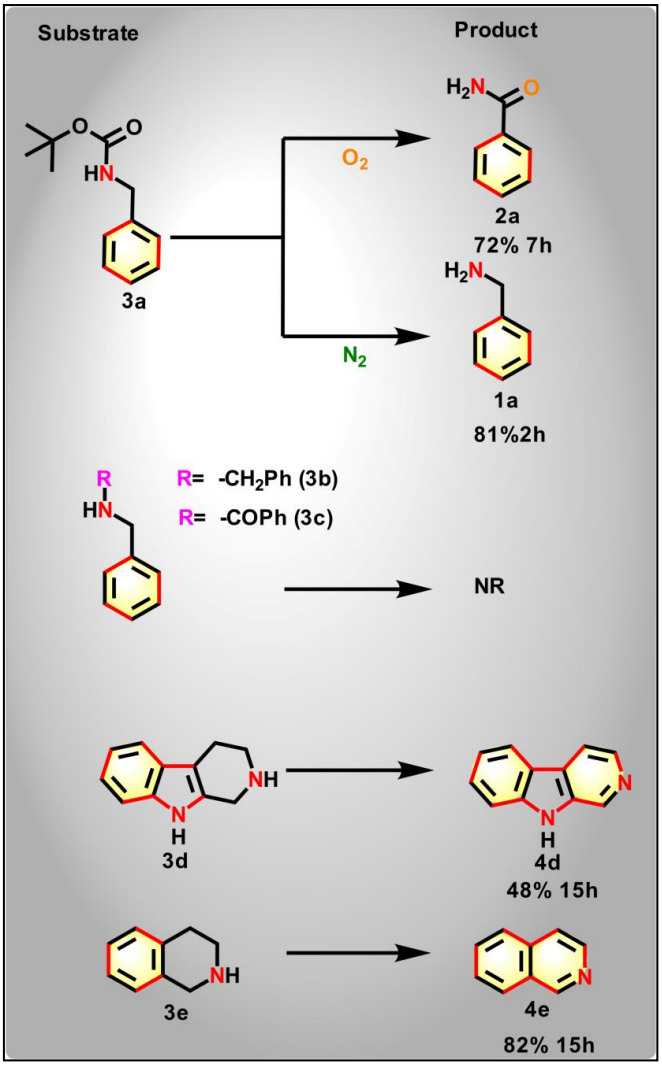

Figure 16. Scope of Secondary Benzylamine. All reactions were carried out with N-benzylamine derivatives (1 mmol), Triton B (1 mmol, 40% w/w in methanol, 454µl), 70°C, O_2 balloon, and isolated yields.

Recently, the elegant synthesis of these heteroarenes was accomplished using metal-catalyzed (iridium, ruthenium, nickel, iron, and cobalt) dehydrogenation reactions of N-heterocycles.[144–147] Even, these synthetic protocols are very atom-efficient but costly and hazardous for the environment. As a result, a straightforward catalytic system with a high yield that can be employed under ambient conditions was always needed. After a thorough study of the literature, it appeared that Triton B-mediated ionic liquid dehydrogenation techniques would become a viable green option.

2.2.5 Benzyl Alcohol Oxidation:

Motivated by the above findings of the aerobic oxidation of benzylamine using Triton B, further investigation into the oxidation of benzyl alcohol under the same conditions was considered.[94] Under optimized conditions **(Table 3)**, several benzyl alcohol derivatives were exposed, and the corresponding benzaldehyde derivatives **(Figure 17)** were produced as main products with lower yields than the corresponding benzamide **(Figure 15)**. But the yields of benzyl alcohols with electron-donating groups (-Me, -OMe, -Br, etc.) were higher than those with electron-withdrawing groups (-CF_3, 3,5-dinitro). Triton B-mediated control oxidation of benzyl alcohol to benzaldehyde derivatives was particularly challenging due to the presence of hydroxide ions. Triton B has a hydroxide ion that made it difficult to control the oxidation process of benzyl alcohol to benzaldehyde derivatives. The presence of hydroxide anion in Triton B may have contributed to the low yield of benzaldehyde derivatives, which were subsequently oxidized to benzoic acid. To prevent the formation of acid, another hydroxide-free quaternary alkylammonium ionic liquid (TBAB) was used. TBAB was utilized to generate various benzaldehyde derivatives (**5a-5j)** under identical optimized conditions, resulting in a higher yield compared to Triton B (**Figure 17**). Hence, it is rational to consider TBAB as a potential alternative reagent for the oxidation of benzyl alcohol, owing to its ability to activate molecular oxygen and C-H bonds in an environmentally sustainable manner.[99,148,149]

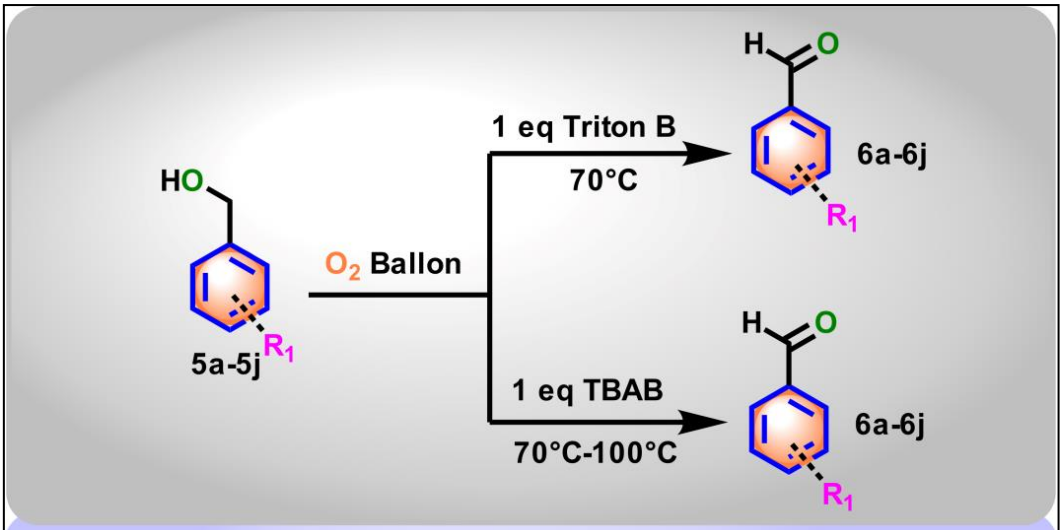

Entry No	R_1	Triton B	TBAB
5a	H	30%, 3h	50%, 48h, 80°C
5b	4-OMe	33%, 24h	47%, 24h, 70°C
5c	3-OMe	40%, 24h	61%, 48h, 80°C
5d	2-OMe	28%, 12h	55%, 48h, 80°C
5e	4-Br	26%, 6h	50%, 24h, 80°C
5f	4-Cl	29%, 6h	55%, 30h, 80°C
5g	4-CF_3	20%, 24h	28%, 48h, 100°C
5h	4-CH_3	52%, 24h	63%, 24h, 90°C
5i	4-(benzyloxy)-3-methoxy	24%, 24h	36%, 48h, 100°C
5j	3,5-dinitro	0%, 24h	0%, 52h, 100°C

Figure 17. Scope of the Benzyl Alcohol reaction using Triton B and TBAB. All reactions were conducted with 1 mmol benzyl alcohol derivatives using 1 mmol Triton B (1 mmol, 40% w/w in methanol, 454µl) and TBAB (1 mmol 322.36mg) under O_2 atmosphere; TBAB, tetrabutylammonium bromide.

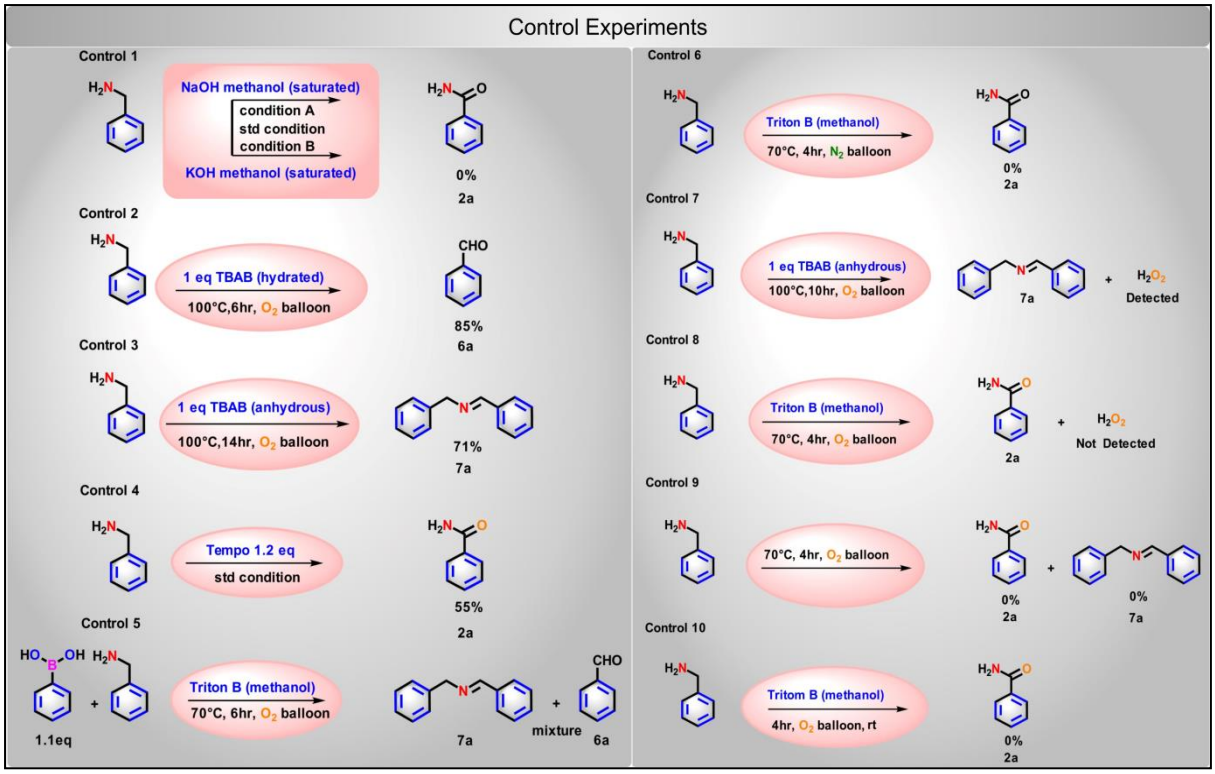

Figure 18. Control Experiment. All control experiments were carried out to know the most possible intermediate of benzylamine oxidation as well as the role of a quaternary ammonium salt. All reagents used 1:1 stoichiometric ratio otherwise mentioned. The standard condition corresponds to 4 hours, 70°C under an oxygen atmosphere.

2.2.6 Control Experiments for Mechanistic Studies:

To investigate the most likely reaction mechanism and the most possible reactive intermediates of oxidative products (**Figure 18**), several control experiments were carried out. The presence of any transition metal ion contamination in the reagents was examined by ICP-AES (**Table 4**). The results from the ICP-AES experiment confirmed that no significant amount of transition metal ion contamination was present in Triton B, TBAB, and benzylamine. However, a significant amount of Na^+ and K^+ ions were detected in the Triton B reagents. The control experiment was conducted to investigate whether the presence of Na^+ and K^+ ions in Triton B as impurities played a role in oxygen activation. In the **Control 1** experiment, the alkali metal salts

saturated NaOH (condition A) or saturated KOH (condition B) in dry methanol were treated with benzylamine at optimized condition. As a result, no intended product was obtained. Next, to explore the formation of oxidative products via benzylimine intermediate, benzylamine was treated with 1 equivalent of hydrated TBAB, leading to the exclusive formation of benzaldehyde (**6a**) as the sole product (**control 2 in Figure 18**).[150] Surprisingly, when benzylamine was treated with 1 eq of anhydrous TBAB at the above mentioned conditions, (*E*)-N-benzyl-1-phenylmethanimine (**7a**) was produced as a sole product with hydrogen peroxide (**control 3**).[151–153] Here, in the presence of TBAB, benzylamine initially generated a benzylimine intermediate, which was subsequently converted into benzaldehyde in the presence of water (**control 2**). In the absence of water, a second molecule of benzylamine reacted with benzylimine intermediate to produce (*E*)-N-benzyl-1-phenylmethanimine (**control 3 in Figure 18**). To investigate the potential radical pathway, Tempo (2,2,6,6-tetramethylpiperidine-1-oxyl) was employed at 1.2 equivalents, resulting in a significant reduction in the yield of benzamide, as expected (**control 4**). When, the counter anion of the ionic liquid was altered from $^{-}$OH (Triton B) to Br^{-} (TBAB), benzamide product did not observe. Instead, a different oxidized product was obtained, as observed in **controls 2** and **3**. This indicates that the hydroxide anion in Triton B played a crucial role in the conversion of benzylamine to benzamide. For additional validation, when benzylamine was treated with Triton B in the presence of phenylboronic acid (1.1 equiv) at standard conditions, only (*E*)-N-benzyl-1-phenylmethanimine (**7a**) and benzaldehyde (6a) were formed as the main products (**control 5 in Figure 18**). This indicates that phenylboronic acid reacted with OH^{-} ions present in Triton B and directed the formation of (*E*)-N-benzyl-1-phenylmethanimine (**7a**) and benzaldehyde (**6a**) instead of benzamide formation. The absence of any desired product (**2a**, **6a**, **7a**) under nitrogen

Table 4. ICP-AES analysis of reactants (Benzylamine, Triton B, TBAB). Values are given in ppm.

Sample	Na	K	Mg	Ca	Sr	Ba	Ti	Zr	Cr	Mn	Fe	Co	Ni	Pb	Cu	Zn	Cd	Al	Pd
Sigma Triton B (1)	30.82	> 2806	0.80	0.94	< dl	< dl	0.026	< dl	0.56	< dl	0.17	0.73	0.05	< dl	< dl	0.64	0.28	< dl	< dl
Sigma Triton B (2)	16.86	>1893	0.69	0.53	< dl	< dl	0.026	< dl	0.16	< dl	0.10	0.94	< dl	< dl	< dl	0.48	0.06	< dl	< dl
Sigma TBAB (1)	< dl	4.12	< dl	< dl	< dl	< dl	< dl	< dl	< dl	< dl	< dl	< dl	< dl	< dl	< dl	< dl	< dl	< dl	< dl
Sigma TBAB (2)	< dl	2.53	< dl	< dl	< dl	< dl	< dl	< dl	< dl	< dl	< dl	< dl	< dl	< dl	< dl	< dl	< dl	< dl	< dl
Benzylamine (1) Sigma	< dl	0.95	< dl	< dl	< dl	< dl	< dl	< dl	< dl	< dl	< dl	< dl	< dl	< dl	< dl	< dl	< dl	<dl	< dl
Benzylamine (2) Sigma	< dl	0.80	< dl	< dl	< dl	< dl	< dl	< dl	< dl	< dl	< dl	< dl	< dl	< dl	< dl	< dl	< dl	< dl	< dl
TCI Triton B (1)	> 6390	10.25	0.63	0.95	< dl	< dl	< dl	< dl	0.55	< dl	0.40	< dl	< dl	< dl	< dl	< dl	< dl	< dl	< dl
TCI Triton B (2)	> 6176	7.00	0.85	0.82	< dl	< dl	< dl	< dl	0.80	< dl	0.29	< dl	< dl	< dl	< dl	< dl	< dl	< dl	< dl

environment (**control 6 in Figure 18**) established the major role of oxygen in this reaction. The importance of the quaternary alkylammonium cation was evident in the above reactions, played a crucial role. The activation of oxygen in the reaction was further confirmed by calorimetric detection of H_2O_2 resulting from the reaction of benzylamine with hydroxide-free ionic liquid TBAB (**control 7**). However, the absence of H_2O_2 from the reaction mixture of benzylamine with Triton B suggests that hydroxide ions reacted in situ to generate H_2O_2, leading to the formation of benzamide product rather than (*E*)-N-benzyl-1-phenylmethanimine (**7a**) (**control 8 in Figure 18**). In order to understand the involvement of the quaternary alkylammonium cation in the reaction mixture, a control experiment (**control 9**) was carried out at 70°C in the presence of oxygen, excluding any quaternary alkylammonium-based ionic liquid. However, no oxidized compounds were obtained under this condition. As a control, Triton B was treated with benzylamine at room temperature without heating it to 70°C to see what effect temperature had. It signified that thermal energy was necessary to carry forward a reaction to form oxidative products as quickly as possible (**control 10 in Figure 18**).

2.2.7 Oxygen Activation and H_2O_2 By-product in the Reaction Mixture:

When oxygen participates in a reaction, hydrogen peroxide emerges as the primary oxidized by-product. The detection of hydrogen peroxide within the reaction medium serves as a crucial indicator for confirming the activation of oxygen. This detection not only verifies the involvement of oxygen in the chemical process but also underscores its role as an oxidizing agent. Consequently, the identification of hydrogen peroxide within the reaction system was an essential step in understanding the mechanisms and outcomes of oxygen-mediated reactions. When benzylamine was treated with 1 eq of anhydrous TBAB at the above-mentioned conditions, (*E*)-N-benzyl-1-

phenylmethanimine (**7a**) was produced as a sole product with hydrogen peroxide (**control 3 in Figure 18**).[151–153]

The detection of hydrogen peroxide in the reaction mixture was confirmed using the KI test as well as H_2O_2 detection strips (**Figures 19** and **20**).[154] However, when benzylamine in the presence of Triton B reacted with oxygen to produce the benzamide product under standard conditions, hydrogen peroxide was not detected in the corresponding reaction mixture (**control 8 in Figure 18**). This observation may suggest that hydrogen peroxide played a crucial role in producing the benzamide product from the benzylimine intermediate. The presence of OH^- ions in Triton B reacted with H_2O_2 to form the hydrogen peroxide anion, which then further reacted as a strong nucleophile with the benzylimine intermediate to produce benzamide.

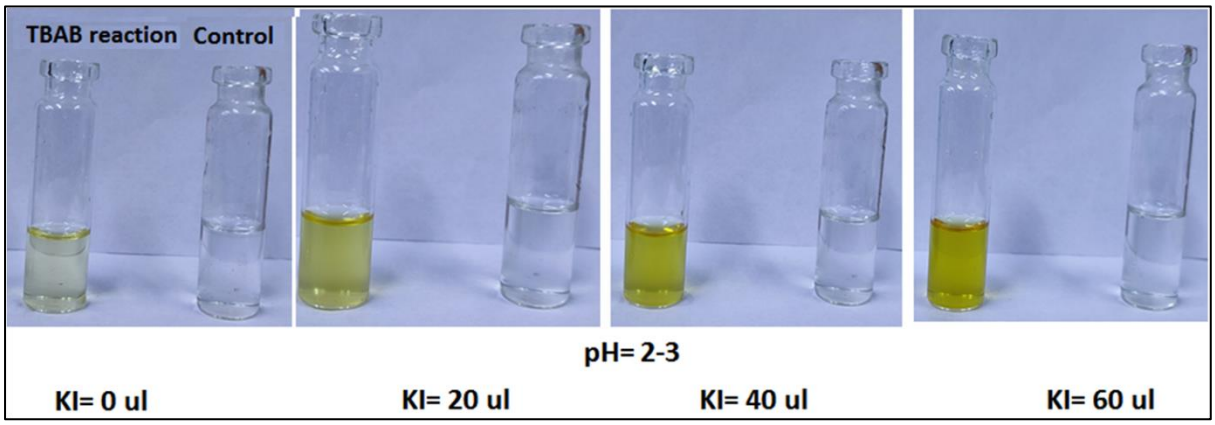

Figure 19. Detection of hydrogen peroxide using KI reaction.

2.2.8 Detection of H_2O_2 in Reaction Mixture using KI

2.2.8.1 Detection of H_2O_2 in Reaction Mixture (Benzylamine + O_2 + TBAB) using KI:

To a solution of Benzylamine (2 mmol), TBAB (2 mmol) were added in a 5 mL RB. The reaction mixture was stirred at 100°C for 14 hours under oxygen atmosphere. After completion of the reaction, 1 mL of water was added to the reaction mixture, followed by 1 mL of ethyl acetate. The total volume of the

resulting mixture was 2.7 mL, with a pH of 8.5. The organic yellow product (upper layer) was isolated through a workup procedure using ethyl acetate (1 mL, three times). Following the workup process, the pH of the aqueous phase was adjusted to 2-3 using 6N HCl, resulting in a total volume of approximately 2 mL for the aqueous phase. Subsequently, the aqueous phase was treated with KI (2% w/v) at a volume of 20 µl, which changed the light yellow reaction mixture to transition to an intense yellow color, indicating the liberation of iodine (**Figure 19)**.

2.2.8.2 Control Experiment for H_2O_2 Detection:

To a solution of Benzylamine (2 mmol), were added TBAB (2 mmol) in a 5 mL RB and reaction mixture was stirred at 100°C for 14 hours under nitrogen atmosphere. Two distinct layers formed as a result of adding 2 mL of water and 2 mL of ethyl acetate to the mixture after the reaction time. The organic phase (upper layer) was separated from the aqueous phase using ethyl acetate workup procedure (1 mL, three times). The addition of 6N HCl subsequently changed the pH to 2-3. After pH adjustment, the total volume of the aqueous phase was approximately 2 mL. Treatment of the aqueous phase with 20 µl of KI (2% w/v), followed by an additional 20 µl, did not result in any observable color change (**Figure 19)**.

2.2.9 Detection of H_2O_2 in Reaction Mixture using H_2O_2 Detection Strips

2.2.9.1 Detection of H_2O_2 in Reaction Mixture (Benzylamine + O_2 + TBAB) using H_2O_2 Detection Strips:

To a solution of Benzylamine (2 mmol), TBAB (2 mmol) were added in a 5 mL RB. The reaction mixture was stirred at 100°C for 14 hours under oxygen atmosphere. It was then cooled to room temperature, diluted with 1 mL of water and 1 mL of ethyl acetate. The pH of the reaction mixture was 8.5, and its total

volume was 2.7 mL. In order to eliminate the organic yellow product (upper portion), a workup procedure was executed using ethyl acetate (1 mL three times). 6N HCl (80–100µl) was added to change the pH of the aqueous solution to 6.5. 2 mL was the entire volume of the aqueous part. After that, the strip was dissolved in a colorless aqueous solution for thirty seconds. The turning yellow of the colorless lower part of the detection strip signifies the existence of hydrogen peroxide (**Figure 20)**.

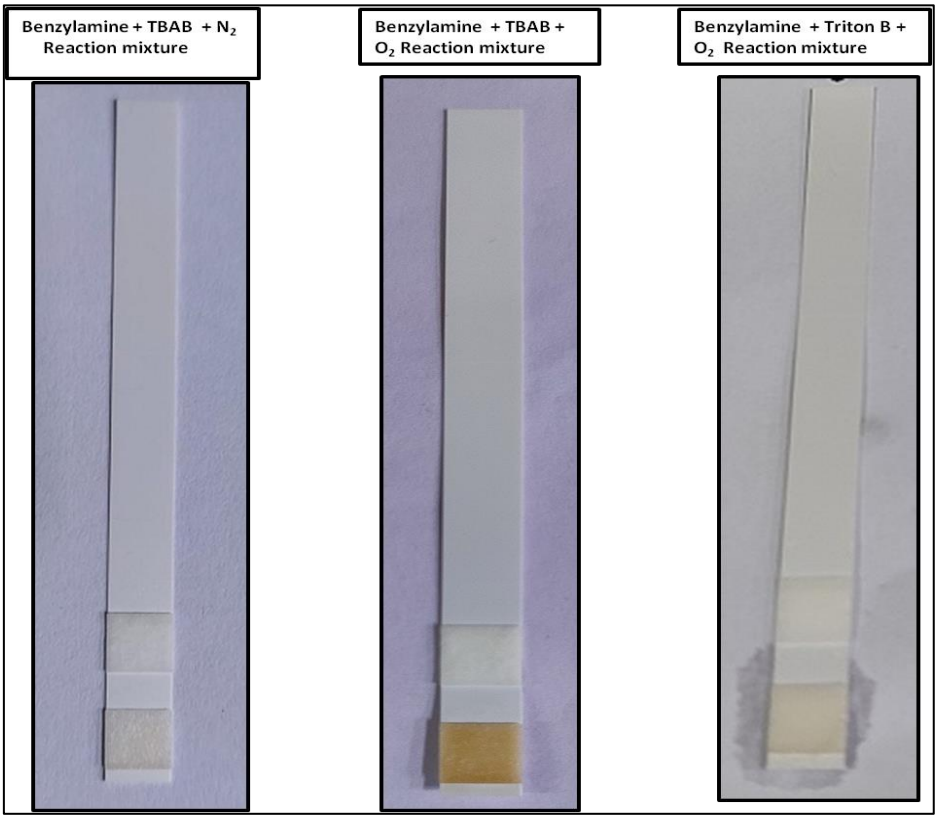

Figure 20: Hydrogen peroxide detection using H_2O_2 detection strips

2.2.9.2 Detection of H_2O_2 in Control Experiment (Benzylamine + N_2 + TBAB) using H_2O_2 Detection Strips:

To a solution of Benzylamine (2 mmol), were added TBAB (2 mmol) in a 5 mL RB and reaction mixture was stirred at 100°C for 14 hours under nitrogen atmosphere. It was then cooled to room temperature, diluted with 2 mL of water followed by the addition of 2 mL of ethyl acetate. The organic part was

separated. The remaining organic parts from the aqueous phase were eliminated using a workup procedure with the addition of ethyl acetate (1 mL, three times). The pH of the aqueous solution was adjusted to 6.5 by adding 6N HCl (80–100µl). The combined volume of the liquid part was 2 mL. The strip was placed in a transparent aqueous solution for duration of 30 seconds. No alteration in color was seen on the lowest part of the strip (**Figure 20)**.

2.2.9.3 Detection of H_2O_2 in Reaction Mixture (Benzylamine + O_2 + Triton B) using H_2O_2 Detection Strips:

To a solution of Benzylamine (2 mmol), were added Triton B (2 mmol) in a 5 mL RB. The reaction mixture was stirred at 70°C for 4 hours under oxygen atmosphere. It was then cooled to room temperature, diluted with 1 mL of water and 1 mL of ethyl acetate, resulting in the formation of two distinct layers. The organic light yellow product (upper layer) was separated through a workup procedure using ethyl acetate (1 mL, three times). Subsequently, the pH of the aqueous solution was adjusted to 6.5 using 6N HCl. Dissolving the strip in a colorless aqueous solution for 30 seconds did not result in a color change in the previously colorless lower part of the detection kit, indicating the absence of hydrogen peroxide (**Figure 20)**.

2.2.10 Time-dependent Proton Nuclear Magnetic Resonance (^{1}H NMR) Study for Understanding Oxidation Reaction Mechanisms:

Time-dependent proton nuclear magnetic resonance (^{1}H NMR) studies are crucial for understanding organic reaction mechanisms. By monitoring chemical shifts and peak intensities over time, ^{1}H NMR spectroscopy provides insights into dynamic transformations, intermediate formation, reaction pathways, and reaction progress rate. It also enables the detection of transient species and intermediates, advancing our understanding of chemical processes and the intricate details of organic reactions, such as the role of reagents via covalent or non-covalent interaction. It was crucial to determine whether Triton B or

TBAB, when reacted with benzylamine under standard conditions, played a covalent or non-covalent role. To understand the covalent or non-covalent roles of Triton B and TBAB with benzylamine or oxygen, a time-dependent ^{1}H NMR experiment was conducted. Five sets of reactions were performed to collect ^{1}H NMR data from t = 0 hr to t = 4 hr at 1 hr intervals using Triton B (1 eq) and benzylamine (1 eq) under standard reaction conditions.

Based on the ^{1}H NMR data, the proton attached to the benzyl group in benzylamine gradually vanished over a period of 4 hours. As a result, a new set of protons appeared in the aromatic region, indicating that Triton B was present throughout the production of benzamide compounds (as shown in **Figure 21a**). Following the process, Triton B's characteristic peaks remained unchanged, indicating that it interacts with benzylamine and oxygen through non-covalent rather than covalent interactions.

The presence of methanol in Triton B led to the absence of detectable amine protons in benzylamine, as evidenced by the ^{1}H NMR analysis. To ascertain which proton, either the benzylic or the amine proton, disappeared first, a ^{1}H NMR experiment was conducted using TBAB with benzylamine in $CDCl_3$. Six sets of reactions were performed to collect ^{1}H NMR data from t = 0 hr to t = 10 hr at 2 hr intervals using TBAB (1 eq) and benzylamine (1 eq) under standard reaction conditions. The ^{1}H NMR data (**Figure 21b**) clearly showed that the benzylic and amine protons were gradually disappearing and giving rise to new aromatic and benzylic proton configurations of the (*E*)-N-benzyl-1-phenylmethanimine (**7a**). The benzylic proton (δ=3.76ppm, 0.73H at 8h) consistently exhibited lower integration value relative to the amine protons (δ=1.87ppm, 1.57H at 8h) during the entire reaction period. This indicates that the benzylic protons exhibit a greater tendency to migrate towards oxygen before the amine protons. A probable reaction mechanism for the oxidative coupling of benzylamine and benzyl alcohol with quaternary alkyl ammonium-

based ionic liquid was hypothesized based on the aforementioned studies and is depicted in **Figure 22**.

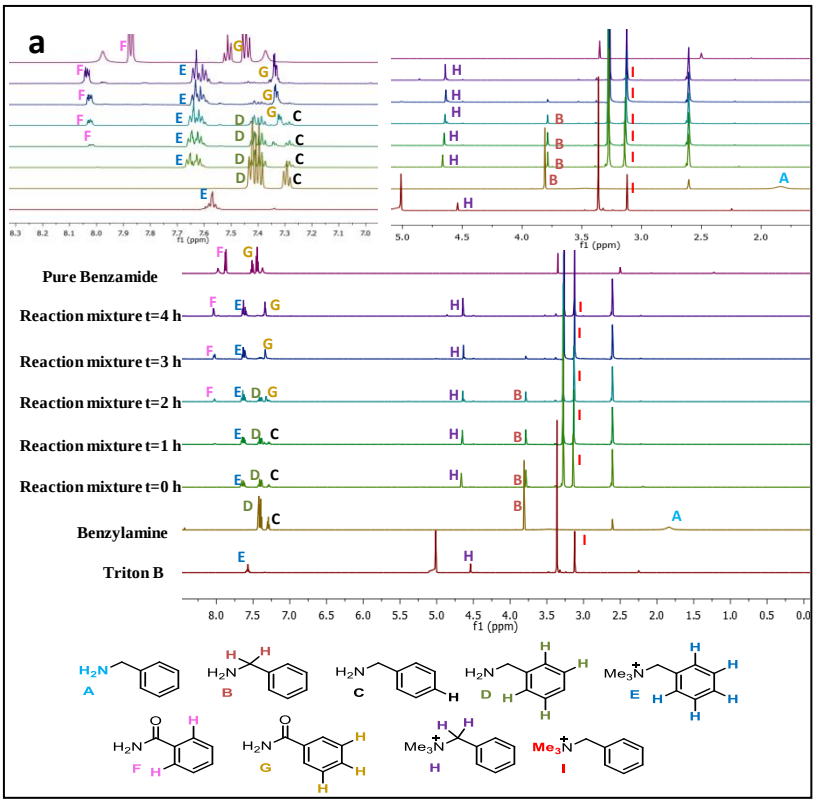

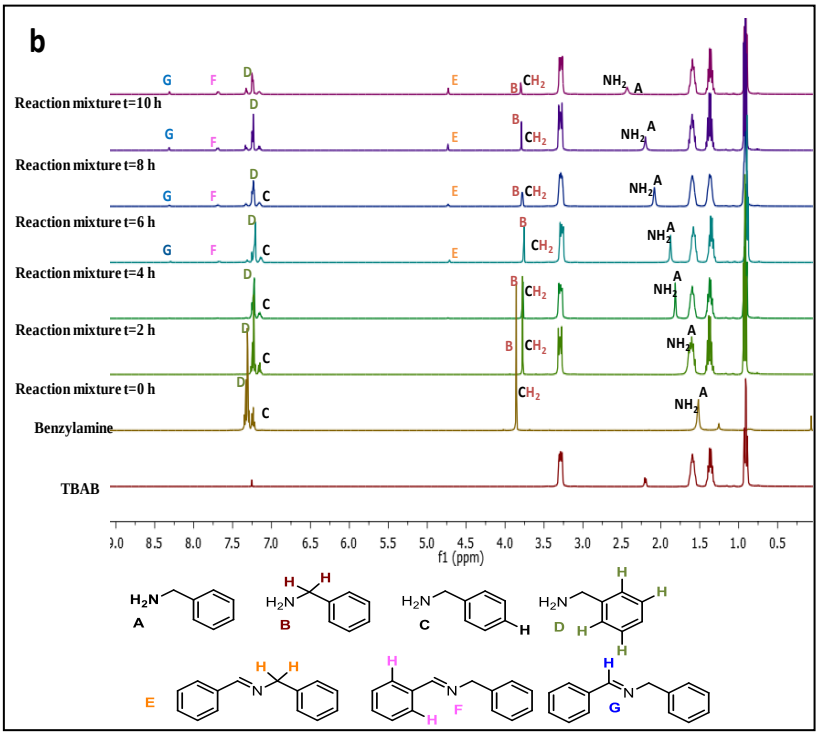

Figure 21. Time dependent ^{1}H NMR. **(a)** Time dependent ^{1}H NMR was recorded with one hour interval to four hours from the reaction mixture of benzylamine (1 eq) with Triton B (40% w/w methanol) (1 eq). The reaction was carried out at 70°C under oxygen. All ^{1}H NMR data was taken in DMSO(d6) solvent. ^{1}H NMR of Triton B was recorded in MeOD solvent. **(b)** to understand the involvement of $–NH_2$ proton in reaction mechanism, time dependent ^{1}H NMR was recorded with two hour intervals upto ten hours from reaction mixture of benzylamine (1 eq) with TBAB (1 eq). The reaction was carried out at 100°C under oxygen. All ^{1}H NMR data was taken in $CDCl_3$ solvent.

2.2.11 Plausible Reaction Mechanism:

In the presence of a quaternary alkylammonium-based ionic liquid, benzylamine and oxygen form a stable complex. Compared to benzylamine, the quaternary alkylammonium-based ionic liquid exhibits a more favorable interaction with oxygen, and this interaction promotes oxygen activation. This favorable interaction facilitates the transfer of a hydrogen atom from the benzylic position of benzylamine (**1ab**, **Figure 22a**) to activated oxygen, resulting in the formation of a hydroperoxyl radical (**1ac**, **Figure 22a**). Due to its high reactivity, the hydroperoxyl radical ($HO_2\cdot$) can remove a hydrogen atom from the $-NH_2$ group of **1ac** (**Figure 22a**).

This process leads to the formation of intermediate **1ad** (**Figure 22a**) and hydrogen peroxide through intramolecular radical coupling (**Figure 22a**). In the presence of methanol and hydroxide ions, in situ generated hydrogen peroxide is converted into an activated nucleophile. The hydroperoxide anion reacts with the benzylimine intermediate of complex **1ad** (**Figure 22a**) to produce complex **1ae** (**Figure 22a**) through nucleophilic addition. This is followed by an intramolecular proton transfer from the benzylic position to nitrogen, resulting in the regeneration of the hydroxide anion and the formation of the product benzamide (**2a**, **Figure 22a**) in the reaction medium (**Figure 22a**).

However, in the case of benzyl alcohol, the reaction mechanism follows almost identical paths to the reaction mechanism of benzylamine. It forms the benzyl

alcohol radical (**5ac**, **Figure 22b**), which is further oxidized in the presence of the hydroperoxyl radical to produce benzaldehyde (**6a**, **Figure 22b**) and hydrogen peroxide (**Figure 22b**).

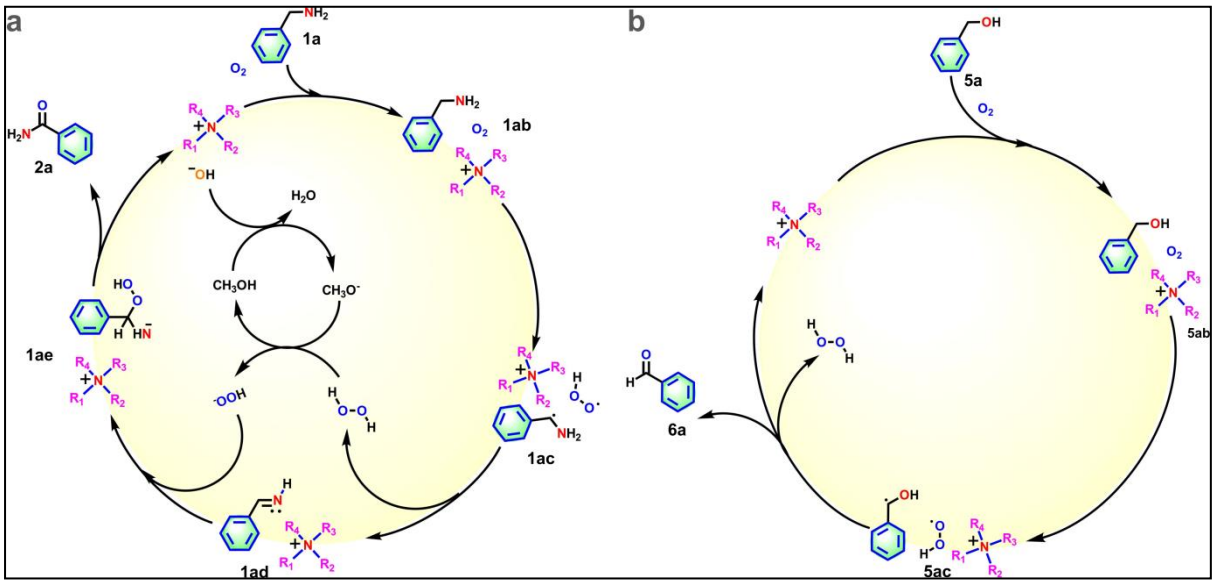

Figure 22. Mechanism of Benzylic amine & alcohol Oxidation**. (a)** catalytic pathway of benzylamine oxidation to benzamide using quaternary ammonium salt. A brown arrow indicates the formation of **7a** in presence of anhydrous TBAB. (**b)** catalytic pathway of benzyl alcohol oxidation to benzaldehyde formation using quaternary ammonium ions.

2.3 Conclusion

In this chapter, the optimize reaction conditions that were employed for the oxidation of benzylamine in order to get a high yield of the desired product. Upon further examination of the experimental data presented in the optimization table, numerous significant findings have emerged. Notably, it has been observed that the product yield exhibits variation in response to the solvent percentage present in the ionic liquid. In this section, quaternary alkylammonium-based ionic liquid systems have been effectively employed with O_2 as an oxidizing agent, enabling the oxidation of primary benzylamine and secondary cyclic benzylamine. The oxidation process of benzyl alcohol to

yield benzaldehyde has been effectively managed by employing a modified ionic liquid system TBAB. By subjecting benzylamine to the reaction conditions including both hydrated TBAB and anhydrous TBAB, a variety of distinct compounds have been obtained from benzylamine. Many control reactions have been examined in order to elucidate the potential reaction mechanism of this oxidation process. The preceding section has discussed the absence of transition metal ions in ionic liquids, as confirmed through an inductively coupled plasma (ICP) experiment. Additionally, it has been demonstrated that the transfer of a hydrogen atom yields a stable singlet oxidative product from triplet oxygen, a process that was previously hindered by the spin forbidden rule. A multifunctional (solvent, oxidant, and base) high-performance alternative to the often used metal-based oxidants ($AgNO_3$, $Cu(OAc)_2$, AgOAc, Ag_2CO_3, $Pd(OAc)_2$/DMSO) may be possible with molecular oxygen and ammonium-based ionic liquid.

2.4 Characterization of Spectral Data

2.4.1 Spectral data of primary benzylamine oxidation:

Benzamide (2a)

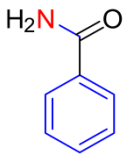

R_f =0.28 (30% ethylacetate/hexane with 5% triethylamine)

Yield (109.00 mg, 90% yield, white solid), Column chromatography (SiO_2, eluting with 40% ethyl acetate/hexane). ^{1}H NMR (600 MHz, DMSO-d_6) δ 7.98 (s, 1H), 7.89 – 7.86 (m, 2H), 7.53 – 7.49 (m, 1H), 7.46 – 7.42 (m, 2H), 7.37 (s, 1H).

^{13}CNMR (151 MHz, DMSO-d_6) δ 167.89, 134.26, 131.21, 128.20, 127.45. HRMS (EI) m/z: [M] Calcd for C_7H_7NO: 121.0528; Found 121.0518.

Picolinamide (2b)

R_f =0.90 (5% methanol/DCM with 5% triethylamine)

Yield (63 mg, 52% yield, white solid), Column chromatography (SiO_2, eluting with 75% ethyl acetate/hexane).^{1}H NMR (400 MHz, DMSO-d_6) δ 8.61 – 8.56 (m, 1H), 8.07 (s, 1H), 8.02 – 7.98 (m, 1H), 7.96 – 7.91 (m, 1H), 7.60 (s, 1H), 7.56 – 7.52 (m, 1H).

^{13}C NMR (101 MHz, DMSO-d_6) δ 166.02, 150.29, 148.43, 137.87, 126.42, 121.88. HRMS (EI) m/z: Calcd for $C_6H_6N_2O$ 122.0480; Found 122.0461

Furan-2-carboxamide (2c)

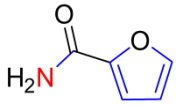

R_f =0.24 (30% ethylacetate/hexane with 5% triethylamine)

Yield (87 mg, 78% yield, white solid), Column chromatography (SiO_2, eluting with 35% ethyl acetate/hexane).^{1}H NMR (400 MHz, DMSO-d_6) δ 7.81 – 7.65 (m, 2H), 7.31 (s, 1H), 7.09 – 7.01 (m, 1H), 6.62 – 6.51 (m, 1H).

^{13}C NMR (101 MHz, DMSO-d_6) δ 159.39, 148.04, 144.99, 113.58, 111.76. HRMS (EI) m/z: Calcd for $C_5H_5NO_2$111.0320 found 111.0211

4-(trifluoromethyl)benzamide (2d)

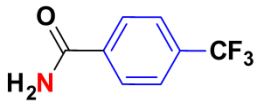

R_f =0.10 (20% ethylacetate/hexane with 5% triethylamine)

Yield (142.00 mg, 75% yield, white solid), Column chromatography (SiO_2, eluting with 50% ethyl acetate/hexane).^{1}H NMR (400 MHz, DMSO-d_6) δ 8.15 (s, 1H), 8.02 (d, *J* = 8.0 Hz, 2H), 7.79 (d, *J* = 8.0 Hz, 2H), 7.57 (s, 1H).

^{13}C NMR (101 MHz, DMSO-d_6) δ 167.25, 138.62, 131.68 (q, *J*=31.3Hz), 128.84, 125.78 (q, *J*=4.04 Hz), 123.13

HRMS (ESI) ($M+H^+$) m/z: Calcd for $C_8H_7F_3NO^+$: 190.0474, Found: 190.0482.

1,3-benzodioxole-4-carboxamide (2e)

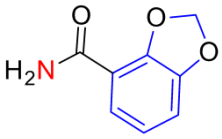

R_f =0.28 (30% ethylacetate/hexane with 5% triethylamine)

Yield (132.00 mg, 80% yield, white solid), Column chromatography (SiO_2, eluting with 40% ethyl acetate/hexane).^{1}H NMR (600 MHz, DMSO-d_6) δ 7.83 (s, 1H), 7.48 – 7.45 (m, 1H), 7.41 – 7.39 (m, 1H), 7.25 (s, 1H), 6.96 (d, *J* = 12 Hz, 1H), 6.08 (s, 2H).

^{13}C NMR (151 MHz, DMSO-d_6) δ 166.90, 149.58, 147.14, 128.16, 122.40, 107.63, 107.44, 101.49. HRMS (ESI) ([M+H]$^+$) m/z: Calcd for $C_8H_8NO_3^+$ 166.0499; Found 166.0517

2-nitrobenzamide (2f)

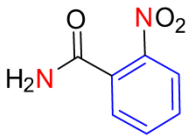

R_f =0.25 (50% ethylacetate/hexane with 5% triethylamine)

Yield (78 mg, 47% yield, white solid), Column chromatography (SiO_2, eluting with 60% ethyl acetate/hexane).^{1}H NMR (400 MHz, DMSO-d_6) δ 8.10 (s, 1H), 7.97 – 7.93 (m, 1H), 7.75 – 7.70 (m, 1H), 7.66 – 7.57 (m, 3H).

^{13}C NMR (101 MHz, DMSO-d_6) δ 167.72, 147.75, 133.87, 133.09, 131.15, 129.36, 124.46. HRMS (EI) m/z: Calcd for $C_7H_6N_2O_3$ 166.0378; Found 166.0349

4-methoxybenzamide (2g)

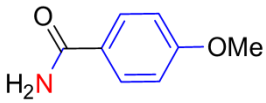

R_f =0.25 (30% ethylacetate/hexane with 5% triethylamine)

Yield (128.00 mg, 85% yield, white solid), Column chromatography (SiO_2, eluting with 45% ethyl acetate/hexane). ^{1}H NMR (600 MHz, DMSO-d_6) δ 7.87 – 7.81 (m, 3H), 7.18 (s, 1H), 6.97 (d, *J* = 12 Hz, 2H), 3.80 (s, 3H).

^{13}C NMR (151 MHz, DMSO-d_6) δ 167.42, 161.57, 129.35, 126.50, 113.38, 55.31. HRMS (EI) m/z: Calcd for $C_8H_9NO_2$: 151.0633, Found: 151.0624.

4-bromobenzamide (2h)

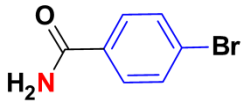

R_f =0.10 (30% ethylacetate/hexane with 5% triethylamine)

Yield (165.00 mg, 83% yield, white solid), Column chromatography (SiO_2, eluting with 70% ethyl acetate/hexane).^{1}H NMR (400 MHz, DMSO-d_6) δ 8.00 (s, 1H), 7.79 – 7.75 (m, 2H), 7.64 – 7.60 (m, 2H), 7.41 (s, 1H).

^{13}C NMR (101 MHz, DMSO-d_6) δ 166.94, 133.40, 131.23, 129.60, 125.01. HRMS (EI) m/z: Calcd for C_7H_6BrNO 198.9633; Found 198.9624

3,5-dimethoxybenzamide (2i)

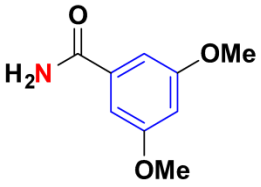

R_f =0.30 (50% ethylacetate/hexane with 5% triethylamine)

Yield (141.00 mg, 78% yield, white solid), Column chromatography (SiO_2, eluting with 50% ethyl acetate/hexane).^{1}H NMR (400 MHz, DMSO-d_6) δ 7.91 (s, 1H), 7.32 (s, 1H), 7.00 (d, *J* = 2.0 Hz, 2H), 6.59 (t, *J* = 2.4 Hz, 1H), 3.73 (s, 6H).

^{13}C NMR (101 MHz, DMSO-d_6) δ 167.98, 160.80, 136.91, 105.93, 103.68, 55.89. HRMS (ESI) ($[M+H]^+$) m/z: Calcd for $C_9H_{12}NO_3^+$: 182.0817, Found: 182.0815.

4-nitrobenzamide (2j)

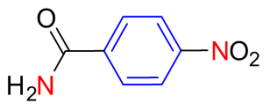

R_f =0.14 (40% ethylacetate/hexane with 5% triethylamine)

Yield (113.00 mg, 68% yield, white solid), Column chromatography (SiO_2, eluting with 75% ethyl acetate/hexane).^{1}H NMR (400 MHz, DMSO-d_6) δ 8.26-

8.24 (m, 3H), 8.07-8.05(m, 2H), 7.68 (s, 1H).^{13}C NMR (101 MHz, DMSO-d_6) δ 166.75, 149.58, 140.51, 129.45, 123.96.

HRMS (EI) m/z: Calcd for $C_7H_6N_2O_3$ 166.0378; Found: 166.0368.

2,4-dimethoxybenzamide (2k)

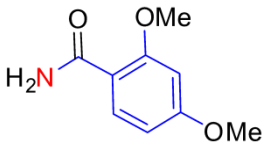

R_f =0.17 (30% ethylacetate/hexane with 5% triethylamine)

Yield (148.00 mg, 82% yield, white solid), Column chromatography (SiO_2, eluting with 55% ethyl acetate/hexane).^{1}H NMR (600 MHz, DMSO-d_6) δ 7.85 (d, *J* = 12 Hz, 1H), 7.51 (s, 1H), 7.38 (s, 1H), 6.64 – 6.59 (m, 2H), 3.89 (s, 3H), 3.81 (s, 3H).

^{13}C NMR (151 MHz, DMSO-d_6) δ 165.68, 162.99, 158.92, 132.74, 114.61, 105.55, 98.35, 55.92, 55.47. HRMS (ESI) ($[M+H]^+$) m/z: Calcd for $C_9H_{12}NO_3^+$: 182.0817, Found: 182.0818.

3-(trifluoromethyl)benzamide (2l)

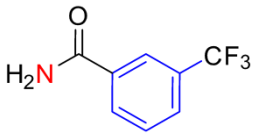

R_f =0.22 (20% ethylacetate/hexane with 5% triethylamine)

Yield (132.00 mg, 70% yield, white solid), Column chromatography (SiO_2, eluting with 32% ethyl acetate/pet ether).^{1}H NMR (400 MHz, DMSO-d_6) δ 8.22 – 8.11 (m, 3H), 7.85 (d, *J* = 8 Hz, 1H), 7.67 (t, *J* = 8 Hz, 1H), 7.57 (s, 1H).

^{13}C NMR (101 MHz, DMSO-d_6) δ 166.89, 135.68, 132.03, 130.10, 129.66 (q, *J*=32.32 Hz), 128.36 (q, *J*=4.04 Hz), 124.53 (q, *J*= 273.71 Hz), 124.60 (q, *J*=4.04Hz)

HRMS (ESI) ($[M+H]^+$) m/z: Calcd for $C_8H_7NOF_3^+$: 190.0480, Found: 190.0477

3-methoxybenzamide (2m)

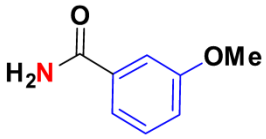

R_f =0.23 (30% ethylacetate/hexane with 5% triethylamine)

Yield (113.00 mg, 75% yield, white solid), Column chromatography (SiO_2, eluting with 45% ethyl acetate/hexane).^{1}H NMR (400 MHz, DMSO-d_6) δ 7.92 (s, 1H), 7.44 – 7.37 (m, 2H), 7.35 – 7.28 (m, 2H), 7.07 – 6.99 (m, 1H), 3.75 (s, 3H).

^{13}C NMR (101 MHz, DMSO-d_6) δ 167.61, 159.12, 135.72, 129.29, 119.67, 117.04, 112.62, 55.20. HRMS (EI) m/z: Calcd for $C_8H_9NO_2$: 151.0633, Found: 151.0644.

4-chlorobenzamide (2n)

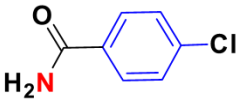

R_f =0.20 (30% ethylacetate/hexane with 5% triethylamine)

Yield (118.00 mg, 76% yield, white solid), Column chromatography (SiO_2, eluting with 50% ethyl acetate/hexane).^{1}H NMR (400 MHz, DMSO-d_6) δ 8.00 (s, 1H), 7.85 (d, *J* = 8.0 Hz, 2H), 7.48 (d, *J* = 8.0 Hz, 2H), 7.41 (s, 1H).

^{13}C NMR (101 MHz, DMSO-d_6) δ 166.87, 136.11, 133.04, 129.42, 128.32. HRMS (ESI) ([M+H]$^+$) m/z: calcd for $C_7H_7NOCl^+$: 156.0216, Found 156.0215

4-(tert-butyl)benzamide (2o)

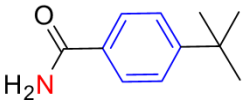

R_f =0.18 (30% ethylacetate/hexane with 5% triethylamine)

Yield (138.00 mg, 78% yield, white solid), Column chromatography (SiO_2, eluting with 55% ethyl acetate/hexane).^{1}H NMR (600 MHz, DMSO-d_6) δ 7.89

(s, 1H), 7.80 (d, *J* = 6.0 Hz, 2H), 7.45 (d, *J* = 12 Hz, 2H), 7.27 (s, 1H), 1.28 (s, 9H).

^{13}CNMR (151 MHz, DMSO-d_6) δ 167.68, 153.81, 131.41, 127.19, 124.81, 34.44, 30.81. HRMS (ESI) ([M+H]$^+$) m/z: Calcd for $C_{11}H_{16}NO^+$: 178.1232, Found: 178.1237.

2-aminobenzamide (2p)

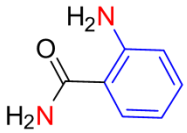

R_f =0.17 (30% ethylacetate/hexane with 5% triethylamine)

Yield (54.00 mg, 40% yield, white solid), Column chromatography (SiO_2, eluting with 55% ethyl acetate/hexane).^{1}H NMR (400 MHz, DMSO-d_6) δ 7.67 (s, 1H), 7.51 – 7.47 (m, 1H), 7.11 – 7.06 (m, 1H), 7.00 (s, 1H), 6.66 – 6.62 (m, 1H), 6.51 (s, 2H), 6.46 – 6.40 (m, 1H).

^{13}C NMR (101 MHz, DMSO-d_6) δ 171.30, 150.18, 131.88, 128.75, 116.40, 114.37, 113.69. HRMS (EI) m/z: Calcd for $C_7H_8N_2O$ 136.0637; Found 136.0622

2-(trifluoromethyl)benzamide (2q)

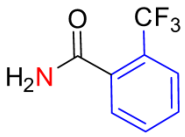

R_f =0.10 (20% ethylacetate/hexane with 5% triethylamine)

Yield (121.00 mg,64% yield, white solid), Column chromatography (SiO_2, eluting with 30% ethyl acetate/hexane).^{1}H NMR (400 MHz, DMSO-d_6) δ 7.90 (s, 1H), 7.74 – 7.71 (m, 1H), 7.69 – 7.64 (m, 1H), 7.61 – 7.53 (m, 2H), 7.52 – 7.48 (m, 1H).

^{13}C NMR (101 MHz, DMSO-d_6) δ 169.60, 137.38 (q, *J*=3.03 Hz), 132.87, 129.98, 128.78, 126.67 (q, *J*=5.05 Hz), 126.16 (q, *J*=32.32 Hz), 124.33 (q,

J=275.73 Hz). HRMS (EI) m/z: Calcd for $C_8H_6NOF_3$: 189.0401, Found: 189.0393

1-naphthamide (2r)

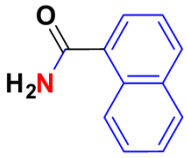

R_f =0.20 (30% ethylacetate/hexane with 5% triethylamine)

Yield (150.00 mg, 88% yield, white solid), Column chromatography (SiO_2, eluting with 50% ethyl acetate/hexane).^{1}H NMR (600 MHz, DMSO-d_6) δ 8.33 – 8.29 (m, 1H), 8.02 – 7.95 (m, 3H), 7.66 – 7.63 (m, 1H), 7.61 – 7.51 (m, 4H).

^{13}C NMR (151 MHz, DMSO-d_6) δ 170.59, 134.66, 133.20, 129.77, 129.71, 128.18, 126.61, 126.13, 125.58, 125.13, 124.94. HRMS (EI) m/z: Calcd for $C_{11}H_9NO$: 171.0684, Found: 171.0682

4-flurobenzylamine (1s) to 4-methoxybenzamide (2g)

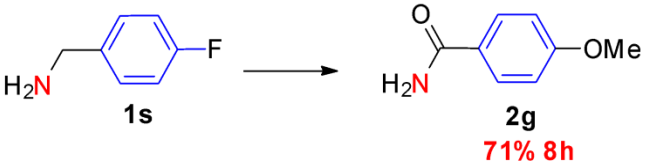

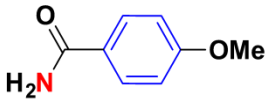

R_f =0.25 (30% ethylacetate/hexane with 5% triethylamine)

Yield (107.00 mg, 71% yield, white solid), Column chromatography (SiO_2, eluting with 45% ethyl acetate/hexane).^{1}H NMR (600 MHz, DMSO-d_6) δ 7.87 – 7.81 (m, 3H), 7.18 (s, 1H), 6.97 (d, *J* = 12 Hz, 2H), 3.80 (s, 3H).

^{13}C NMR (151 MHz, DMSO-d_6) δ 167.42, 161.57, 129.35, 126.50, 113.38, 55.31. HRMS (ESI) ($[M+H]^+$) m/z: Calcd for $C_8H_{10}NO_2^+$: 152.0706, Found: 152.0712.

2.4.2 Spectral data of secondary benzylamine:

Benzylamine (1a)

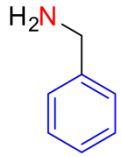

R_f =0.40 (30% ethylacetate/hexane with 5% triethylamine).

Yield (87.00 mg, 81% yield, colourless liquid), Column chromatography (SiO_2, eluting with 30% ethyl acetate/hexane with 5% triethylamine).^{1}H NMR (400 MHz, Chloroform-d) δ 7.36 – 7.28 (m, 4H), 7.26 – 7.21 (m, 1H), 3.86 (s, 2H), 1.52 (s, 2H).

^{13}C NMR (101 MHz, Chloroform-d) δ 143.43, 128.64, 127.16, 126.88, 46.62

Benzamide (2a)

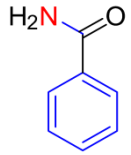

R_f =0.28 (30% ethylacetate/hexane with 5% triethylamine).

Yield (87.00 mg, 72% yield, white solid), Column chromatography (SiO_2, eluting with 40% ethyl acetate/hexane).^{1}H NMR (600 MHz, DMSO-d_6) δ 7.98 (s, 1H), 7.89 – 7.86 (m, 2H), 7.53 – 7.49 (m, 1H), 7.46 – 7.42 (m, 2H), 7.37 (s, 1H).

^{13}C NMR (151 MHz, DMSO-d_6) δ 167.89, 134.26, 131.21, 128.20, 127.45

HRMS (EI) m/z: Calcd for C_7H_7NO: 121.0528; Found 121.0518.

Norharmane (4d)

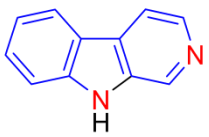

R_f =0.20 (5% methanol/DCM).

Yield (81.00 mg, 48% yield, yellow solid), Column chromatography (SiO_2, eluting with 2.5% methanol/DCM with 5% triethylamine).^{1}H NMR (600 MHz, DMSO-d_6) δ 11.61 (s, 1H), 8.89 (s, 1H), 8.37 – 8.19 (m, 2H), 8.15 – 8.05 (m, 1H), 7.65 – 7.50 (m, 2H), 7.29 – 7.19 (m, 1H).

^{13}C NMR (151 MHz, DMSO-d_6) δ 140.52, 140.11, 138.11, 134.03, 128.11, 127.43, 122.11, 121.79, 119.25, 114.66, 111.95.HRMS (EI) m/z: Calcd for $C_{11}H_8N_2$: 168.0687, Found: 168.0685.

Isoquinolene (4e)

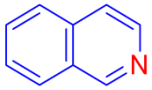

R_f =0.45 (20% ethylacetate/hexane).

Yield (105.00 mg, 82% yield, colourless liquid), Column chromatography (SiO_2, eluting with 7% ethyl acetate/hexane with 5% triethylamine).^{1}H NMR (600 MHz, DMSO-d_6) δ 9.32 (s, 1H), 8.50 (d, J = 6 Hz, 1H), 8.14 – 8.10 (m, 1H), 7.98 – 7.94 (m, 1H), 7.83 – 7.76 (m, 2H), 7.71 – 7.66 (m, 1H).

^{13}C NMR (151 MHz, DMSO-d_6) δ 152.34, 142.87, 135.18, 130.57, 128.24, 127.58, 127.49, 126.43, 120.34. HRMS (EI) m/z: Calcd for C_9H_7N : 129.0578, Found: 129.0570.

2.4.3 Spectral data of benzylalcohol oxidation

Benzaldehyde (6a)

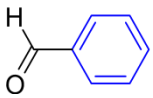

R_f =0.60 (5% ethylacetate/hexane).

Yield (31.00 mg, 30% yield, using Triton B, colourless liquid), Yield (53.00 mg, 50% yield, using TBAB, colourless liquid), Flash Column chromatography (SiO_2, eluting with 1.5% ethyl acetate/hexane).^{1}H NMR (400 MHz,

Chloroform-d) δ 10.01 (s, 1H), 7.89 – 7.86 (m, 2H), 7.64 – 7.60 (m, 1H), 7.54 – 7.50 (m, 2H).

^{13}C NMR (101 MHz, Chloroform-d) δ 192.98, 137.03, 135.06, 130.35, 129.61

4-methoxybenzaldehyde (6b)

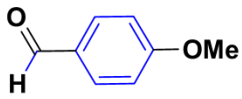

R_f =0.30 (5% ethylacetate/hexane)

Yield (53.00 mg, 33% yield, using Triton B, colourless liquid), Yield (63.00 mg, 47% yield, using TBAB, colourless liquid), Flash Column chromatography (SiO_2, eluting with 2.5% ethyl acetate/hexane).^{1}H NMR (400 MHz, Chloroform-d) δ 9.87 (s, 1H), 7.84 – 7.80 (m, 2H), 7.01 – 6.97 (m, 2H), 3.88 (s, 3H).

^{13}C NMR (101 MHz, Chloroform-d) δ 189.80, 163.60, 130.97, 128.96, 113.27, 54.57. HRMS (ESI) ([M+H]$^+$) m/z: Calcd for $C_8H_9O_2^+$: 137.0597, Found: 137.0609.

3-methoxybenzaldehyde (6c)

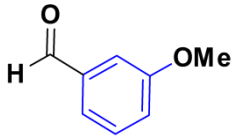

R_f =0.60 (5% ethylacetate/hexane).

Yield (54.00 mg, 40% yield, using Triton B, colourless liquid), Yield (82.00 mg, 61% yield, using TBAB, colourless liquid), Flash Column chromatography (SiO_2, eluting with 1.4% ethyl acetate/hexane).^{1}H NMR (400 MHz, Chloroform-d) δ 9.96 (s, 1H), 7.45 – 7.42 (m, 2H), 7.39 – 7.37 (m, 1H), 7.18 – 7.15 (m, 1H), 3.85 (s, 3H).

^{13}C NMR (101 MHz, Chloroform-d) δ 192.24, 160.25, 137.90, 130.12, 123.64, 121.63, 112.13, 55.55.

2-methoxybenzaldehyde (6d)

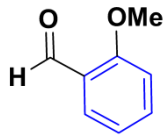

R_f =0.35(10% ethylacetate/hexane).

Yield (38.00 mg, 28% yield, using Triton B, colourless liquid), Yield (75.00 mg, 55% yield, using TBAB, colourless liquid), Flash Column chromatography (SiO_2, eluting with 2.3% ethyl acetate/hexane)^{1}H NMR (400 MHz, Chloroform-d) δ 10.46 – 10.45 (m, 1H), 7.83 – 7.79 (m, 1H), 7.56 – 7.51 (m, 1H), 7.03 – 6.96 (m, 2H), 3.91 (s, 3H).

^{13}C NMR (101 MHz, Chloroform-d) δ 189.91, 161.93, 136.02, 128.64, 124.94, 120.75, 111.71, 55.71. HRMS (ESI) ($[M+H]^+$) m/z: Calcd for $C_8H_9O_2^+$: 137.0597, Found: 137.0607.

4-bromobenzaldehyde (6e)

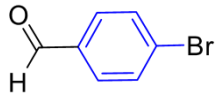

R_f =0.60 (5% ethylacetate/hexane).

Yield (48.00 mg, 26% yield, using Triton B, white solid), Yield (93.00 mg, 50% yield, using TBAB, white solid), Flash Column chromatography (SiO_2, eluting with 1.5% ethyl acetate/hexane).^{1}H NMR (400 MHz, Chloroform-d) δ 9.96 (s, 1H), 7.75 – 7.72 (m, 2H), 7.69 – 7.66 (m, 2H).

^{13}C NMR (101 MHz, Chloroform-d) δ 191.13, 135.16, 132.53, 131.05, 129.86.

4-chlorobenzaldehyde (6f)

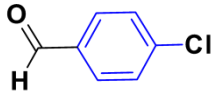

R_f =0.50 (5% ethylacetate/hexane).

Yield (41.00 mg, 29% yield, using Triton B, white solid), Yield (77.00 mg, 55% yield, using TBAB, white solid), Flash Column chromatography (SiO_2, eluting with 1.6% ethyl acetate/hexane).^{1}H NMR
(400 MHz, Chloroform-d) δ 9.97 (s, 1H), 7.83 – 7.78 (m, 2H), 7.53 – 7.48 (m, 2H).^{13}C NMR (101 MHz, Chloroform-d) δ 190.99, 141.11, 134.86, 131.05, 129.60.

4-(trifluoromethyl) benzaldehyde (6g)

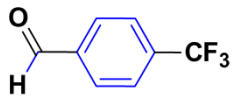

R_f =0.50(5% ethylacetate/hexane).

Yield (35.00 mg, 20% yield, using Triton B, colourless liquid), Yield (49.00 mg, 28% yield, using TBAB), Flash Column chromatography (SiO_2, eluting with 1.8% ethyl acetate/hexane).^{1}H NMR (400 MHz, Chloroform-d) δ 10.09 (s, 1H), 8.02 – 7.97 (m, 2H), 7.82 – 7.77 (m, 2H).

^{13}C NMR (101 MHz, Chloroform-d) δ 191.14, 138.74, 135.69 (q, *J*=33.33), 129.99, 126.19 (q, *J*=4.04), 123.5(q, *J*=274.72)

4-methylbenzaldehyde (6h)

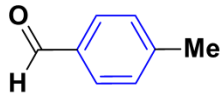

R_f =0.55 (5% ethylacetate/hexane).

Yield (62.00 mg, 52% yield, using Triton B, colourless liquid), Yield (76.00 mg, 63% yield, using TBAB, colourless liquid), Flash Column chromatography (SiO_2, eluting with 1.6% ethyl acetate/hexane).^{1}H NMR (400 MHz, Chloroform-d) δ 9.95 (s, 1H), 7.78 – 7.74 (m, 2H), 7.34 – 7.29 (m, 2H), 2.42 (s, 3H). ^{13}C NMR (101 MHz, Chloroform-d) δ 192.16, 145.72, 134.39, 129.93, 129.79, 22.06.

4-(benzyloxy)-3-methoxybenzaldehyde (6i)

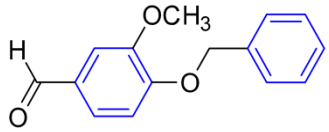

R_f =0.30 (5% ethylacetate/hexane).

Yield (58.00 mg, 24% yield, using Triton B, white solid), Yield (83.00 mg, 36% yield, using TBAB, white solid), Flash Column chromatography (SiO_2, eluting with 4.1% ethyl acetate/hexane). ^{1}H NMR (400 MHz, Chloroform-d) δ 9.83 (s, 1H), 7.45 – 7.41 (m, 3H), 7.40 – 7.35 (m, 3H), 7.34 – 7.29 (m, 1H), 6.98 (d, *J* = 8.2 Hz, 1H), 5.24 (s, 2H), 3.94 (s, 3H).

^{13}C NMR (101 MHz, Chloroform-d) δ 191.07, 153.76, 150.25, 136.16, 130.46, 128.88, 128.37, 127.35, 126.74, 112.56, 109.53, 71.04, 56.22.

2.4.4 Spectral data of control experiments

Control 2

Benzaldehyde (6a)

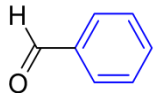

Column chromatography (SiO_2, eluting with 2% ethyl acetate/hexane).^{1}H NMR (400 MHz, Chloroform-d) δ 10.02 (s, 1H), 7.90 – 7.86 (m, 2H), 7.65 – 7.60 (m, 1H), 7.55 – 7.50 (m, 2H).

^{13}C NMR (101 MHz, Chloroform-d) δ 192.51, 136.56, 134.59, 129.87, 129.14.

Control 3

(E)-N-benzylidene-1-phenylmethanamine (7a)

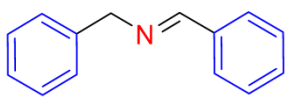

Column chromatography (SiO_2, eluting with 2% ethyl acetate/hexane with 5% triethylamine). ^{1}H NMR (400 MHz, Chloroform-d) δ 8.40 (s, 1H), 7.81 – 7.76

(m, 2H), 7.44 – 7.39 (m, 3H), 7.37 – 7.32 (m, 4H), 7.29 – 7.27 (m, 1H), 4.83 (s, 2H).

^{13}C NMR (101 MHz, Chloroform-d) δ 162.11, 130.89, 129.90, 129.16, 128.75, 128.64, 128.44, 128.14, 127.13, 65.20. HRMS (EI) m/z: Calcd for $C_{14}H_{13}N$: 195.1048, Found: 195.1047

Control 5

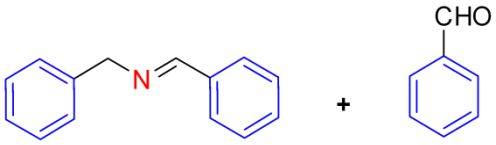

Column chromatography (SiO_2, eluting with 2% ethyl acetate/hexane with 5% triethylamine).^{1}H NMR (400 MHz, Chloroform-d) δ 10.02 (s, 0.42H), 8.40 – 8.39 (m, 1H), 7.90 – 7.87 (m, 0.86H), 7.80 – 7.76 (m, 2H), 7.66 – 7.61 (m, 0.43H), 7.56 – 7.51 (m, 0.90H), 7.43 – 7.40 (m, 3H), 7.35-7.34 (m, 4H), 7.28 – 7.25 (m, 1H), 4.83 – 4.82 (m, 2H).

^{13}C NMR (101 MHz, Chloroform-d) δ 192.46, 162.08, 139.38, 136.52, 136.25, 134.54, 130.85, 129.83, 129.09, 128.69, 128.58, 128.37, 128.07, 127.07, 65.13.

NMR spectral data of primary benzylamine oxidation

^{1}H NMR in DMSO (d_6) 600 MHz (2a)

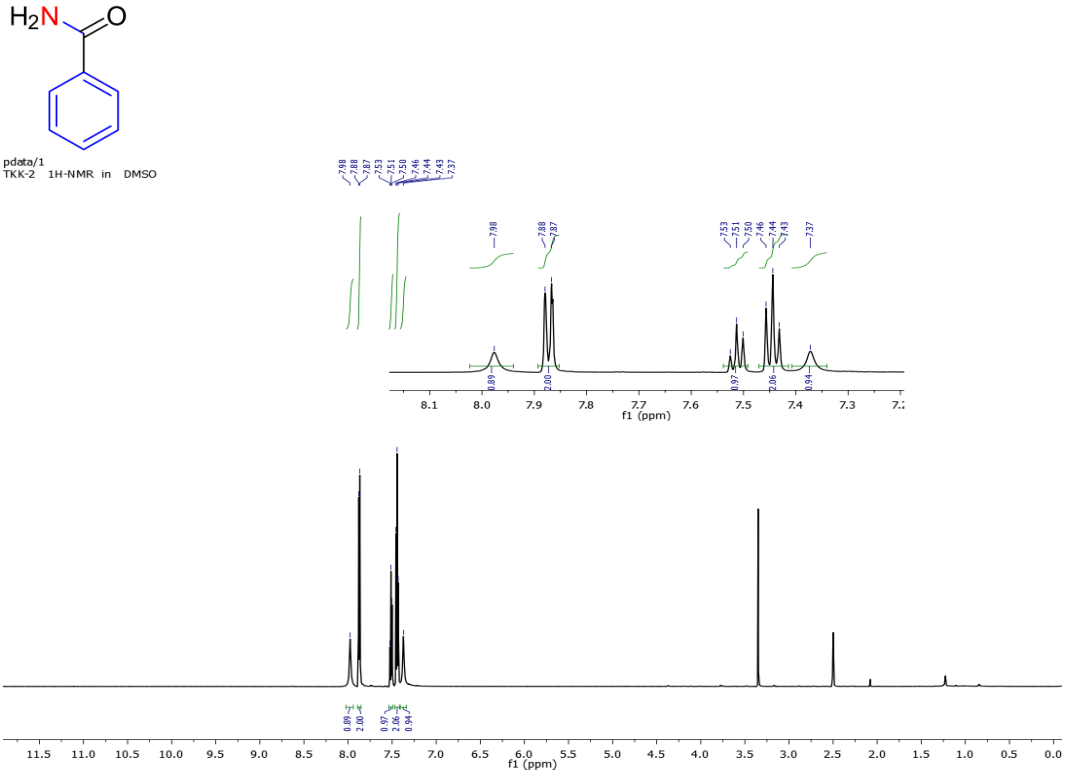

^{13}C NMR in DMSO (d_6) 151 MHz (2a)

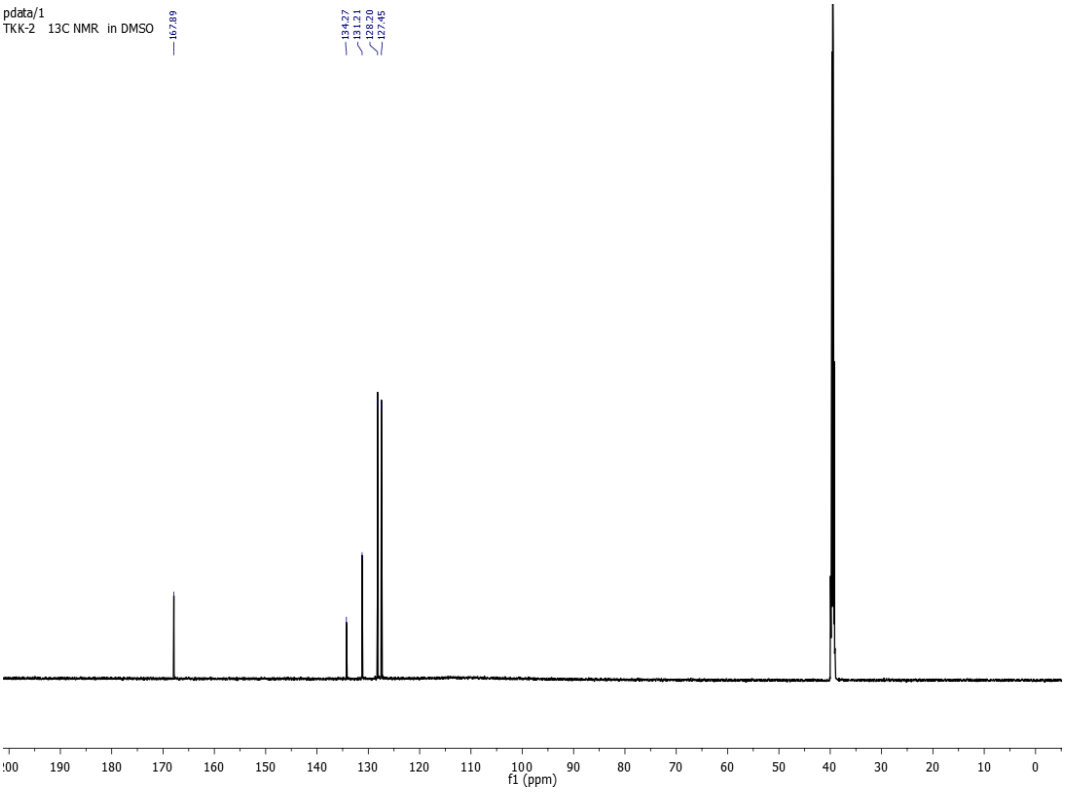

^{1}H NMR in DMSO (d_6) 400 MHz (2b)

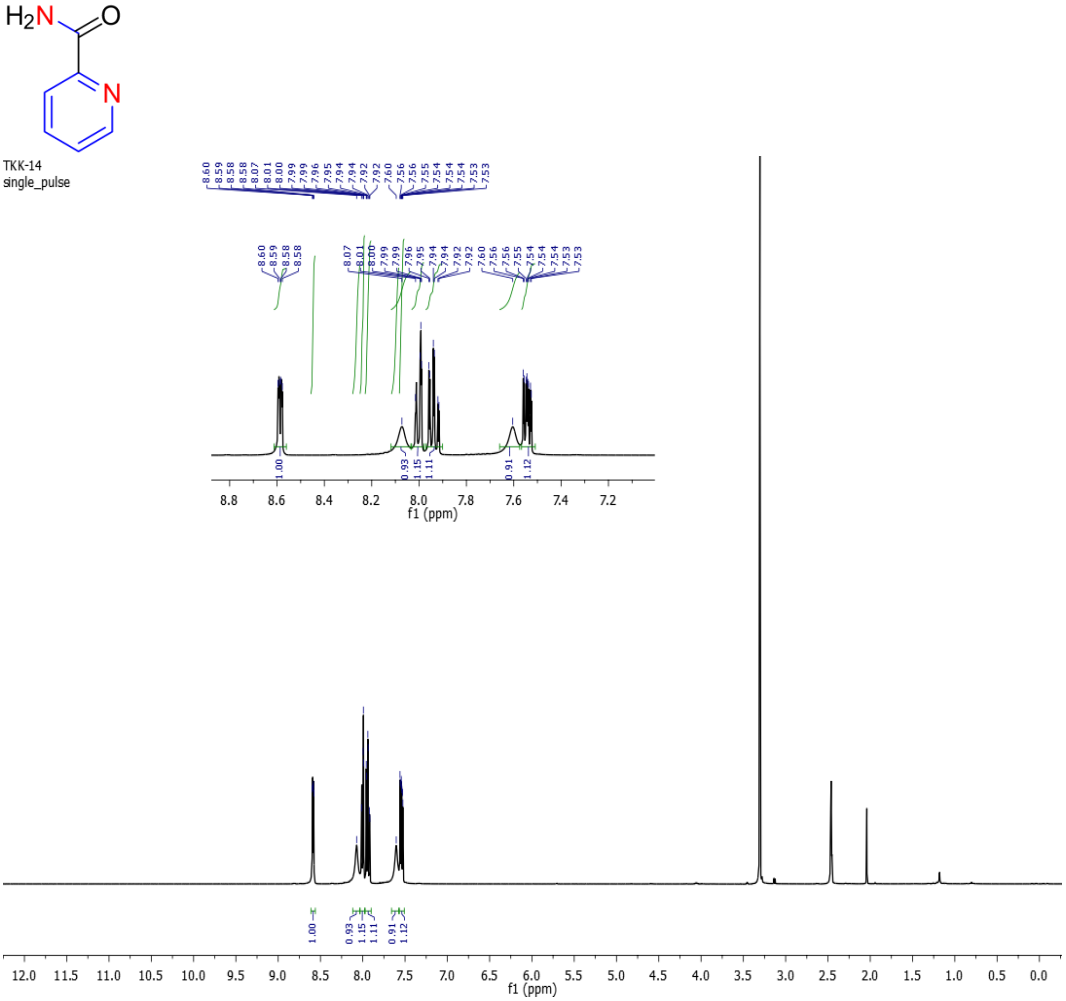

^{13}C NMR in DMSO (d_6) 101 MHz (2b)

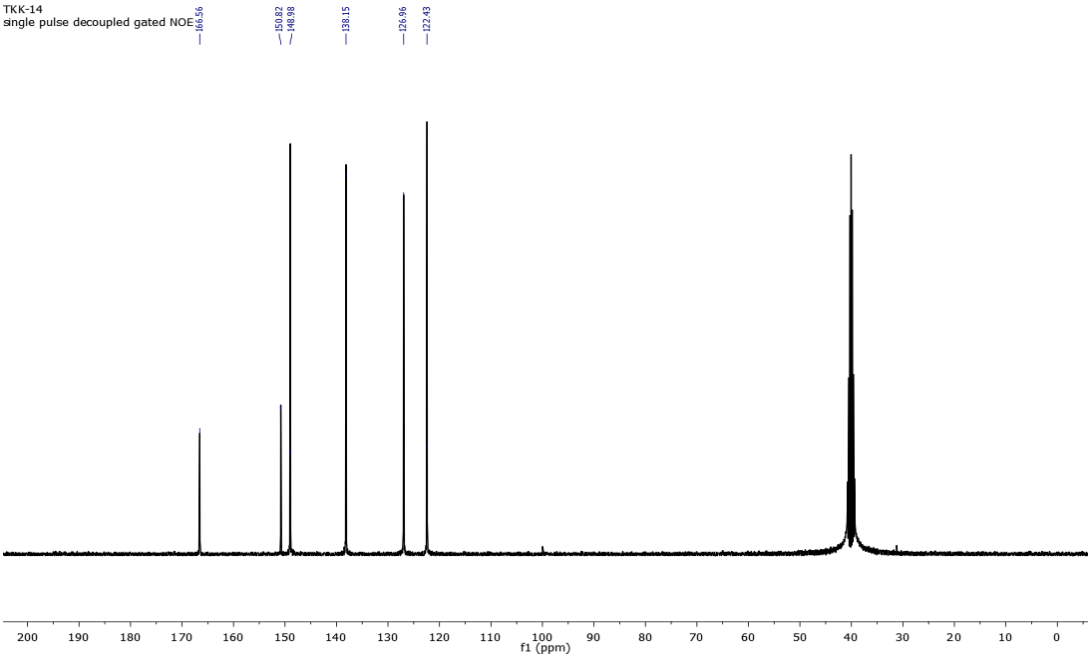

^{1}H NMR in DMSO (d_6) 400 MHz (2c)

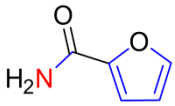

TKK-=15
single_pulse

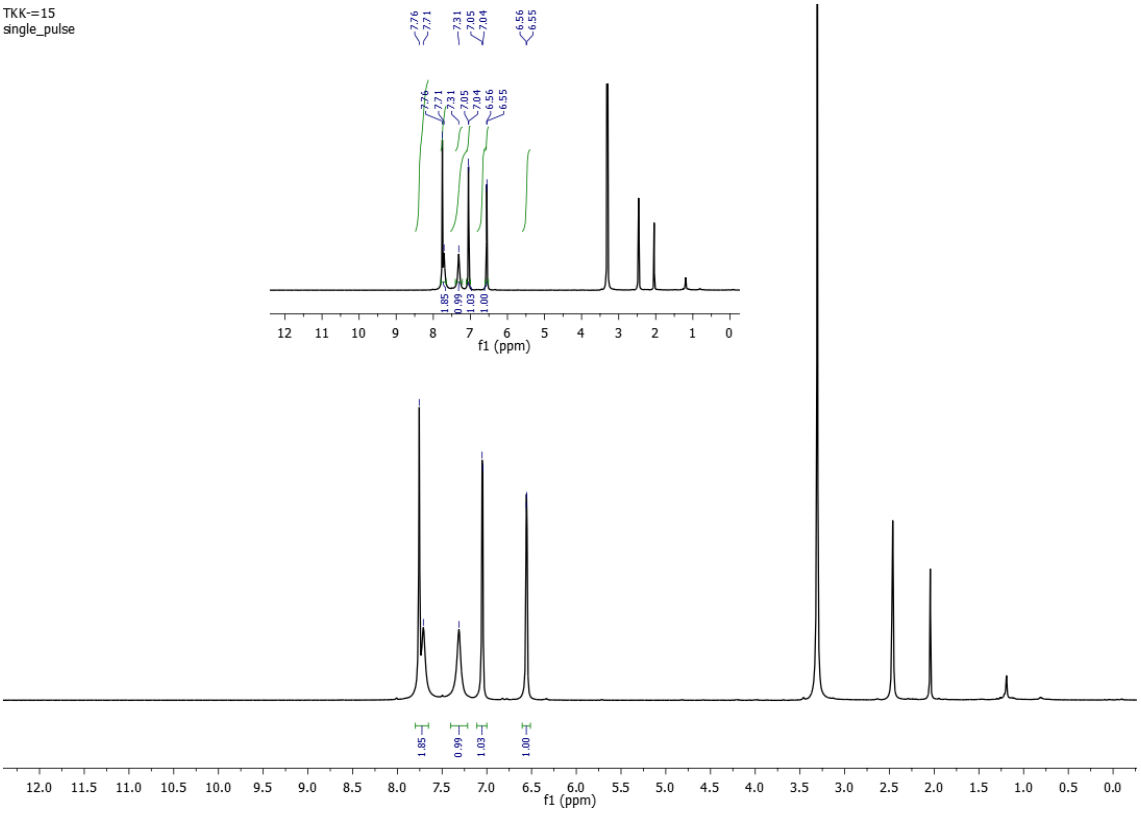

^{13}C NMR in DMSO (d_6) 101 MHz (2c)

TKK-=15
single pulse decoupled gated NOE

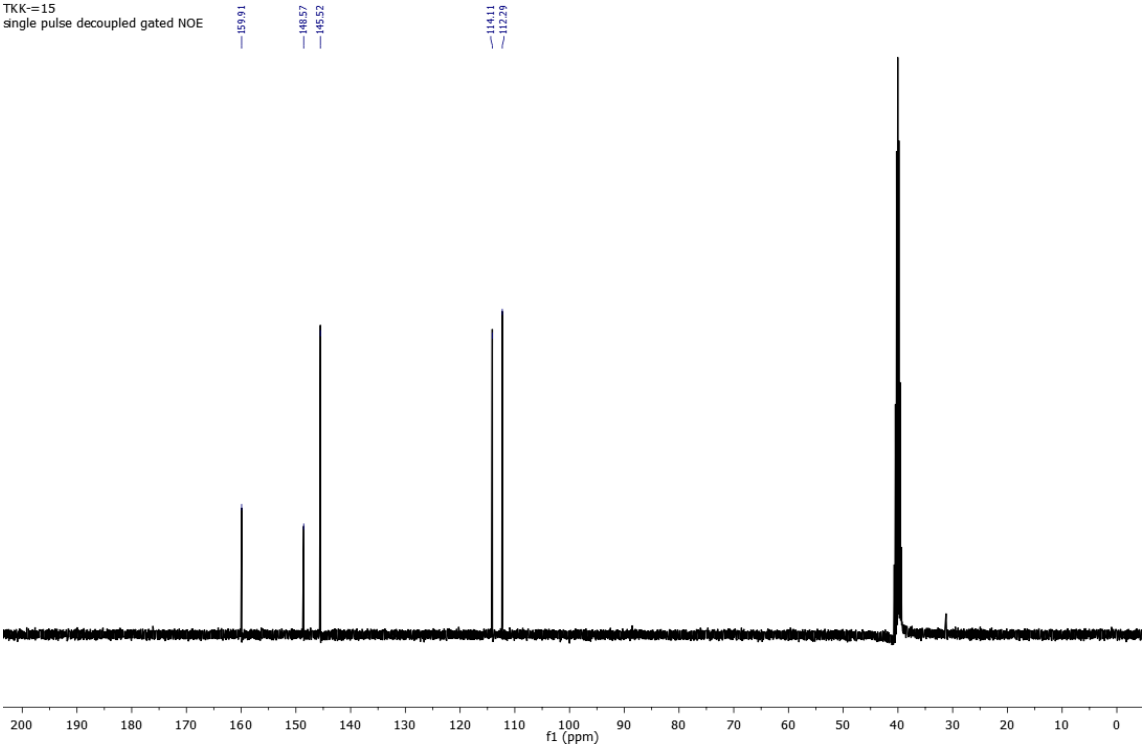

^{1}H NMR in DMSO (d_6) 400 MHz (2d)

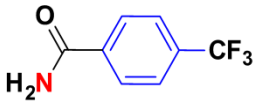

TKK-57
single_pulse

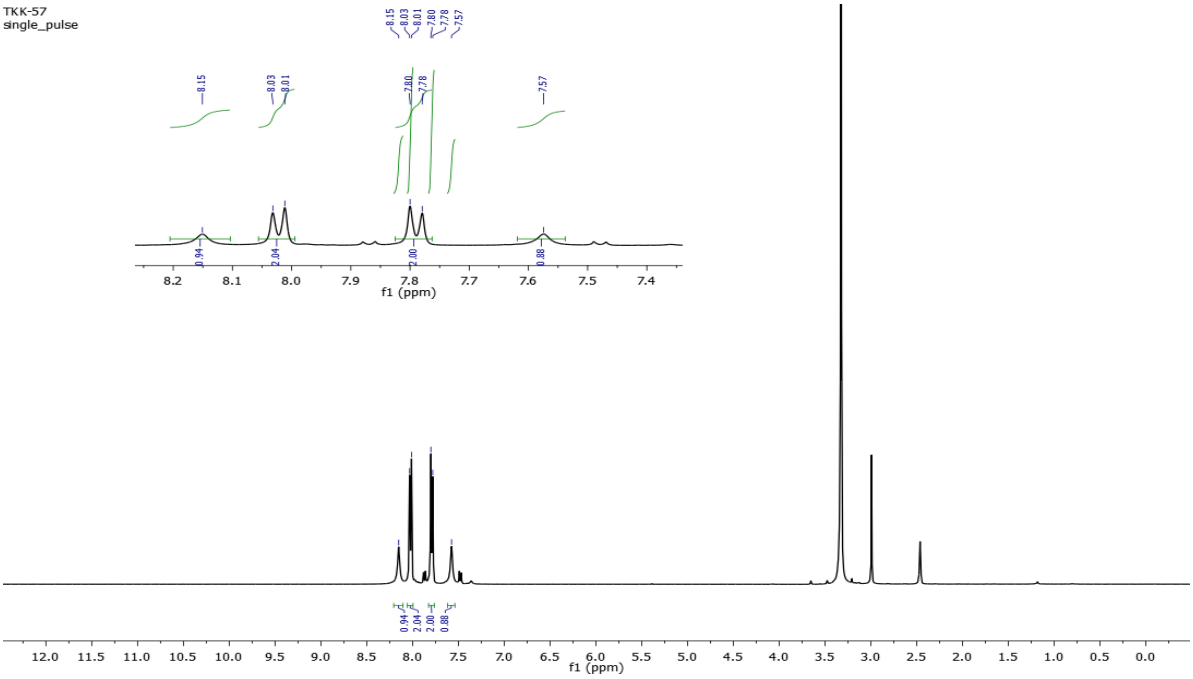

^{13}C NMR in DMSO (d_6) 101 MHz (2d)

TKK-57
single pulse decoupled gated NOE

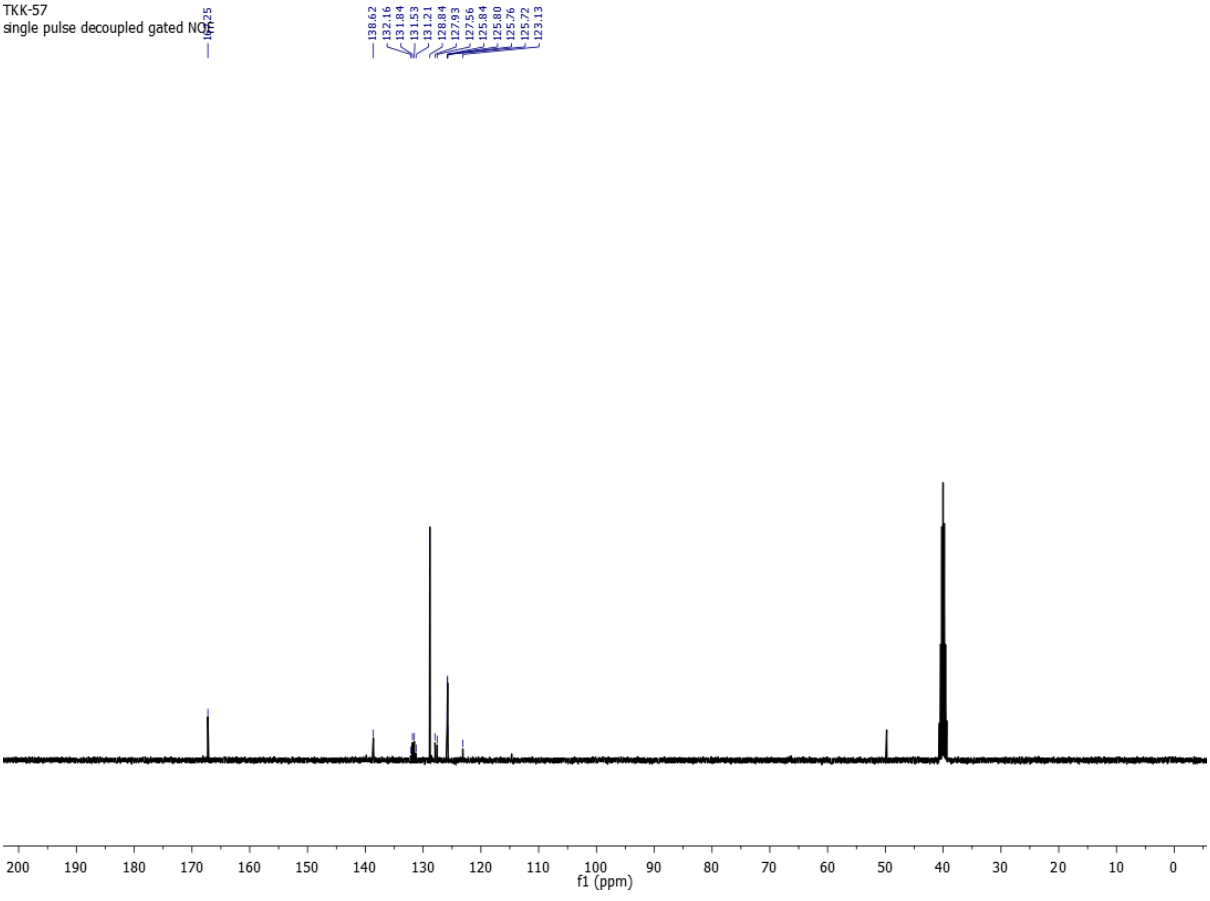

^{1}H NMR in DMSO (d_6) 600 MHz (2e)

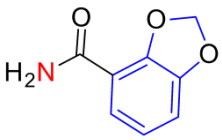

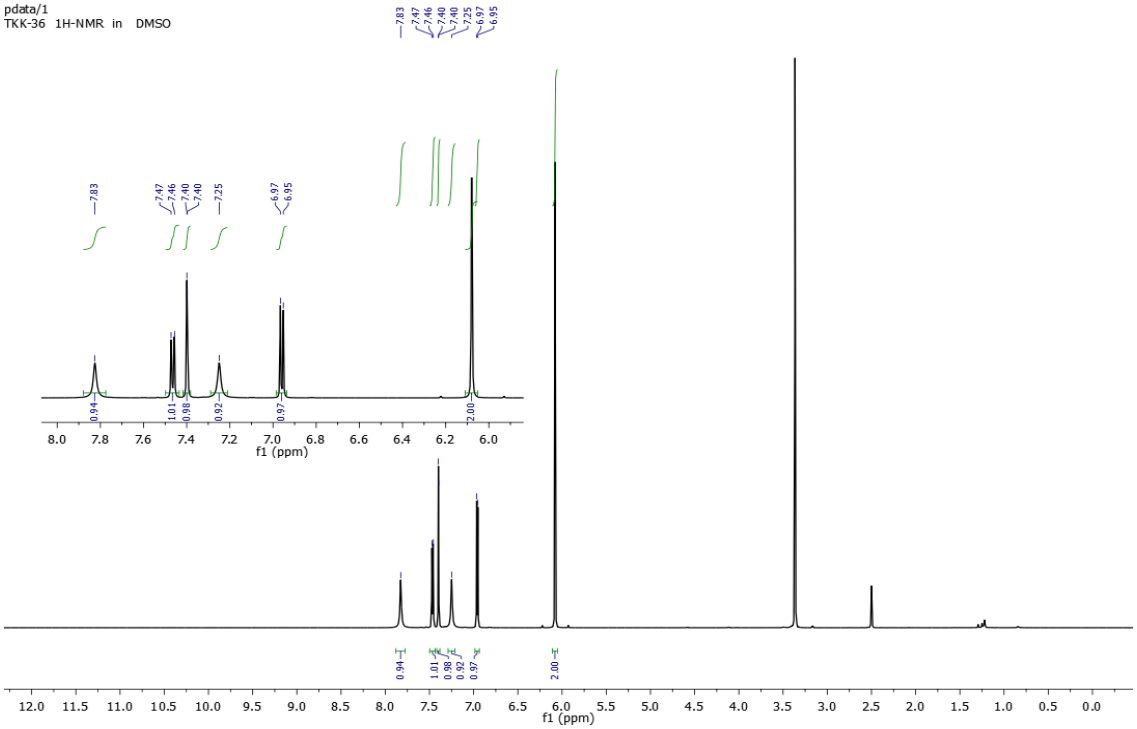

^{13}CNMR in DMSO (d_6) 151 MHz (2e)

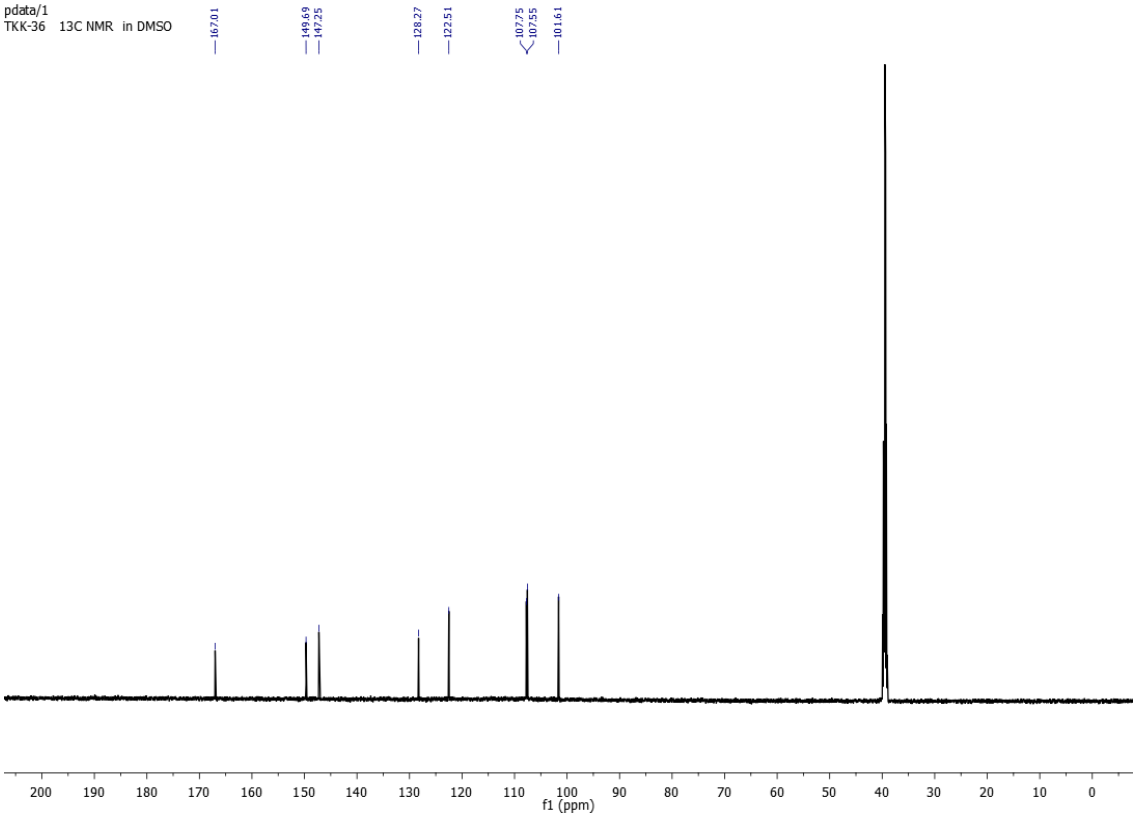

^{1}H NMR in DMSO (d_6) 400 MHz (2f)

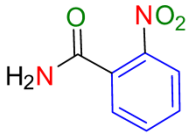

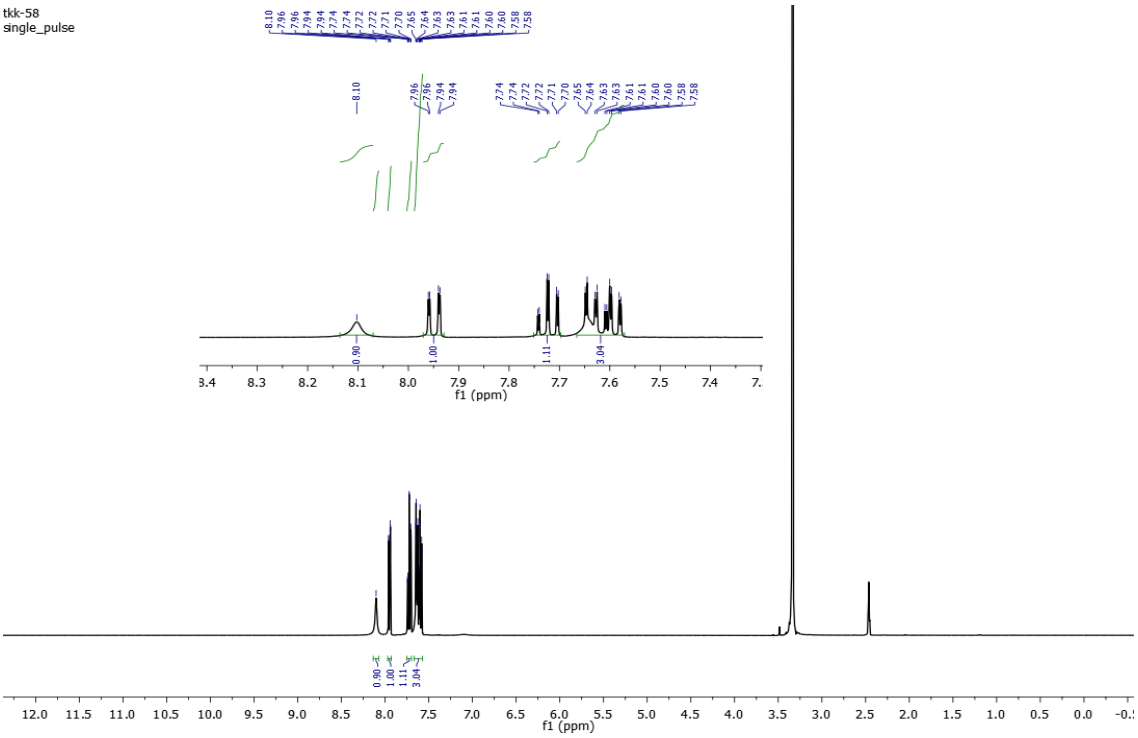

^{13}C NMR in DMSO (d_6) 101 MHz (2f)

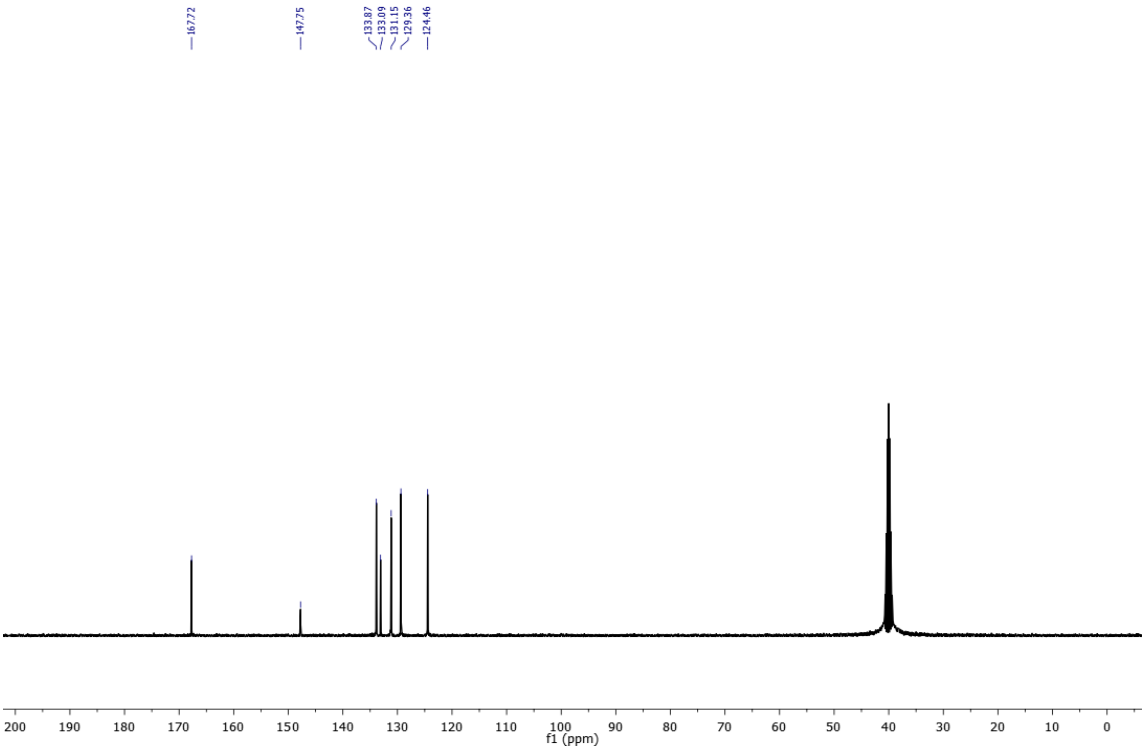

^{1}H NMR in DMSO (d_6) 600 MHz (2g)

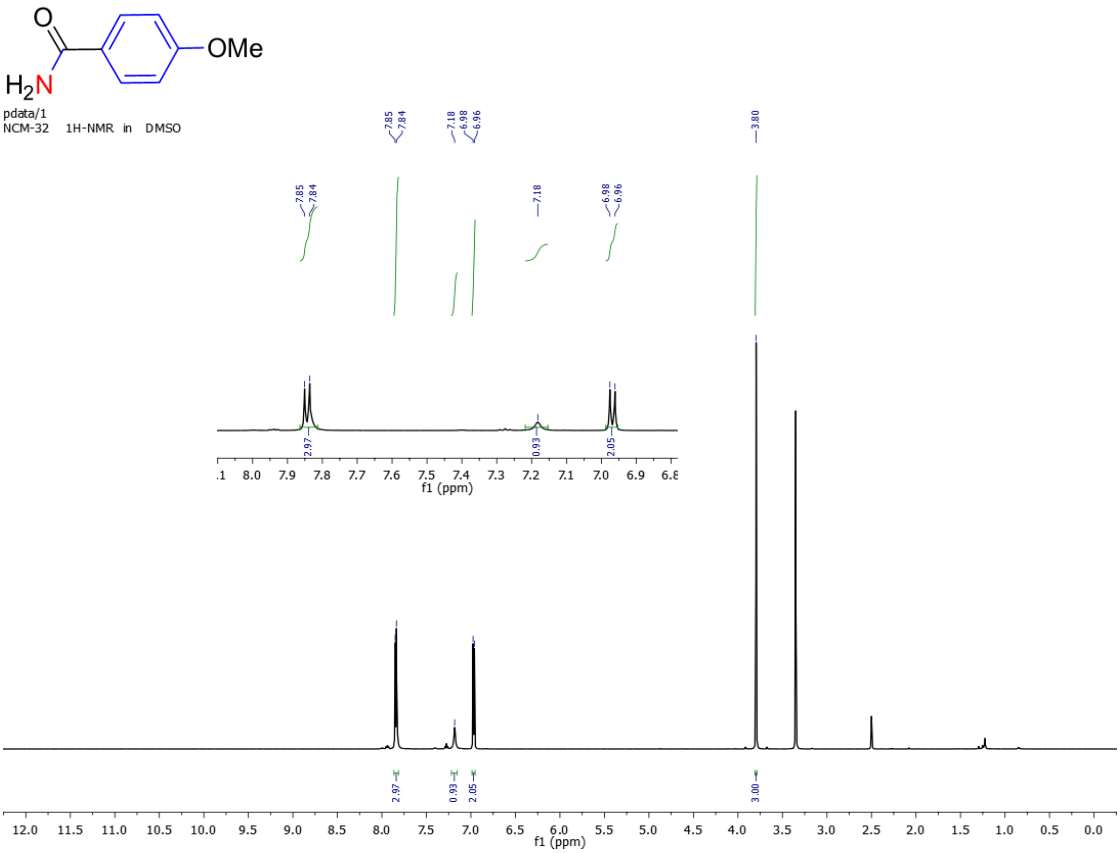

^{13}CNMR in DMSO (d_6) 151 MHz (2g)

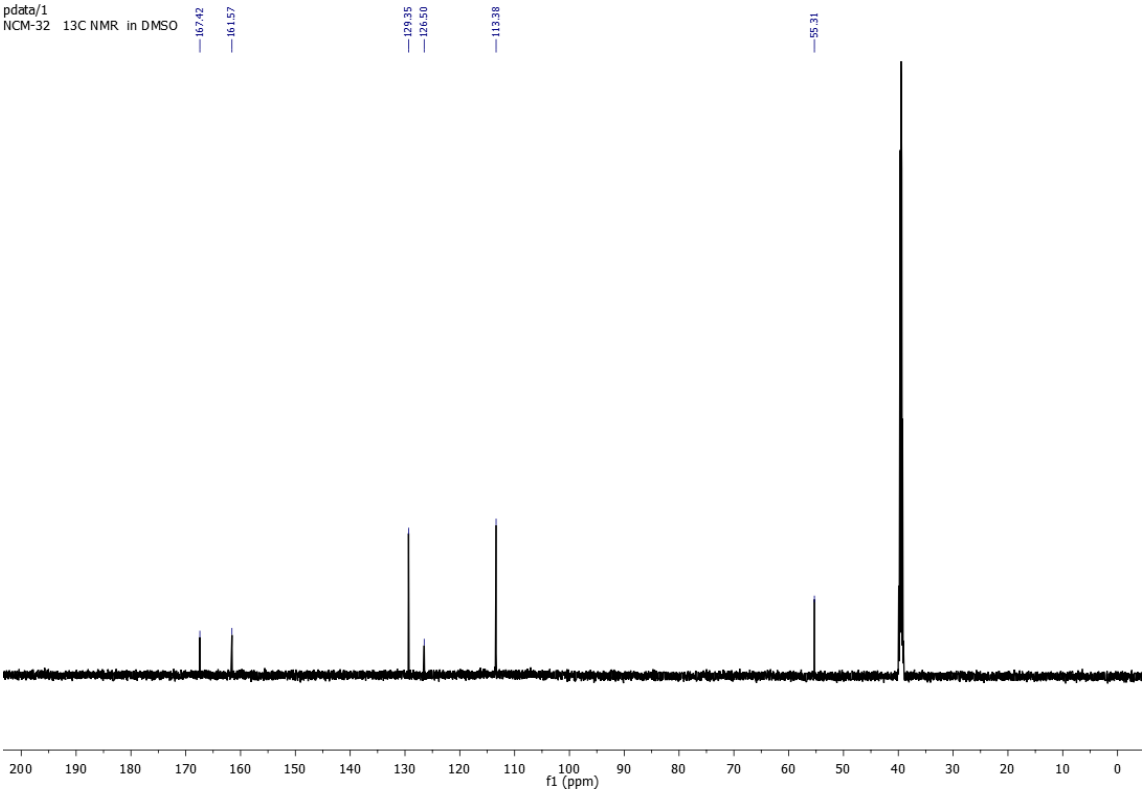

^{1}H NMR in DMSO (d_6) 400 MHz (2h)

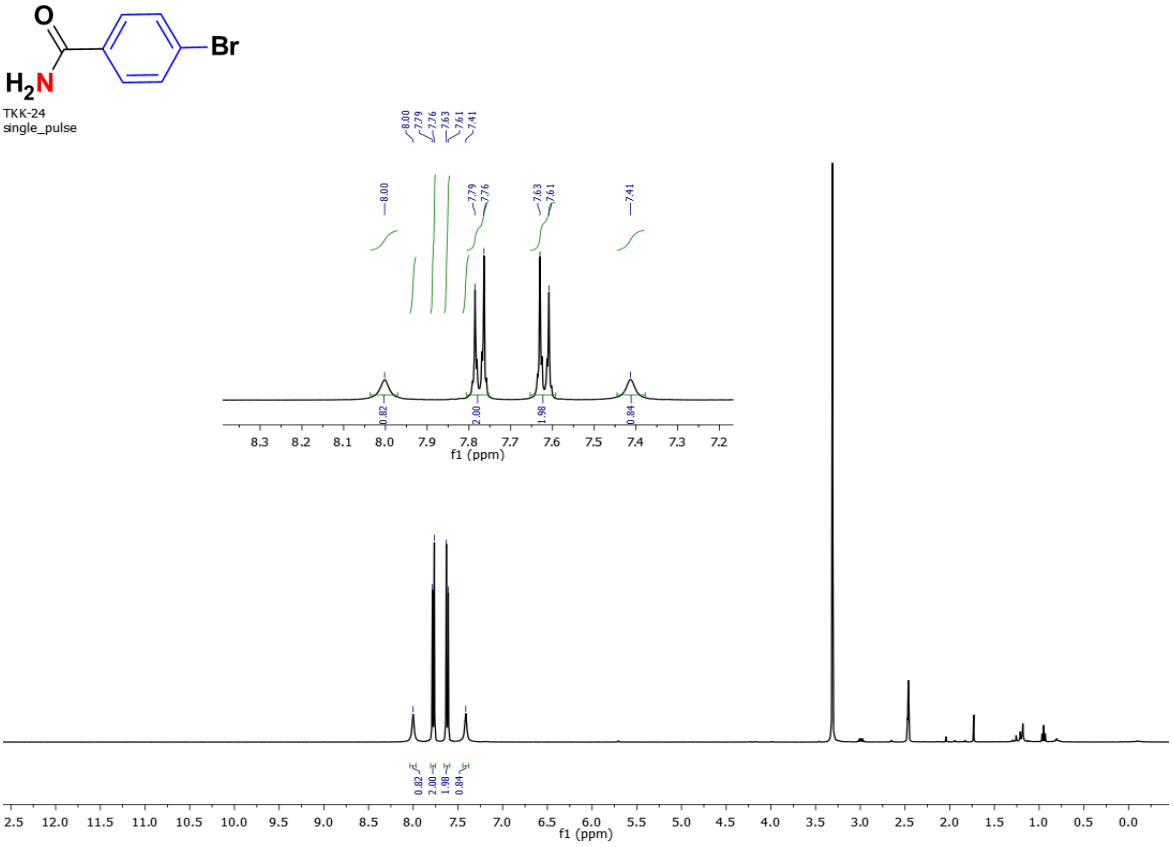

^{13}C NMR in DMSO (d_6) 101 MHz (2h)

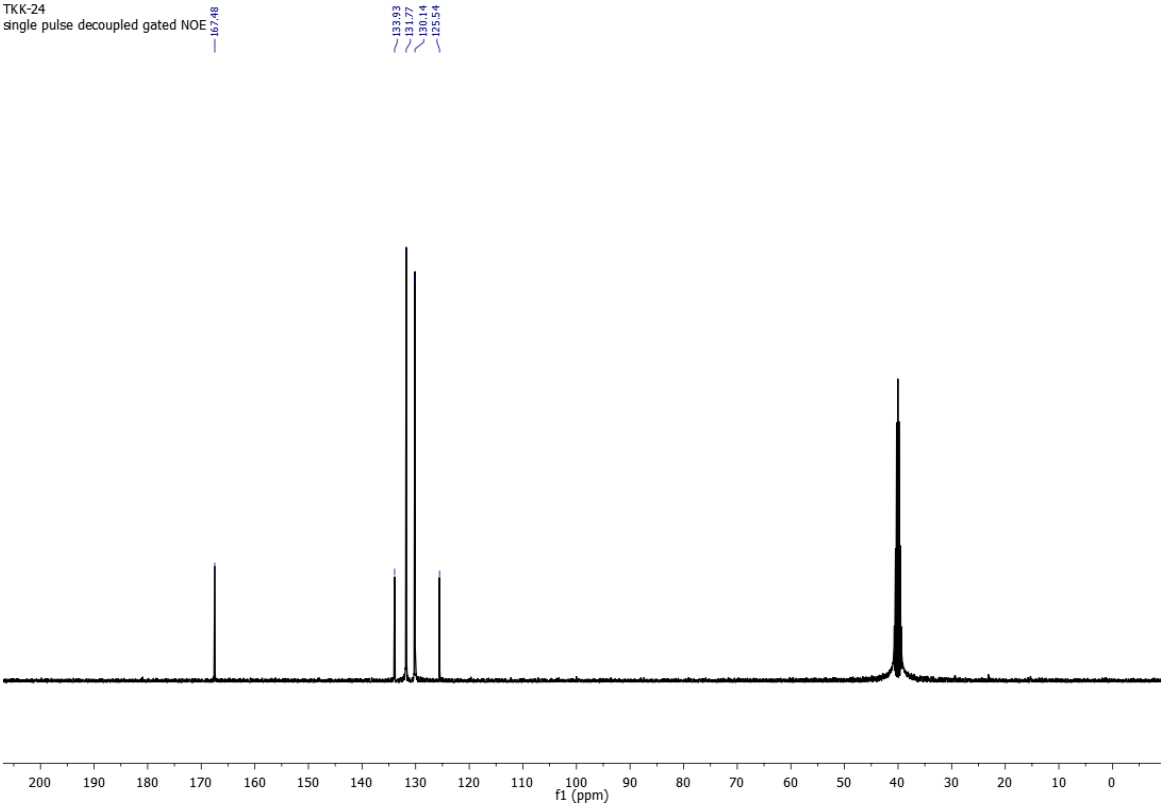

^{1}H NMR in DMSO (d_6) 400 MHz (2i)

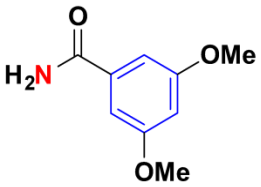

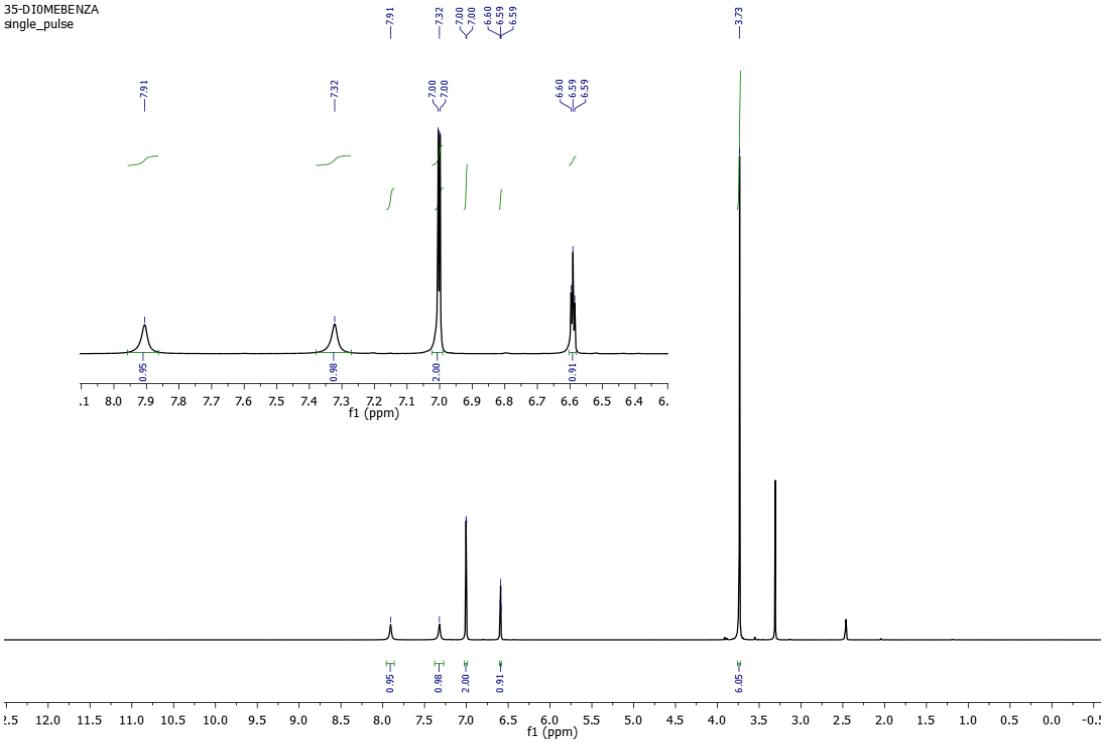

^{13}C NMR in DMSO (d_6) 101 MHz (2i)

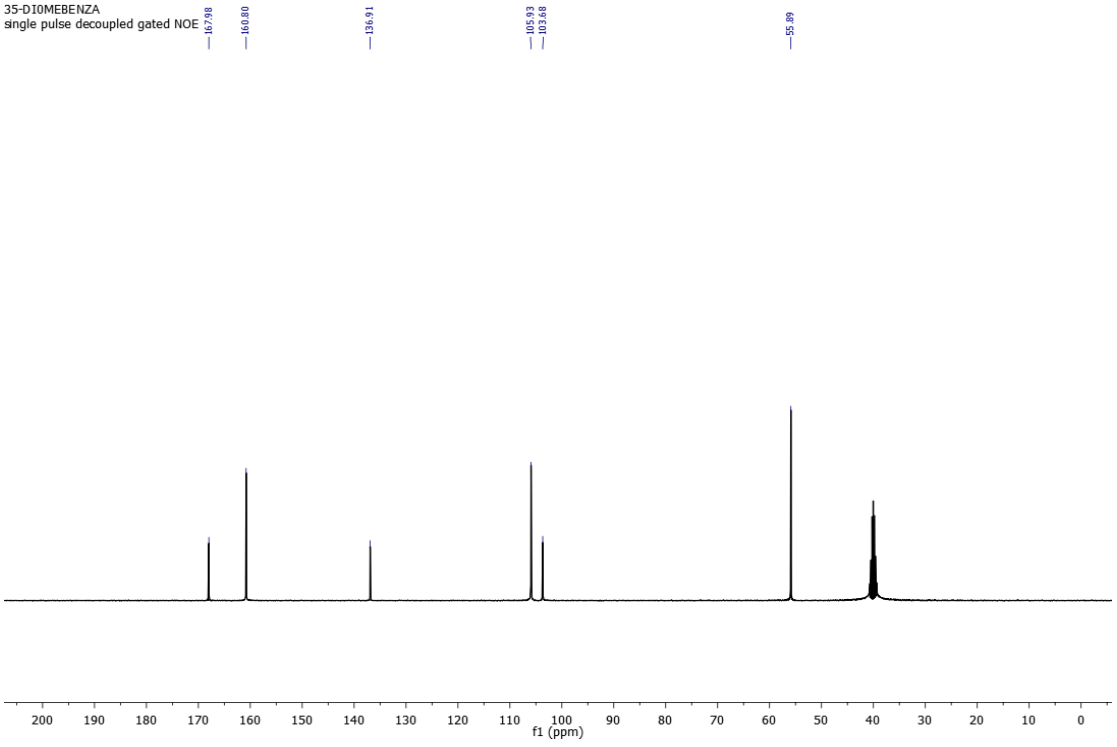

^{1}H NMR in DMSO (d_6) 400 MHz (2j)

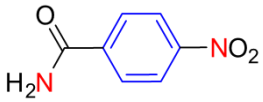

TKK-22
single_pulse

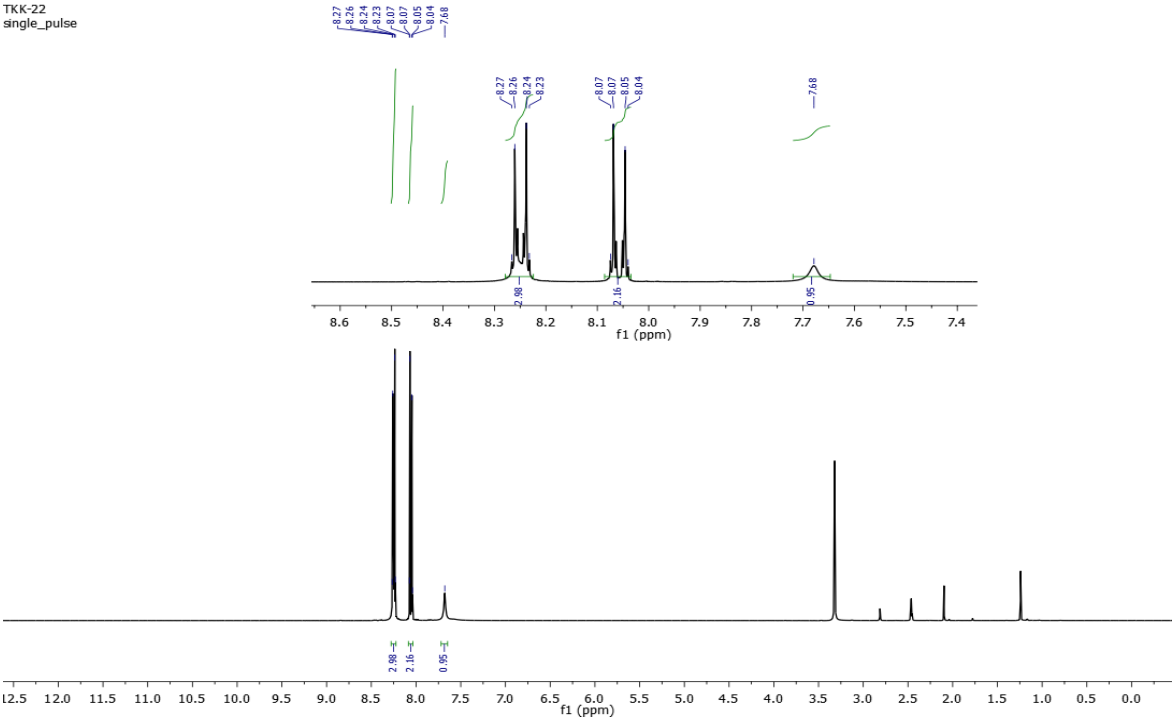

^{13}C NMR in DMSO (d_6) 101 MHz (2j)

TKK-22
single pulse decoupled gated NOE

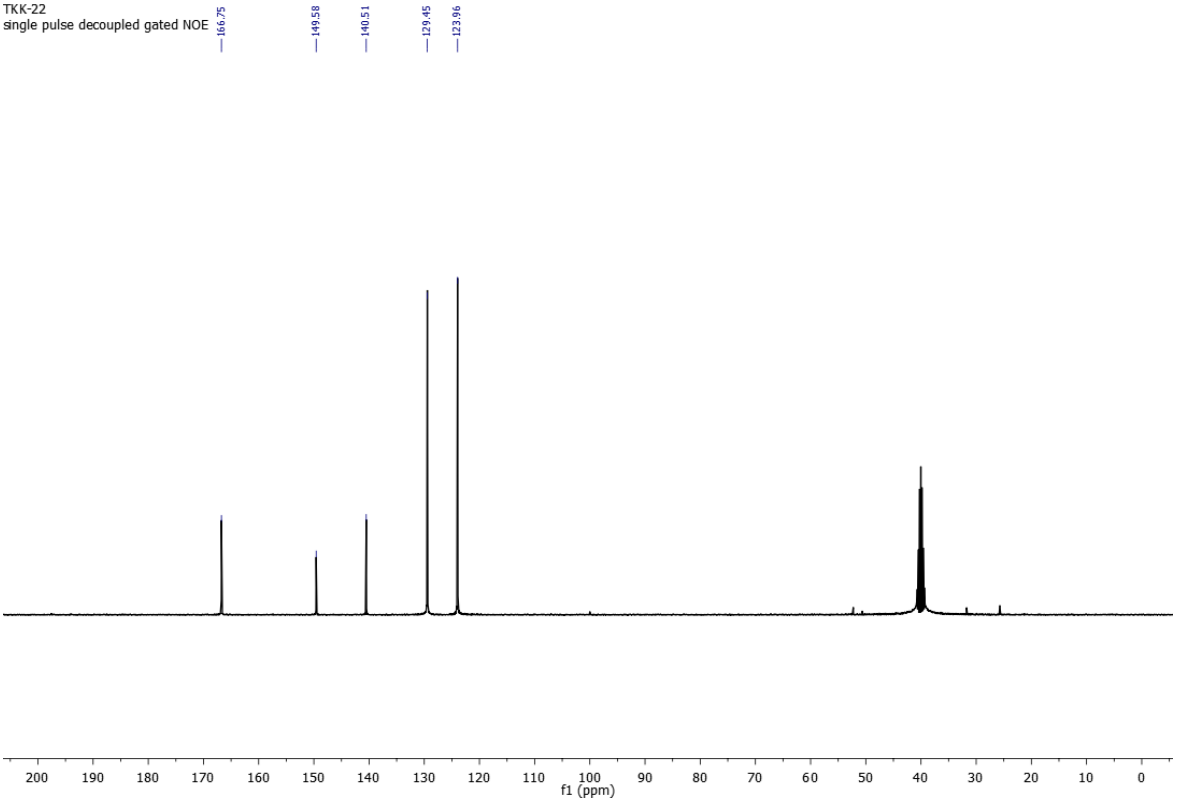

^{1}H NMR in DMSO (d_6) 600 MHz (2k)

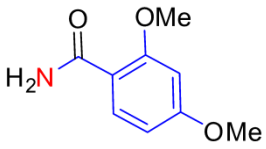

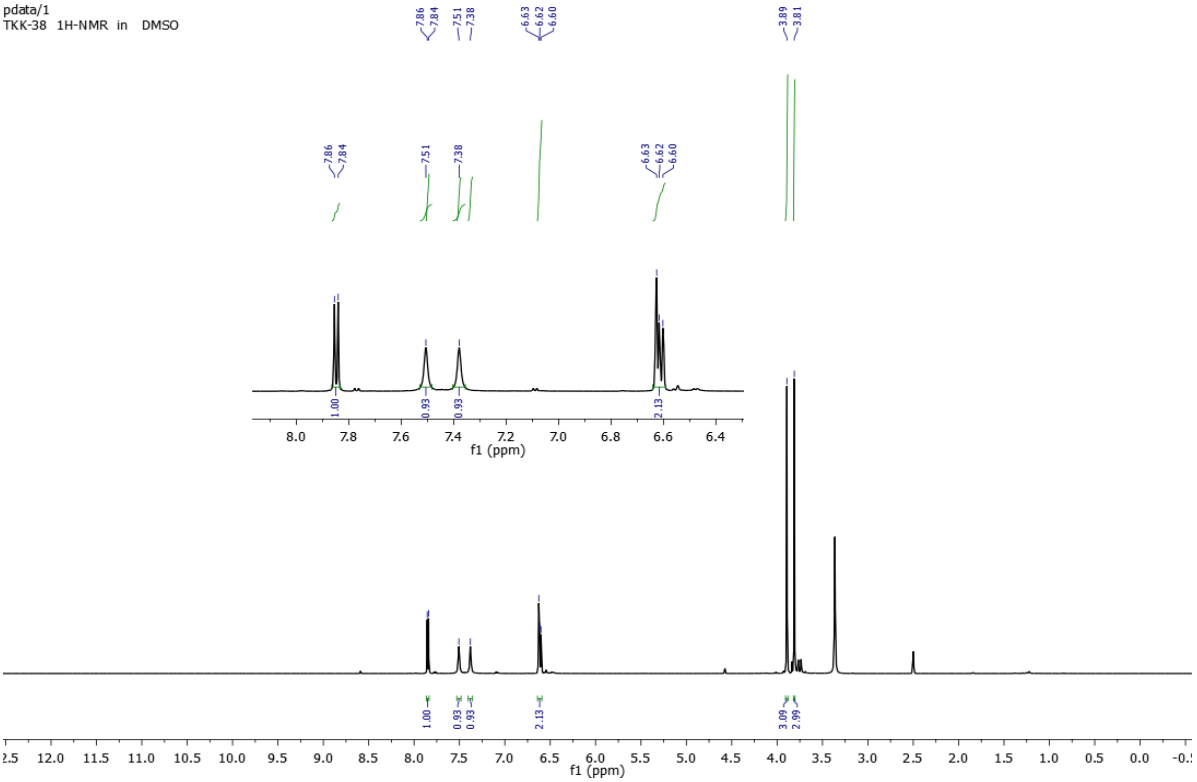

^{13}C NMR in DMSO (d_6) 151 MHz (2k)

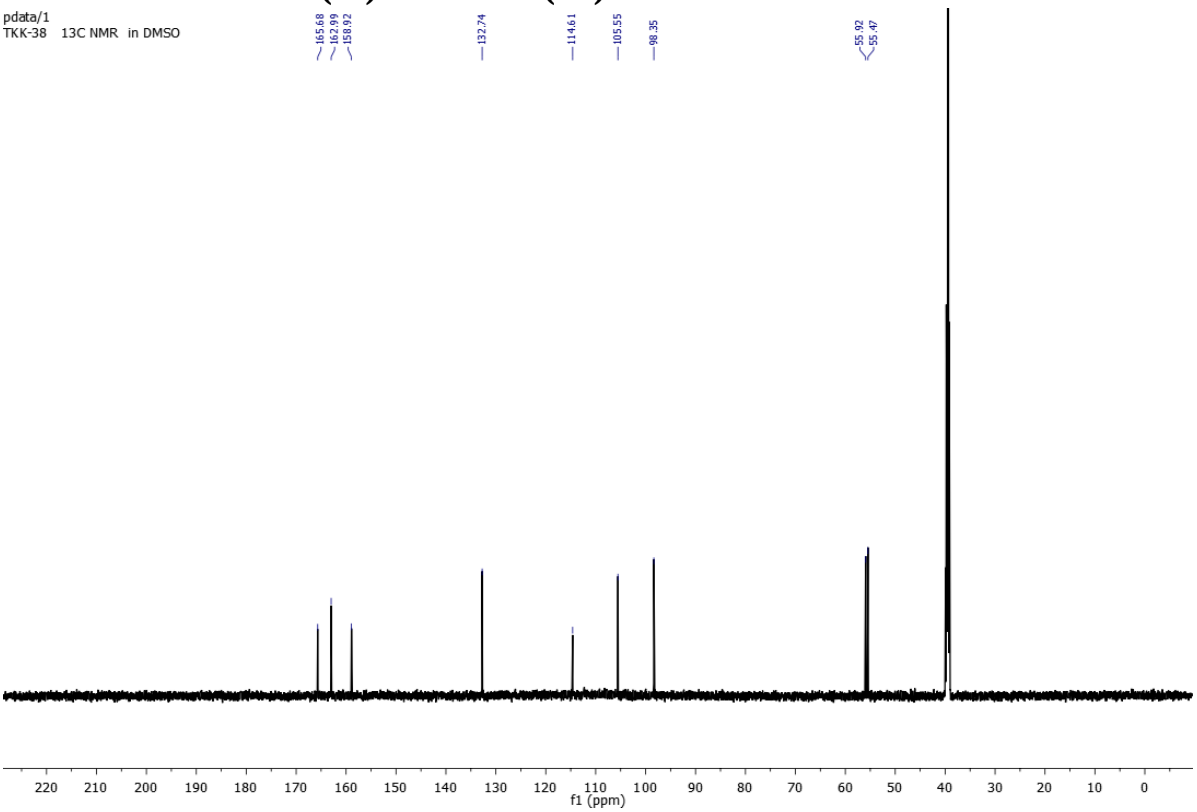

^{1}H NMR in DMSO (d_6) 400 MHz (2l)

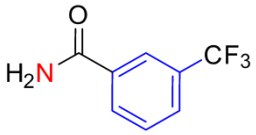

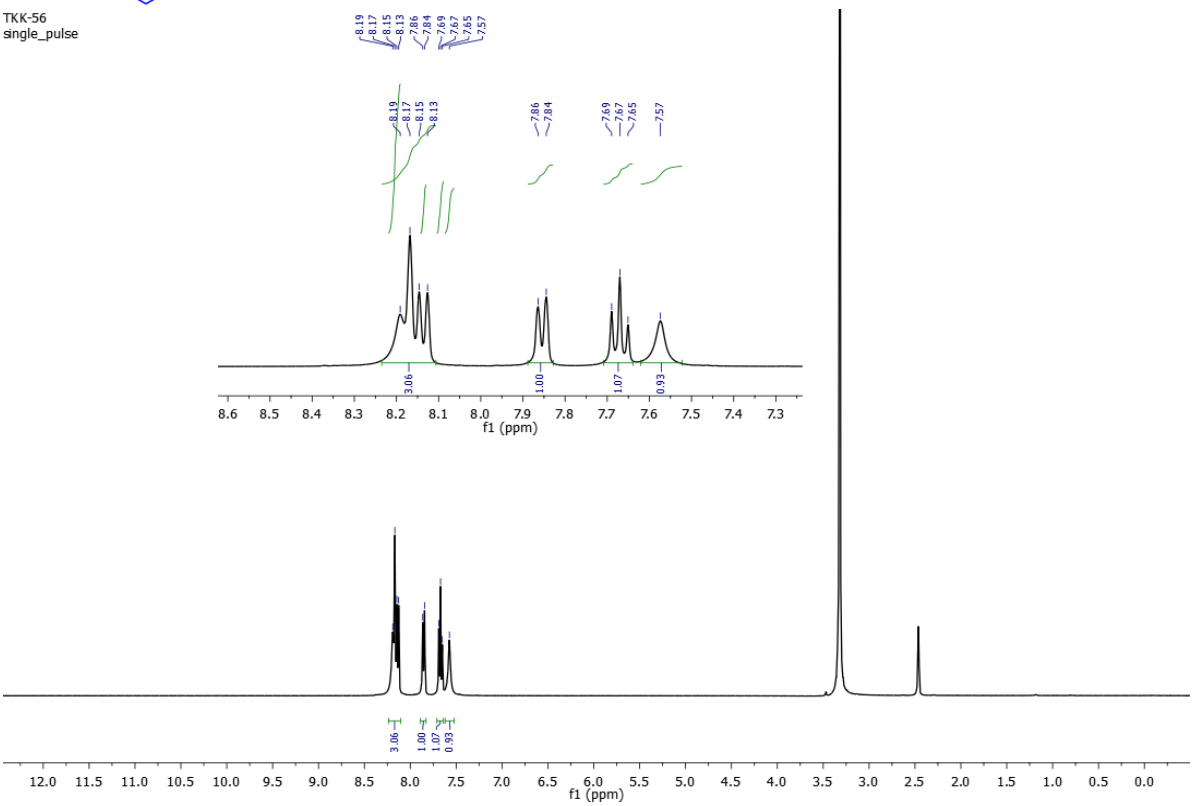

^{13}C NMR in DMSO (d_6) 101 MHz (2l)

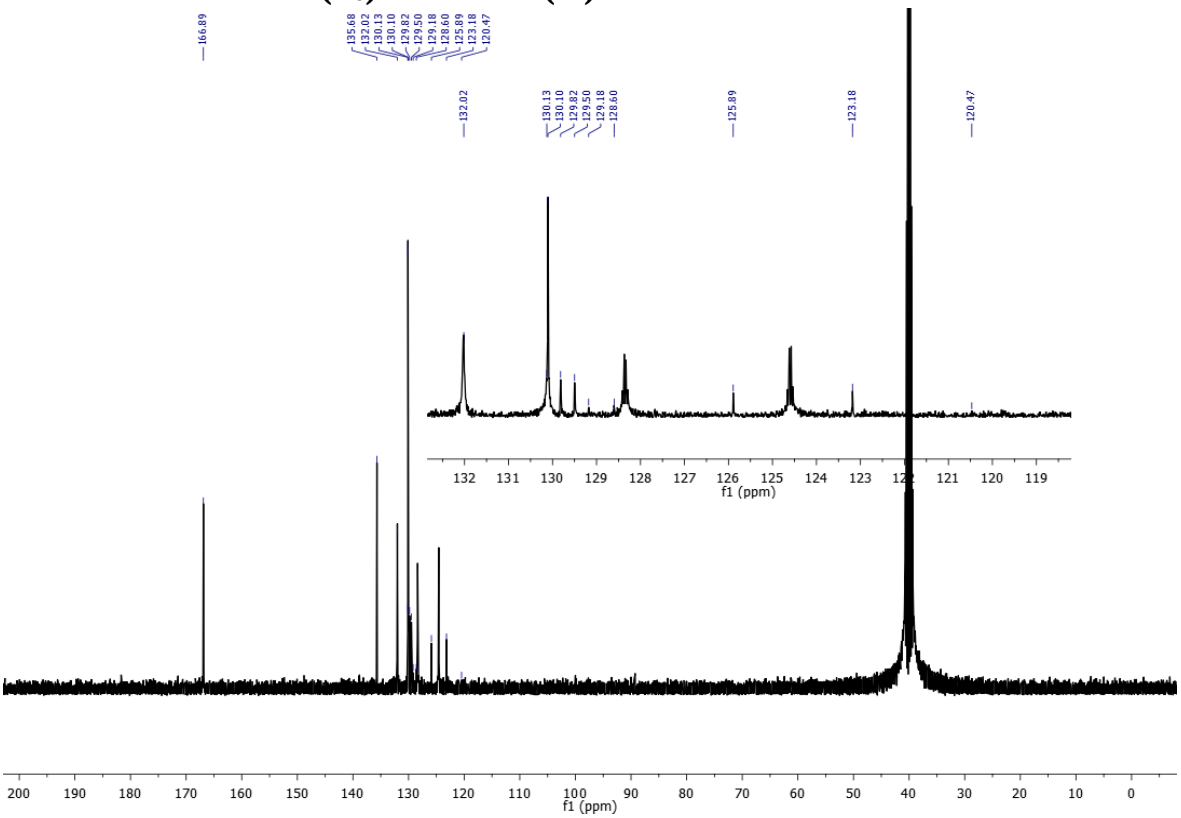

^{1}H NMR in DMSO (d_6) 400 MHz (2m)

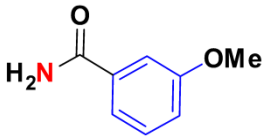

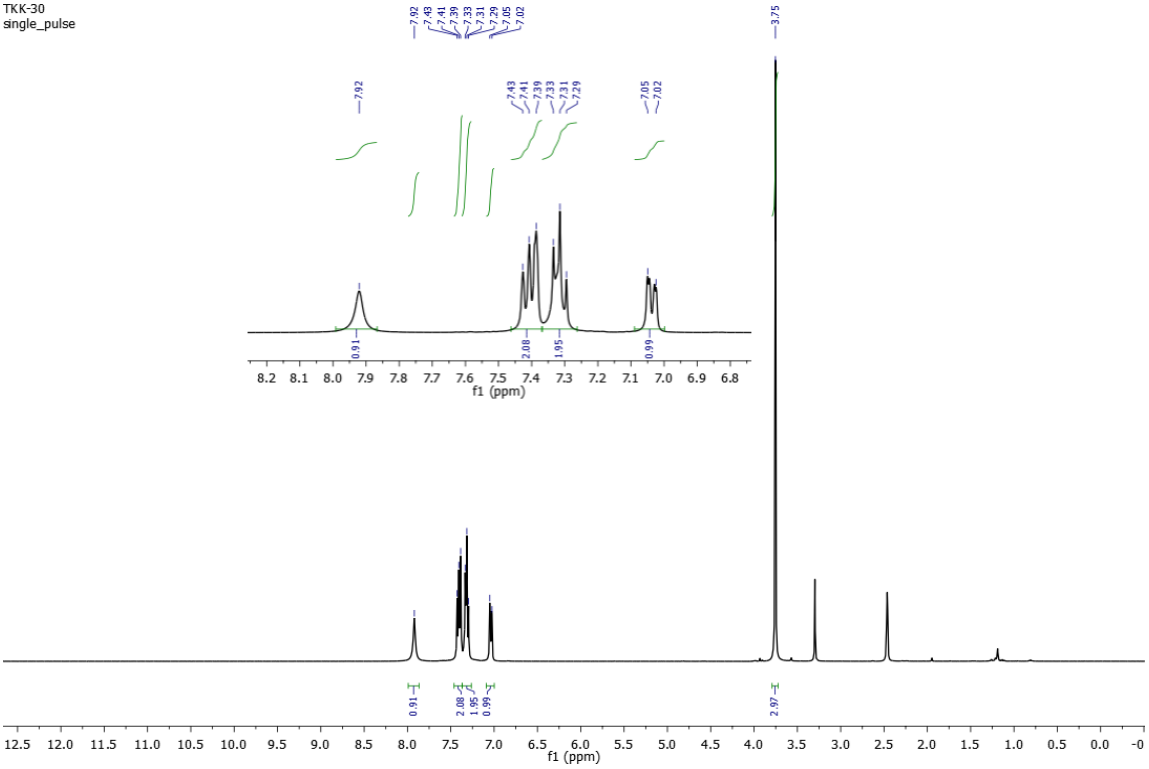

^{13}C NMR in DMSO (d_6) 101 MHz (2m)

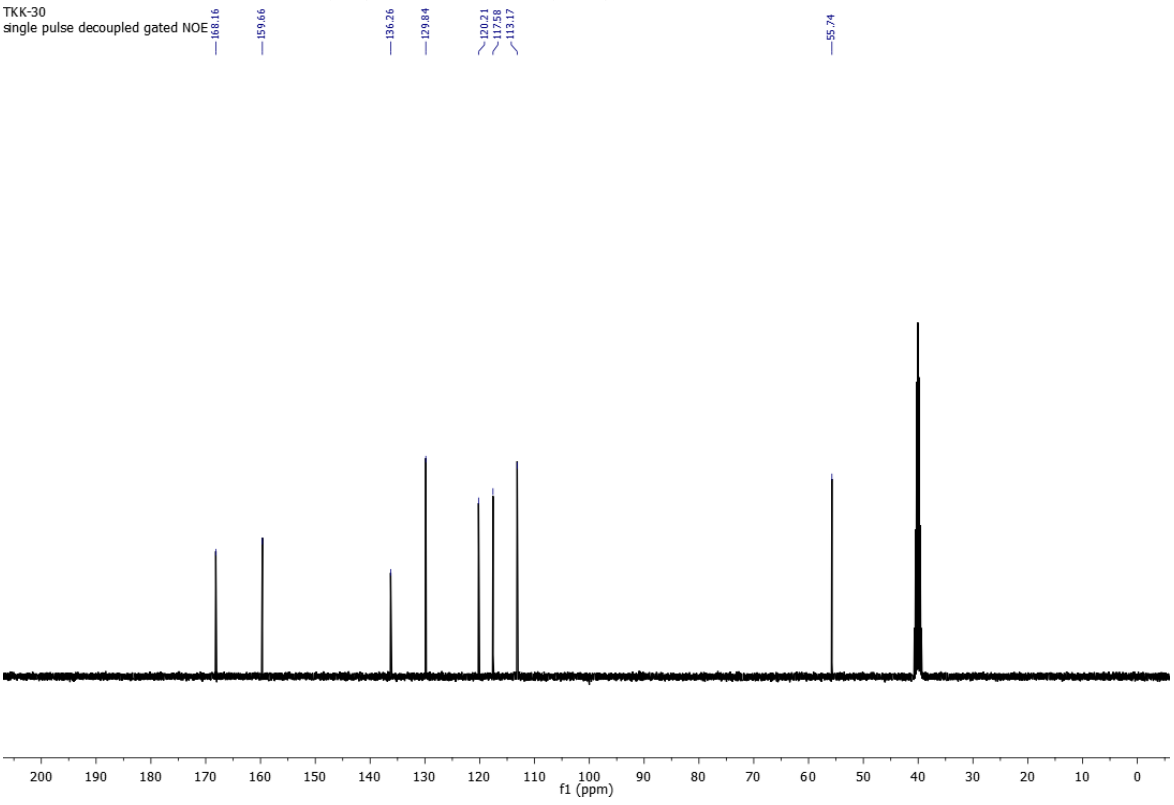

^{1}H NMR in DMSO (d_6) 400 MHz (2n)

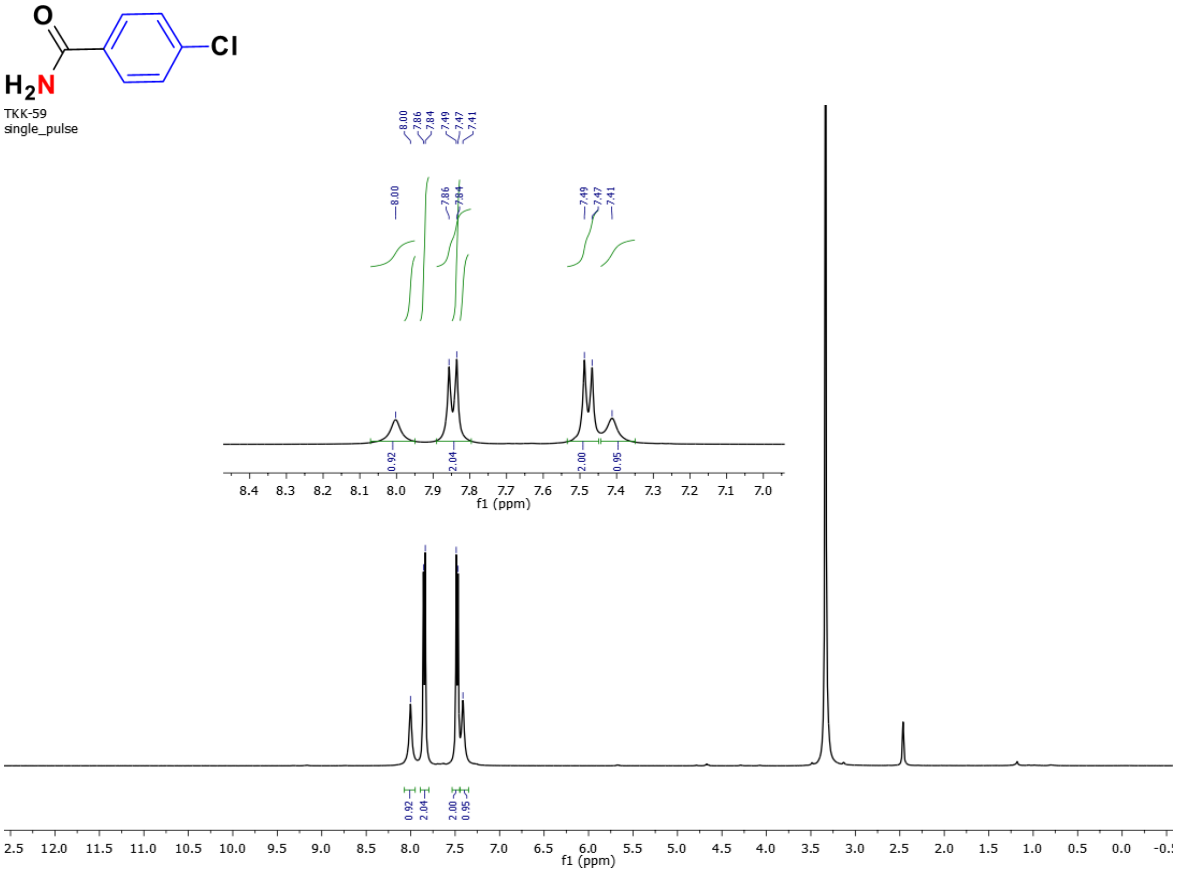

^{13}C NMR in DMSO (d_6) 101 MHz (2n)

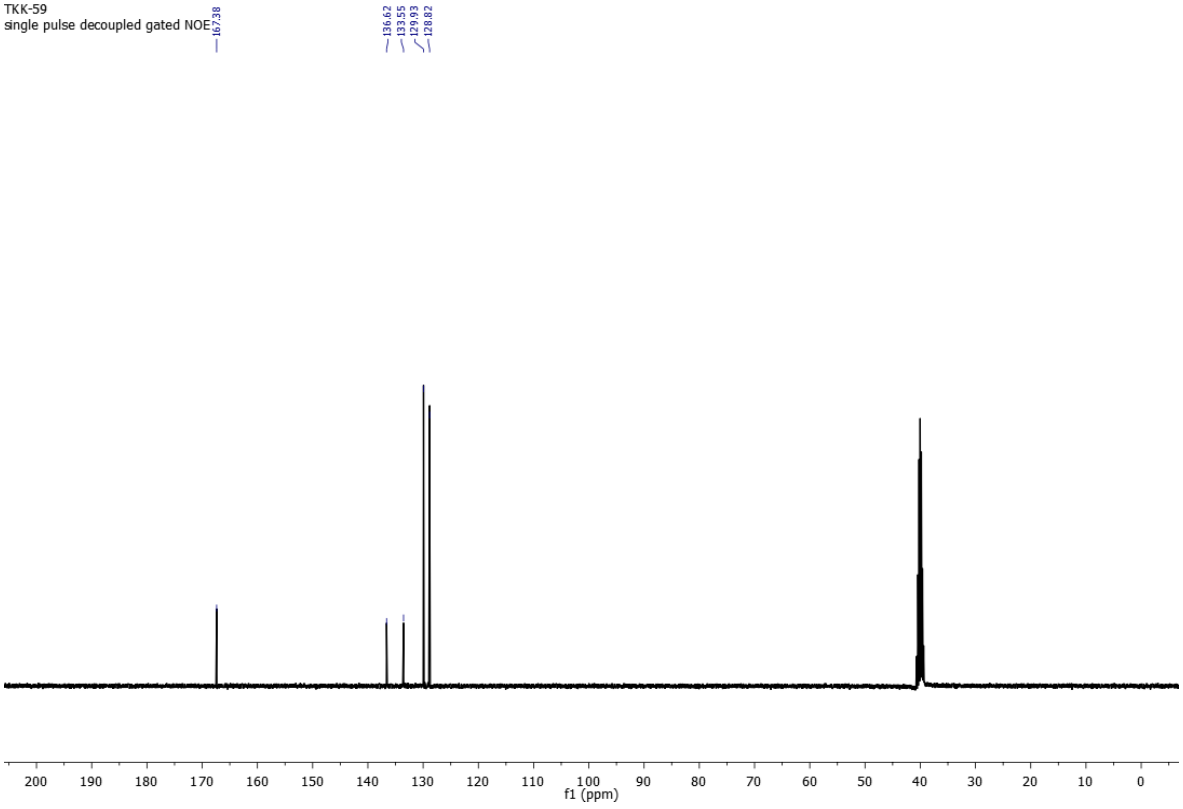

^{1}H NMR in DMSO (d_6) 600 MHz (2o)

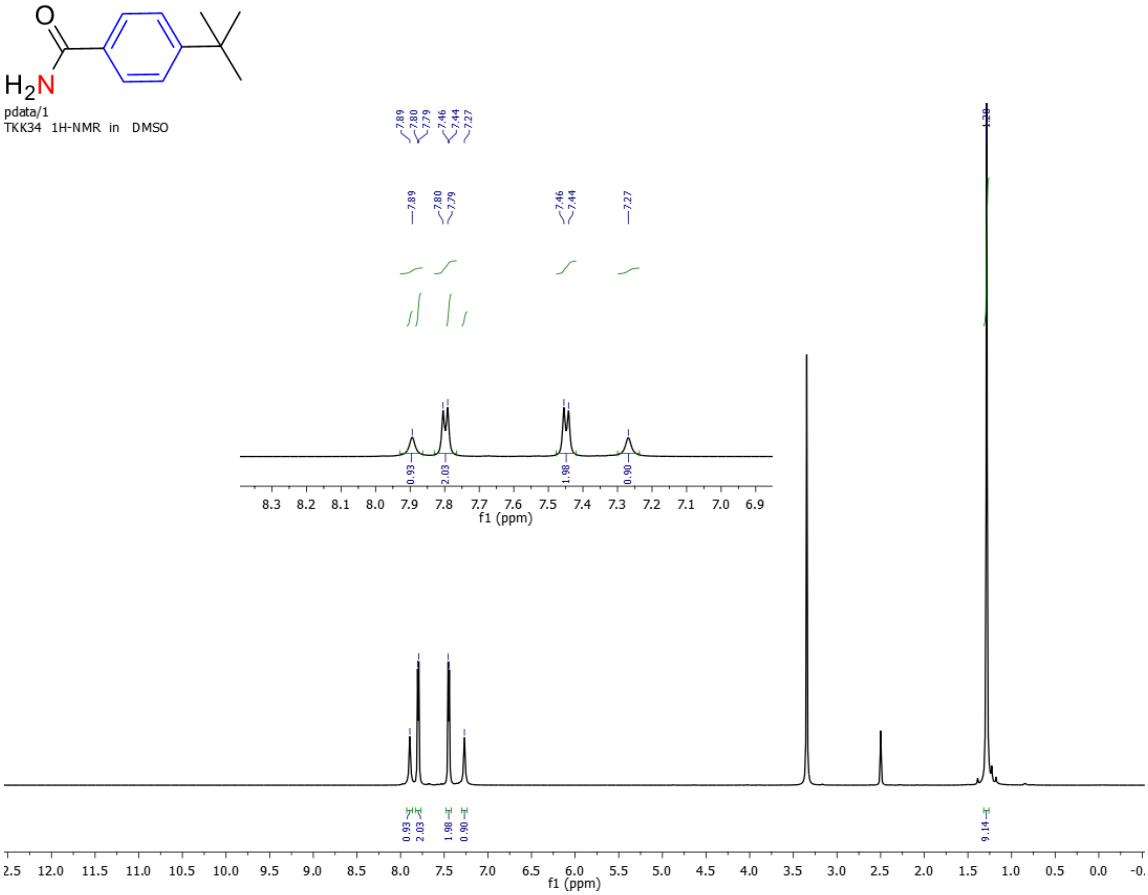

^{13}C NMR in DMSO (d_6) 151 MHz (2o)

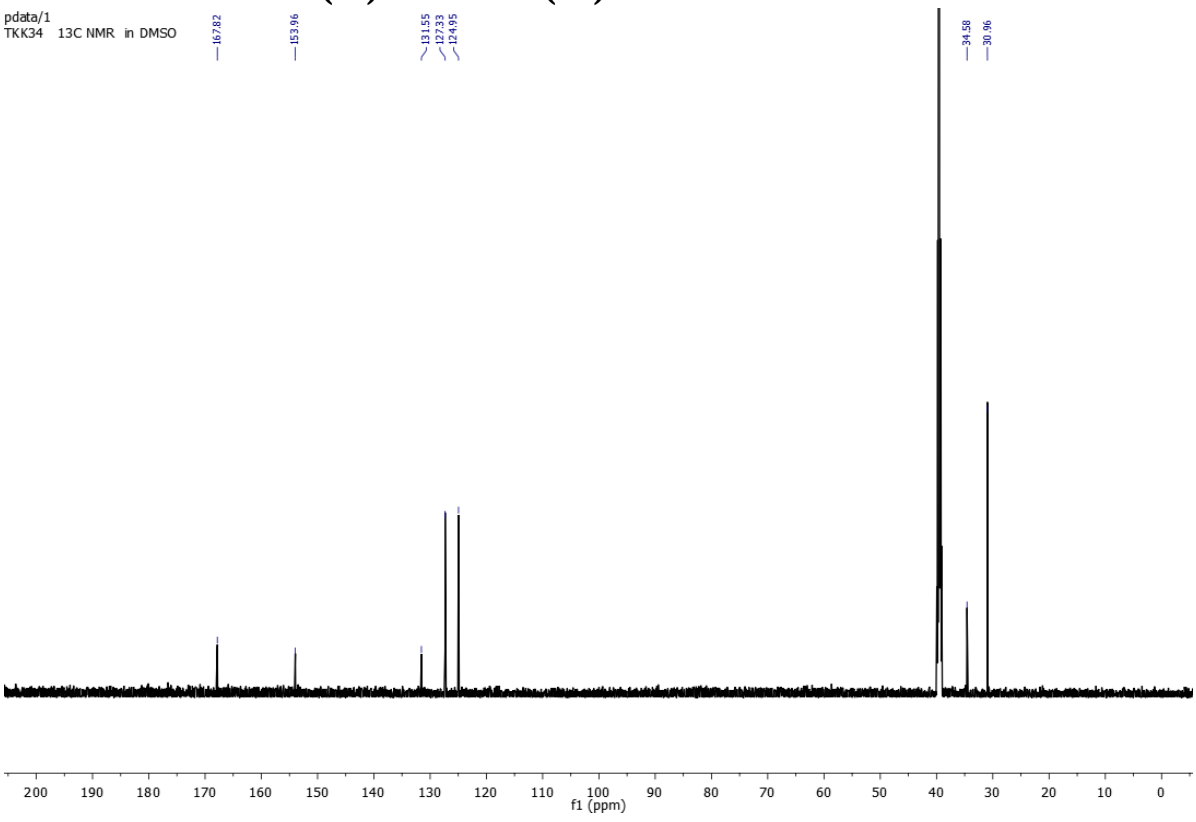

^{1}H NMR in DMSO (d_6) 400 MHz (2p)

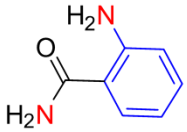

TKK-12
single_pulse

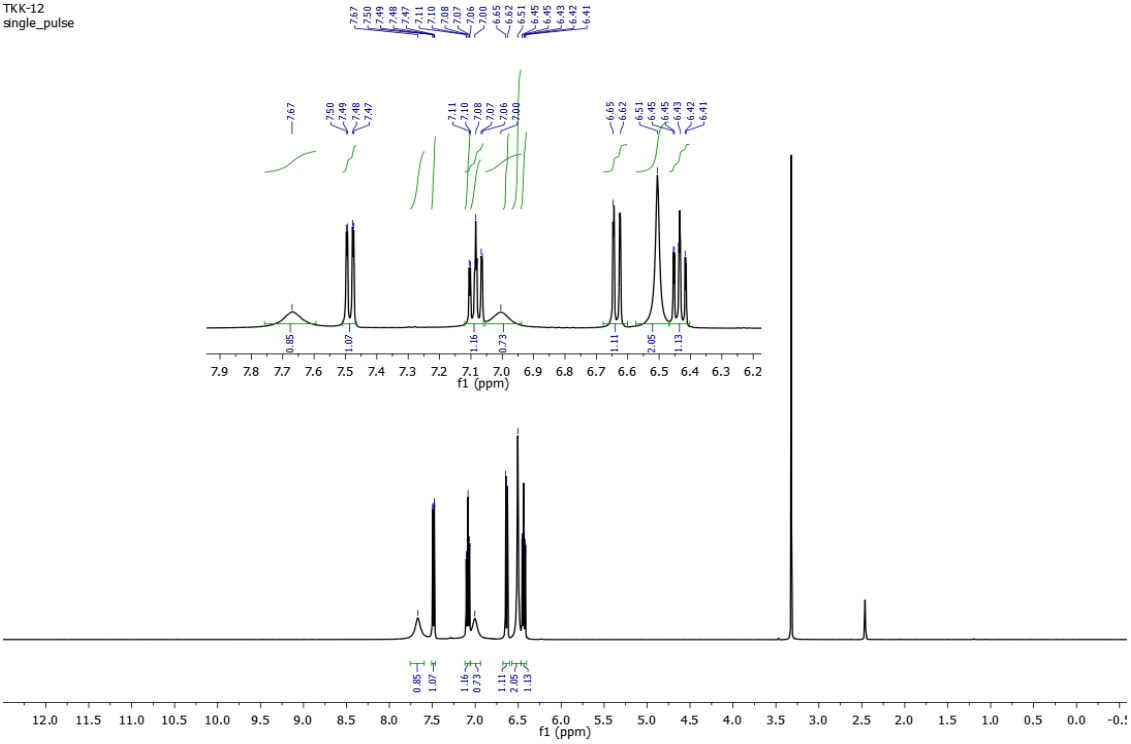

^{13}C NMR in DMSO (d_6) 101 MHz (2p)

TKK-12
single pulse decoupled gated NOE

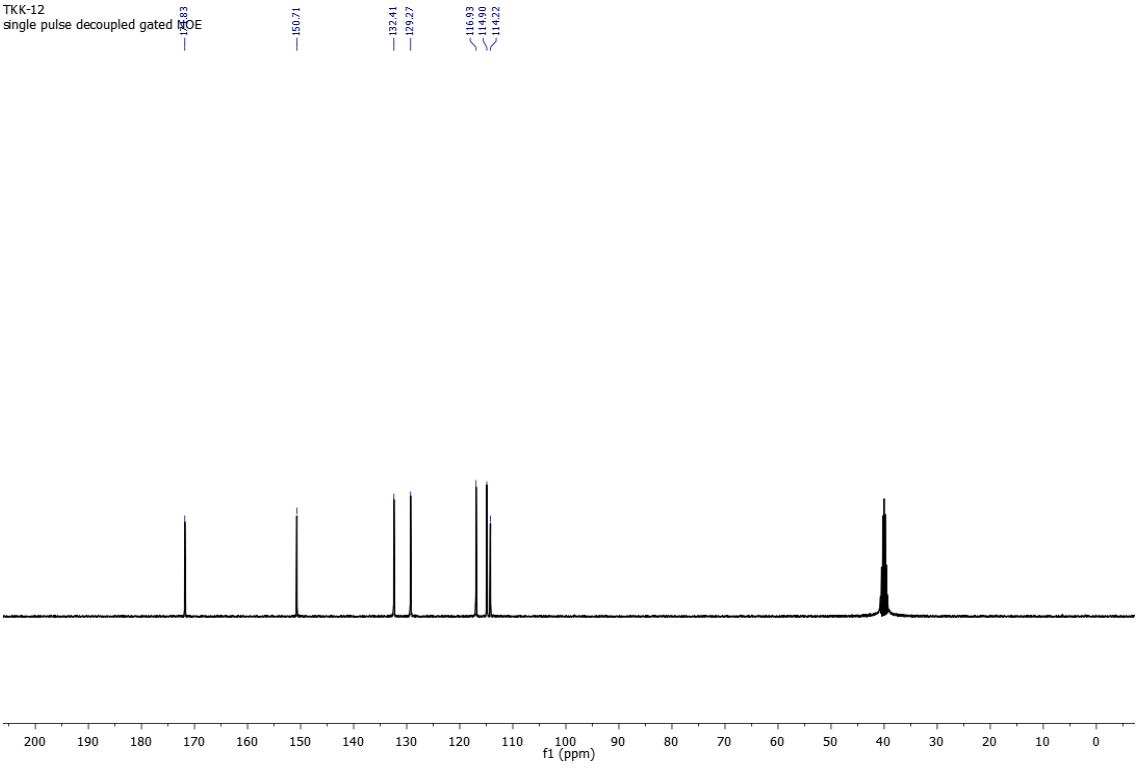

^{1}H NMR in DMSO (d_6) 400 MHz (2q)

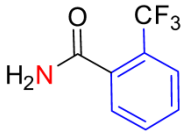

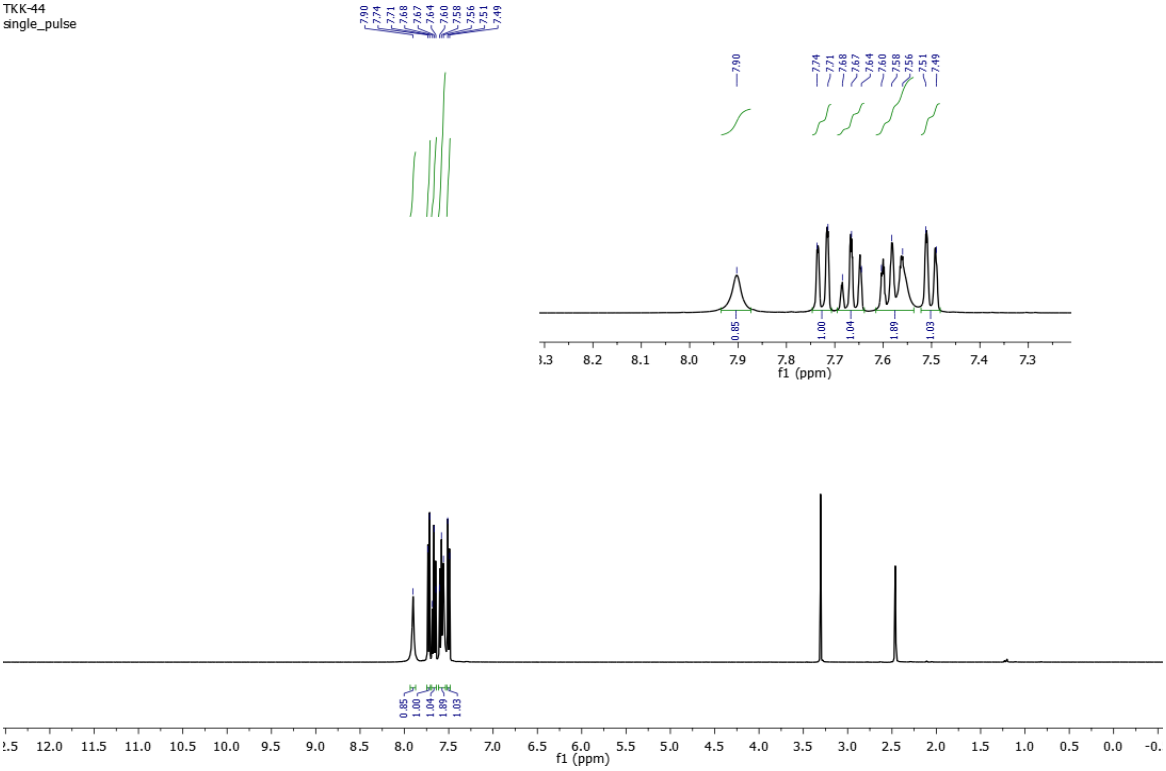

^{13}C NMR in DMSO (d_6) 101 MHz (2q)

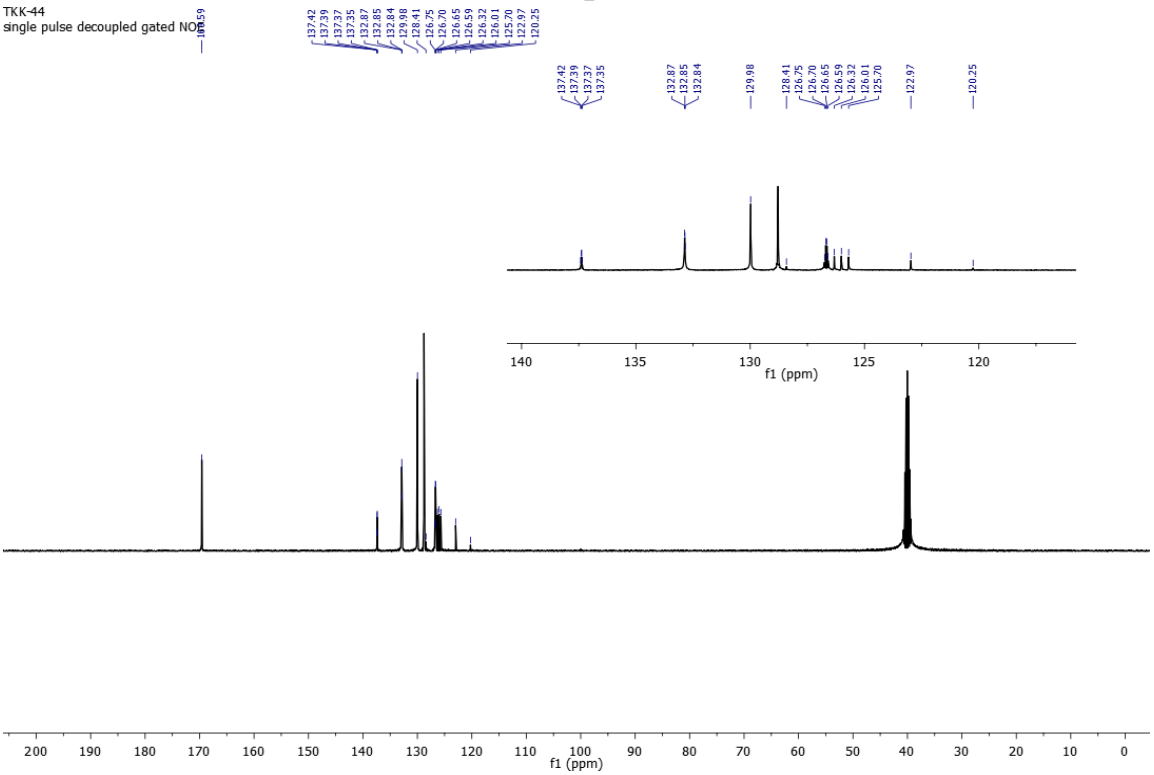

^{1}H NMR in DMSO (d_6) 600 MHz (2r)

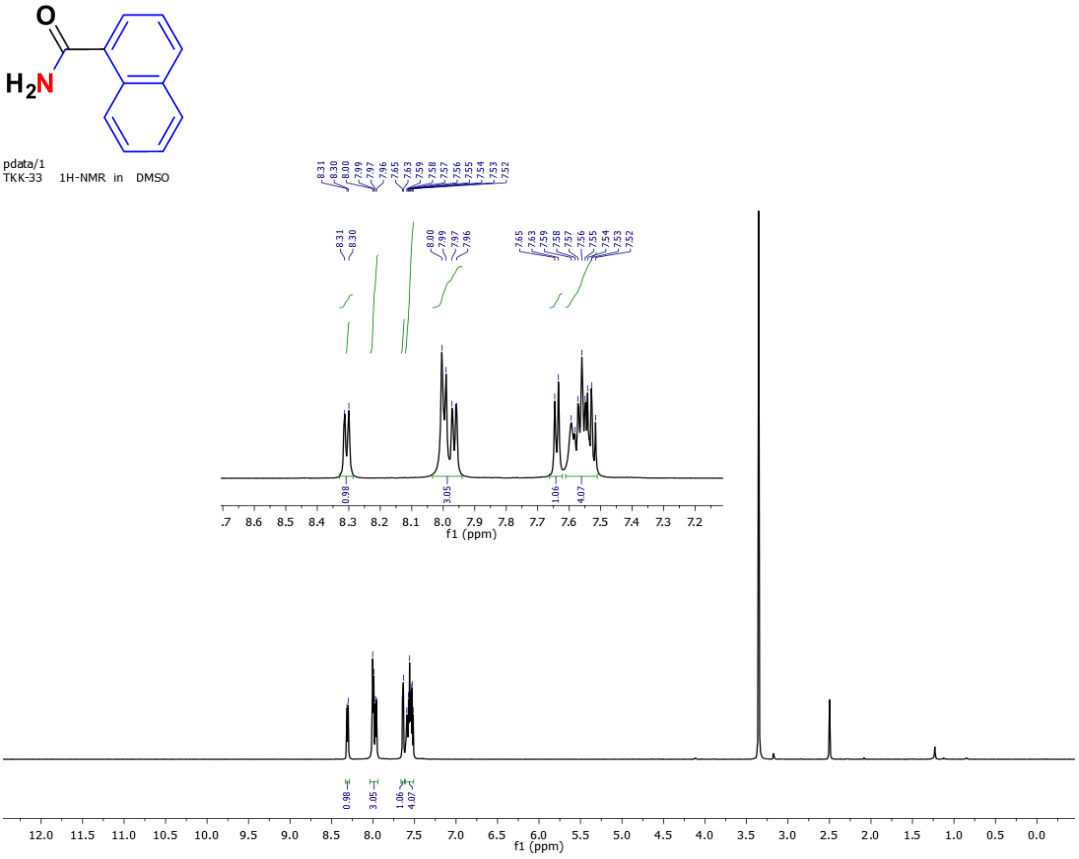

^{13}C NMR in DMSO (d_6) 151 MHz (2r)

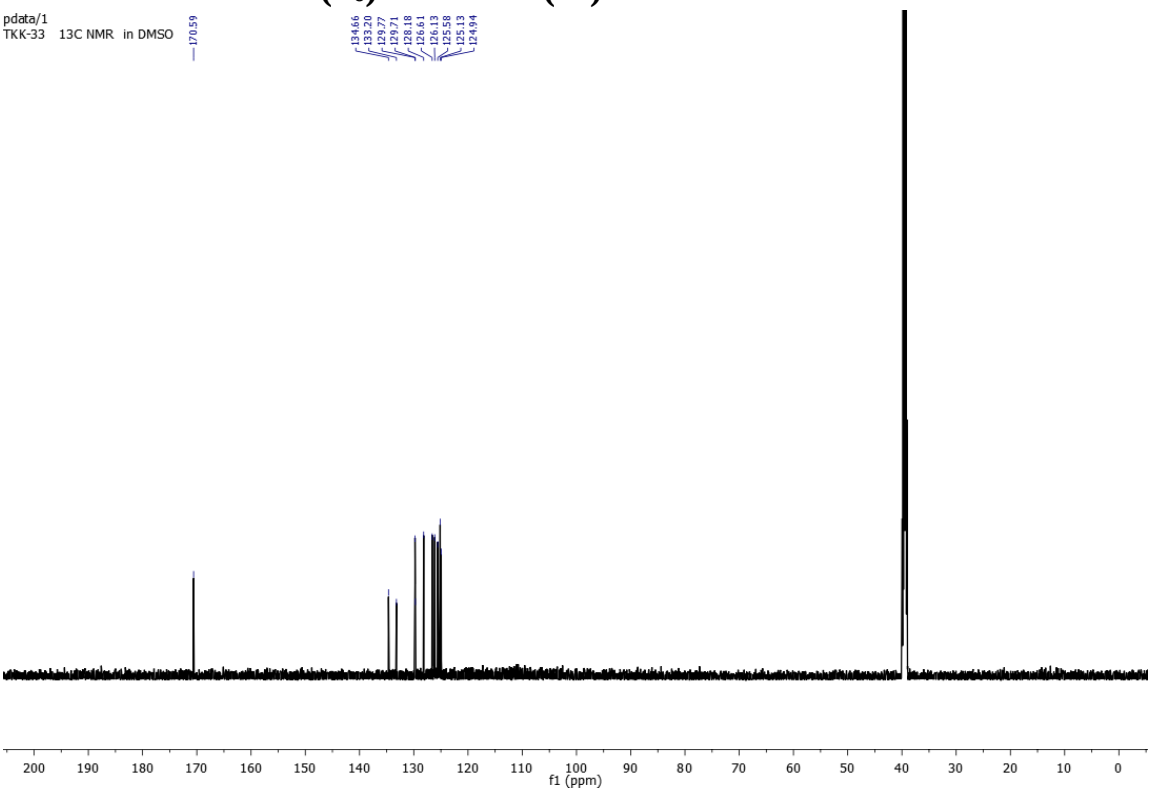

^{1}H NMR in DMSO (d_6) 600 MHz (2g) from 1s substrate

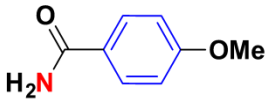

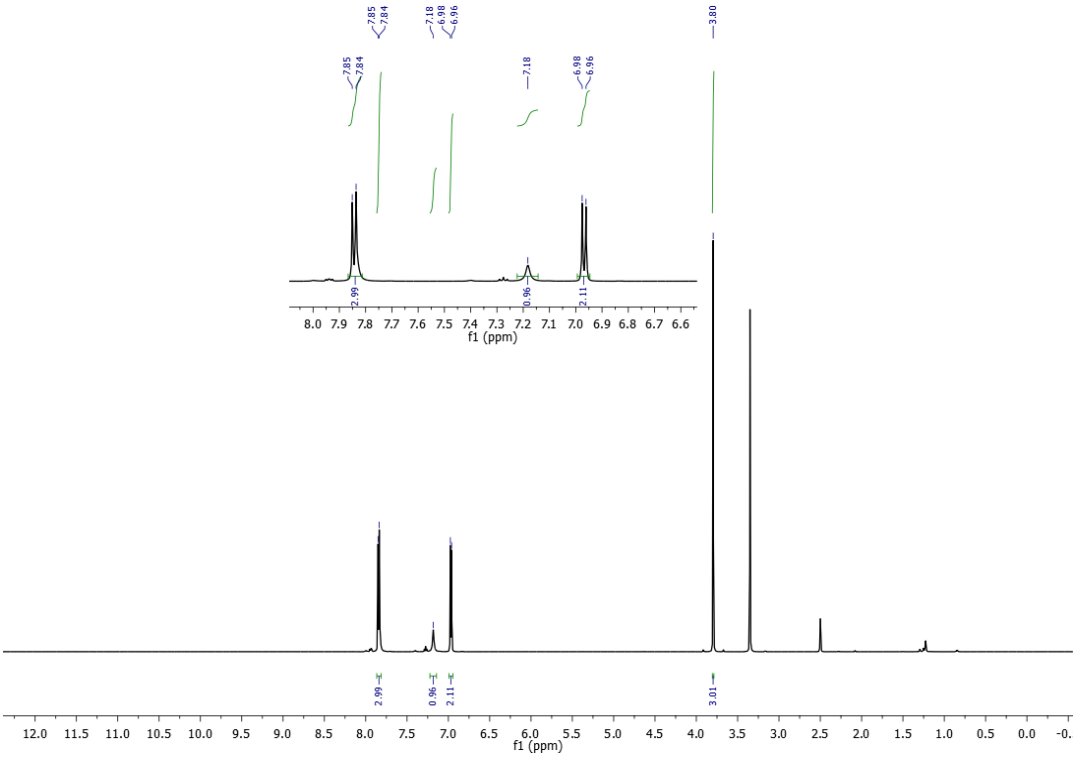

^{13}C NMR in DMSO (d_6) 151 MHz (2g)

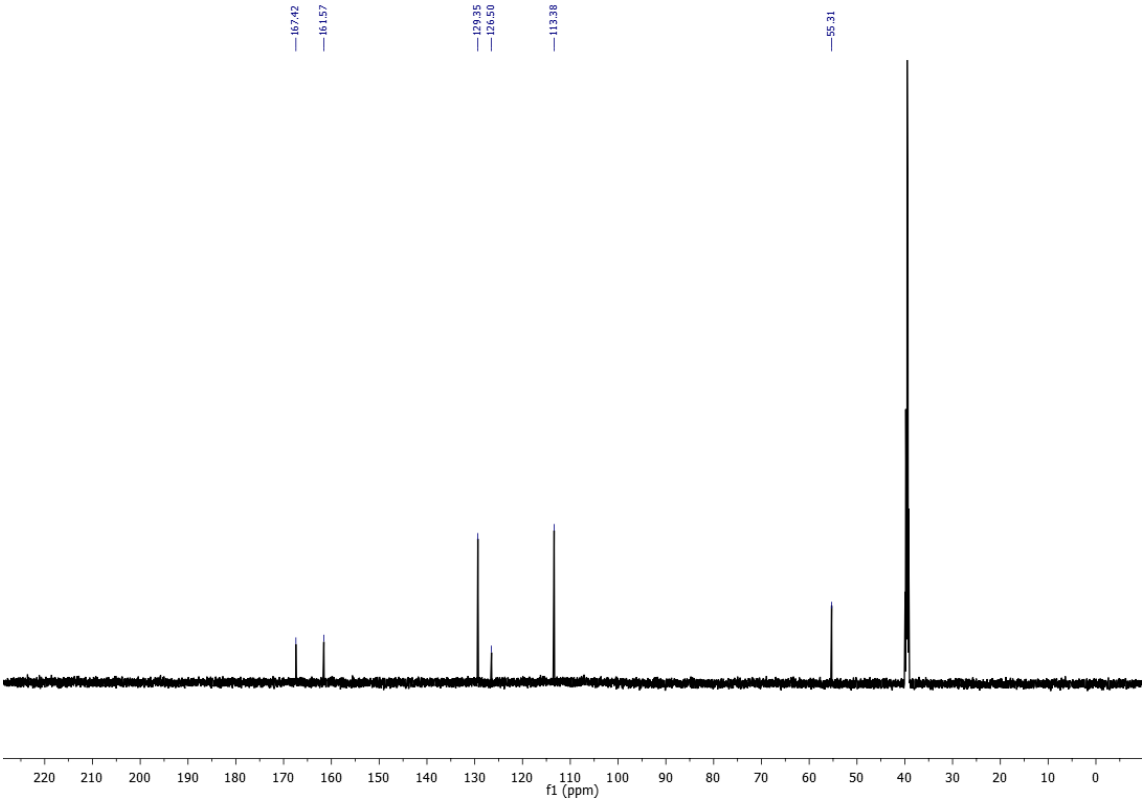

NMR spectral data of secondary benzylamine substrate

^{1}H NMR in $CDCl_3$ 400 MHz (1a)

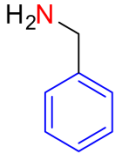

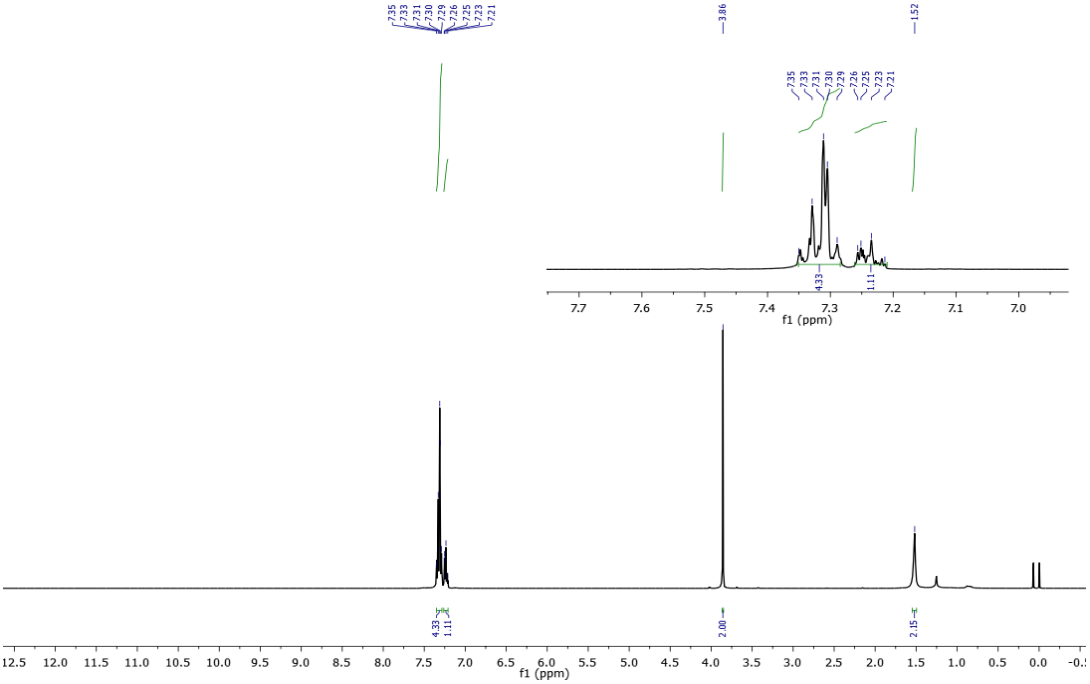

^{13}C NMR in $CDCl_3$ 101 MHz

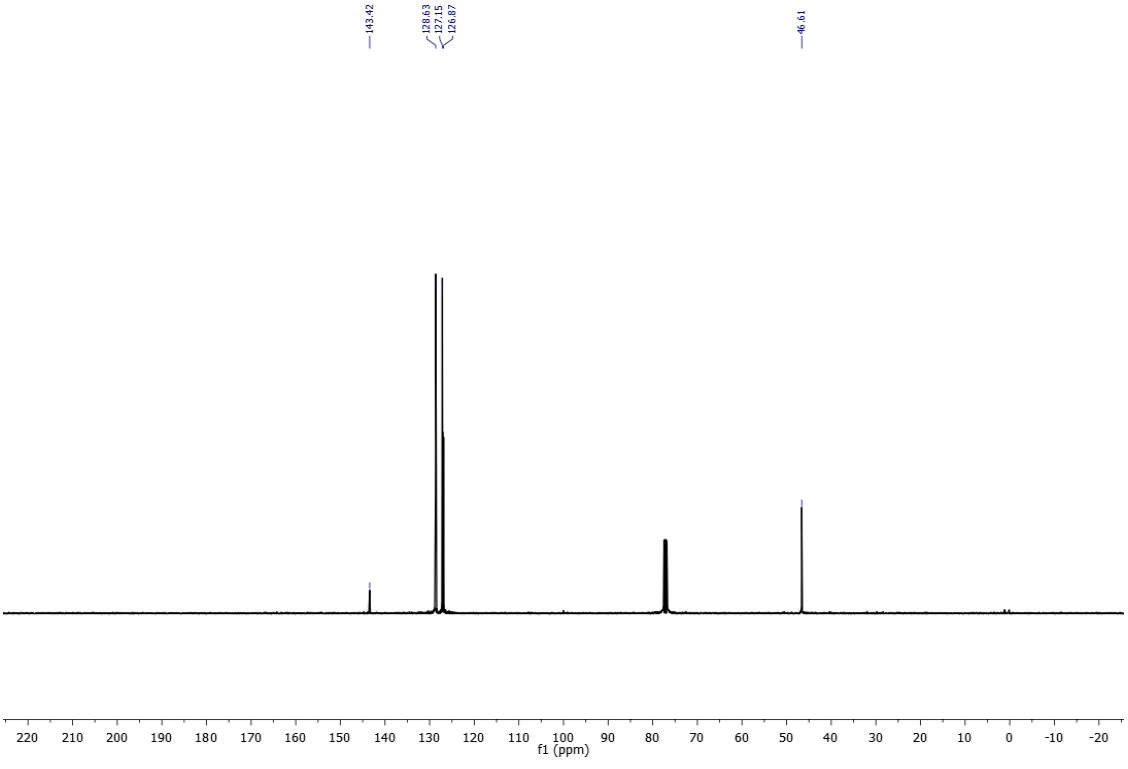

^{1}H NMR in DMSO (d_6) 600 MHz (2a)

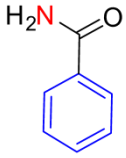

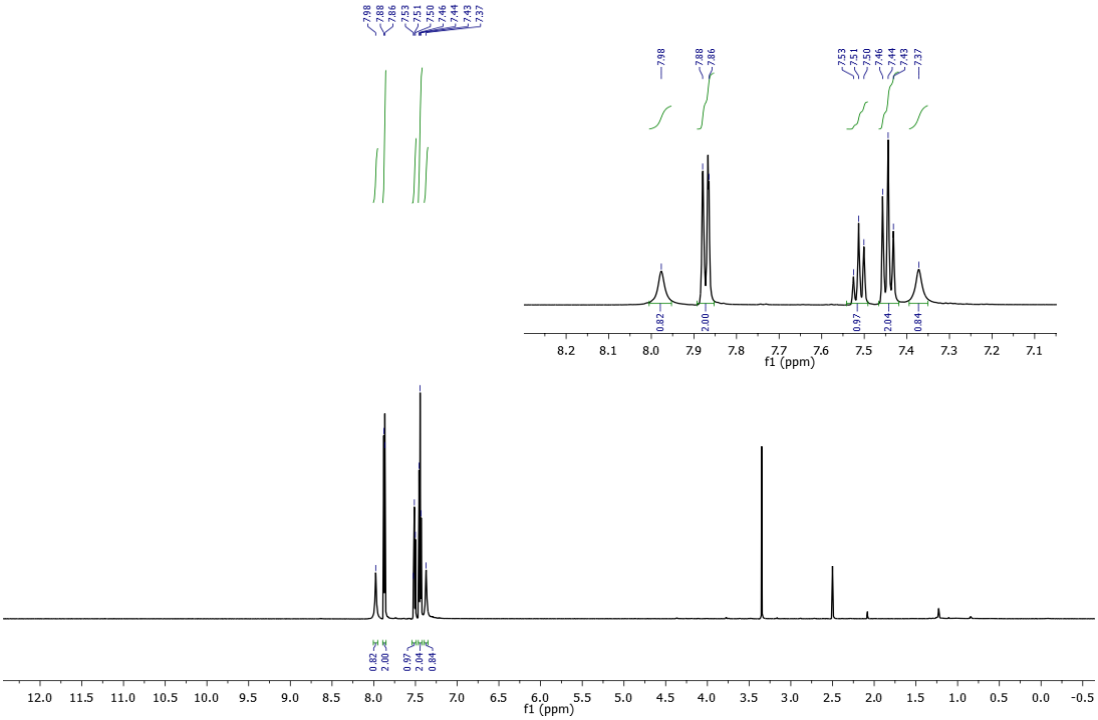

^{13}C NMR in DMSO (d_6) 151 MHz

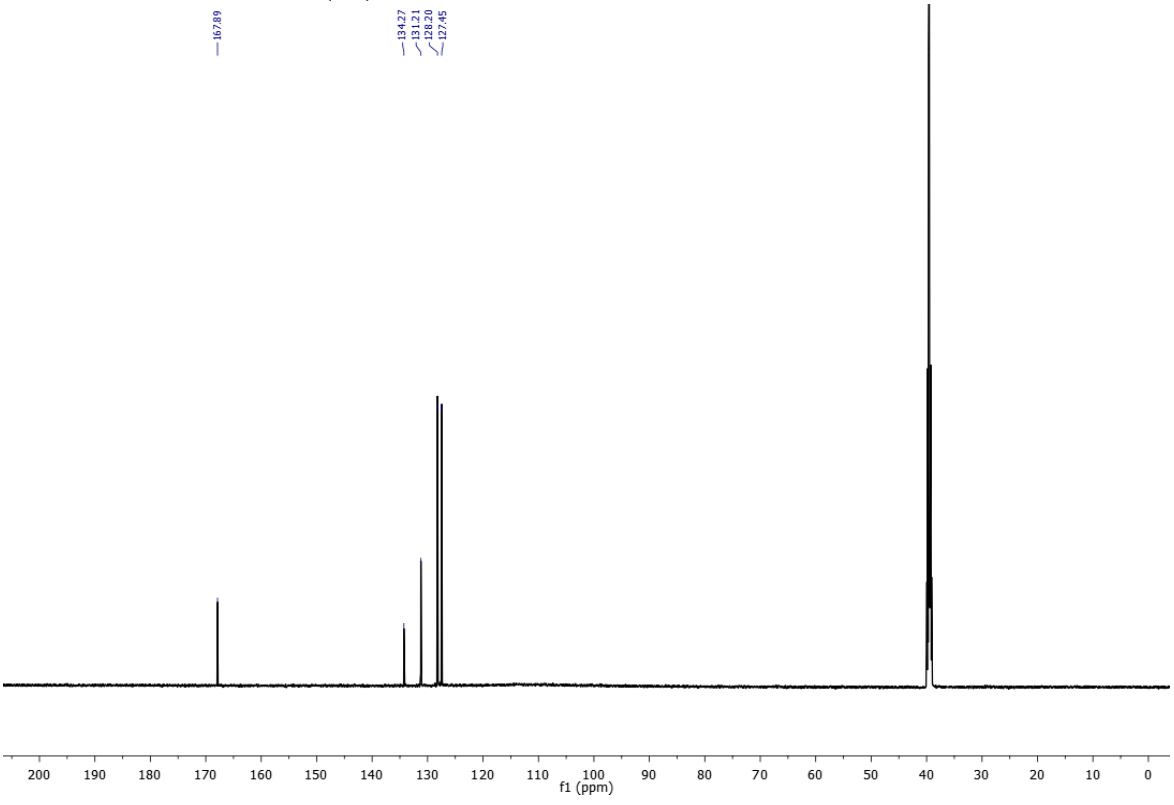

^{1}H NMR in DMSO (d_6) 600 MHz (4e)

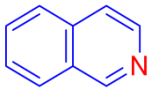

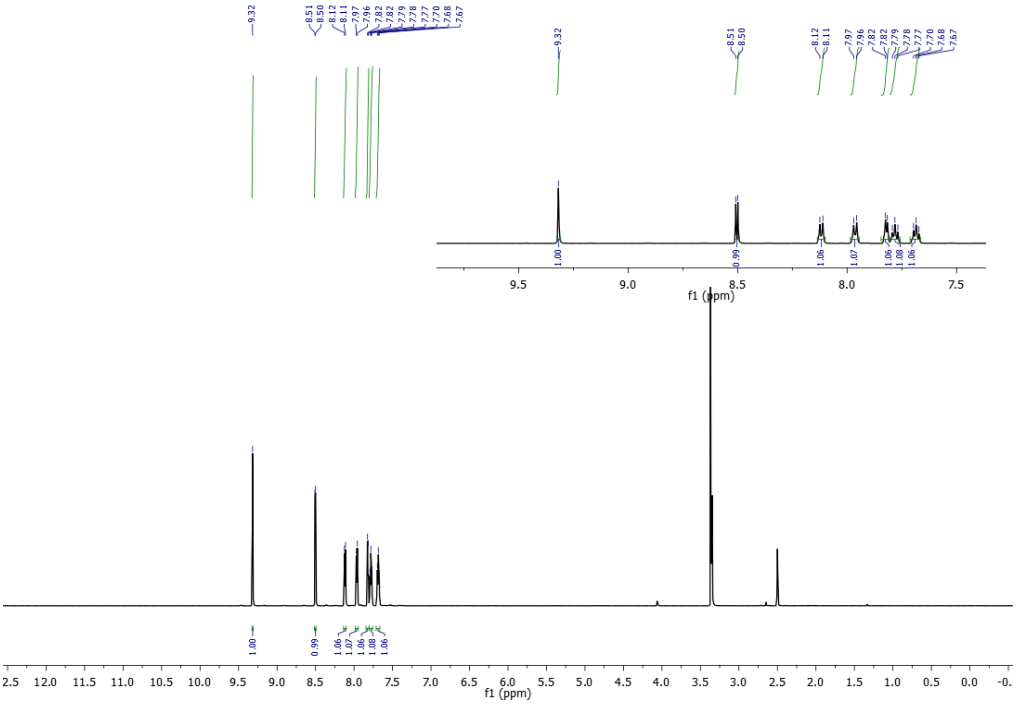

^{13}C NMR in DMSO (d_6) 151 MHz

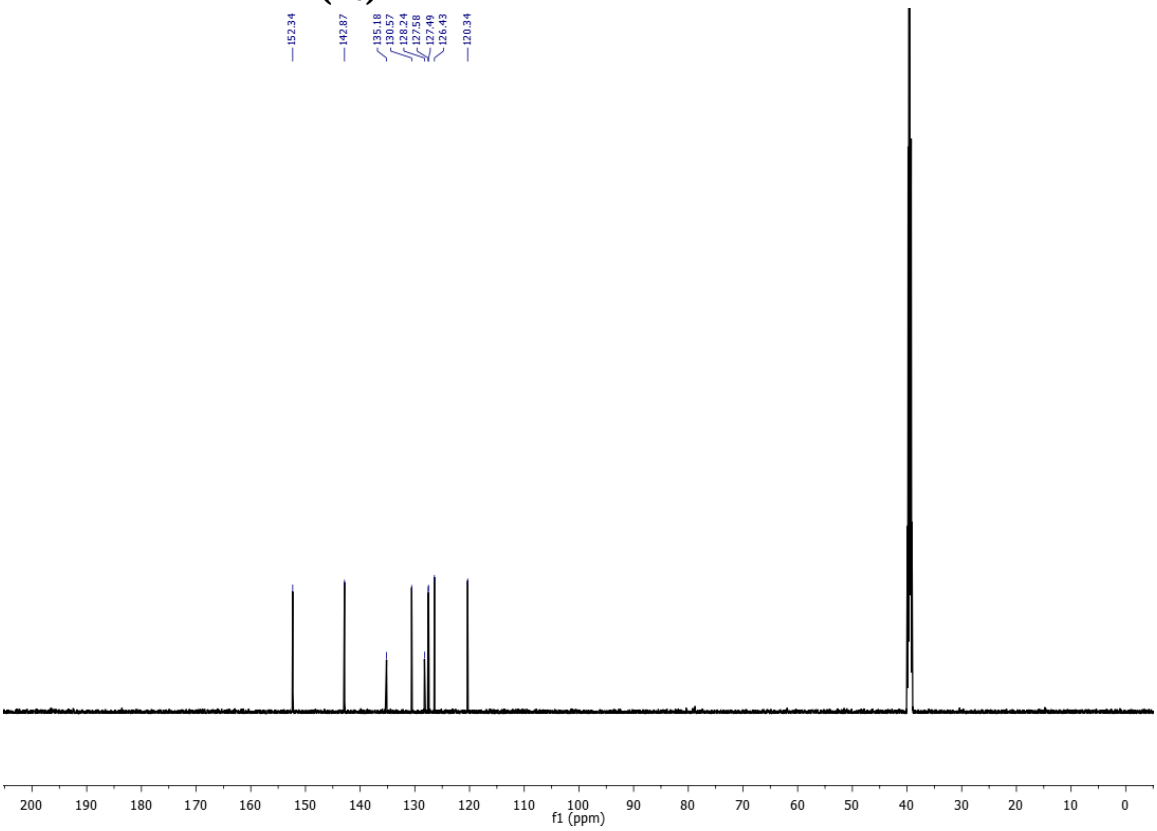

^{1}H NMR in DMSO (d_6) 600 MHz (4d)

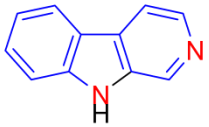

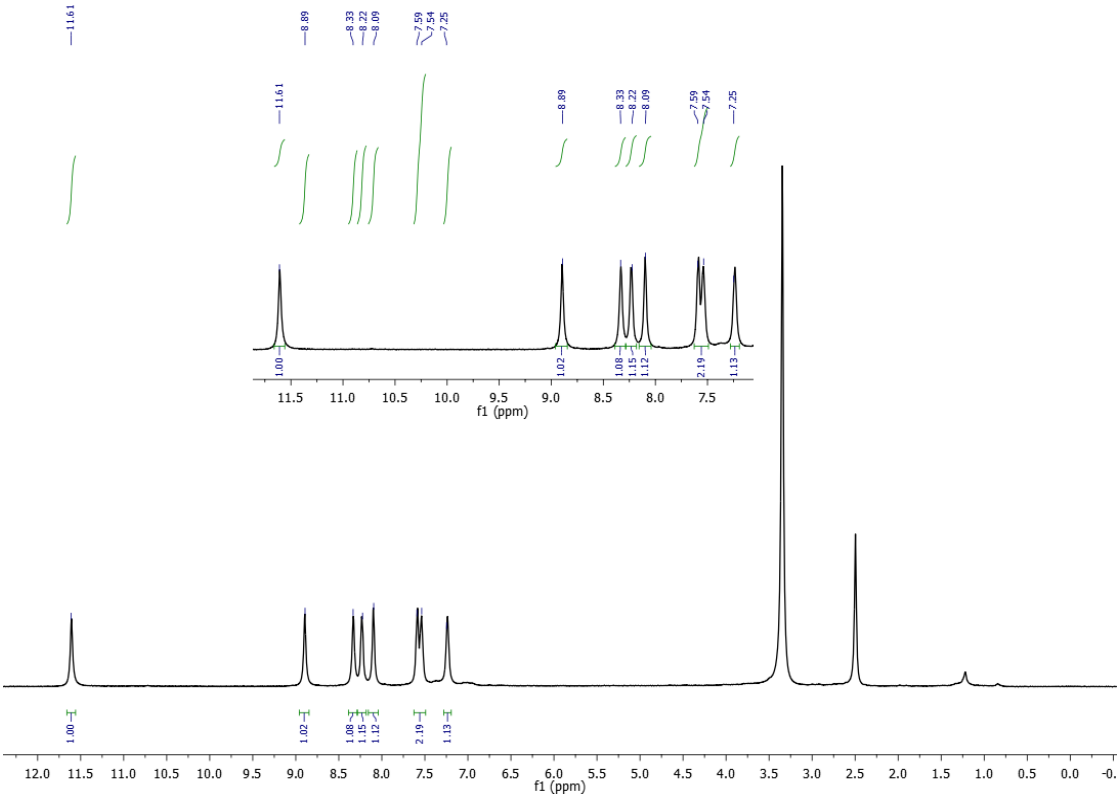

^{13}C NMR in DMSO (d_6) 151 MHz

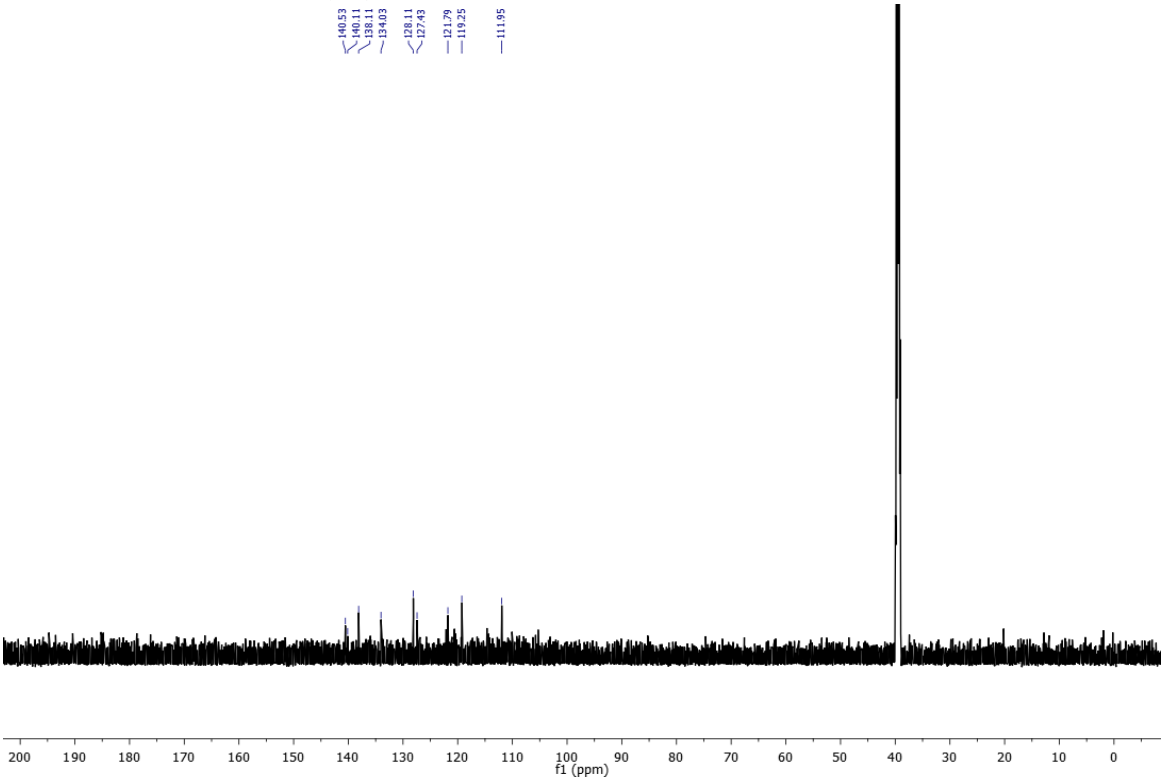

NMR spectral data of benzyl alcohol oxidation

^{1}H NMR in $CDCl_3$ 400 MHz (6a)

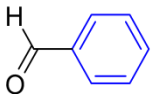

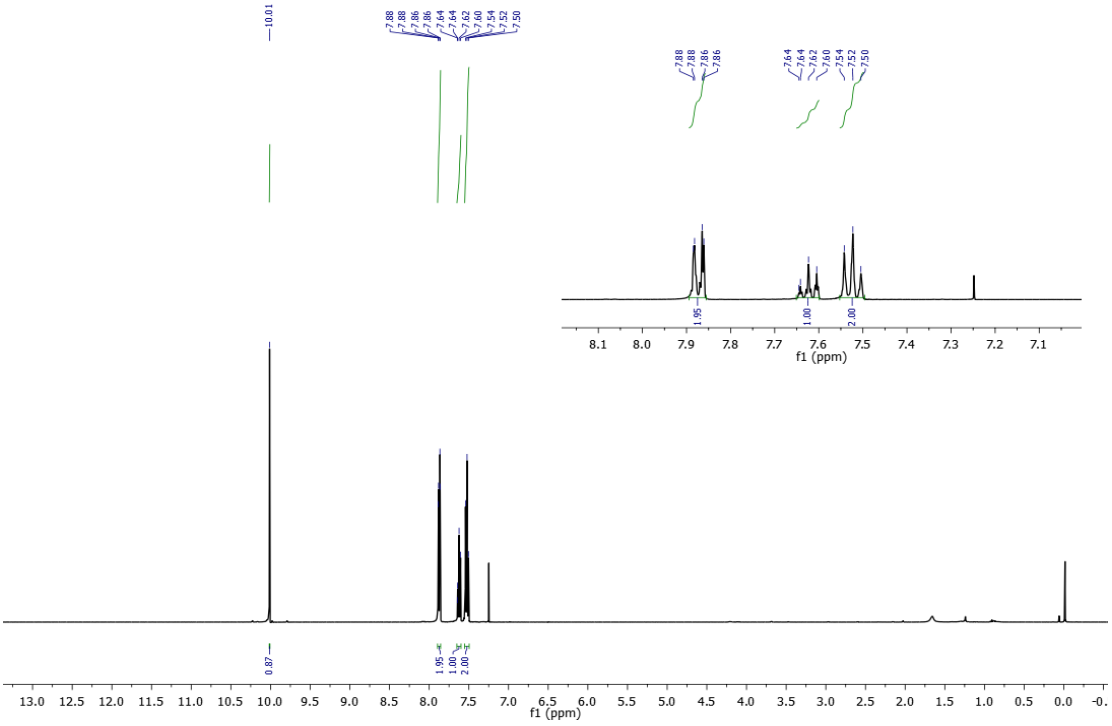

^{13}C NMR in $CDCl_3$ 101 MHz

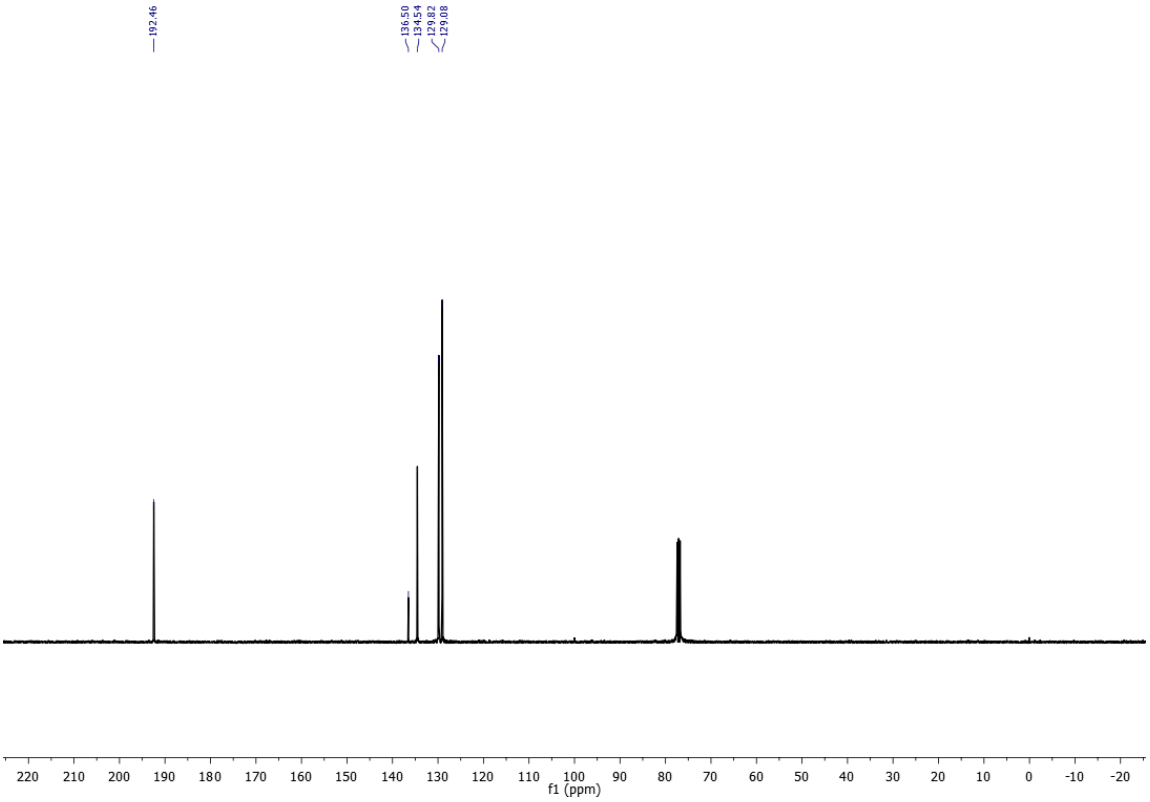

^{1}H NMR in $CDCl_3$ 400 MHz (6b)

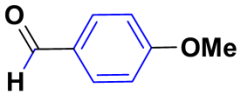

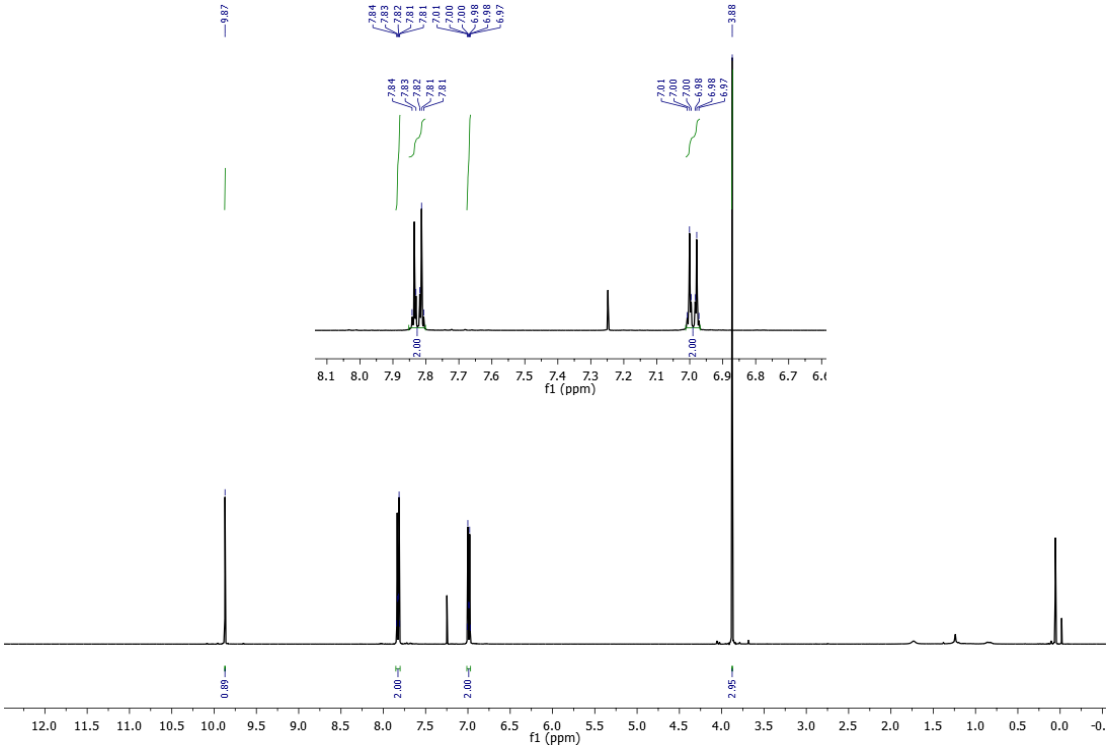

^{13}C NMR in $CDCl_3$ 101 MHz

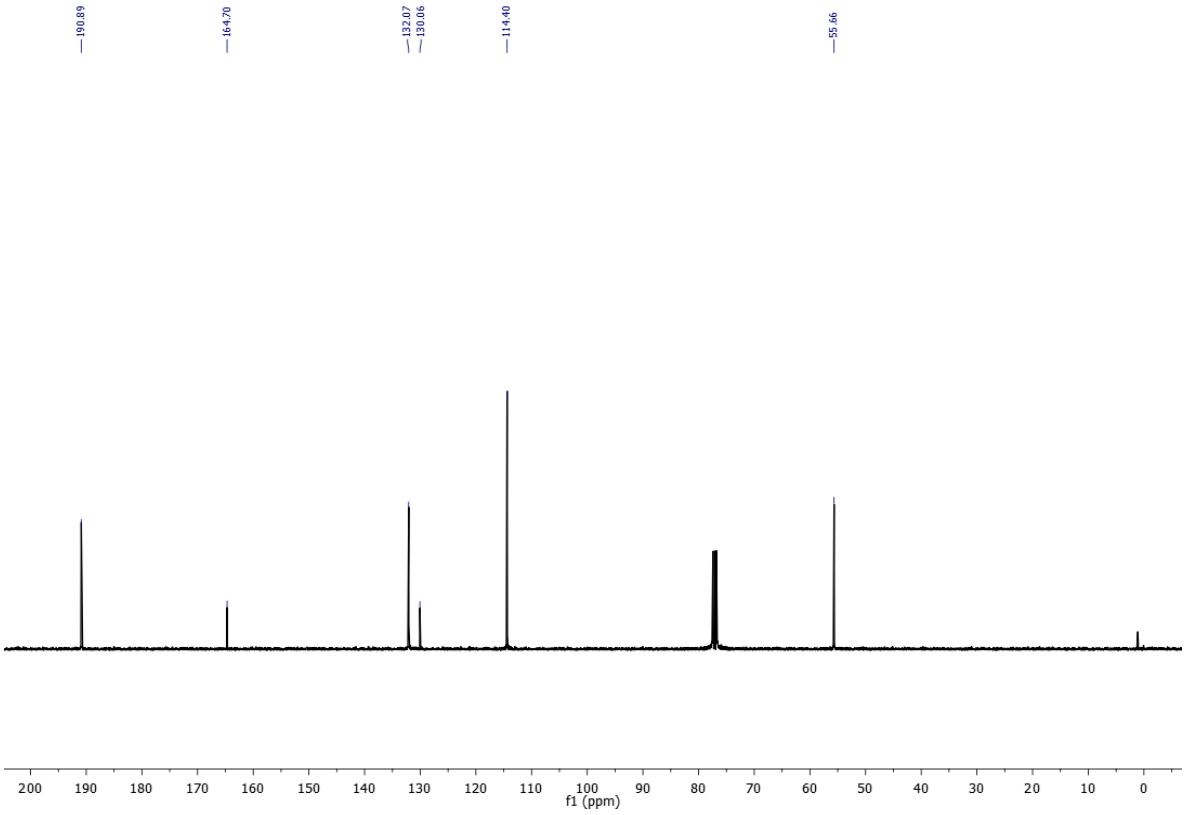

^{1}H NMR in $CDCl_3$ 400 MHz (6c)

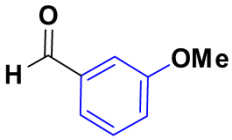

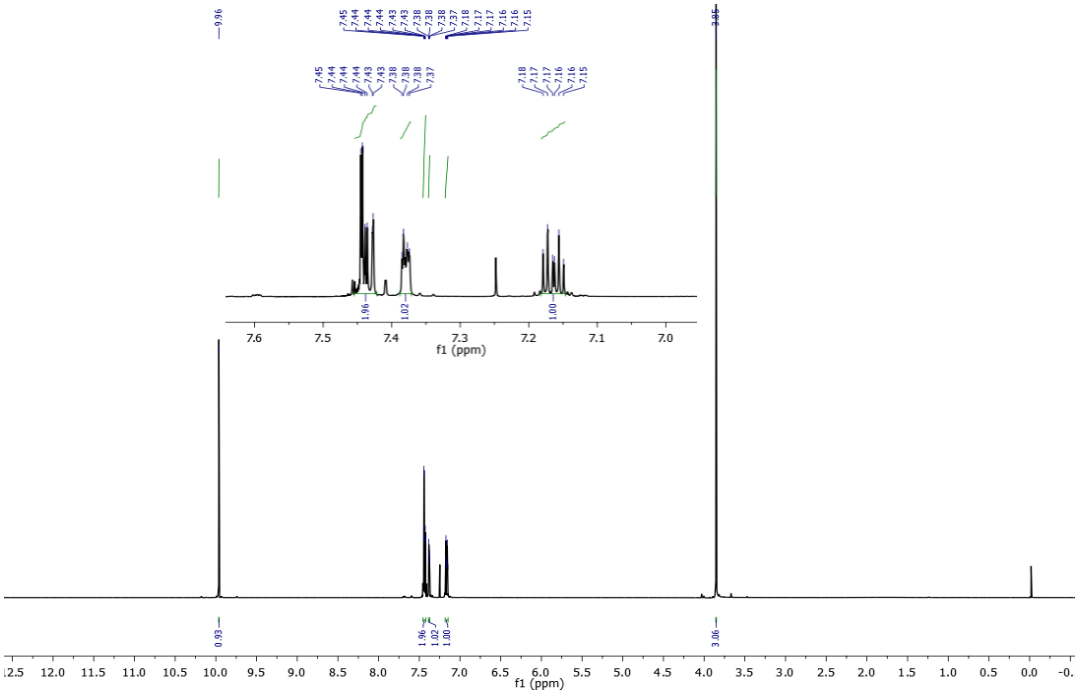

^{13}C NMR in $CDCl_3$ 101 MHz

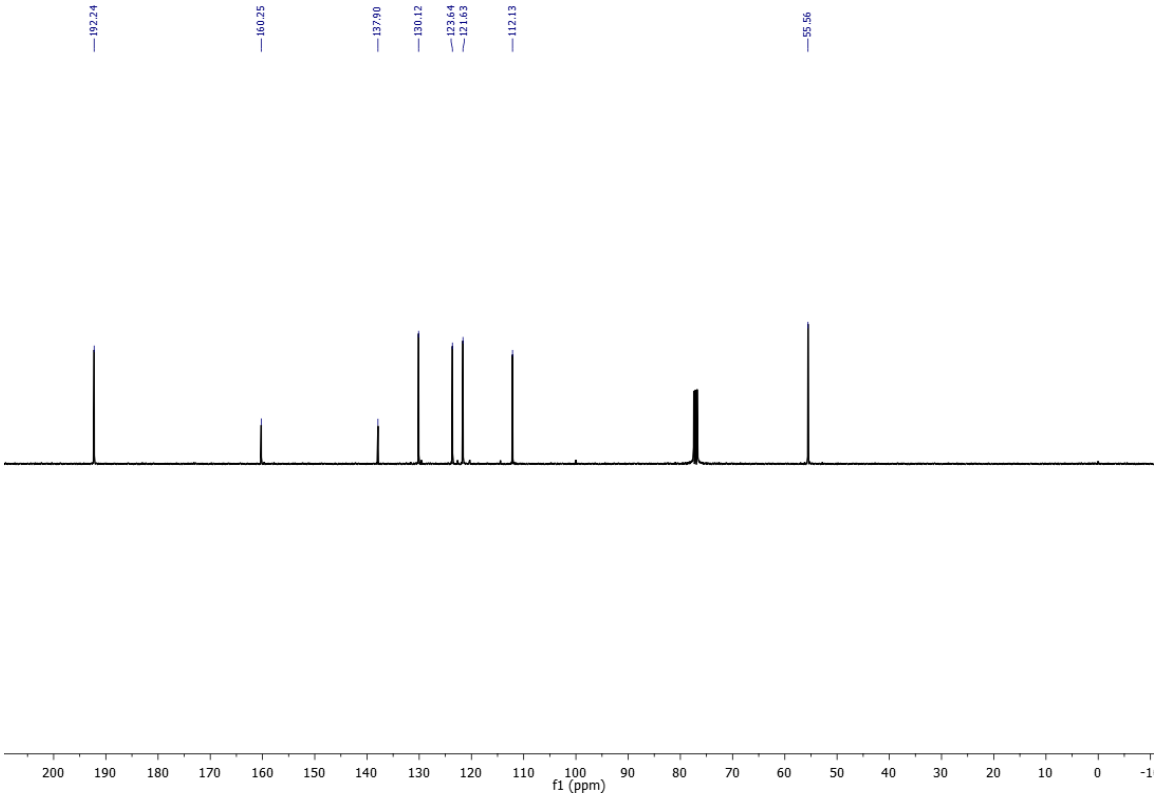

^{1}H NMR in $CDCl_3$ 400 MHz (6d)

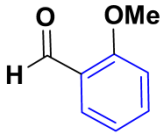

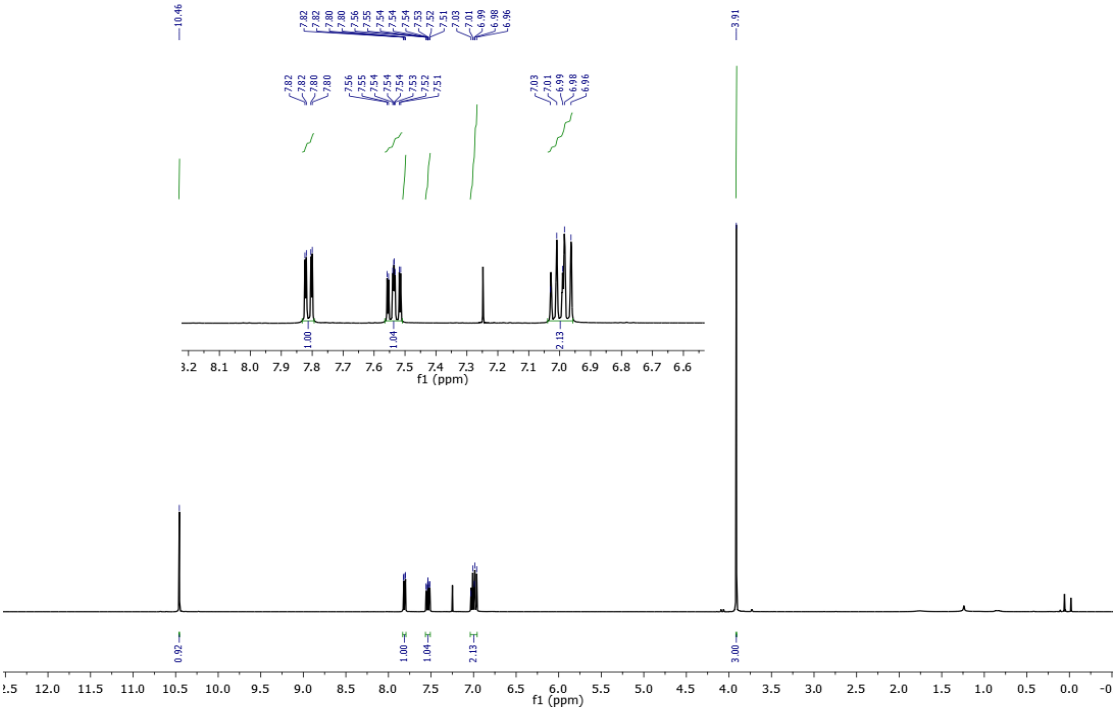

^{13}C NMR in $CDCl_3$ 101 MHz

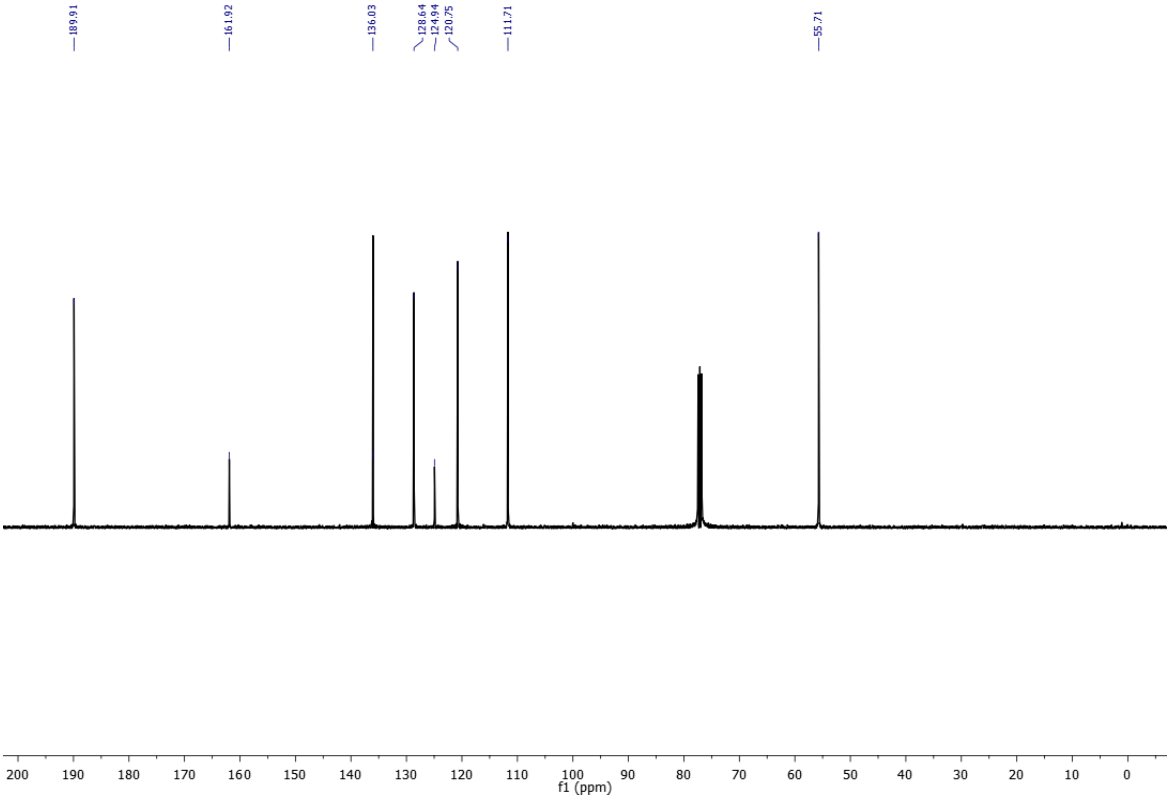

^{1}H NMR in $CDCl_3$ 400 MHz (6e)

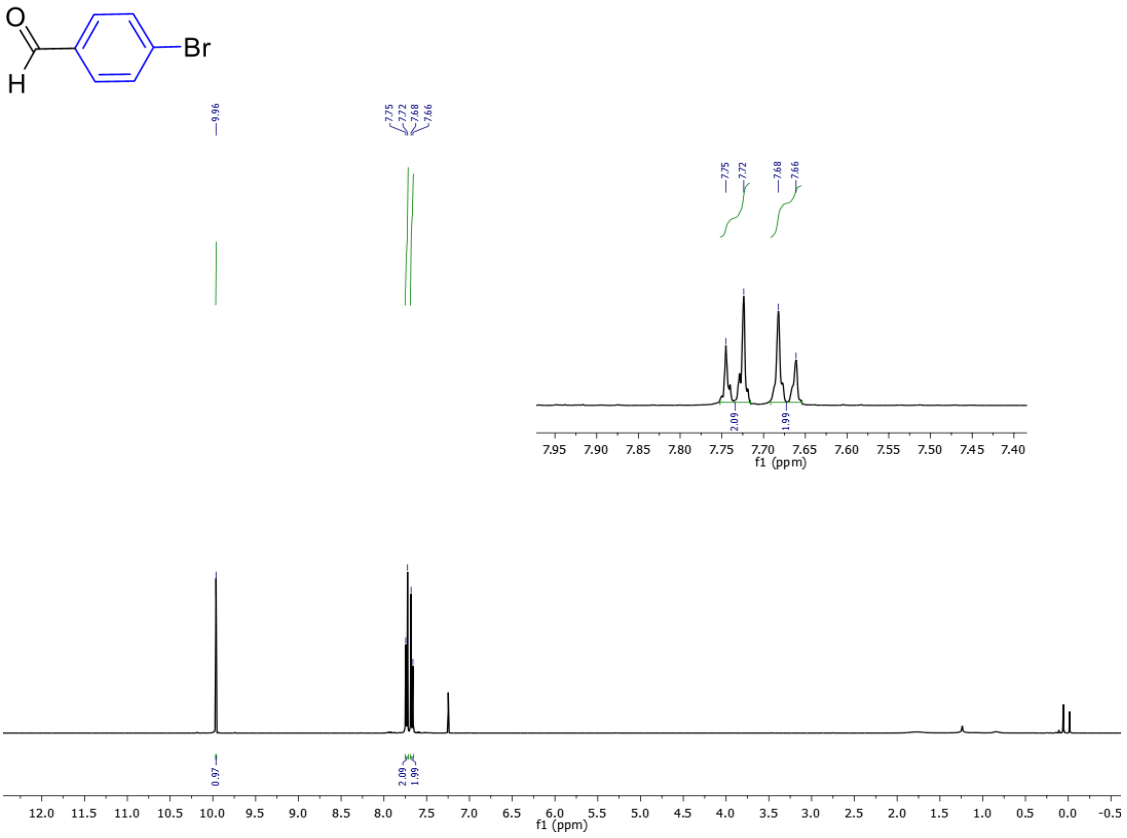

^{13}C NMR in $CDCl_3$ 101 MHz

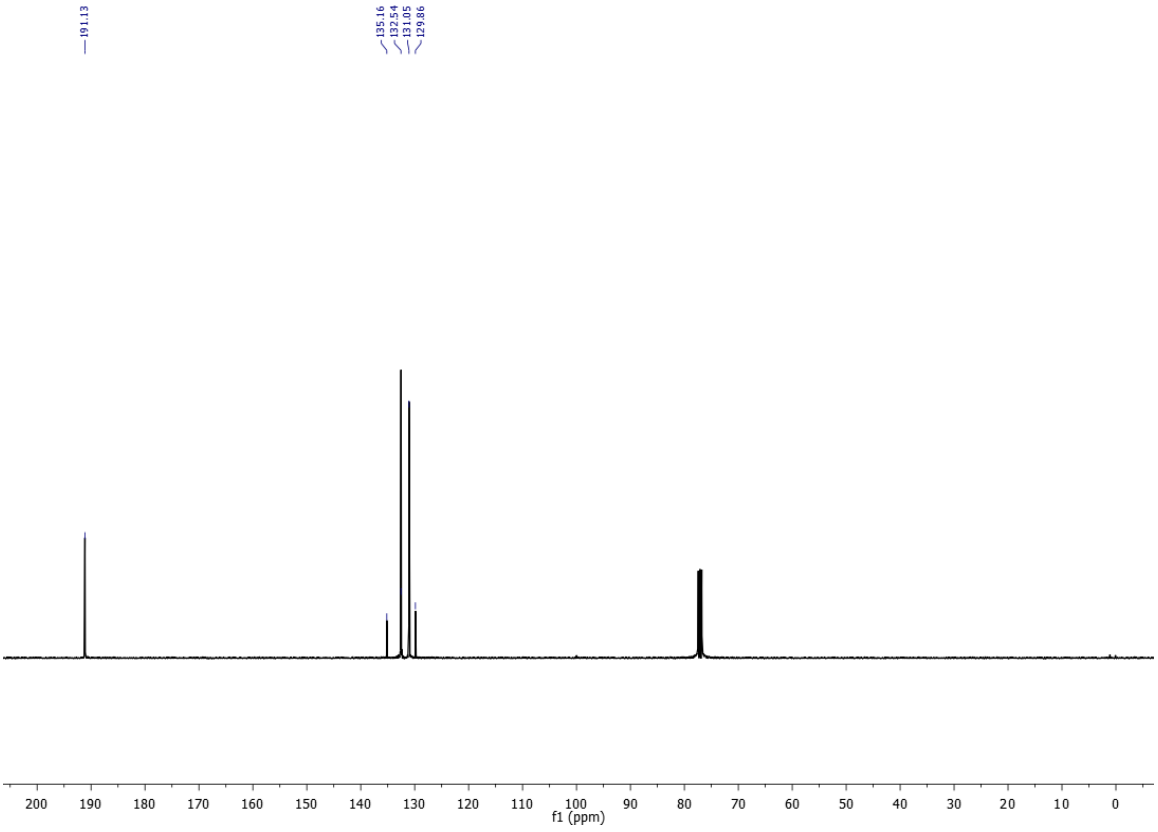

^{1}H NMR in $CDCl_3$ 400 MHz (6f)

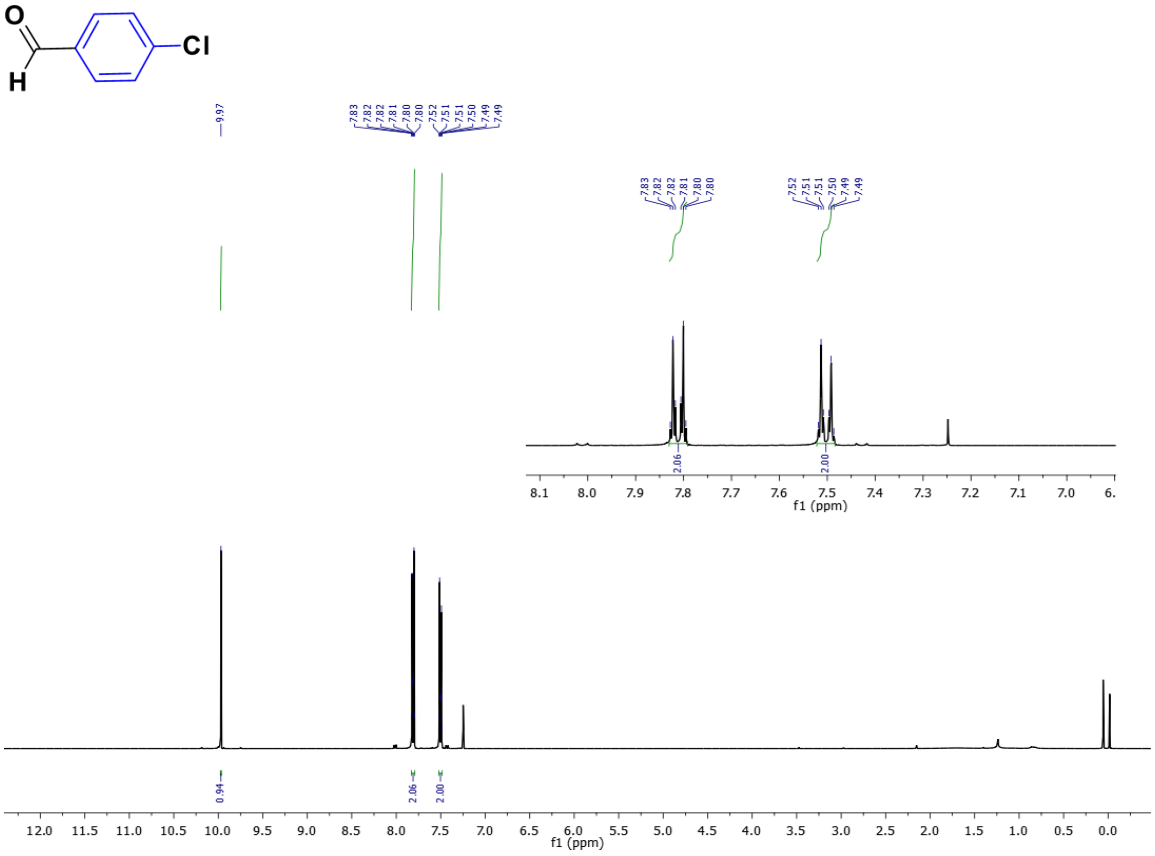

^{13}C NMR in $CDCl_3$ 101 MHz

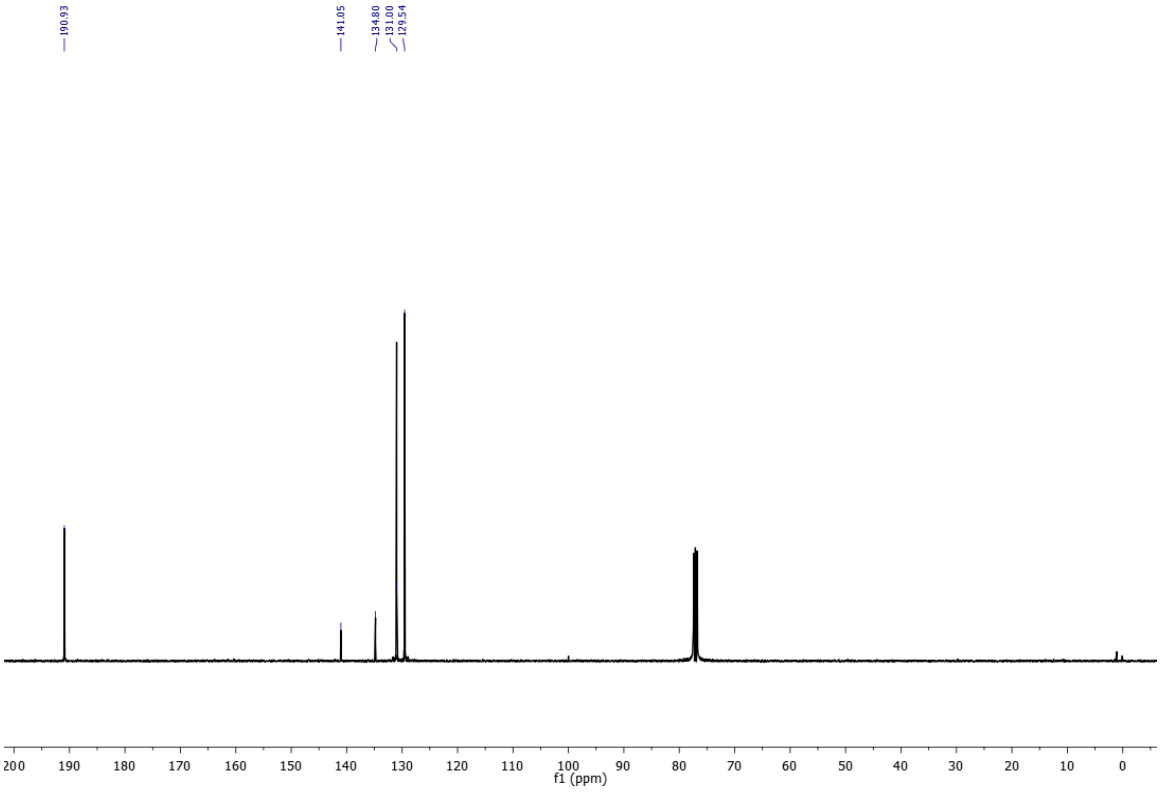

^{1}H NMR in $CDCl_3$ 400 MHz (6g)

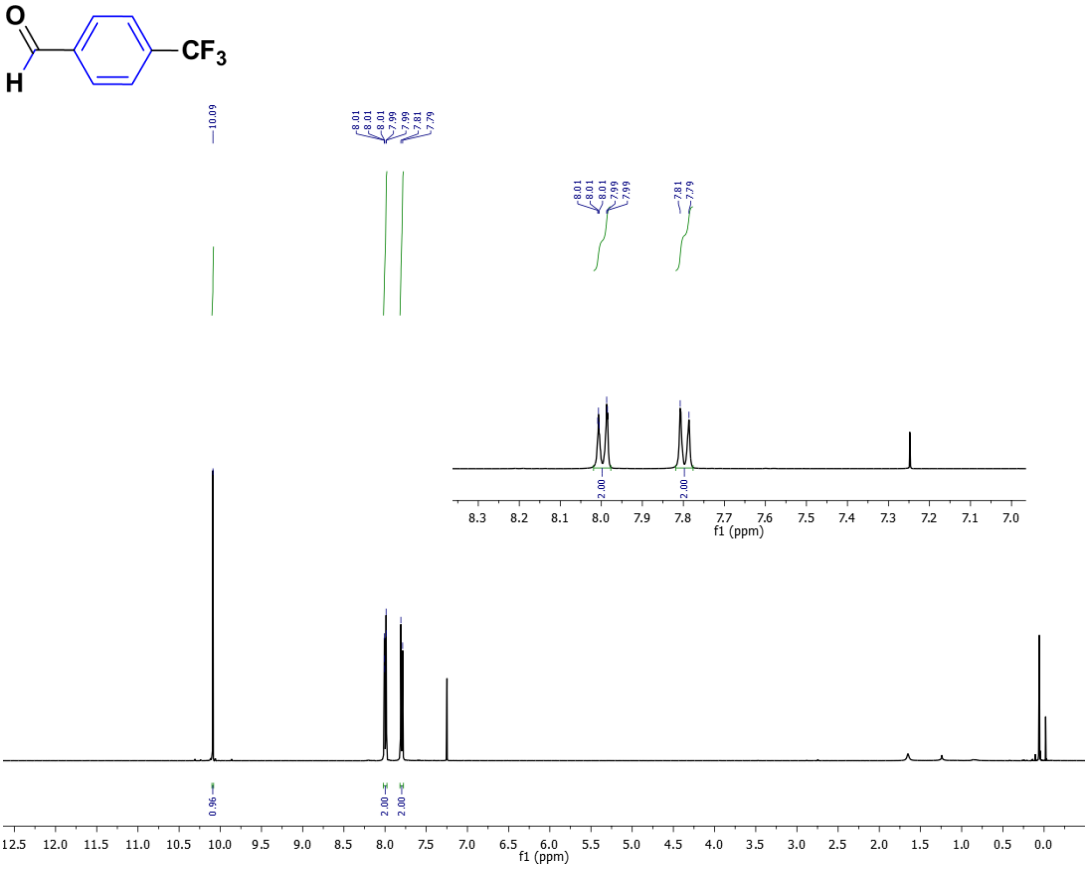

^{13}C NMR in $CDCl_3$ 101 MHz

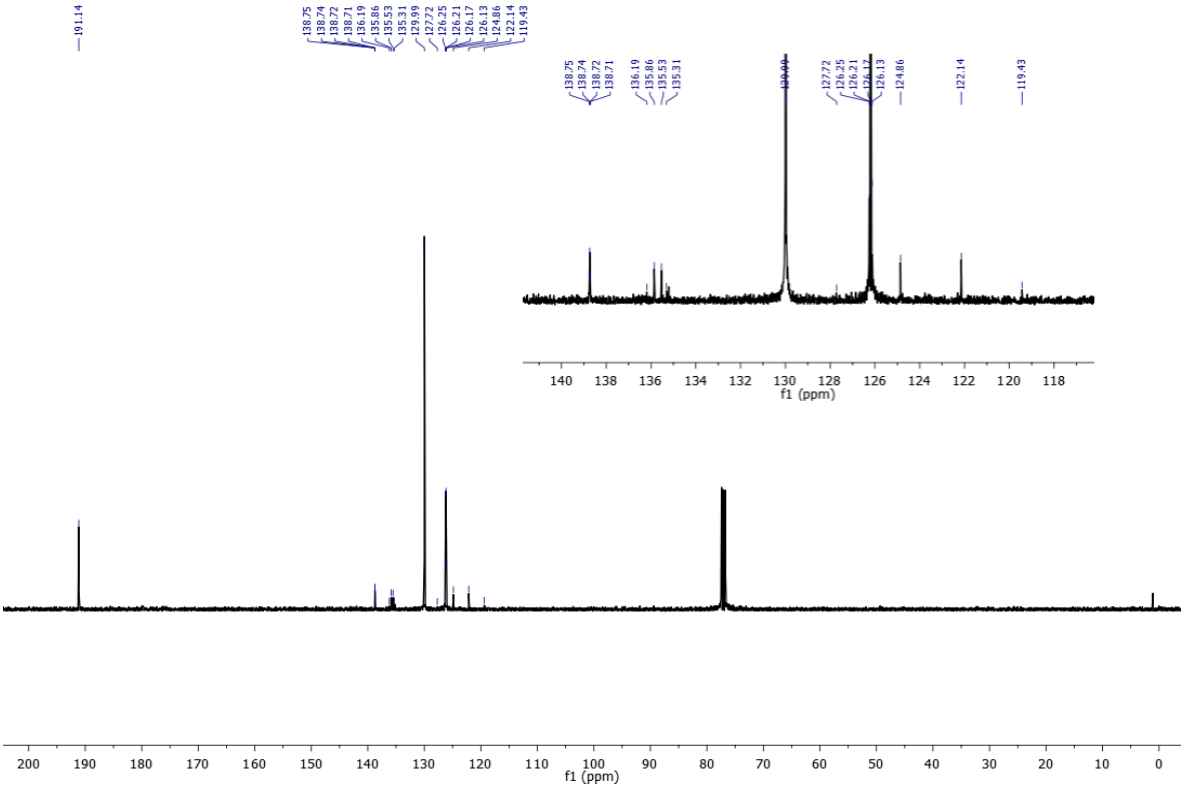

^{1}H NMR in $CDCl_3$ 400 MHz (6h)

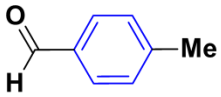

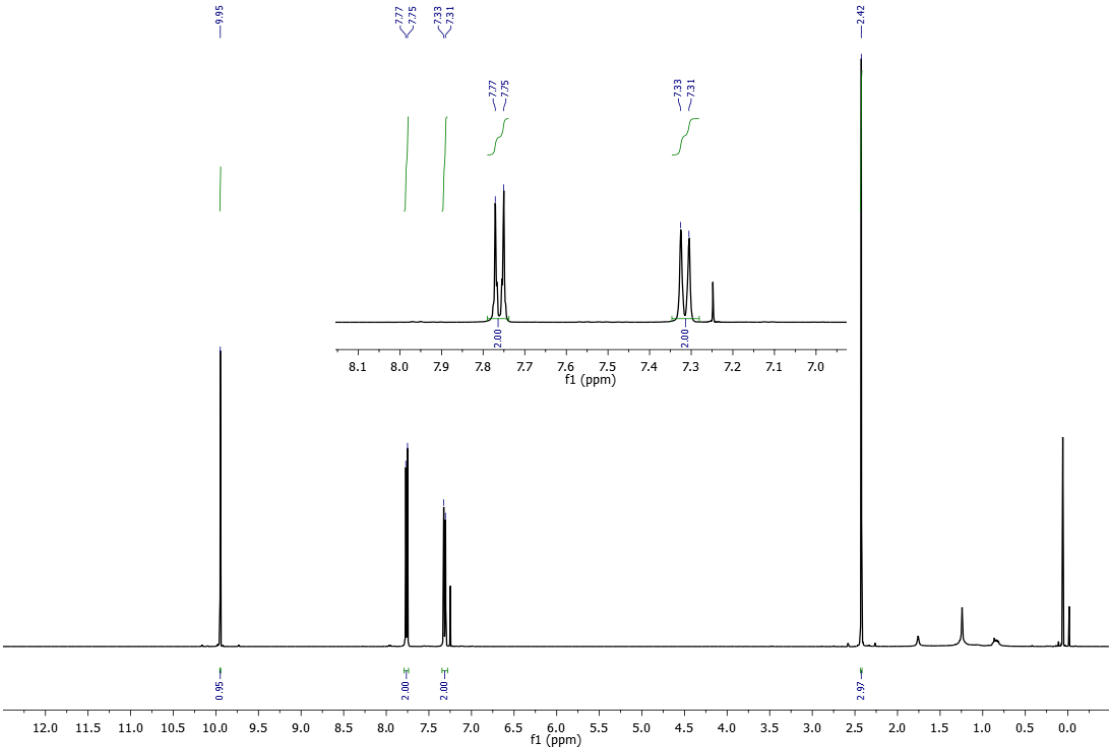

^{13}C NMR in $CDCl_3$ 101 MHz

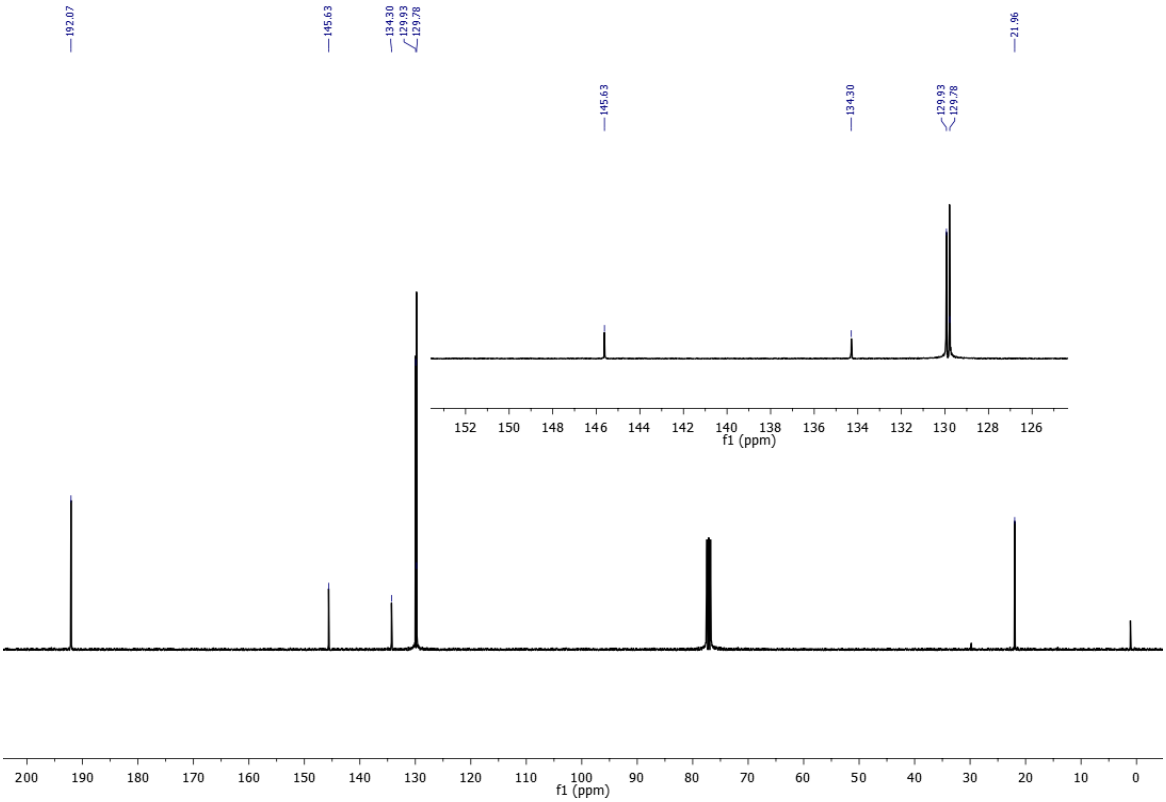

^{1}H NMR in $CDCl_3$ 400 MHz (6i)

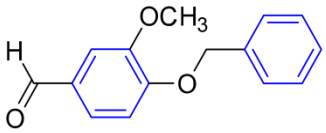

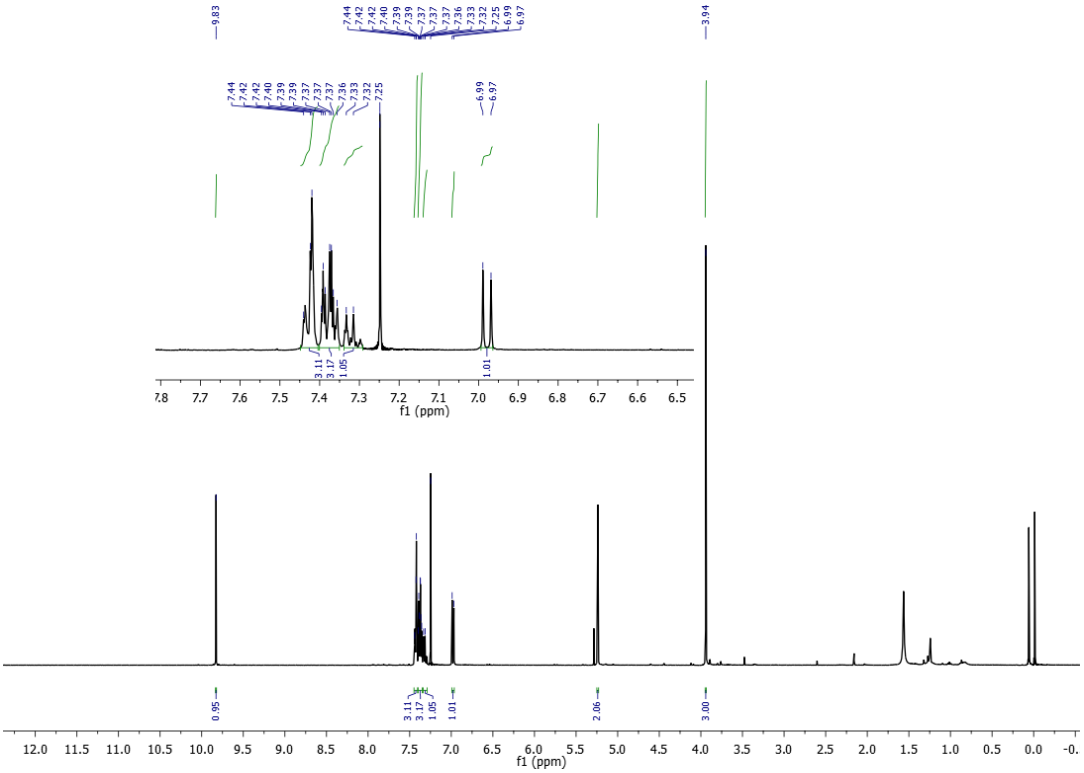

^{13}C NMR in $CDCl_3$ 101 MHz

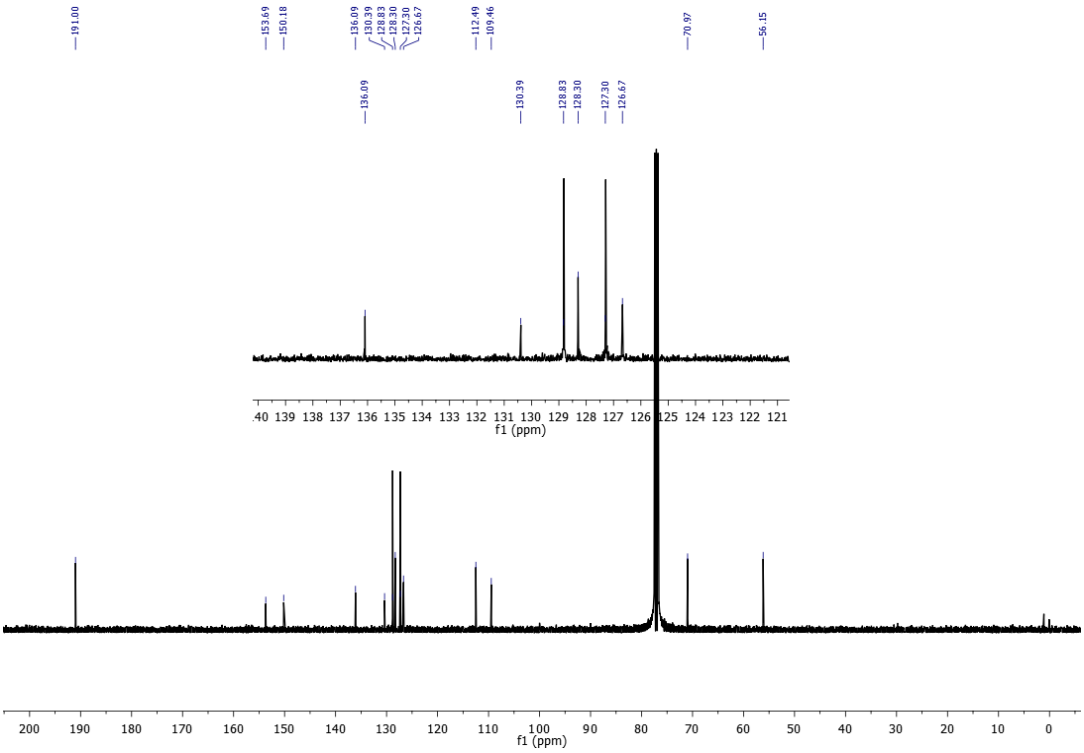

NMR spectral data of Control Experiment

Control 2: ^{1}H NMR in $CDCl_3$ 400 MHz (6a)

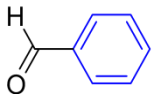

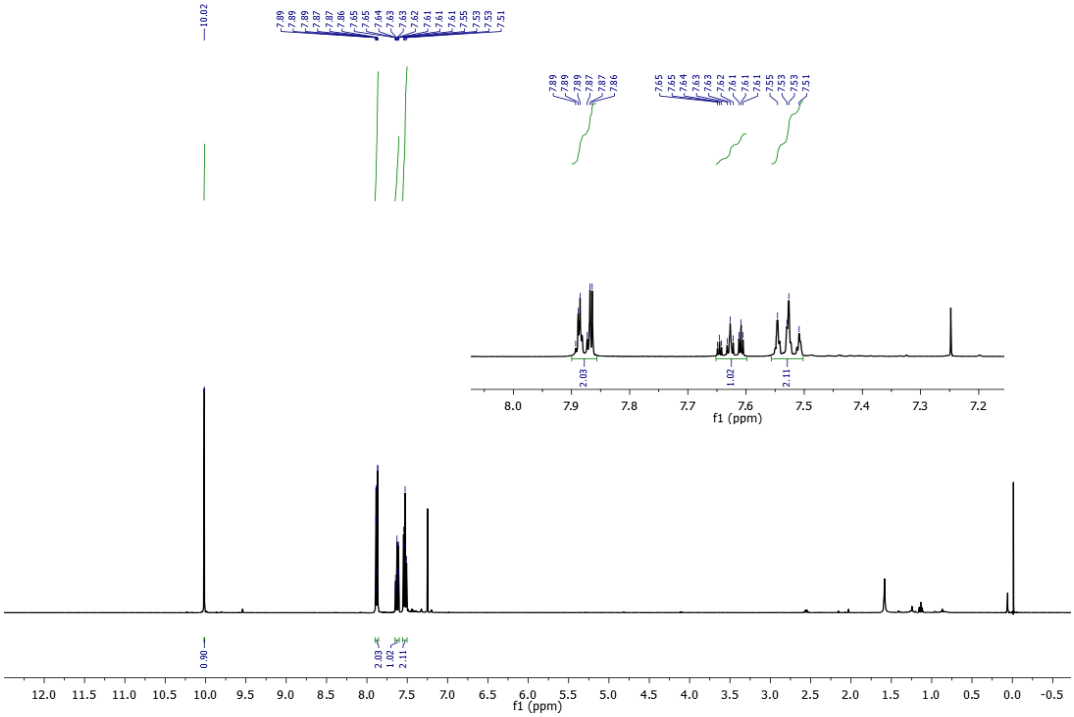

^{13}C NMR in $CDCl_3$ 101 MHz

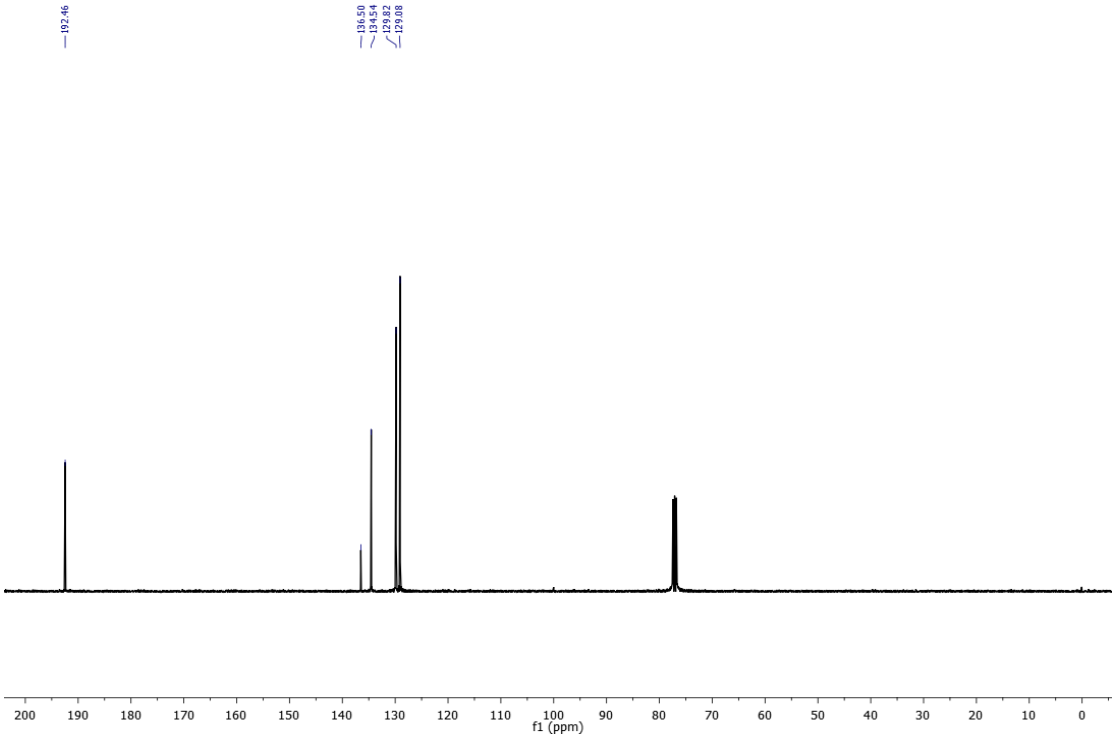

Control 3: ^{1}H NMR in $CDCl_3$ 400 MHz (7a)

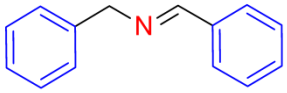

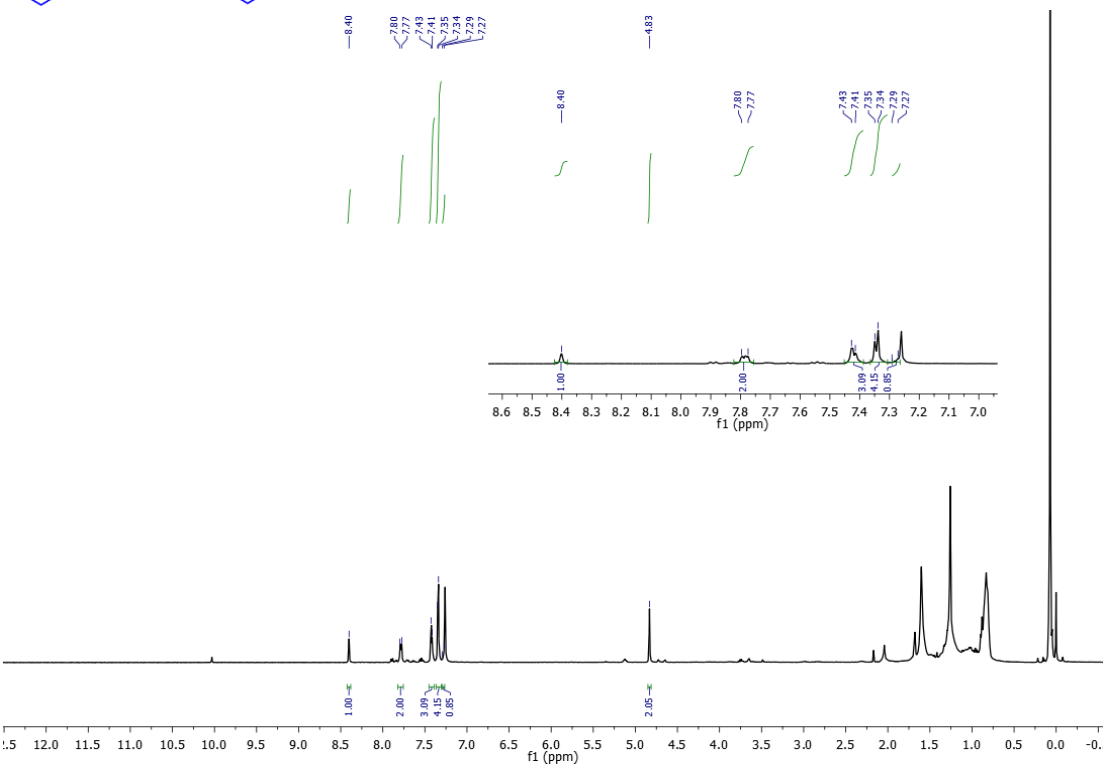

^{13}C NMR in $CDCl_3$ 101 MHz

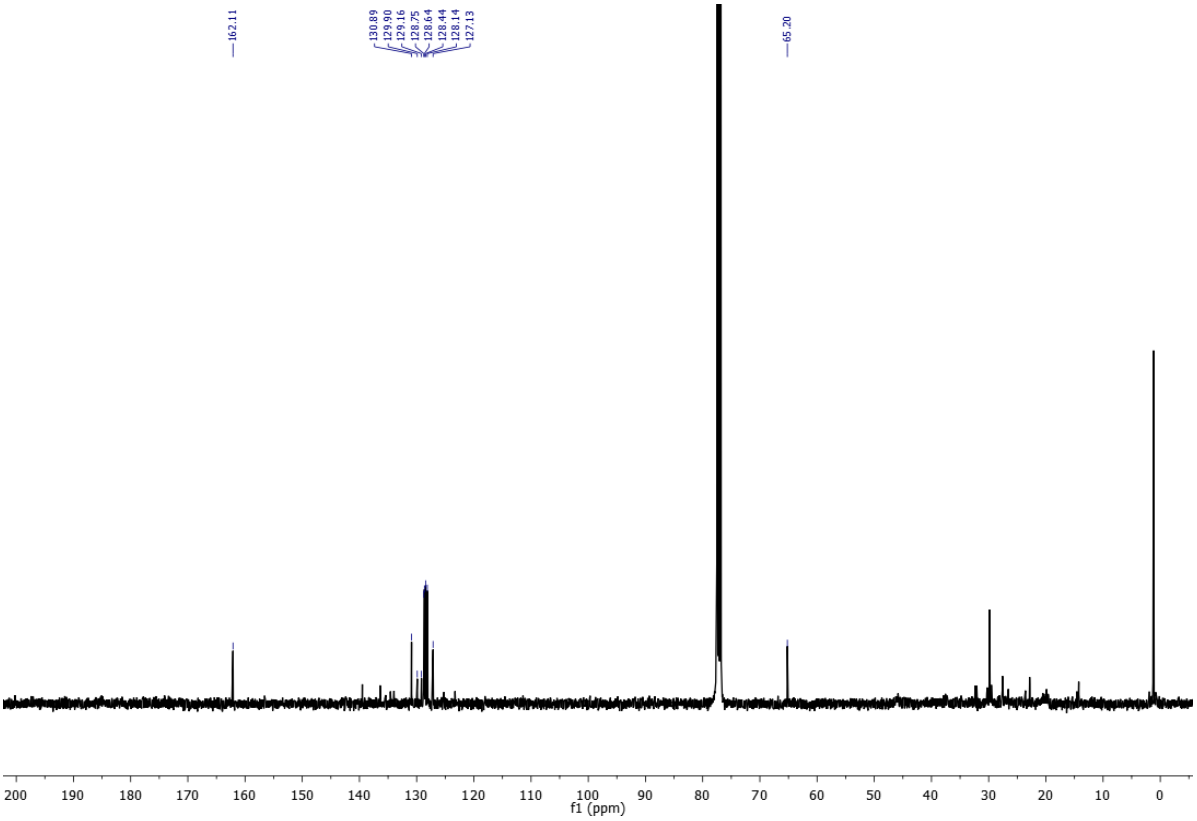

Control 5: ^{1}H NMR in $CDCl_3$ 400 MHz (7a+6a)

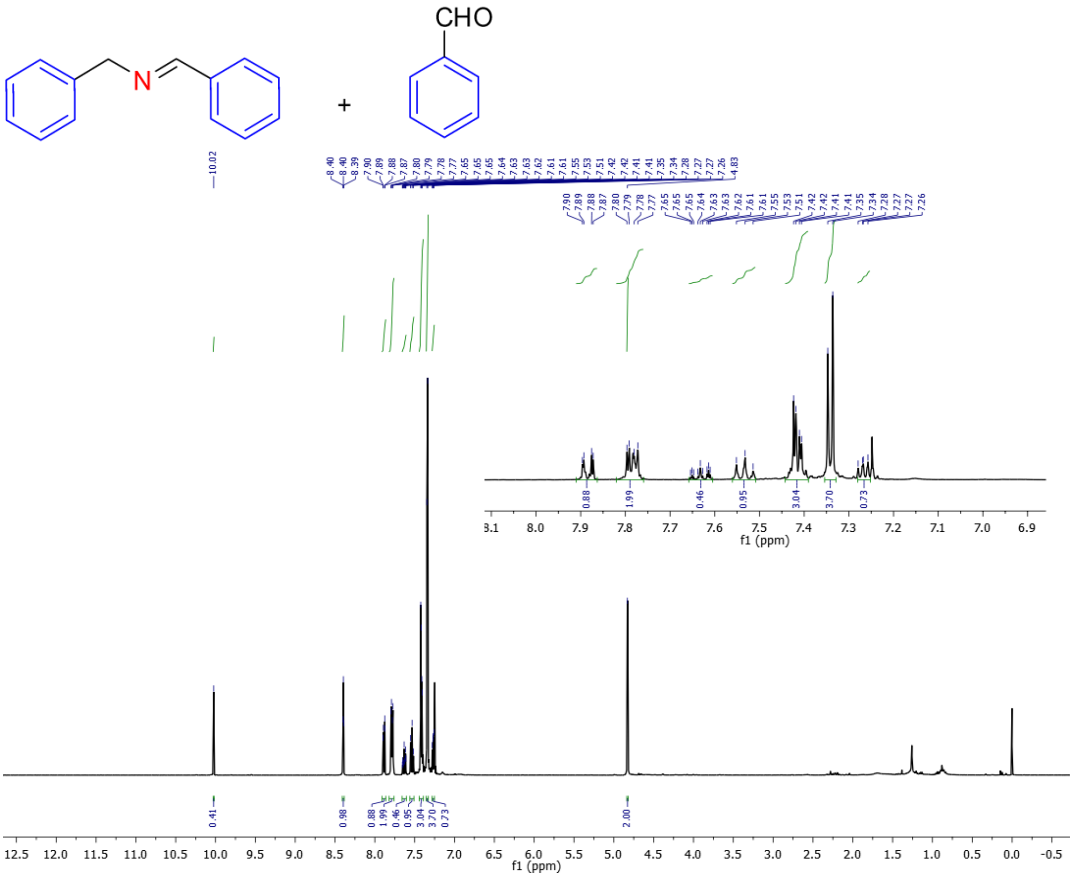

^{13}C NMR in $CDCl_3$ 101 MHz

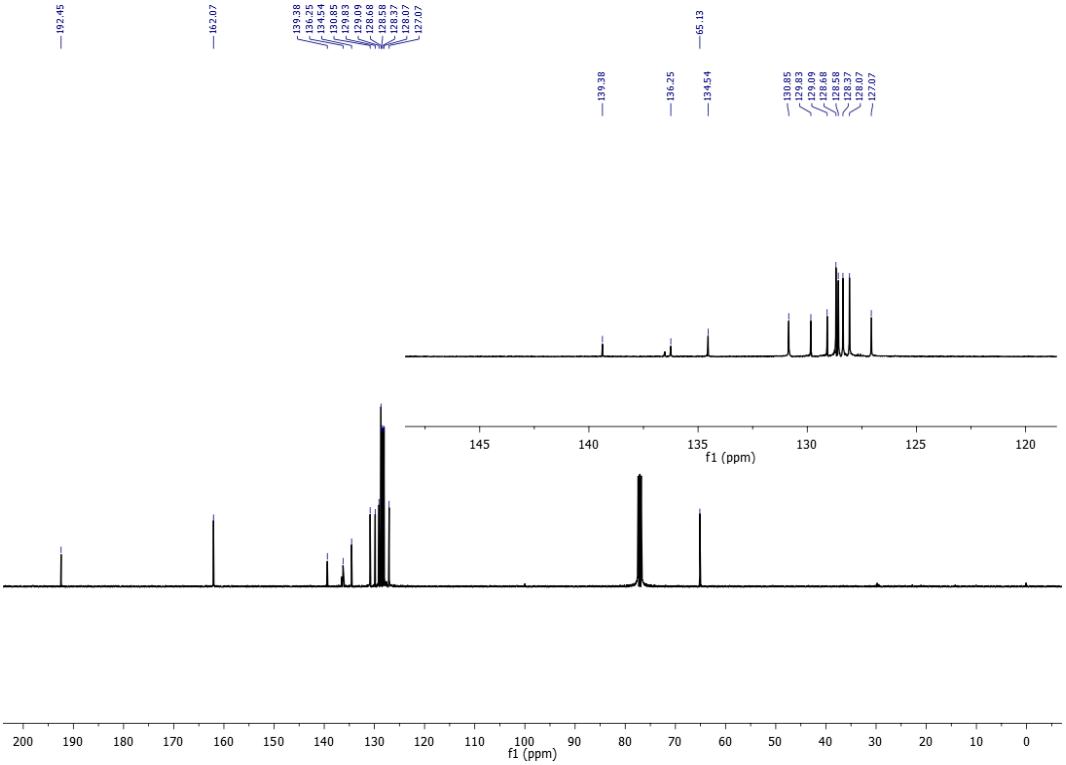

Chapter 3

Oxygen Activation by Ionic Liquid: A Detail Mechanistic Study

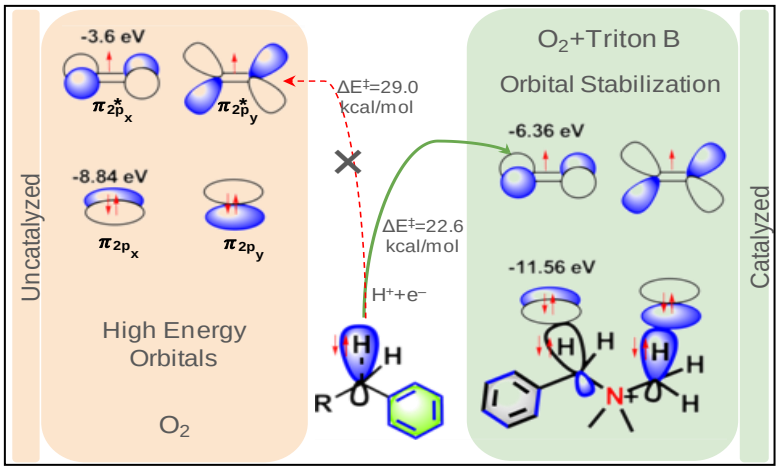

The importance of theoretical mechanistic studies over experimental ones is highlighted in the opening of this chapter. It presents a detailed study of molecular dynamics (MD) and systematically modified density functional theory (DFT) to validate the experimental oxygen activation protocol and conduct an in-silico mechanistic investigation of benzylamine oxidation. The MD studies describe the presence of a unique microenvironment in the Triton B ionic liquid. Moreover, the chapter offers a comparative analysis of energy profiles for benzylamine oxidation with and without the Triton B catalyst, using various quantum chemical models and methods. The study reveals that the entropy term and dispersion correction in the free energy profile clearly indicate Triton B plays a catalytic role in activating oxygen. Thie chapter clarifies the mechanism of hydrogen atom abstraction from benzylamine to oxygen, highlighting proton-coupled electron transfer (PCET) over hydrogen atom transfer (HAT). Finally, it presents a unique study of the most valuable and fundamental orbital calculation (pDOS) of oxygen activation by the ionic liquid.

3.1 Introduction

Experimental organic reactions play a crucial role in advancing the field of organic chemistry. They have numerous applications and advantages that contribute to our understanding of chemical reactions and the development of new compounds and materials. Organic reactions are used to synthesize a wide range of compounds, including pharmaceuticals, agrochemicals, dyes, polymers, and other functional materials. These reactions enable the synthesis of novel substances with desirable properties and functionalities. As well as organic reactions play a vital role in medicinal chemistry, where researchers design and synthesize potential drug candidates.[155] Experimental studies help identify bioactive molecules and optimize their pharmacological properties and also many natural products with important biological activities are challenging to obtain from natural sources in sufficient quantities. Experimental organic reactions enable the synthesis of these compounds, facilitating further studies on their medicinal, ecological, and other applications. By modifying the structure of organic compounds through various reactions, researchers can study the relationship between the molecular structure and its biological or physical properties. SAR studies aid in the design of more potent and selective compounds.[156]

This optimization helps improve reaction yields and selectivity, making synthetic processes more efficient and cost-effective.[157] Developing environmentally friendly and sustainable synthetic methods is a critical aspect of organic chemistry. Thus optimization of organic reactions contributes to the advancement of green chemistry by minimizing waste generation, using renewable resources, and reducing the use of hazardous reagents.[158] Experimental organic reactions provide some hints of reaction pathways, intermediate species only. This information is critical for understanding the underlying mechanisms governing chemical transformations.[159] By conducting

kinetic studies and monitoring reaction progress, experimental reactions help elucidate reaction mechanisms and provide insight into factors affecting reaction rates and selectivity. Experimental organic reactions provide essential data for validating computational predictions, such as those obtained from Density Functional Theory (DFT) calculations.[160] This reciprocal relationship between experiment and theory leads to a better understanding of chemical phenomena.

While experimental techniques are essential for validating and verifying reactions, they often have limitations, and DFT can provide valuable insights and overcome some of these limitations. Some ways DFT can help solve the drawbacks of experimental organic reaction mechanism studies.[160] Experimental studies often provide indirect evidence for proposed reaction mechanisms, leading to uncertainties and alternative interpretations. DFT can offer detailed atomistic insights into the energetics, geometries, and electronic structures of reactants, intermediates, and products, thereby validating or proposing specific reaction pathways with higher accuracy. Determining the transition state using experimental procedures is not feasible due to the high energy and transient nature of these species. DFT can accurately locate transition states and provide valuable information about the activation energies and barriers involved in the reaction, helping to understand the rate-determining step.[161]

DFT calculations can validate or refine experimental results by comparing predicted reaction energetics and intermediates with experimental data. This cross-validation can confirm the proposed mechanisms and help in resolving discrepancies between experimental observations and interpretations. Experimental investigations might not always provide a complete understanding of the factors influencing stereoselectivity and regioselectivity. DFT can predict the energies of different stereoisomers and regioisomers, allowing for a comprehensive analysis of reaction outcomes and selectivity. Experimental

studies often focus on the major reaction pathway, neglecting minor pathways that may play crucial roles in complex reactions. DFT can explore multiple reaction paths and identify alternative reaction routes, giving a more complete picture of the reaction mechanism.[162] DFT can study the stability and reactivity of unstable or short-lived intermediates that are challenging to isolate and characterize experimentally. It offers a way to examine these intermediates, which are often essential for understanding the overall reaction mechanism. DFT also allows for the incorporation of solvent effects, enabling the study of reactions in various solvents and understanding the influence of solvent polarity and interactions on reaction mechanisms.[163] By combining DFT calculations with experimental data, researchers can gain a more comprehensive understanding of organic reaction mechanisms. DFT helps overcome some of the limitations of experimental studies and provides valuable complementary information, ultimately advancing the knowledge of chemical reactions and enabling the design of more efficient and selective synthetic routes.[164]

The DFT (Density Functional Theory) calculated energy profile diagram, also known as the reaction energy profile or potential energy surface (PES), is of significant importance in various areas of chemistry and materials science. This diagram represents the variation in potential energy as a function of reaction progress or changes in molecular geometry. The energy profile diagram provides insights into the reaction mechanism by identifying transition states, intermediates, and the energy barriers associated with each step.[165] It helps to understand the sequence of bond-breaking and bond-forming events during a chemical reaction. DFT-calculated energy profile diagrams allow for the determination of activation energies and reaction enthalpies.[165] These energetic parameters are crucial in predicting the rate and feasibility of chemical reactions. The energy profile diagram enables the precise localization of transition states, which are critical points on the reaction pathway. Transition

state structures represent the highest-energy points and help determine the rate-determining step of a reaction. By analyzing the relative energies of reactants, intermediates, and products, the energy profile diagram can predict the favored reaction outcome and the formation of possible side products. DFT-calculated energy profiles are particularly valuable in elucidating the factors governing reaction selectivity. By comparing the energy barriers for different reaction pathways, researchers can determine the preferred product formation.[159] Energy profile diagrams are essential for the design and optimization of catalysts.[166] They help identify the transition states involved in catalytic reactions and understand the catalyst's effect on lowering activation energies.[166] The energy profile diagram can be used to study the influence of solvents on reaction mechanisms. But DFT does not consider exclusive solvent molecules in calculation.[167] So It is a corner of drawback in case of DFT, when a reaction proceeds with only when concentrate condition whereas does not proceeds with dilute condition vice versa.[168] So to understand the arrangement of the calculated molecules with particular solvent is very crucial for studies. MD simulations can provide valuable insights into various aspects of molecular behavior with solvent molecules.[169]

Molecular Dynamics (MD) is a powerful computational simulation technique used in various scientific disciplines, especially in the field of theoretical and computational chemistry, materials science, and biophysics. It provides insights into the dynamic behavior of molecular systems by numerically solving the equations of motion for individual atoms and molecules.[169] The main goal of MD simulations is to study the time-dependent behavior of a collection of interacting particles with solvent molecules, such as atoms and molecules, as they evolve according to the laws of classical or quantum mechanics.[169]

In a molecular dynamics simulation, the basic idea is to track the positions and velocities of all particles over time while considering their interactions. The

interactions between particles are usually described by force fields, which are mathematical functions that model the potential energy of the system based on factors like atomic bonding, van der Waals forces, and electrostatic interactions. MD simulations can provide valuable insights into various aspects of molecular behaviour. By observing the movement and interactions of molecules over time, MD simulations can provide a guess of microenvironment of reactants before going to reaction. Thus MD simulation can provide a information of making arrangement of reactants before in silico calculation of energy profile diagrame by DFT.[170]

3.2 Methods

3.2.1 Molecular Dynamics Methods:

In the present study, molecular dynamics (MD) analysis was carried out to comprehend real Triton B's surroundings as well as under dilute condition. Simulations of molecular dynamics were performed using the Desmond molecular dynamics program as implemented in the Schrodinger Maestro (Academic version 2020-4).[171] To replicate the optimized reaction conditions, a system was considered with a 1:1:8 ratio of Triton B to benzylamine to methanol. This system comprised 20 cations ($PhCH_2N^+(CH_3)_3$), 20 benzylamine molecules, and 160 methanol molecules. Additionally, 20 O_2 molecules and 20 counter ions (OH^-) were included to neutralize the system. Thus one unit cell of the system contained a total of 240 residues. A cubic periodic boundary box was defined that converged to 27.19x27.19x27.19 $Å^3$. Another system was defined to mimic the 1:1:50 ratio of Triton B to benzylamine to methanol which contained a total of 228 molecules including 4 cations ($PhCH_2N^+(CH_3)_3$**)**, 4 benzylamine, and 200 methanol. It contained 4 counter ions (OH^-) to neutralize the system and 16 O_2 molecules to achieve similar oxygen concentration as the previous system. A cubic periodic boundary box was defined that converged to 25.42x25.42x25.42 $Å^3$. MD was run in OPLS (optimized potentials for liquid

simulations) force field.[172,173] Ensembles were defined as canonical (NVT) or isothermal-isobaric (NPT) with a constant number of atoms (N), a defined volume (V) or pressure (P) and a defined temperature (T). Four step relaxation protocol was used to equilibrate the system prior to the production run starting with Brownian dynamics for 100 ps with restraints on solute heavy atoms at NVT (with T = 10 K) followed by 12 ps of dynamics with restraints at NVT (T = 10 K) and then at NPT (T = 10 K; P = 1 bar) using Berendsen method. Then the temperature was raised to 300 K for 10 ns. The production MD was run at NPT with T = 300 K and P = 1 bar for 12 ns without restraints. The RESPA (reference system propagator algorithm) integrator was employed with time steps of 2 fs for near interactions, 2 fs for far interactions, and 6 fs for out interactions.[171,174,175] The Martyna-Tobias-Klein barostat method was used to apply isotropic pressure, with relaxation duration of 2 ps. The Nose-Hoover chain thermostat method was implemented with a relaxation time of 1 picosecond. The PME (particle mesh Ewald) approach was utilised to address the long-range coulombic interaction. For short-range coulombic interactions, the cutoff radius was 9 Å. Schrodinger Maestro timeline tools were used to analyze trajectories to derive the radial distribution of one type of atom with respect to another.

3.2.2 Quantum Chemical Computation Details:

Quantum chemical calculations were performed using the Gaussian 16 suite of programs. The popularity of B3LYP originates from the fact that it is well-validated for organic systems and performs pretty well for the prediction of several critical molecular and reaction parameters, such as geometries, bond energies, and barrier heights.[176] Application of the B3LYP functional in combination with the 6-31+G(d) basis set is currently the best compromise between cost and accuracy in organic chemistry.[177] Geometry optimizations and transition states were performed using the 6-31+G(d) basis set in conjunction

with the B3LYP method. In this contribution, all calculations have examined using experimental reaction conditions at 298 K, 1 atm. All geometries of minima and transition states were performed in the gas phase as well as solvent phase. For each transition-state, IRC calculations were performed in both directions to locate the nearest stationary points; the resulting structures were subjected to geometry optimization and frequency calculations. Unrestricted B3LYP methods were employed to find broken-symmetry solutions for the open-shell triplet, with Grimme's advanced dispersion-corrected approach (DFT-D3) chosen using the 6-31+G(d) basis set.[178]

The minimum energy crossing points (MECP) optimization was performed in ORCA 4.1.2, where it follows the principle suggested by Harvey et al.[179] In the optimization process, the geometry converges to a structure where two different potential energy surfaces (PES1 and PES2) cross each other. In order to verify that a stationary point in a MECP optimization is a minimum, numerical frequency calculations were performed using the "SurfCrossNumFreq" keyword.

Multiconfigurational self-consistent field (MCSCF) calculations have been carried out using DFT optimized structures. The active space (20,14) was considered for all complexes, resulting in 20 active electrons in 14 active orbitals (CAS(20,14)). cc-pVDZ basis sets[180,181] have been used in these calculations. The active space of (CAS(20,14)) includes the bonding π, antibonding π*, and nonbonding orbitals. Molpro 2010.1 version has been used to calculate multi-reference CASSCF(20,14) and CASPT2 calculations. DLPNO-CCSD(T) single point calculations were performed for the DFT optimized geometries using def2-TZVP basis set.[182,183] The first excited singlet molecular oxygen was considered, and the energetics were corrected using the approximate spin-projection (AP) method proposed by the Yamaguchi group.[184] ORCA 4.1.2[185] was used for the DFT, DLPNO-CCSD(T) and MECP

calculations. The solvent effects were considered via the CPCM solvation model[186–189] with methanol solvent medium. The corrected free energies were calculated using the methods described in the previous paper.[190] In this study, the effects of mixing of structures and symmetry numbers on entropy were not considered. Here, the following equation has been followed: $G_{50\%} = H_{harm} - T(0.5 * S_{harm,1atm} - Rln(24.5))$

3.3 Results and Discussion

3.3.1 Molecular Dynamics Results:

In this study, molecular dynamics (MD) analysis was performed to comprehend the environment of Triton B both under real and dilute conditions. Triton B contains 60% (w/w) methanol, which is approximately equivalent to 8 molecules of methanol per Triton B molecule. Molecular dynamics simulation was performed using an OPLS forcefield to gain insights into the microenvironment of the reaction mixture under real (1:1:1:8) and dilute (1:1:1:50) conditions.[191] At ambient temperature and pressure, the system was equilibrated. The radial distribution of N^+ and HO^- in the Triton B indicated atleast separation of 4Å to 6Å between the cation (benzyltrimethylammonium cation) and anion (hydroxide) (**Figure 23A**). The calculated radial distribution (as depicted in **Figure 23B and 23C**) of different molecules indicated that OH^- counter anion of Triton B is completely solvated by methanol molecules.[192]

In the reaction mixture, methanol molecules exhibit a greater propensity for making strong hydrogen bonding with the hydroxide ion compared to other ions or molecules. Upon the addition of benzylamine to Triton B, hydrogen bonds can be formed between benzylamine and methanol as well as the hydroxide ion. Furthermore, benzylamine has the capability to engage in cation-lone pair interactions with the benzyltrimethylammonium cation present within Triton B.

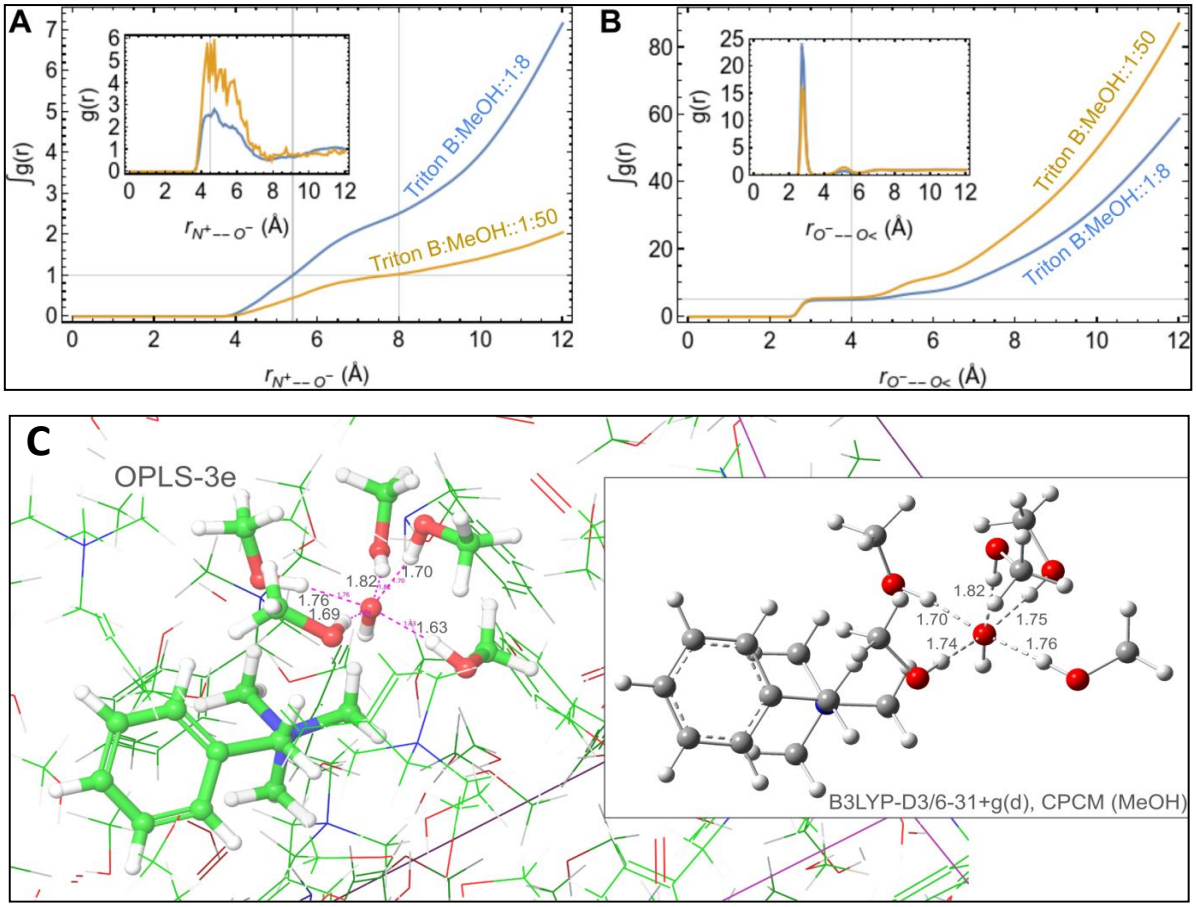

Figure 23. Radial distribution of OH^- with respect to N^+ and methanol around OH^- of reaction mixture under 1:1:1:8 and 1:1:1:50 condition **(A)** Distribution of OH^- around N^+ of reaction mixture. The inset line represents the radial distribution function g(r) of OH^- around N^+ of reaction mixture under 1:1:1:8 (Benzylamine: Triton B: Oxygen: MeOH) concentration as well as dilute (Benzylamine: Triton B: Oxygen: MeOH: 1:1:1:50) concentration. With dilution, separation between counter-ions increases. **(B)** Distribution of methanol around OH^- under 1:1:1:8 (Benzylamine: Triton B: Oxygen: MeOH) concentration, a real mimic microenvironment of reaction mixture as well as under a dilute concentration (Benzylamine: Triton B: Oxygen: MeOH: 1:1:1:50). The inset represents the radial distribution function, g(r). The integration of the first peak indicates the presence of five methanols in the first solvation sphere, which is similar to the hydration of the hydroxide ion as observed by Chen et al.[192,193] **(C)** Snapshot of MD simulation in OPLS-3e force field for reaction mixture, showing cation, anion (hydroxide) and five methanols in the first solvation sphere in ball-and-stick model. Inset shows the DFT optimized geometry of cation with solvated hydroxide anion.

In order to investigate all of these probable interactions, MD calculation was carried out using a ratio of 1:1:1:8 for Triton B, benzylamine, oxygen, and methanol. The radial distribution analysis of the amine group with methanol (depicted in **Figure 24C**) indicated that benzylamine formed strong hydrogen

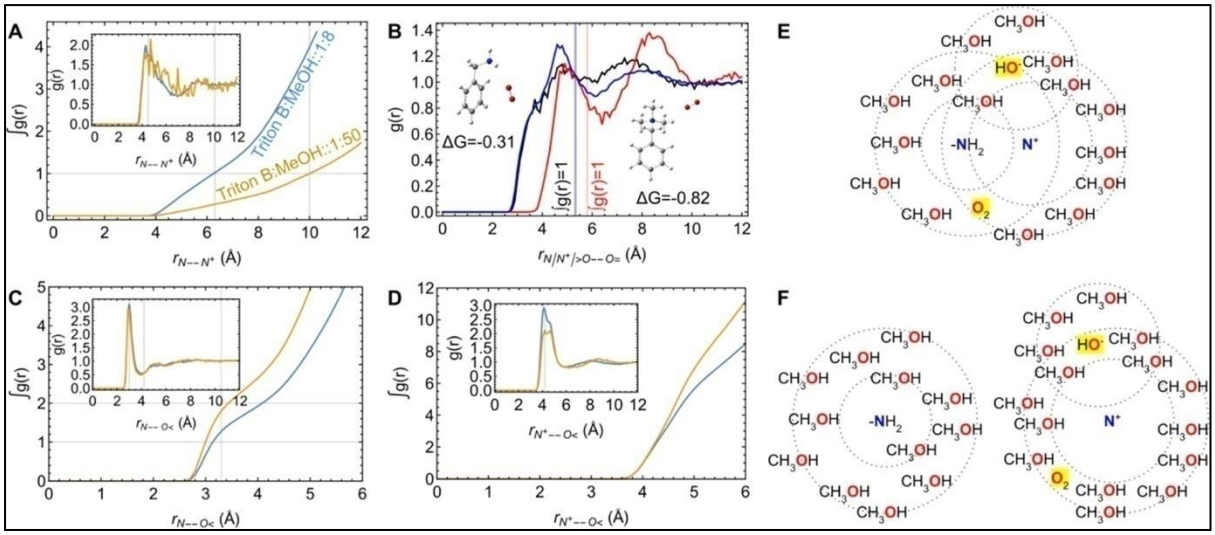

Figure 24. The microenvironment of the reactants as obtained from MD simulation. **(A)** Distribution of Triton B around benzylamine. **(B)** Distribution of oxygen with three different molecules present in the reaction mixture. The blue color indicates the interaction of benzylamine with oxygen, the gray color corresponds to methanol with oxygen, and the red color represents Triton B with oxygen under real mimic reaction conditions. **(C)** The interaction of NH_2 of benzylamine with methanol under (1:8 methanol) and (1:50 methanol). **(D)** The interaction of N^+ in Triton B with methanol under (1:8 methanol) and (1:50 methanol). (**E)** and (**F)** The schematic diagram of a mimic reaction condition (1:1:1:8 methanol) and under dilution or a high percentage of methanol (1:1:1:50 methanol).

bonds, with a distance of within 3Å, involved one methanol molecule. Analysis of the radial distribution curve revealed the integration of the first peak between N^+ and NH_2, indicated a 1:1 interaction between benzylamine and the benzyltrimethylammonium cation (as depicted in **Figure 24A**), characterized by an average distance of approximately 6.2 Å.

The interaction between benzylamine and methanol increases in diluted conditions, with a ratio of 1:1:1:50 of Triton B to benzylamine to oxygen and methanol, which mimics reaction mixture of Triton B 40% w/w methanol with an additional 2 ml of methanol (**Table 3, entry no 16**). As shown in **Figure 24C**, it was found that one more methanol molecule forms a hydrogen bond with the $-NH_2$ group of benzylamine. In the solvation sphere of the benzyltrimethylammonium cation, the number of methanol molecule also increases. This leads to a significant reduction in the interaction between the benzyltrimethylammonium cation and benzylamine **(Figures 24A and 24F)**. As a result, methanol molecules inhibit the formation of complexes between benzylamine, benzyltrimethylammonium cation, and oxygen, as well as subsequent reactions, as evidenced by the product yield **(Table 3, entries 13–16)**. Under diluted conditions, the radius required to find one molecule of benzyltrimethylammonium cation around benzylamine increases to 10 Å. Consequently, the reduced catalytic activity of Triton B in the presence of excessive methanol is suggested by MD simulation data, which supports the lower yield of oxidative products reported in the above oxidation reaction **(Table 3, entries 13–16)**.

The observation of methoxy group incorporation into the substrates (**1s**) (**Figure 15**) under specific experimental conditions suggests the presence of methoxide ions rather than hydroxide ions in Triton B.

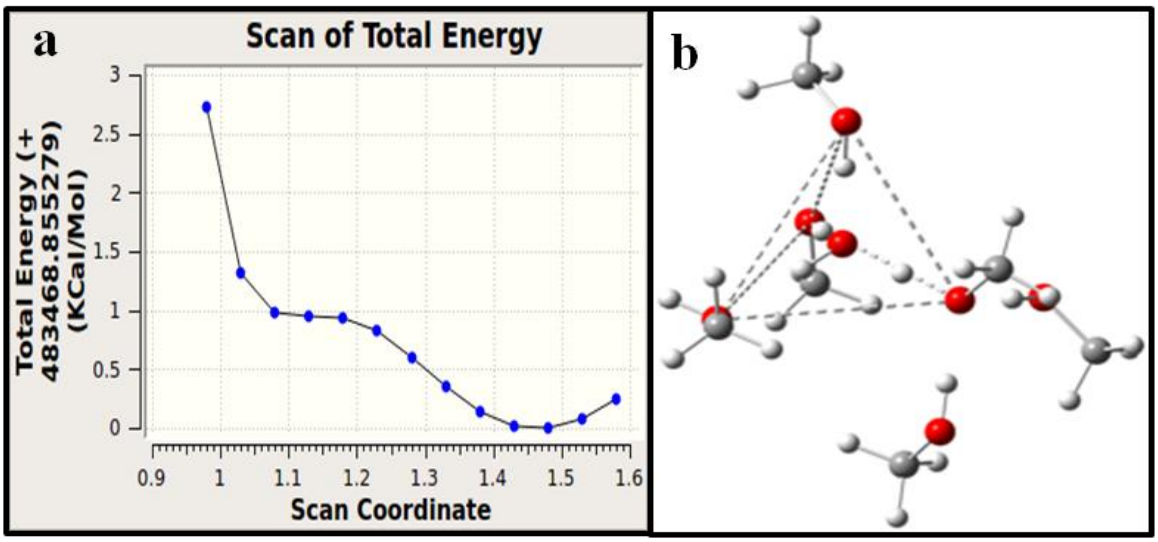

Figure 25. Solvation of the hydroxide ion in methanol. Four methanol molecules are observed in the first solvation sphere, including three hydrogen bond donors and one H bond acceptor, forming a tetrahedral geometry similar to the hydration of a hydroxide ion.[193] **(a)** Potential energy surface of hydrogen abstraction by OH^- from methanol obtained at DFT level. This PES indicates that the proton abstraction from the methanol solvent by hydroxide ions is almost barrierless process to generate methoxide ions in Triton B. The methoxide formation is strongly supported by the experimental evidence of methoxide ion substitution in 4-flurobenzylamine **(1s)** (see **Figure 15**). **(b)** The transition state geometry of proton transfer from methanol to hydroxide ions. The TS was confirmed by a frequency calculation, which shows one imaginary frequency toward the product.

When the hydroxide ion abstracts a proton from methanol, it produces the methoxide ion. Strong hydrogen bonds between methanol molecules and hydroxide ions are evidenced by MD simulations. To investigate the proton transfer pathway from a methanol of the first hydration sphere to the hydroxide ion, quantum chemical calculations were performed. Transition state calculations **(Figure 25)** revealed that proton transfer from methanol to hydroxide ions was completely barrierless, indicating the presence of methoxide ions in the reaction mixture under experimental conditions.

3.3.2 First Principle Calculations:

The control tests mentioned in the experimental section have revealed that the benzylimine intermediate acts as the primary precursor, yielding various products (including benzamide, (*E*)-N-benzyl-1-phenylmethanimine, and benzaldehyde), which depend on the specific experimental conditions employed (**Figure 18)**. Similar to the formation of benzaldehyde (**6a**) from benzyl alcohol, benzylimine (**1ac**) can be formed as a transient intermediate from benzylamine. Both oxygen and organic cations (quaternary alkylammonium cation) play significant roles in influencing the formation of oxidative products. The reaction stopped completely under an inert atmosphere, indicating its dependence on molecular oxygen for oxidation. Furthermore, the partial inhibition of the reaction by a radical scavenger (Tempo) suggests radical-mediated processes, such as hydrogen atom transfer. It is anticipated that hydrogen atom abstraction from benzylic CH_2 and geminal NH_2 will result in the production of oxidized product (benzylimine). However, the question remains whether the first hydrogen atom abstraction will take place from the benzylic CH_2 or the geminal NH_2. The potential energy profiles of benzylic C-H bond distance perturbation and N-H bond distance perturbation at the DFT level were calculated with a step size of 0.01 Å and 20 steps, with geometry optimization performed at each step using the "opt=modredundant" keyword. The computed bond dissociation energy (BDE) of α(C-H) was found to be 16 kcal/mol lower than that of N-H BDEs **(Figure 26)**, while DFT calculations also demonstrated that benzylic radical species were thermodynamically more stable, with a difference of 19.14 kcal/mol compared to amine radical species **(Figure 27)**. These findings strongly suggest that the initial hydrogen atom abstraction is likely to occur from the benzylic C-H_2 position.

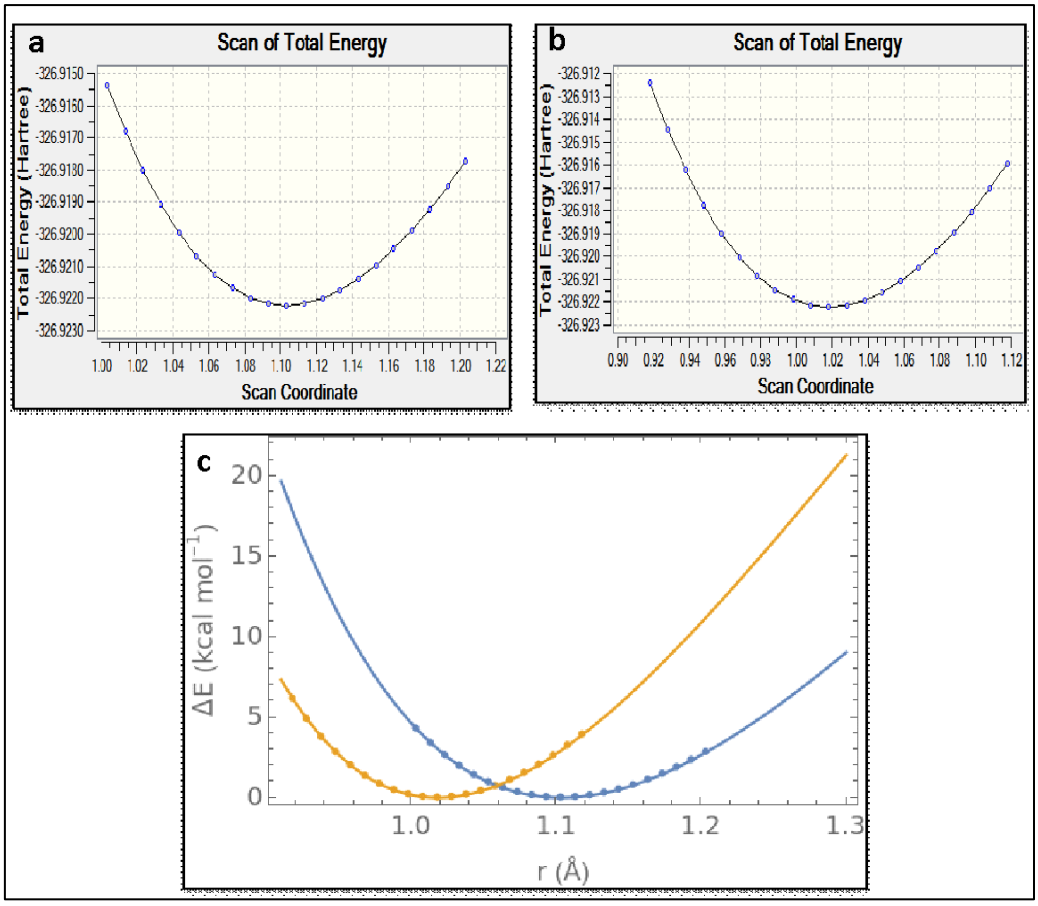

Figure 26. Bond dissociation energy of C-H vs N-H of benzylamine at DFT level. **(a)** Potential energy profile of benzylic C-H bond distance perturbation at DFT level. Step size 0.01 Å, number of steps 20 and the geometry was optimized at each step (with keyword opt=modredundant). **(b)** Potential energy profile of N-H bond distance perturbation at DFT level. **(c)** Bond dissociation energy (BDE) calculation using the equation: $E(r) = D_0(1-Exp[-\alpha(r-r_e)])^2$ where D_0 is the bond dissociation energy, α is the well depth, r is the intermolecular distance and r_e is the equilibrium bond distance. The blue line presents relative potential energy of benzylic C-H bond and the yellow line is that of N-H bond. BDE of benzylic C-H is 79.82 kcal/mol whereas BDE of N-H is 96.25 kcal/mol indicating that the first hydrogen abstraction is more feasible from benzylic position than the amine.

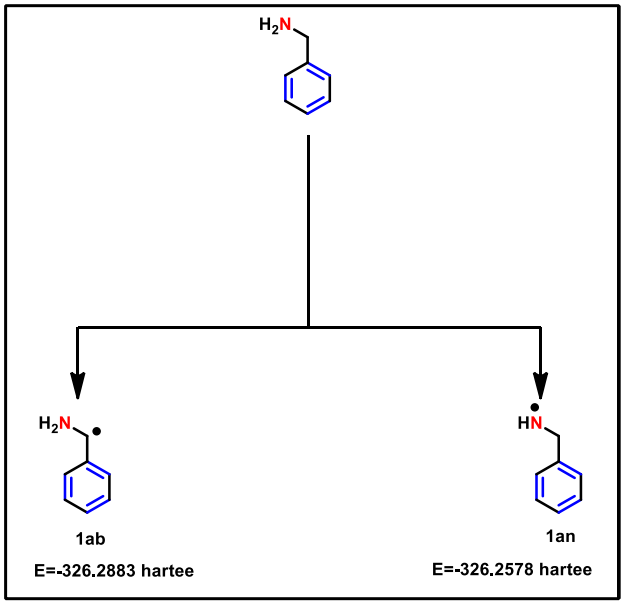

Figure 27. Thermodynamics stability calculation by DFT. The calculations were carried out using B3lyp/6-31+G(d) in the gas phase. The energy difference between two structures is -19.14kcal/mol.

3.3.2.1 Free Energy Profile of Benzylamine Oxidation in the Presence of Oxygen:

In order to explore the reaction mechanism, calculate electronic and free energies, and understand the effect of Triton B on oxygen activation, it was essential to examine the electronic structures of benzylamine and oxygen using DFT-based methods. The electronic energy and free energy profiles depicting the formation of benzylimine from benzylamine oxidation by molecular oxygen are presented in **Figures 28a-28c**, along with corresponding energy values listed in **Tables 5**. In the gas phase, it was observed that triplet O_2 does not form a stable pre-reaction complex (**Int-1T**) with benzylamine **1a**. The activation free energy barrier for H atom abstraction by triplet O_2 was determined to be 26.5 kcal/mol (B3LYP-D3), in comparison to the intermediate (**Int-1T**). Similarly, literature reports indicate various activation energy values for hydrogen atom abstraction by triplet oxygen from other compounds, such as $CH_3C\mathbf{H}_2COOCH_3$

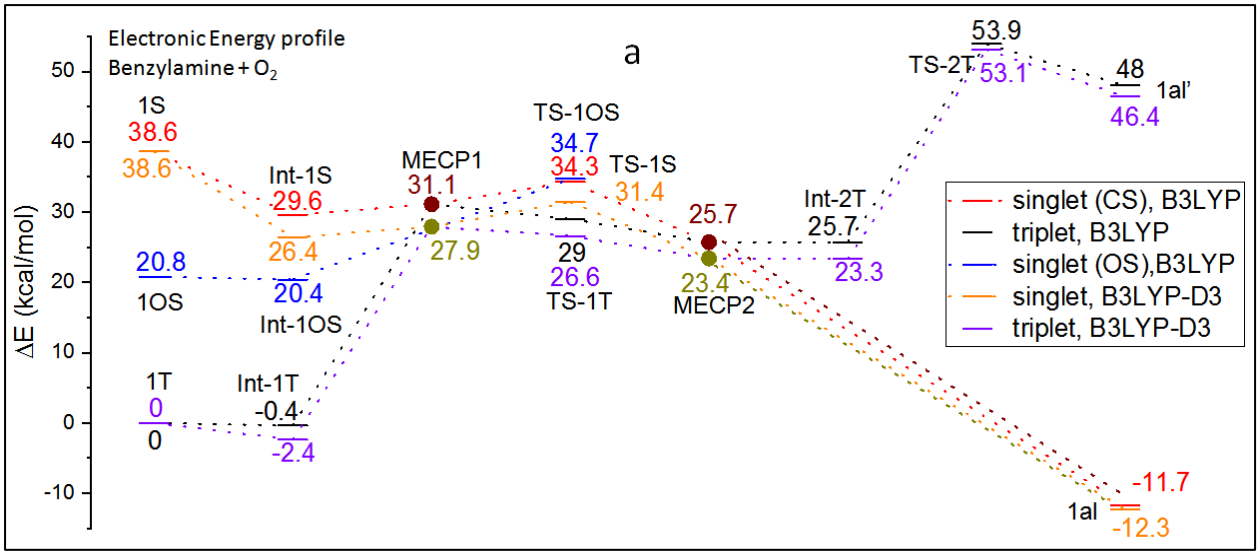
a
Electronic Energy profile
Benzylamine + O_2
ΔE (kcal/mol)
1S
38.6
38.6
Int-1S
29.6
26.4
MECP1
31.1
27.9
TS-1OS
34.7
34.3
TS-1S
31.4
29
26.6
TS-1T
25.7
23.4
MECP2
Int-2T
25.7
23.3
TS-2T
53.9
53.1
48
46.4
1al'
20.8
1OS
20.4
Int-1OS
1T
0
0
Int-1T
-0.4
-2.4
-11.7
-12.3
1al
singlet (CS), B3LYP
triplet, B3LYP
singlet (OS),B3LYP
singlet, B3LYP-D3
triplet, B3LYP-D3

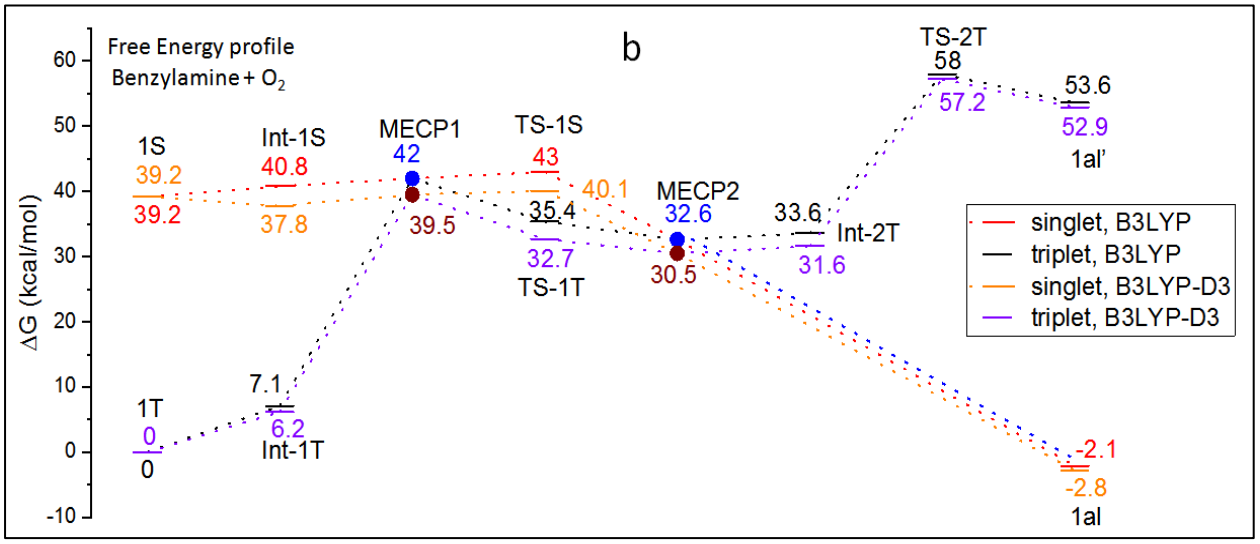
b
Free Energy profile
Benzylamine + O_2
ΔG (kcal/mol)
1S
39.2
39.2
Int-1S
40.8
37.8
MECP1
42
39.5
TS-1S
43
40.1
35.4
32.7
TS-1T
MECP2
32.6
30.5
33.6
Int-2T
31.6
TS-2T
58
57.2
53.6
52.9
1al'
7.1
1T
0
0
6.2
Int-1T
-2.1
-2.8
1al
singlet, B3LYP
triplet, B3LYP
singlet, B3LYP-D3
triplet, B3LYP-D3

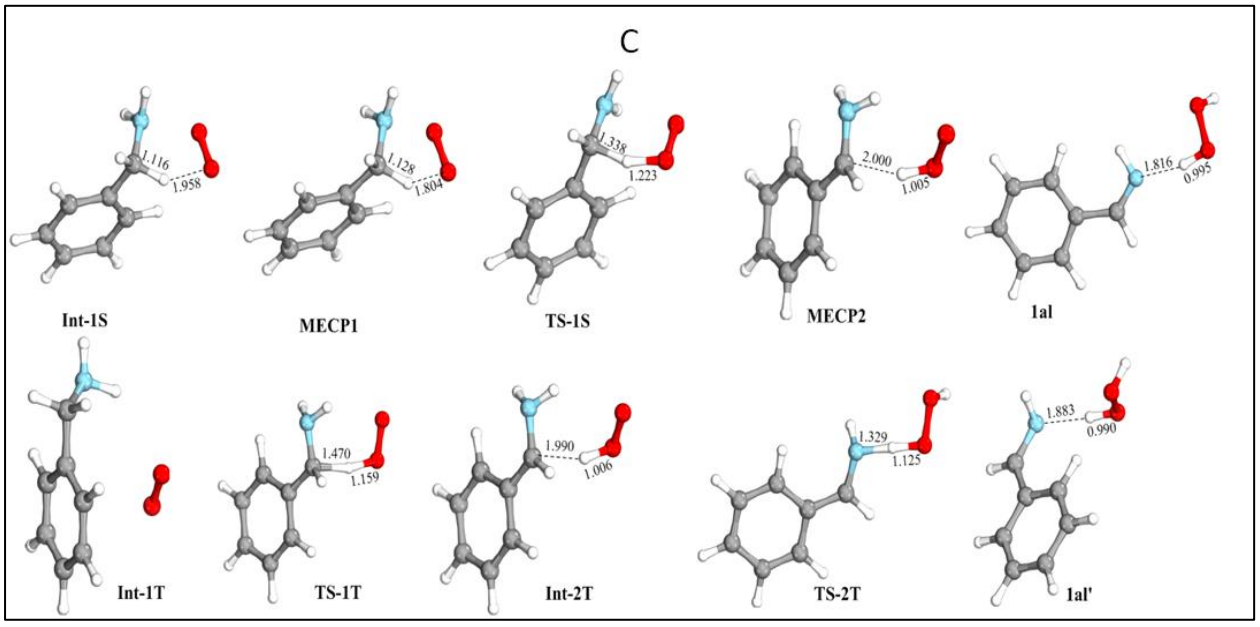
c
Int-1S
MECP1
TS-1S
MECP2
1al
Int-1T
TS-1T
Int-2T
TS-2T
1al'

Figure 28. DFT calculations. (**a)** Potential energy diagram and **(b)** Free energy diagram obtained using the B3LYP/6-31+G(d) method for the formation of **1aI** from benzylamine and oxygen in the gas phase mimicking control 9 in **Figure 18 (c)** The optimized geometries of various intermediates and transition states for the formation of **1aI** and **1aI'** from benzylamine with oxygen in the gas phase. All the distances are in Å [C: grey, N: cyan, H: hydrogen., O: red].

Table 5. Calculated energy and free energies value (in Hartrees) of intermediates and transition states in the gas phase using the B3lyp/6-31+G(d) level of theory for uncatalyzed system (Benzylamine + O_2). Dispersion-corrected values are given in parenthesis.

Structure	Electronic Energy	Free Energy
Oxygen (triplet)	-150.32559 (-150.32559)	-150.34183 (-150.34183)
Oxygen (Singlet)	-150.26412 (-150.26412)	-150.27934 (-150.27934)
Oxygen (open-shell Singlet) corrected	-150.292478	NA
Benzylamine	-326.916414 (-326.92657)	-326.80145 (-326.81150)
1S (Benzylamine + singlet O_2)	-477.180529 (-477.19069)	-477.08078 (-477.09084)
1T (Benzylamine + triplet O_2)	-477.242004 (-477.25216)	-477.14327 (-477.15332)
Int-1S (pre-complex)	-477.194841(-477.21013)	-477.0783 (-477.09302)
Int-1T(pre-complex)	-477.242593 (-477.25603)	-477.13201 (-477.14340)
MECP-1	-477.192491 (-477.20770)	-477.07635 (-477.09043)
1OS (corrected)	-477.208891	NA
Int-1OS (corrected)	-477.209547	NA
TS-1S	-477.187339 (-477.20217)	-477.07482 (-477.08937)
TS-1T	-477.195784 (-477.20983)	-477.08679 (-477.10126)
TS-1OS (corrected)	-477.186775	NA
MECP-2	-477.201034 (-477.21494)	-477.09132 (-477.10468)
Int-2T	-477.201127 (-477.21498)	-477.08969 (-477.10299)
TS-2T	-477.156075 (-477.16757)	-477.05085 (-477.06225)
1aI	-477.260574 (-477.27181)	-477.14659 (-477.15771)
1aI'	-477.165596 (-477.17825)	-477.05791 (-477.06908)

(44.2 kcal/mol)[194], SiH_4 (38.8 kcal/mol)[16], $C_{14}H_9O$**H** (9-anthrol**)** (28.9 kcal/mol)[195], C_2H_6NO**H** (dimethylhydroxylamine) (26.5 kcal/mol)[195].

The reactions between benzylamine and triplet oxygen to form benzylimine and hydrogen peroxide do not appear to occur spontaneously due to the very low Gibbs free energy of the reaction (-2.8 kcal/mol, B3LYP-D3). Furthermore, the reactions exhibit kinetic inertness due to the high activation energy required for triplet O_2 to extract a hydrogen atom from benzylamine, which corresponds to 26.5 kcal/mol of (B3LYP-D3) free energy. The low free energy difference indicates that this molecule remains "kinetically stable" in earth atmosphere and will persist for a long time under ambient conditions.

Under the specified experimental conditions (70°C, 4 hours) in **control 9**, benzylamine alone in the presence of oxygen fails to produce any oxidized product. This experimental finding further corroborates the DFT data for the uncatalyzed reaction pathway.

3.3.2.2 Free Energy Profile of Benzylamine Oxidation in Presence of Benzyltrimethylammonium Cation:

Electronic energy and free energy profiles for both triplet and singlet reaction pathways have been calculated **(Figures 29a-29c)** to elucidate how oxygen interacts with the benzyltrimethylammonium cation, with corresponding energy values listed in **Tables 6**. The apparent activation-free energy for hydrogen atom abstraction from the benzylic position by triplet O_2 was determined to be 27.4 kcal/mol in the presence of benzyltrimethylammonium cation **(Figure 29b)** using (B3LYP-D3). Interestingly, the activation-free energy of benzylamine oxidation remains nearly identical with and without the benzyltrimethylammonium cation. This prompts further examination into the nature of the relationship between the benzyltrimethylammonium cation and oxygen, questioning its energetic stability.

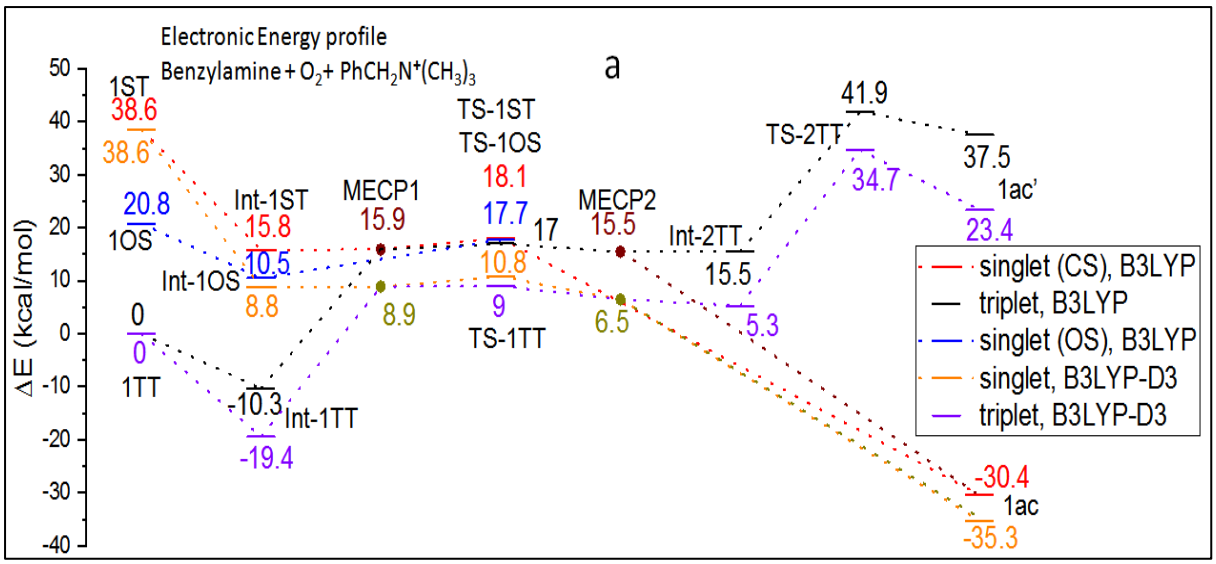
Electronic Energy profile
Benzylamine + O_2 + $PhCH_2N^+(CH_3)_3$
a
ΔE (kcal/mol)
1ST
38.6
38.6'
20.8
1OS
0
0'
1TT
Int-1ST
15.8
10.5
Int-1OS
8.8
-10.3
Int-1TT
-19.4
MECP1
15.9
8.9
TS-1ST
TS-1OS
18.1
17.7
17
10.8
9
TS-1TT
MECP2
15.5
6.5
Int-2TT
15.5
5.3
TS-2TT
41.9
34.7
37.5
1ac'
23.4
-30.4
1ac
-35.3
singlet (CS), B3LYP
triplet, B3LYP
singlet (OS), B3LYP
singlet, B3LYP-D3
triplet, B3LYP-D3

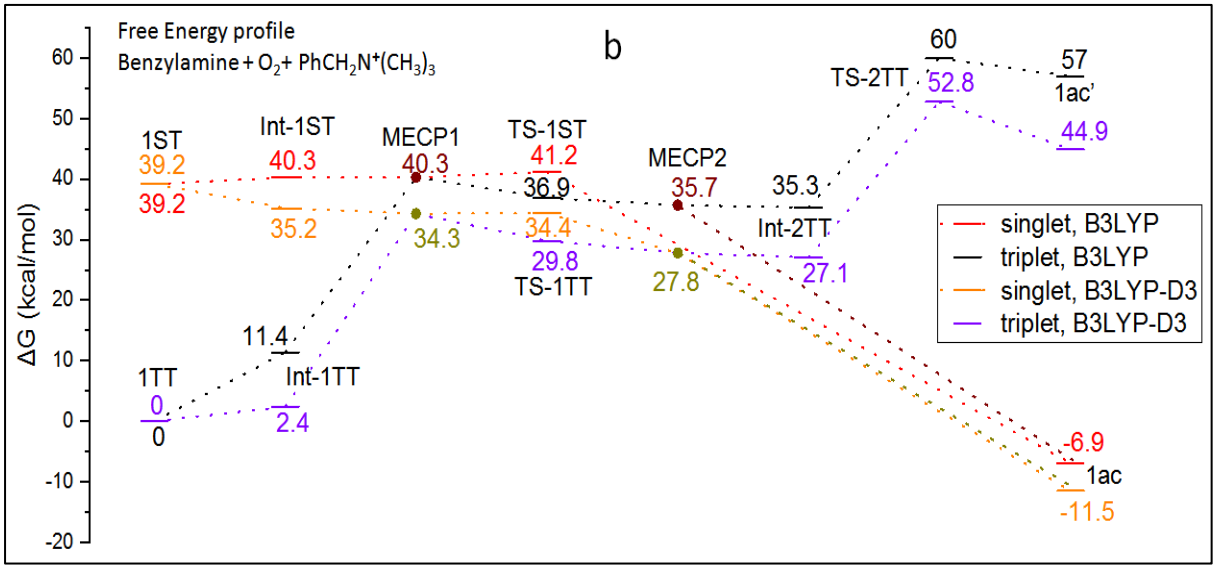
Free Energy profile
Benzylamine + O_2 + $PhCH_2N^+(CH_3)_3$
b
ΔG (kcal/mol)
1ST
39.2
39.2
Int-1ST
40.3
35.2
MECP1
40.3
34.3
TS-1ST
41.2
36.9
34.4
29.8
TS-1TT
MECP2
35.7
27.8
35.3
Int-2TT
27.1
TS-2TT
60
52.8
57
1ac'
44.9
11.4
1TT
0
0
Int-1TT
2.4
-6.9
1ac
-11.5
singlet, B3LYP
triplet, B3LYP
singlet, B3LYP-D3
triplet, B3LYP-D3

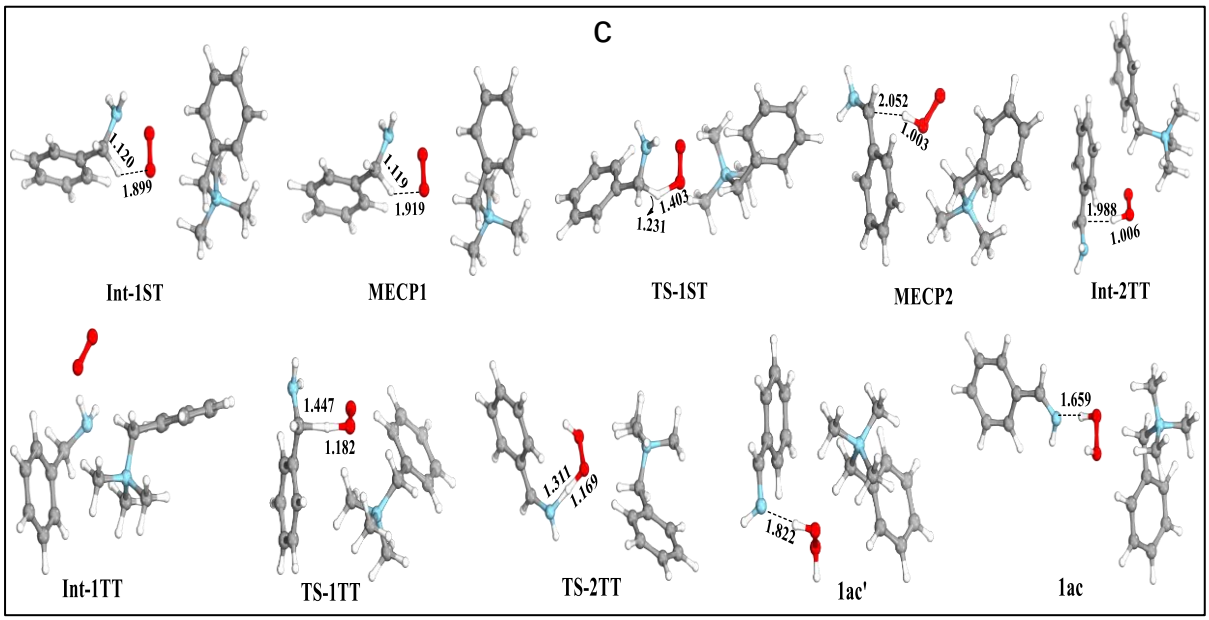
c
1.120
1.899
Int-1ST
1.119
1.919
MECP1
1.403
1.231
TS-1ST
2.052
1.003
MECP2
1.988
1.006
Int-2TT
Int-1TT
1.447
1.182
TS-1TT
1.311
1.169
TS-2TT
1.822
1ac'
1.659
1ac

Figure 29.(a) Potential energy surface to find the quaternaryammonium cation ($PhCH_2N^+(CH_3)_3$) role using B3LYP/6-31+G(d) method for the formation of **1ac** from benzylamine and $PhCH_2N^+(CH_3)_3$ with oxygen in the gas phase. **(b)** Free energy profile to find the quaternaryammonium cation role using B3LYP/6-31+G(d) method for the formation of **1ac** from benzylamine and $PhCH_2N^+(CH_3)_3$ with oxygen in the gas phase. **(c)** The optimized geometries of various intermediates and transition states for the formation of **1ac and 1ac'** from benzylamine with oxygen in the gas phase. All the distances are in Å [C: grey, N: cyan, H: hydrogen., O: red]

Table 6. Calculated energy and free energies value (in Hartrees) of intermediates and transition states in the gas phase using the B3lyp/6-31+G(d) level of theory for catalyzed system (benzylamine + O_2 + $PhCH_2N^+(CH_3)_3$). Dispersion-corrected values are given in parenthesis.

Structure	Electronic Energy	Free Energy
Triton B (cation)	-445.222921 (-445.24840)	-445.01204 (-445.03663)
1ST	-922.403449 (-922.43908)	-922.09282 (-922.12746)
1TT	-922.464925 (-922.50056)	-922.15531 (-922.18995)
1OS (corrected)	-922.431812	NA
Int-1ST (pre-complex)	-922.439809 (-922.48648)	-922.09112 (-922.13387)
Int-1TT(pre-complex)	-922.48133 (-922.53145)	-922.13721 (-922.18605)
Int-1OS (corrected)	-922.448226	NA
MECP-1	-922.439659 (-922.48635)	-922.09112 (-922.13534)
TS-1ST	-922.436167 (-922.48334)	-922.08965 (-922.13514)
TS-1TT	-922.437868 (-922.48626)	-922.09658 (-922.14252)
TS-1OS (corrected)	-922.436726	NA
MECP-2	-922.440273 (-922.49020)	-922.09846 (-922.14559)
Int-2TT	-922.440154 (-922.49216)	-922.09914 (-922.14683)
TS-2TT	-922.398208 (-922.44520)	-922.05975 (-922.10579)
1ac	-922.51341 (-922.55684)	-922.16622 (-922.20828)
1ac'	-922.4051 (-922.46334)	-922.0645 (-922.11844)

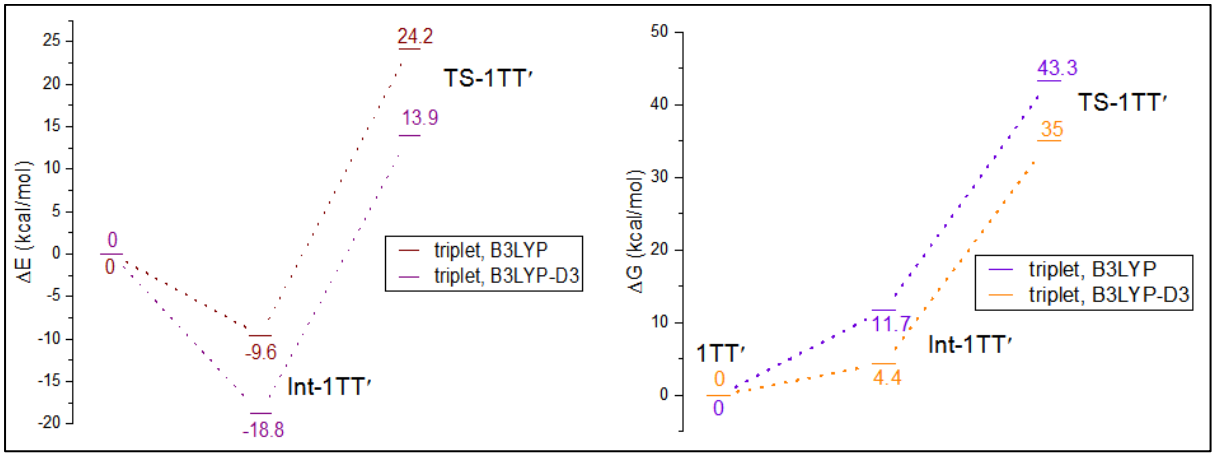

Figure 30. The electronic energy and free energy profile diagram with cation computed at B3LYP/6-31+G(d) in gas phase.

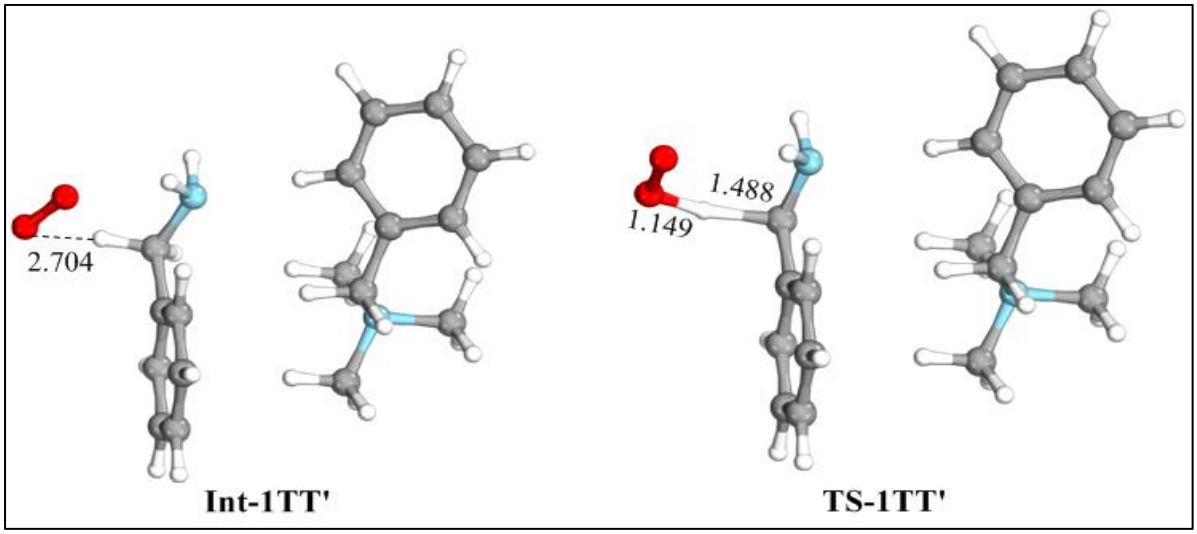

Figure 31. The optimized geometries of intermediate and transition state, where cation ($PhCH_2N^+(CH_3)_3$) interacts with benzylamine rather than oxygen in the gas phase. All the distances are in Å [C: grey, N: cyan, H: hydrogen., O: red].

An alternative conformation of the transition state (**TS-1TT'**) was examined as depicted in **Figure 30 and 31**, to validate the role of benzyltrimethylammonium cation with oxygen. In this configuration, the benzyltrimethylammonium cation does not interact with oxygen but instead interacts with the benzylamine (as

shown in **Figure 31**). Interestingly, this TS configuration exhibits a higher free energy 3.2 kcal/mol or 4.3 kcal/mol (**B3LYP-D3**) electronic energy compared to the **TS-1TT** (as shown in **Figure 30 and 31)**. This study provides compelling evidence that oxygen was activated by the benzyltrimethylammonium cation, which stabilized the transition state more than any other conformation.

Table 7. The calculated distortion (E_{dist}) and interaction (E_{int}) energies (kcal/mol) for C-H hydrogen transfer transition states (TS-1TT and TS-1ST, Figure 29a), obtained with respect to the respective isolated reactants.

	E_{dist}	E_{int}
TS-1ST	23.4	-12.6
TS-1TT	34.6	-25.7
TS-1S	31.9	-0.5
TS-1T	34.4	-7.8

For further insights, a distortion/interaction-activation strain analysis was employed to compare the influence of the benzyltrimethylammonium cation on the transition state. This analysis divides the activation energy, $\Delta E^{\ddagger}$, into two components: $\Delta E_{dist}^{\ddagger}$, which represents the energy required to distort the reactants to their transition state geometries without any interactions, and $\Delta E_{int}^{\ddagger}$, which represents the interaction energy between the distorted reactants **(Table 7)**.[196] The $\Delta E_{int}^{\ddagger}$ term encompasses exchange-repulsive and stabilizing electrostatic, polarization, and orbital effects in the transition state geometries. The sum of $\Delta E_{dist}^{\ddagger}$ and $\Delta E_{int}^{\ddagger}$ gives the total activation energy, $\Delta E^{\ddagger}$. The findings reveal nearly identical distortion energies of **TS-1T** and **TS-1TT** (34.4 kcal/mol

vs. 34.6 kcal/mol for the transition state). However, a stronger interaction energy, $\Delta E_{int}^{\ddagger}$, for **TS-1TT** (-25.7 kcal/mol) compared to **TS-1T** (-7.8 kcal/mol) accounts for the reduction of the activation energy barrier for benzyltrimethylammonium cation.

The oxidation of benzylamine in the presence of a benzyltrimethylammonium cation, leading to the formation of benzylimine and hydrogen peroxide, is exothermic by -11.5 kcal/mol (B3LYP-D3), refers to it as a kinetically labile process compared to uncatalyzed reactions. However, the energy barrier for hydrogen atom abstraction by triplet O_2 from benzylamine in the presence of a benzyltrimethylammonium cation is calculated to be approximately 27.4 kcal/mol (B3LYP-D3). The activation free energy of the forward reaction is 27.4 kcal/mol, significantly lower than the activation free energy of the backward reaction, estimated at 41.3 kcal/mol.

Hence, the sole use of benzyltrimethylammonium cation in vacuum calculations might not adequately portray the catalyst's influence on the free energy profile, as the presence of other molecules and their respective free energy values could significantly impact the reaction progression. It is important to note that the benzyltrimethylammonium cation remains dissolved in approximately 60% (w/w) methanol. Initially, the influence of both the counter anion and the methanol solvent was ignored during calculations. To ensure accurate free energy values from DFT studies, it is recommended to account for as many relevant factors as possible to closely replicate experimental conditions. As a result, the computational study was expanded to a more realistic model, incorporating a solvated anion alongwith a benzyltrimethylammonium cation, and an implicit solvation model with methanol as the solvent **(Figure 32a-32c)**.

3.3.2.3 Free energy profile of benzyltrimethylammonium cation with solvated anaions:

The free energy profile has been calculated with the inclusion of a methanol-solvated anion with benzyltrimethylammonium cation **(Figure 32b)** to get better free energy values for transition states, intermediates, and products, with

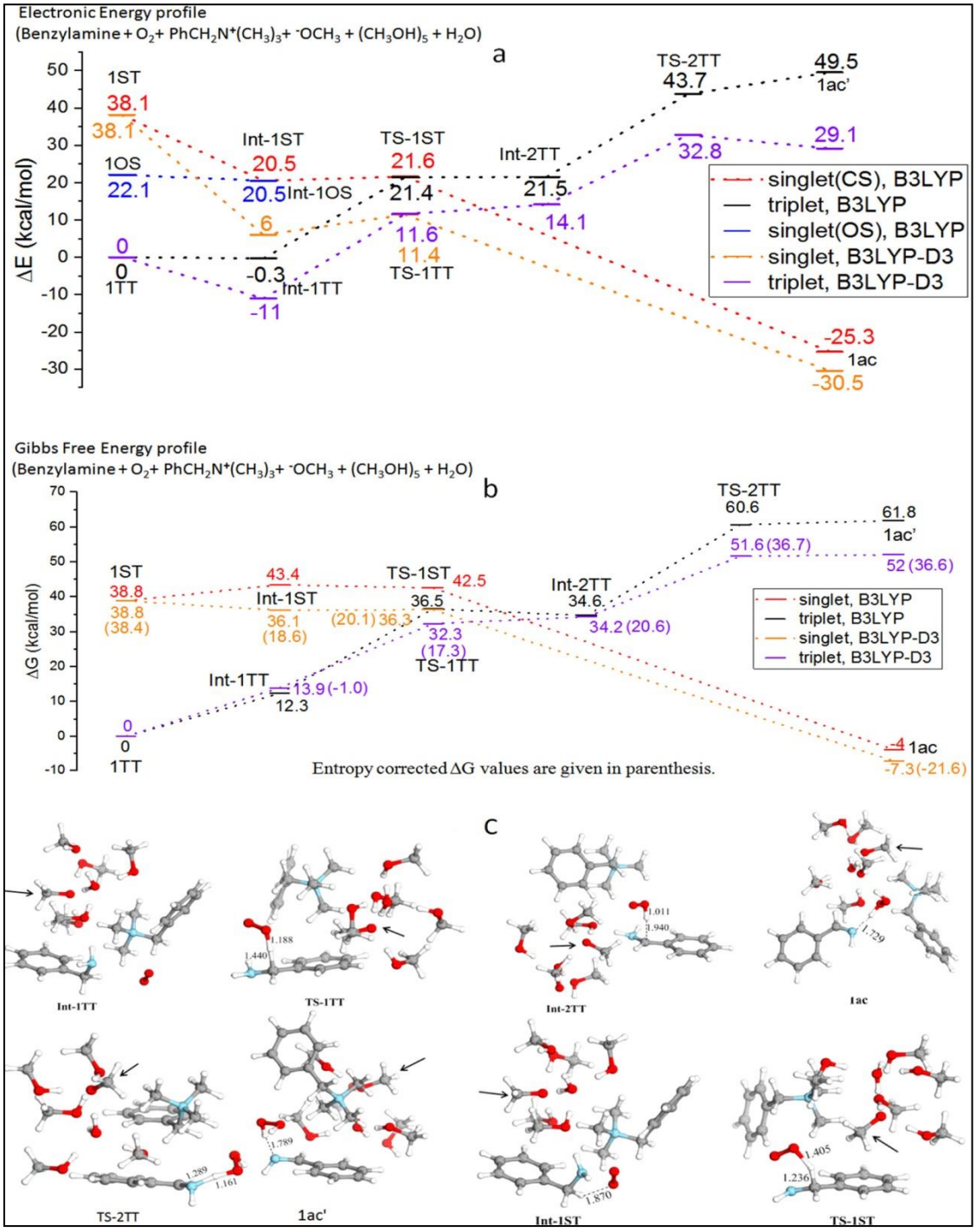

Figure 32. (a) Potential energy diagram and **(b)** Free energy diagram using the B3LYP/6-31+G(d) method for the formation of **1ac** or **1ac'** from benzylamine and benzyltrimethyl ammonium cation with solvated anion in the implicit solvent (methanol) model mimicking the experimental condition. **(c)** The optimized geometries of various intermediates and transition states for the formation of **1ac** and **1ac'** from benzylamine with oxygen. All the distances are in Å [C: grey, N: cyan, H: white, O: red]. Electronic energy and free energy are given in kcal/mol. Black arrow represents the presence of methoxy ion.

corresponding energy values listed in **Table 8**. The activation free energy for hydrogen atom abstraction from the benzylic position by triplet O_2 was observed to decrease from 27.4 kcal/mol (B3LYP-D3) **(Figure 29b)** to 18.4 kcal/mol (B3LYP-D3) **(Figure 32b)** upon the incorporation of a methanol-solvated anion with a benzyltrimethylammonium cation. It is worth mentioning that adding solvation to the free energy profile sufficiently lowered the free energy value by 9 kcal/mol (B3LYP-D3) **(Figure 28b)**. Furthermore, considering an experimental mimic environment in the free energy profile **(Figure 32b)** revealed that the free energy activation barrier is 8.1 kcal/mol (B3LYP-D3) lower than that of the uncatalyzed process **(Figure 28b)**. It could be argued that integrating dispersion corrections might mitigate errors and potentially enhance the accuracy of B3LYP energies.[197–199] From a thermodynamic perspective, under optimized experimental conditions, the process may exhibit kinetic spontaneity because the activation free energy of H atom abstraction is 18.4 kcal/mol (B3LYP-D3), whereas the thermodynamic stability of the products (benzylimine and H_2O_2) is -7.3 kcal/mol (B3LYP-D3). A notable energy difference has been observed between the dispersion-corrected electronic energy (-30.5 kcal/mol) and the Gibbs free energy (-7.3 kcal/mol) of the product, **1ac (Figures 32a and 32b)**. The incorporation of thermal free energy correction significantly impacts product stability (from -30.5 kcal/mol to -7.3 kcal/mol), indicating that the inclusion of entropy terms in the free energy

profile may be crucial, particularly when reactions involve a more random gaseous substance, such as triplet oxygen.

3.3.2.4 Entropy Contribution in the Free Energy Profile:

It's important to note that calculating entropy in a solution poses a challenge when using quantum chemical methods.[200–203] This complexity makes it difficult to accurately determine or factor in entropy through quantum-chemical calculations. Implicit solvation models, which treat solvents as homogeneous and isotropic media, struggle to capture molecular solute-solvent interactions and solvent-specific effects, potentially resulting in inaccuracies when replicating the real experimental environment through quantum-chemical analysis.

Table 8. Calculated energy and free energies value (in Hartrees) of intermediates and transition states in the solvent phase (MeOH) using the B3lyp/6-31+G(d) level of theory for catalyzed system (benzylamine + O_2 + Triton B). Dispersion-corrected values are given in parenthesis.

Structure	Electronic Energy	Free Energy
Triton B (cation) with solvated anion	-1215.70775 (-1215.77708)	-1215.223489 (-1215.27802)
1ST	-1692.903399 (-1692.98289)	-1692.320451 (-1692.38480)
1TT	-1692.964143 (-1693.04364)	-1692.382208 (-1692.44655)
1OS (corrected)	-1692.928923	NA
Int-1ST	-1692.931476 (-1693.03415)	-1692.313096 (-1692.38903)
Int-1TT	-1692.964638 (-1693.06121)	-1692.36267 (-1692.42445)
Int-1OS (corrected)	-1692.931515	NA
TS-1ST	-1692.92976 (-1693.02543)	-1692.314402 (-1692.38863)
TS-1TT	-1692.930073 (-1693.02508)	-1692.324039 (-1692.39509)
Int-2TT	-1692.929899 (-1693.02114)	-1692.327084 (-1692.39210)
TS-2TT	-1692.894434 (-1692.991407)	-1692.285651 (-1692.36426)
1ac	-1693.0044 (-1693.092232)	-1692.388527 (-1692.45812)
1ac'	-1692.885224 (-1692.99725)	-1692.283652 (-1692.36375)

There are numerous documented methods for calculating changes in solution entropy using quantum-chemical calculation.[197,204–207] The revised free energy was computed by halving the original entropy. Incorporating the entropy correction, the activation free energy (dispersion and entropy corrected) barrier in the presence of the Triton B molecule is 18.3 kcal/mol, while the formation of products is stabilized by -21.6 kcal/mol **(Figure 32b)**. Considering the thermodynamic aspect of free energy profile **(Figure 32)**, it is now evident that, under optimized experimental conditions, Triton B-mediated benzylamine oxidation via activated oxygen is both kinetically labile and highly spontaneous.

3.3.2.5 Minimum Energy Crossing Point (MECP):

A spin-flipping process is expected to occur because the reaction begins with triplet oxygen but yields singlet products. To pinpoint the location on the potential energy surface (PES) where spin flipping takes place, the Minimum Energy Crossing Point (MECP) was computed, representing the minimum energy point where the PESs of two different spin states intersect, causing the transition from triplet to singlet PESs **(Figure 29)**.[208] The hydrogen atom abstraction initiates from the stable triplet intermediate (**Int-1TT**); however, the

Table 9. The calculated bond distances and Mayer bond order of various intermediates, transition states and MECPs.

	Distance (Å)			Bond order
	O...H(C)	**C-H**	**N...O**	**O-O**
Int-1ST	1.899	1.120	1.967	1.567
Int-1TT	4.633	1.100	3.462	2.234
MECP1	1.919	1.119	1.989	1.760
TS-1ST	1.403	1.231	2.158	1.393
TS-1TT	1.182	1.447	3.085	1.628
MECP2	1.003	2.052	3.568	1.390
Int-2TT	1.006	1.988	3.460	1.592
1ac				0.915

formation of triplet products from the triplet intermediate is hindered by the high free energy of the triplet final products. Hence, a spin transition in this free energy profile diagram is also expected.[209] Consequently, two Minimum Energy Crossing Points (MECPs) were identified **(Figure 29a)**: the first MECP was positioned before the transition state at 34.3 kcal/mol, only 4.5 kcal/mol above the high-spin transition state (**TS-1TT**). The calculated geometrical data indicates that the O---H distance in MECP1 is 1.919 Å, which decreases in **TS-1ST** (1.403 Å) or **TS-1TT** (1.182 Å) **(Table 9 and Figure 29c)**. The energy profile (electronic energy and free energy) **(Figures 29a and 29b)** also suggests that due to its low energy activation barrier, benzylamine oxidation by triplet oxygen with benzyltrimethylammonium cation would favor the H atom abstraction pathway (**TS-1TT**) over MECP1. If the spin-flip does not occur at MECP1, the reaction will proceed with a more favorable triplet **TS-1TT** and will go forward directly to form singlet products through MECP2 without any activation barrier.

Due to the involvement of spin crossing between singlet and triplet states in the potential energy surface for benzylimine and hydrogen peroxide formation, a multireference configuration may offer a better explanation of the electronic states of the geometries. Hence, complete active space self-consistent field (CASSCF) calculations were conducted with a (20,14) active space, followed by second-order multi-reference perturbation theory based on CASSCF (20,14)/CASPT2 calculations on the DFT optimized geometries. These calculations considered 20 active electrons in 14 active orbitals, and the obtained results exhibited a similar trend **(Table 10)**.

Additionally, domain-based Local Pair Natural Orbital-CCSD(T) (DLPNO-CCSD(T)) calculations for the DFT-optimized geometries were employed, which yielded a similar energy profile diagram **(Figure 33)**. The performance of

DLPNO-CCSD(T) in the spin crossing reaction showed acceptable agreement with the CASPT2 calculations.

Table 10. The relative energies calculated at CASPT2 (20,14) with the cc-pVDZ basis set.

	CASPT2 (20,14)
Int-1ST	40.2
Int-1TT	0.0
Int-2TT	35.0
1ac	-6.8
1ac′	50.9

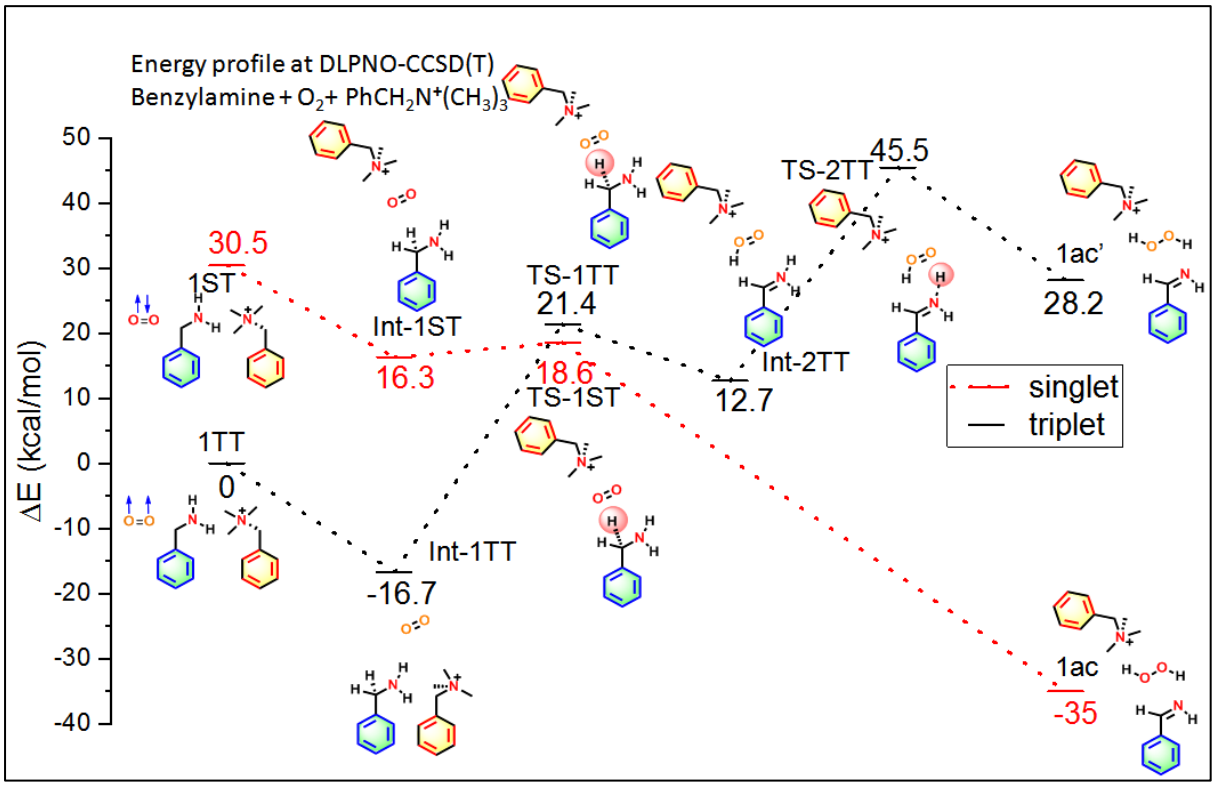

Figure 33. Potential energy surface was calculated to find the $PhCH_2N^+(CH_3)_3$ role using the DLPNO-CCSD(T) method for the formation of **1ac** from benzylamine and $PhCH_2N^+(CH_3)_3$ with oxygen in the gas phase. Electronic energy is given in kcal/mol.

3.3.2.6 Proton Coupled Electron Transfer (PCET) Process:

It's evident that in the presence of the ionic liquid (Triton B), hydrogen atom abstraction by molecular oxygen occurs with a lower activation energy barrier compared to an uncatalyzed reaction. The mechanism of hydrogen atom abstraction was examined through spin density and Mulliken charge analysis. The negligible spin density observed on the mobile hydrogen atom in **TS-1TT (Figure 34a-34c)** confirms that the hydrogen atom is not transferred as a radical (as in hydrogen atom transfer, HAT), but rather through a proton-coupled electron transfer (PCET) process from benzylamine to oxygen.[210] Analysis of global electron density transfer (GEDT) at **TS-1TT** indicates that electron density flows globally from benzylamine to oxygen and from oxygen to benzyltrimethylammonium cation **(Figures 34a-34c)**. Furthermore, the charge transfer properties for the ground adiabatic electronic states of intermediates and transition states were assessed **(Figure 34d)**.[211] The dipole moment magnitude undergoes a substantial increase throughout the reaction progression **(Table 11)**, leading to notable changes in the electronic charge distribution within the benzylamine-O_2 system. Calculations during the reaction process reveal alterations in the charges on the donor (benzylamine) and acceptor (O_2) molecules, as well as the transferring hydrogen. Specifically, charges on the donor molecule transition from negative to positive values **(Table 11)**.[212,213]

Moreover, the charge on the transferring hydrogen atom is observed to become more positive for **Int-2TT** (0.51 e) compared to **Int-1TT** (0.22 e). This observation aligns with the PCET mechanism, where a positively charged proton is involved alongside electron transfer from the donor to the acceptor molecule.[211,214]

Table 11. The calculated dipole moments (D) and Mulliken charges on donor (benzylamine) and acceptor (O_2) molecules. The charges on transferring H are also given.

	Dipole moment (D)	Mulliken charge		
		donor molecule	acceptor molecule	H atom
Int-1TT	4.231	-0.021	0.074	0.224
TS-1TT	4.034	0.389	-0.332	0.368
Int-2TT	5.951	0.543	-0.408	0.513

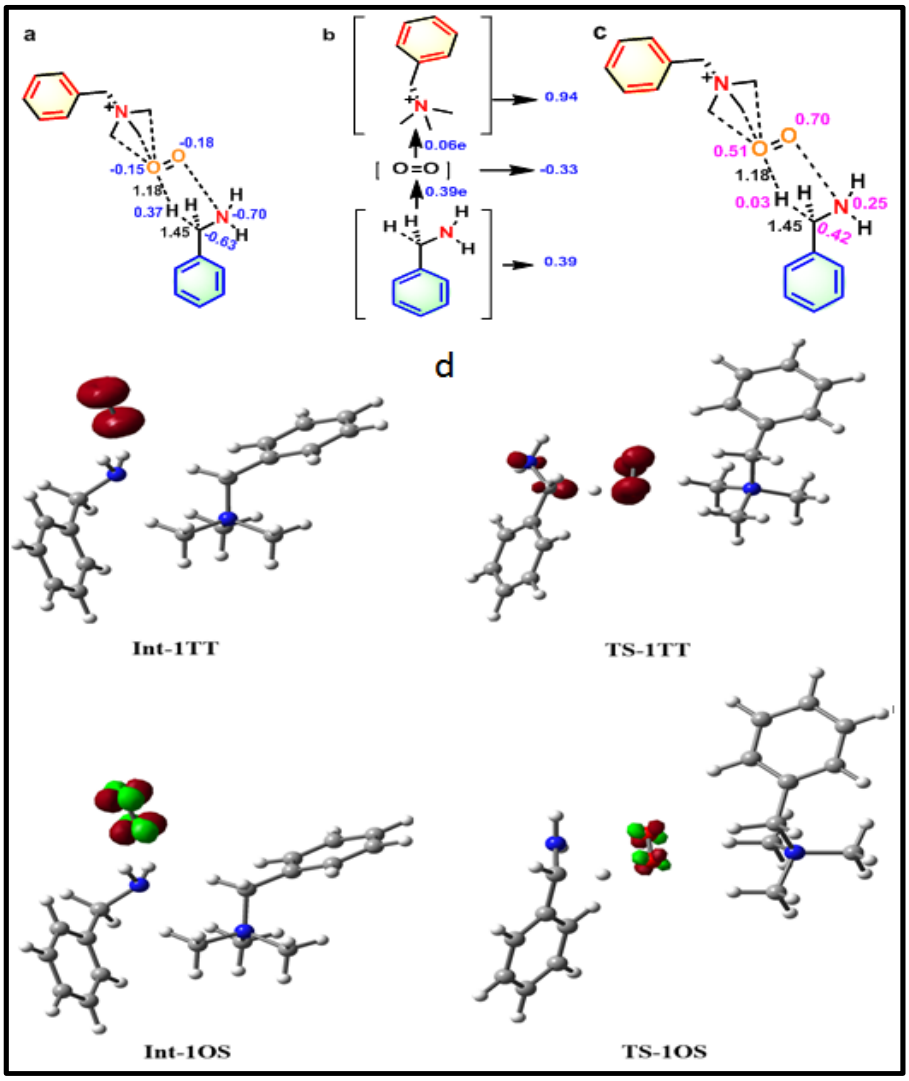

Figure 34. **(a)** shows moving benzylic hydrogen atom at TS-1TT towards triplet oxygen is carrying a partial charge of +0.33. **(b)** Global electron density transfer (GEDT) profile at TS-1TT shows partial charges on benzylamine, oxygen, and $PhCH_2N^+(CH_3)_3$ cation (0.39, -0.33, and 0.94, respectively) at TS-1TT. **(c)** The electron spin density of individual atoms at TS-1TT. Spin density on O_2 decreases to 1.21 from 2 whereas the transfer of one electron from benzylamine results in a spin density of 0.78 on benzylamine. A spin density of 0.03 on transferring H indicates proton coupled electron transfer (PCET) rather than hydrogen atom transfer (HAT). Blue texts correspond to partial charge and pink texts correspond to spin density. Distances are shown in dotted lines. **(d)** The spin density of various intermediates and transition states formed from benzylamine and Triton B with oxygen in the gas phase at the iso-surface value of 0.03. The brown and green colors indicate two opposite regions. [C: grey, N: blue, H: hydrogen., O: red]

The frontier molecular orbitals of the transition state (TS) can be observed in **Figure 35**, while the active space natural orbitals derived from MCSCF calculations are depicted in **Figure 36**. In **Int-1TT**, both orbitals 78 and 79 singly occupy the π* orbital of O_2. Conversely, in **Int-2TT**, orbital 79 exhibits contribution from HOO• radical species, while orbital 78 shows contribution from PhCH•—NH_2 radical species **(Figure 36)**.

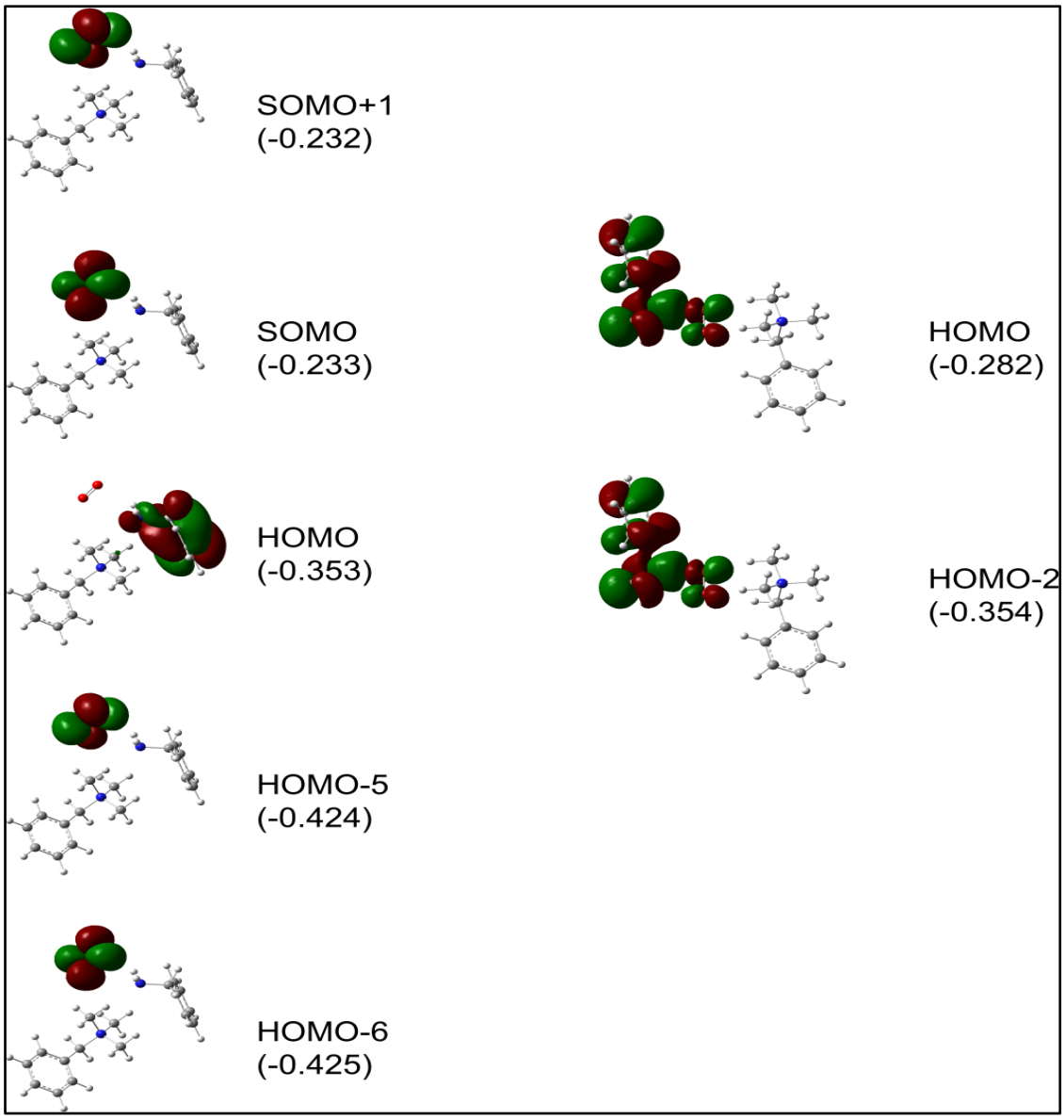

Figure 35. The frontier molecular orbitals of Int-1TT (left panel) and TS-1TT(right panel). The orbital energies value in a.u. The iso-surface value is 0.02.

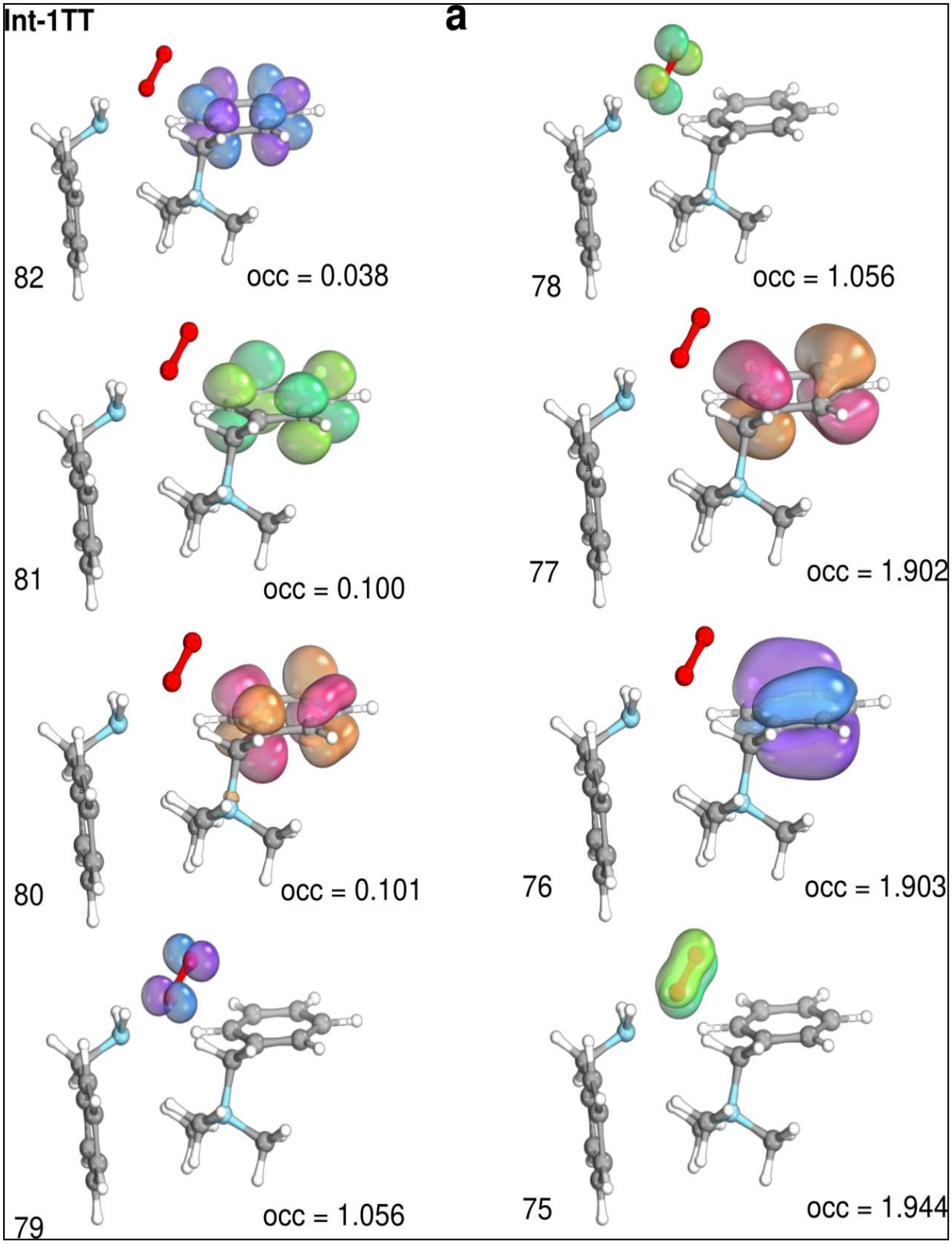
Int-1TT
a
82
occ = 0.038
78
occ = 1.056
81
occ = 0.100
77
occ = 1.902
80
occ = 0.101
76
occ = 1.903
79
occ = 1.056
75
occ = 1.944

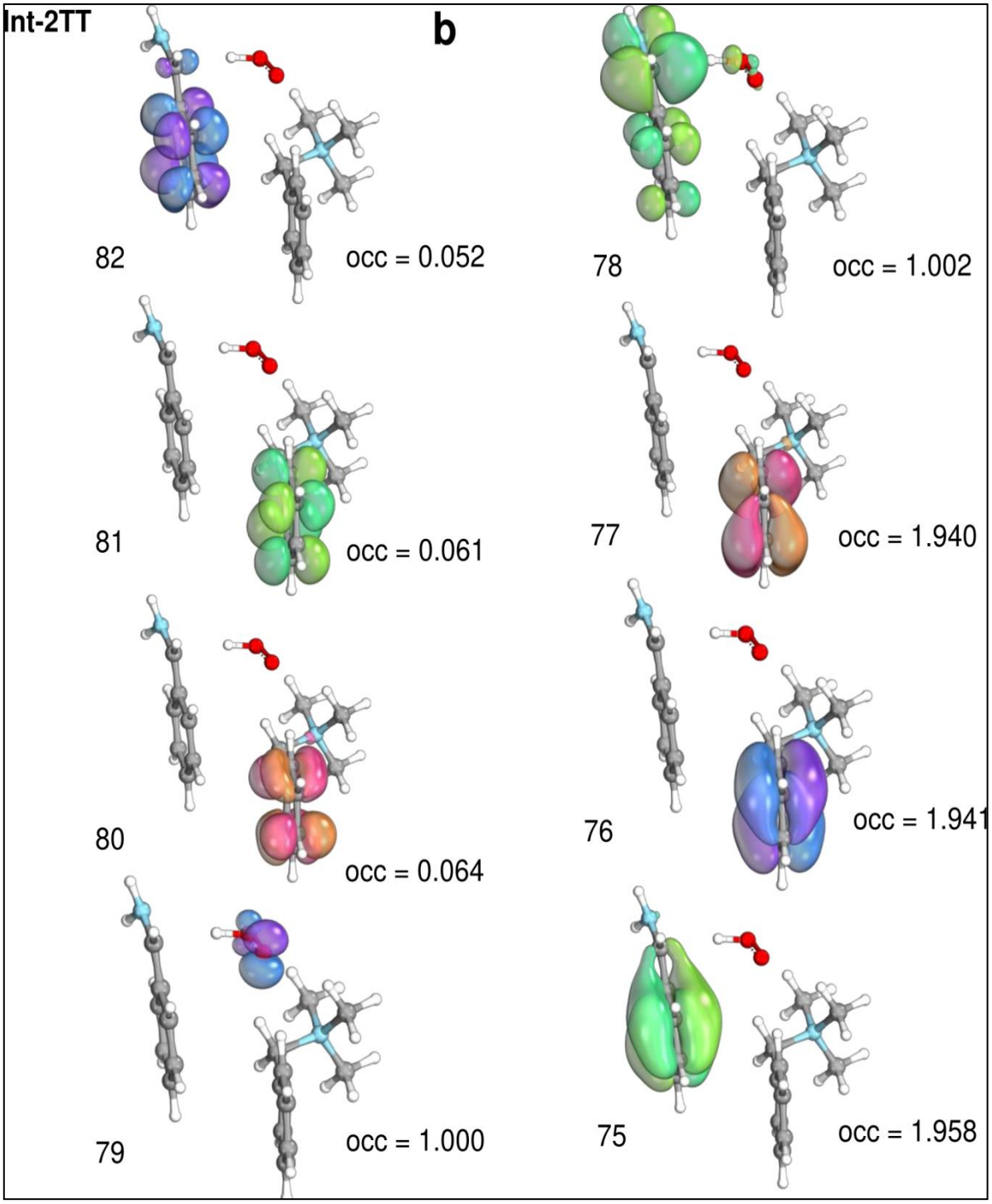

Figure 36. Molecular orbitals of (a) Int-1TT and b) Int-2TT obtained from MCSCF calculations.

3.3.2.7 Role of Benzyltrimethylammonium Cation:

Detailed DFT studies support that the reaction cannot proceed to produce the intended products in the absence of Triton B, aligning with the experimental findings. Various aspects have been investigated through DFT studies, encompassing the mechanism of the benzylamine oxidation reaction, electronic energy and free energy values, entropy contribution, PCET process, and the

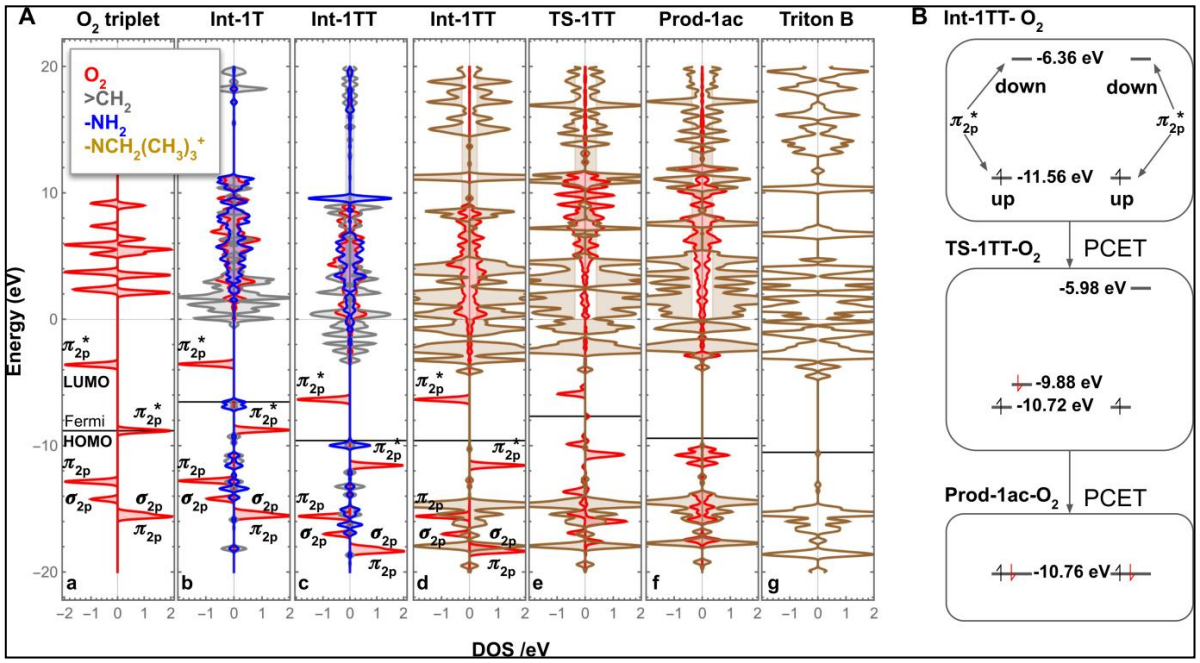

Figure 37. (**A**) The pDOS diagram. **(Aa)** The energy of electrons in triplet oxygen (red). **(Ab)** The energy of electrons in **Int-1T**, where red corresponds to triplet oxygen, blue corresponds to NH_2 of benzylamine, and gray corresponds to benzylic CH_2 of benzylamine. **(Ac)** The energy of electrons in **Int-1TT**, where electrons of oxygen with benzylamine in presence of Triton B have been compared. **(Ad)** The energy of electrons of **Int-1TT** where electrons of oxygen with Triton B have been compared; the color brown corresponds to electrons of N^+-$CH_2(CH_3)_3$. **(Ae)** The energy of electrons in **TS-1TT**. **(f)** The energy of electrons in product **1ac**. **(Ag)** The energy of electrons in Triton B alone. (**B**) Schematics of orbital destinations in PCET. Incoming electrons are shown in red.

non-covalent interaction between the benzyltrimethylammonium cation and oxygen. Exploration of different transition state orientations of the benzyltrimethylammonium cation relative to oxygen **(Figures 30 and 31)** confirms its specific affinity with oxygen through non-covalent interaction **(Figures 30 and 31)**. However, the energy profile diagrams alone do not elucidate the role of the benzyltrimethylammonium cation in Triton B with oxygen in benzylamine oxidation, necessitating further investigation into molecular orbitals. To understand non-covalent interactions, the focus has been on the orbitals of oxygen and the benzyltrimethylammonium cation. Orbitals play a crucial role in modeling molecular bonding, interactions between molecules and surfaces, and the reactivity of a molecule. Investigating the interaction between the benzyltrimethylammonium cation and oxygen requires understanding the energy of molecular orbitals involved in the interaction or reaction. Partial density of states (pDOS) serves as a vital descriptor for elucidating the energy of corresponding orbitals or electrons participating in the mentioned reaction **(Figure 37Aa-37Ag)**.[215,216] To investigative the delocalization of the orbitals, the partial density of states (pDOS) was analyzed by weighting the individual Gaussians with the gross orbital populations. In **Figure 37Aa**, the spin-down and spin-up DOS for free oxygen display peaks at -3.6 eV (vacant) and -8.84 eV (occupied), respectively, each originating from degenerate states representing the two antibonding π_{2p}^{*}orbitals. The splitting between spin-up and spin-down arises due to the triplet nature of the O_2 ground state, leading to different exchange interactions for the distinct spin channels. In an uncatalyzed reaction with benzylamine and oxygen, the two antibonding π_{2p}^{*} orbitals of oxygen manifest at -3.56 eV (vacant) and -8.76 eV (occupied). Compared to free triplet oxygen, no stabilization of the antibonding orbitals of oxygen with the benzylamine complex **(Figure 37Ab)** was observed. However, in the presence of the benzyltrimethylammonium cation, the partial density of

states (pDOS) reveals a decrease in both the vacant and occupied π^*_{2p} orbital energies of oxygen to -6.36 eV and -11.56 eV, respectively, while the orbital energy of the benzyltrimethylammonium cation increases, facilitating hybridization **(Figure 37Ac-37Ag)**. Orbital hybridization was observed between the filled bonding pi orbitals (π_{2p}) of oxygen **(Figure 37Ad and 37Ae)** and the -$N^+(CH_3)_3$ (Triton B) orbitals, which significantly reduces the orbital energies of oxygen (**TS-1TT**).[215] This reduction by 2.8 eV activates the oxygen, bringing the unoccupied antibonding π^*_{2p} orbitals of oxygen in close proximity to benzylamine, making them susceptible to accepting hydrogen atoms. Rather than directly participating in reactions, the benzyltrimethylammonium cation acts as a catalyst by activating oxygen molecules through non-covalent interaction.

The orbital destinations of the proton-coupled electron transfer process are evident from the pDOS and schematically depicted in **Figure 37B**. Interacting with the benzyltrimethylammonium cation, the energy of the vacant π^*_{2p} orbitals of oxygen decreases by 2.8 eV in the **Int-1TT**, facilitating the transfer of a hydrogen atom from -CH_2-NH_2 (benzylamine) to one of the vacant π^*_{2p} orbitals of oxygen (**Int-1TT**). Thus, in the **TS-1TT**, an electron accompanied by a hydrogen atom could be observed in one of the vacant π^*_{2p} orbitals of oxygen. Another electron is transferred in the subsequent step along with the second hydrogen atom from -NH_2, thereby confining the electronic states to low-energy ground-state singlet products.

3.4 Conclusion

In this chapter, both uncatalyzed and catalyzed energy profiles for the oxidation of benzylamine using oxygen as an oxidant were demonstrated. Initially, the uncatalyzed energy profile was examined to understand the influence of Triton B on benzylamine oxidation. In this profile, hydrogen atom transfer (HAT) was identified as the rate-determining step. To further grasp the impact of Triton B,

the Triton B cation was included in the energy profile diagram without the counterion. A very low activation energy/free energy difference (2 kcal/mol) between the two routes was observed using an energy profile diagram of catalyzed and uncatalyzed reactions. The non-covalent interaction between the Triton B cation, oxygen and benzylamine resulted in a low activation energy difference due to interaction and dispersion energy of the transition state. Subsequently, a diagram of the energy profile under actual reaction conditions was considered for calculation. In this energy profile, methanol, Triton B and counterions were present. In this scenario, a low activation barrier (8 kcal/mol) was achieved compared to both catalyzed and uncatalyzed reactions (where only cations were present). A low difference in free energy activation and a significantly higher barrier height (nearly twice as high) than the electronic energy profiles were noted when comparing the free energy profiles of different catalyzed and uncatalyzed reactions (in the presence of cations or cations and anions) in all cases where the catalyst was still present. The presence of the entropy term as well as dispersion correction in the free energy profile entirely misrepresented Triton B's function in the reaction. Additionally, the entropic contribution was calculated in the free energy profile diagram. The calculated free energy profile confirms that the reaction mechanism is both kinetically labile and spontaneous. The study investigated hydrogen abstraction in **TS-1TT** using spin density and Mulliken charge analysis. It was found that hydrogen atoms were transferred from benzylamine to oxygen via a proton-coupled electron transfer mechanism, rather than as HAT. Furthermore, first-principle calculations elucidated the activation of O_2 within the framework of molecular orbital theory. The orbital overlap between the benzyltrimethylammonium cation and oxygen stabilizes the high-energy π_{2p}^{*} orbital of oxygen. Consequently, the π_{2p}^{*} orbital of oxygen, acting as the electron or H acceptor, approaches the orbitals of organic molecules, such as benzylamine.

3.5 References

(1) Maoka, T. Carotenoids as Natural Functional Pigments. *J Nat Med* **2020**, *74* (1), 1–16. https://doi.org/10.1007/s11418-019-01364-x.

(2) Bartee, L.; Shriner, W.; Creech, C. The Light-Dependent Reactions. **2017**.

(3) *Photolysis - an overview | ScienceDirect Topics*. https://www.sciencedirect.com/topics/earth-and-planetary-sciences/photolysis (accessed 2023-08-31).

(4) *Light-Independent Reactions - an overview | ScienceDirect Topics*. https://www.sciencedirect.com/topics/agricultural-and-biological-sciences/light-independent-reactions (accessed 2023-08-31).

(5) *History of the Origin of the Chemical Elements and Their Discoverers*. https://www.nndc.bnl.gov/content/elements.html (accessed 2023-09-02).

(6) Stuhr, R.; Bayer, P.; von Wangelin, A. J. The Diverse Modes of Oxygen Reactivity in Life & Chemistry. *ChemSusChem* **2022**, *15* (24), e202201323. https://doi.org/10.1002/cssc.202201323.

(7) Wiberg, E.; Wiberg, N.; Holleman, A. F. *Inorganic Chemistry*, 1st English ed.; Academic Press ; De Gruyter: San Diego, Berlin, 2001.

(8) US Department of Commerce, N. *Global Monitoring Laboratory - Carbon Cycle Greenhouse Gases*. https://gml.noaa.gov/ccgg/about.html (accessed 2023-08-31).

(9) *Do Diradicals Behave Like Radicals? | Chemical Reviews*. https://pubs.acs.org/doi/10.1021/acs.chemrev.9b00260 (accessed 2023-08-31).

(10) Abe, M. Diradicals. *Chem. Rev.* **2013**, *113* (9), 7011–7088. https://doi.org/10.1021/cr400056a.

(11) Roothaan, C. C. J. New Developments in Molecular Orbital Theory. *Rev. Mod. Phys.* **1951**, *23* (2), 69–89. https://doi.org/10.1103/RevModPhys.23.69.

(12) *Effects of electron repulsion in conjugated hydrocarbon diradicals | Journal of the American Chemical Society*. https://pubs.acs.org/doi/10.1021/ja00456a010 (accessed 2023-08-31).

(13) Kearns, D. R. Physical and Chemical Properties of Singlet Molecular Oxygen. *Chem. Rev.* **1971**, *71* (4), 395–427. https://doi.org/10.1021/cr60272a004.

(14) Wu, Q.; Cheng, C.-L.; Van Voorhis, T. Configuration Interaction Based on Constrained Density Functional Theory: A Multireference Method. *The Journal of Chemical Physics* **2007**, *127* (16), 164119. https://doi.org/10.1063/1.2800022.

(15) Qu, Z. Reactivities of Singlet Oxygen: Open-Shell or Closed-Shell? *Phys. Chem. Chem. Phys.* **2020**, *22* (24), 13373–13377. https://doi.org/10.1039/D0CP02466J.

(16) Borden, W. T.; Hoffmann, R.; Stuyver, T.; Chen, B. Dioxygen: What Makes This Triplet Diradical Kinetically Persistent? *J. Am. Chem. Soc.* **2017**, *139* (26), 9010–9018. https://doi.org/10.1021/jacs.7b04232.

(17) Heitler, W.; Pöschl, G. Ground State of C2 and O2 and the Theory of Valency. *Nature* **1934**, *133* (3370), 833–834. https://doi.org/10.1038/133833c0.

(18) *A valence bond study of the dioxygen molecule*. https://onlinelibrary.wiley.com/doi/epdf/10.1002/jcc.20490 (accessed 2023-09-05).

(19) *Frontmatter - A Chemist's Guide to Valence Bond Theory - Wiley Online Library*. https://onlinelibrary.wiley.com/doi/pdf/10.1002/9780470192597.fmatter (accessed 2023-09-05).

(20) Wu, W.; McWeeny, R. A Study of the C-Li Bond in Methyllithium and of the Potential Energy Surface for Bond Breaking. *Journal of Molecular Structure: THEOCHEM* **1995**, *341* (1), 279–288. https://doi.org/10.1016/0166-1280(95)93229-G.

(21) Harcourt, R. D. Valence Bond Studies of Oxygen and Superoxide: A Note on One-Electron and Two-Electron Transfer Resonances. *J. Phys. Chem.* **1992**, *96* (19), 7616–7619. https://doi.org/10.1021/j100198a023.

(22) Kistiakowsky, G. B.; Ruhoff, J. R.; Smith, H. A.; Vaughan, W. E. Heats of Organic Reactions. IV. Hydrogenation of Some Dienes and of Benzene. *J. Am. Chem. Soc.* **1936**, *58* (1), 146–153. https://doi.org/10.1021/ja01292a043.

(23) *Activation of Triplet Dioxygen by Glucose Oxidase: Spin−Orbit Coupling in the Superoxide Ion*. https://doi.org/10.1021/jp014013q.

(24) Carbogno, C.; Behler, J.; Groß, A.; Reuter, K. Fingerprints for Spin-Selection Rules in the Interaction Dynamics of ${\mathrm{O}}_{2}$ at Al(111). *Phys. Rev. Lett.* **2008**, *101* (9), 096104. https://doi.org/10.1103/PhysRevLett.101.096104.
(25) Westbrook, C. K.; Dryer, F. L. Chemical Kinetic Modeling of Hydrocarbon Combustion. *Progress in Energy and Combustion Science* **1984**, *10* (1), 1–57. https://doi.org/10.1016/0360-1285(84)90118-7.
(26) Curran, H. J. Developing Detailed Chemical Kinetic Mechanisms for Fuel Combustion. *Proceedings of the Combustion Institute* **2019**, *37* (1), 57–81. https://doi.org/10.1016/j.proci.2018.06.054.
(27) *Fire Protection Guide to Hazardous Materials*, 13th ed.; Spencer, A. B., National Fire Protection Association, Eds.; National Fire Protection Association: Quincy, Mass, 2002.
(28) *PDB101: Molecule of the Month: Hemoglobin*. RCSB: PDB-101. http://pdb101.rcsb.org/motm/41 (accessed 2024-05-15).
(29) Decker, H.; Holde, K. E. van. *Oxygen and the Evolution of Life*; Springer Science & Business Media, 2010.
(30) Bugg, T. D. H. Dioxygenase Enzymes: Catalytic Mechanisms and Chemical Models. *Tetrahedron* **2003**, *36* (59), 7075–7101. https://doi.org/10.1016/S0040-4020(03)00944-X.
(31) *Redox Reactions Catalyzed by Isolated Enzymes | Chemical Reviews*. https://pubs.acs.org/doi/full/10.1021/cr100334x (accessed 2023-09-06).
(32) *Yellow-Green and Red Firefly Bioluminescence from 5,5-Dimethyloxyluciferin | Journal of the American Chemical Society*. https://pubs.acs.org/doi/10.1021/ja017400m (accessed 2023-09-06).
(33) Hermans, I.; Spier, E. S.; Neuenschwander, U.; Turrà, N.; Baiker, A. Selective Oxidation Catalysis: Opportunities and Challenges. *Top Catal* **2009**, *52* (9), 1162–1174. https://doi.org/10.1007/s11244-009-9268-3.
(34) Smalley, J. F.; Nesbitt, F. L.; Klemm, R. B. *Branching ratio for the hydrogen atom product channel in the reaction of ground-state atomic oxygen with ethylene*. ACS Publications. https://doi.org/10.1021/j100275a028.
(35) Whetten, R. L.; Cox, D. M.; Trevor, D. J.; Kaldor, A. Free Iron Clusters React Readily with Oxygen and Hydrogen Sulfide, but Are Inert toward Methane. *J. Phys. Chem.* **1985**, *89* (4), 566–569. https://doi.org/10.1021/j100250a004.
(36) Jin, N.; Groves, J. T. Unusual Kinetic Stability of a Ground-State Singlet Oxomanganese(V) Porphyrin. Evidence for a Spin State Crossing Effect. *J. Am. Chem. Soc.* **1999**, *121* (12), 2923–2924. https://doi.org/10.1021/ja984429q.
(37) *Activation of Molecular Oxygen - Henrici-Olivé - 1974 - Angewandte Chemie International Edition in English - Wiley Online Library*. https://onlinelibrary.wiley.com/doi/epdf/10.1002/anie.197400291 (accessed 2023-09-07).
(38) Dickman, M. H.; Pope, M. T. *Peroxo and Superoxo Complexes of Chromium, Molybdenum, and Tungsten*. ACS Publications. https://doi.org/10.1021/cr00027a002.
(39) Brückner, A. In Situ Electron Paramagnetic Resonance: A Unique Tool for Analyzing Structure–Reactivity Relationships in Heterogeneous Catalysis. *Chem. Soc. Rev.* **2010**, *39* (12), 4673–4684. https://doi.org/10.1039/B919541F.
(40) Zhou, M.; Crabtree, R. H. C–H Oxidation by Platinum Group Metal Oxo or Peroxo Species. *Chem. Soc. Rev.* **2011**, *40* (4), 1875–1884. https://doi.org/10.1039/C0CS00099J.
(41) Deubel, D. V.; Sundermeyer, J.; Frenking, G. Mechanism of the Olefin Epoxidation Catalyzed by Molybdenum Diperoxo Complexes: Quantum-Chemical Calculations Give an Answer to a Long-Standing Question. *J. Am. Chem. Soc.* **2000**, *122* (41), 10101–10108. https://doi.org/10.1021/ja0006649.
(42) Shetti, V. N.; Rani, M. J.; Srinivas, D.; Ratnasamy, P. Chemoselective Alkane Oxidation by Superoxo−Vanadium(V) in Vanadosilicate Molecular Sieves. *J. Phys. Chem. B* **2006**, *110* (2), 677–679. https://doi.org/10.1021/jp0565296.
(43) Di Valentin, C.; Gisdakis, P.; Yudanov, I. V.; Rösch, N. Olefin Epoxidation by Peroxo Complexes of Cr, Mo, and W. A Comparative Density Functional Study. *J. Org. Chem.* **2000**, *65* (10), 2996–3004. https://doi.org/10.1021/jo9916784.

(44) Mayer, J. M. *Metal-oxygen multiple bond lengths: a statistical study*. ACS Publications. https://doi.org/10.1021/ic00295a006.
(45) Holm, R. H. Metal-Centered Oxygen Atom Transfer Reactions. *Chem. Rev.* **1987**, *87* (6), 1401–1449. https://doi.org/10.1021/cr00082a005.
(46) *Oxo-transfer reactions of chromium and titanium porphyrins | Inorganic Chemistry*. https://pubs.acs.org/doi/pdf/10.1021/ic00345a002 (accessed 2023-09-07).
(47) Katsuki, T. Catalytic Asymmetric Oxidations Using Optically Active (Salen)Manganese(III) Complexes as Catalysts. *Coordination Chemistry Reviews* **1995**, *140*, 189–214. https://doi.org/10.1016/0010-8545(94)01124-T.
(48) *Mechanism of epoxidation of olefins by covalent peroxides of molybdenum(VI) | Journal of the American Chemical Society*. https://pubs.acs.org/doi/10.1021/ja00756a062 (accessed 2023-09-07).
(49) Wu, Y.-D.; Lai, D. K. W. A Density Functional Study on the Stereocontrol of the Sharpless Epoxidation. *J. Am. Chem. Soc.* **1995**, *117* (45), 11327–11336. https://doi.org/10.1021/ja00150a034.
(50) Lee, Y.-M.; Hong, S.; Morimoto, Y.; Shin, W.; Fukuzumi, S.; Nam, W. Dioxygen Activation by a Non-Heme Iron(II) Complex: Formation of an Iron(IV)−Oxo Complex via C−H Activation by a Putative Iron(III)−Superoxo Species. *J. Am. Chem. Soc.* **2010**, *132* (31), 10668–10670. https://doi.org/10.1021/ja103903c.
(51) Sheldon, R. A.; Arends, I. W. C. E.; Lempers, H. E. B. Liquid Phase Oxidation at Metal Ions and Complexes in Constrained Environments. *Catalysis Today* **1998**, *41* (4), 387–407. https://doi.org/10.1016/S0920-5861(98)00027-3.
(52) Piera, J.; Bäckvall, J.-E. Catalytic Oxidation of Organic Substrates by Molecular Oxygen and Hydrogen Peroxide by Multistep Electron Transfer—A Biomimetic Approach. *Angewandte Chemie International Edition* **2008**, *47* (19), 3506–3523. https://doi.org/10.1002/anie.200700604.
(53) Brink, G.-J. ten; Arends, I. W. C. E.; Sheldon, R. A. Green, Catalytic Oxidation of Alcohols in Water. *Science* **2000**, *287* (5458), 1636–1639. https://doi.org/10.1126/science.287.5458.1636.
(54) Torres Pazmiño, D. E.; Winkler, M.; Glieder, A.; Fraaije, M. W. Monooxygenases as Biocatalysts: Classification, Mechanistic Aspects and Biotechnological Applications. *Journal of Biotechnology* **2010**, *146* (1), 9–24. https://doi.org/10.1016/j.jbiotec.2010.01.021.
(55) Li, Q.-S.; Ogawa, J.; Shimizu, S. Critical Role of the Residue Size at Position 87 in H2O2-Dependent Substrate Hydroxylation Activity and H2O2 Inactivation of Cytochrome P450BM-3. *Biochemical and Biophysical Research Communications* **2001**, *280* (5), 1258–1261. https://doi.org/10.1006/bbrc.2001.4261.
(56) Decker, A.; Solomon, E. I. Dioxygen Activation by Copper, Heme and Non-Heme Iron Enzymes: Comparison of Electronic Structures and Reactivities. *Current Opinion in Chemical Biology* **2005**, *9* (2), 152–163. https://doi.org/10.1016/j.cbpa.2005.02.012.
(57) Lang, D.; Yeung, C.; Peter, R.; Ibarra, C.; Gasser, R.; Itagaki, K.; Philpot, R.; Rettie, A. Isoform Specificity of Trimethylamine N-Oxygenation by Human Flavin-Containing Monooxygenase (FMO) and P450 Enzymes: Selective Catalysis by Fmo3. *Biochemical Pharmacology* **1998**, *56* (8), 1005–1012. https://doi.org/10.1016/S0006-2952(98)00218-4.
(58) Massey, V. Activation of Molecular Oxygen by Flavins and Flavoproteins. *Journal of Biological Chemistry* **1994**, *269* (36), 22459–22462. https://doi.org/10.1016/S0021-9258(17)31664-2.
(59) Tang, Y.; Li, Y.; (Feng) Tao, F. Activation and Catalytic Transformation of Methane under Mild Conditions. *Chem. Soc. Rev.* **2022**, *51* (1), 376–423. https://doi.org/10.1039/D1CS00783A.
(60) Chen, K.; Zhang, P.; Wang, Y.; Li, H. Metal-Free Allylic/Benzylic Oxidation Strategies with Molecular Oxygen: Recent Advances and Future Prospects. *Green Chem.* **2014**, *16* (5), 2344. https://doi.org/10.1039/c3gc42135j.
(61) *C–H Activation: Toward Sustainability and Applications*. https://doi.org/10.1021/acscentsci.0c01413.
(62) *Green Chemistry is Good Process Chemistry*. https://doi.org/10.1021/op200366y.
(63) *Oxidative Coupling Mechanisms: Current State of Understanding*. https://doi.org/10.1021/acscatal.7b02974.

(64) *An Efficient Rh/O2 Catalytic System for Oxidative C–H Activation/Annulation: Evidence for Rh(I) to Rh(III) Oxidation by Molecular Oxygen*. https://doi.org/10.1021/ja404414q.
(65) *Catalytic Dehydrogenative Cross-Coupling: Forming Carbon−Carbon Bonds by Oxidizing Two Carbon−Hydrogen Bonds*. https://doi.org/10.1021/cr100280d.
(66) Sharma, R. K.; Bandichhor, R.; Mishra, V.; Sharma, S.; Yadav, S.; Mehta, S.; Arora, B.; Rana, P.; Dutta, S.; Solanki, K. Advanced Metal Oxide-Based Nanocatalysts for the Oxidative Synthesis of Fine Chemicals. *Mater. Adv.* **2023**, *4* (8), 1795–1830. https://doi.org/10.1039/D2MA00977C.
(67) Ishii, Y.; Sakaguchi, S.; Iwahama, T. Innovation of Hydrocarbon Oxidation with Molecular Oxygen and Related Reactions. *Advanced Synthesis & Catalysis* **2001**, *343* (5), 393–427. https://doi.org/10.1002/1615-4169(200107)343:5<393::AID-ADSC393>3.0.CO;2-K.
(68) *Oxidation of organic compounds by zinc permanganate | Journal of the American Chemical Society*. https://pubs.acs.org/doi/epdf/10.1021/ja00364a054 (accessed 2023-08-25).
(69) *Chromium-catalyzed oxidations in organic synthesis | Chemical Reviews*. https://pubs.acs.org/doi/epdf/10.1021/cr00009a005 (accessed 2023-08-25).
(70) Jayakumar, J.; Priyadarshini, D.; Parthasarathy, A.; Reddy, S. R. Recent Advances in Molecular Oxygen Assisted Laccase Catalyzed Sustainable Organic Transformations. *Asian Journal of Organic Chemistry* **2023**, *12* (1), e202200564. https://doi.org/10.1002/ajoc.202200564.
(71) Böhm, M. C. L. Salem: Electrons in Chemical Reactions, First Principles. John Wiley and Sons, New York, Chichester, Brisbane, Toronto, Singapore 1982. 260 Seiten, Preis: £ 27.25. In *Berichte der Bunsengesellschaft für physikalische Chemie*; 1983; Vol. 87, pp 547–548. https://doi.org/10.1002/bbpc.19830870625.
(72) Wang, H.; Chen, S.; Yong, D.; Zhang, X.; Li, S.; Shao, W.; Sun, X.; Pan, B.; Xie, Y. Giant Electron–Hole Interactions in Confined Layered Structures for Molecular Oxygen Activation. *J. Am. Chem. Soc.* **2017**, *139* (13), 4737–4742. https://doi.org/10.1021/jacs.6b12273.
(73) Ye, L.; Deng, K.; Xu, F.; Tian, L.; Peng, T.; Zan, L. Increasing Visible-Light Absorption for Photocatalysis with Black BiOCl. *Phys. Chem. Chem. Phys.* **2011**, *14* (1), 82–85. https://doi.org/10.1039/C1CP22876E.
(74) Sun, K.; Shan, H.; Lu, G.-P.; Cai, C.; Beller, M. Synthesis of N-Heterocycles via Oxidant-Free Dehydrocyclization of Alcohols Using Heterogeneous Catalysts. *Angewandte Chemie International Edition* **2021**, *60* (48), 25188–25202. https://doi.org/10.1002/anie.202104979.
(75) *Surface Structure-Dependent Molecular Oxygen Activation of BiOCl Single-Crystalline Nanosheets*. https://doi.org/10.1021/ja4092903.
(76) Luo, L.; Zhang, T.; Wang, M.; Yun, R.; Xiang, X. Recent Advances in Heterogeneous Photo-Driven Oxidation of Organic Molecules by Reactive Oxygen Species. *ChemSusChem* **2020**, *13* (19), 5173–5184. https://doi.org/10.1002/cssc.202001398.
(77) *Generation and Detection of Reactive Oxygen Species in Photocatalysis*. https://doi.org/10.1021/acs.chemrev.7b00161.
(78) Kessler, A.; Hedberg, J.; Blomberg, E.; Odnevall, I. Reactive Oxygen Species Formed by Metal and Metal Oxide Nanoparticles in Physiological Media—A Review of Reactions of Importance to Nanotoxicity and Proposal for Categorization. *Nanomaterials* **2022**, *12* (11), 1922. https://doi.org/10.3390/nano12111922.
(79) *Metal-Free, NHPI Catalyzed Oxidative Cleavage of C–C Double Bond Using Molecular Oxygen as Oxidant*. https://doi.org/10.1021/ol3018215.
(80) Melone, L.; Punta, C. Metal-Free Aerobic Oxidations Mediated by *N* -Hydroxyphthalimide. A Concise Review. *Beilstein J. Org. Chem.* **2013**, *9*, 1296–1310. https://doi.org/10.3762/bjoc.9.146.
(81) Hollmann, F.; Arends, I. W. C. E.; Buehler, K.; Schallmey, A.; Bühler, B. Enzyme-Mediated Oxidations for the Chemist. *Green Chem.* **2011**, *13* (2), 226–265. https://doi.org/10.1039/C0GC00595A.
(82) Rickert, A.; Krombach, V.; Hamers, O.; Zorn, H.; Maison, W. Enzymatic Allylic Oxidations with a Lyophilisate of the Edible Fungus Pleurotus Sapidus. *Green Chem.* **2012**, *14* (3), 639. https://doi.org/10.1039/c2gc16317a.
(83) *High-Valent Iron(IV)–Oxo Complexes of Heme and Non-Heme Ligands in Oxygenation Reactions*. https://doi.org/10.1021/ar700027f.

(84) *Metalloporphyrin−Dioxygen Interactions and the Effects of Neutral Axial Ligands*. https://doi.org/10.1021/jp901620a.
(85) Hu, J.; Hu, Y.; Mao, J.; Yao, J.; Chen, Z.; Li, H. A Cobalt Schiff Base with Ionic Substituents on the Ligand as an Efficient Catalyst for the Oxidation of 4-Methyl Guaiacol to Vanillin. *Green Chem.* **2012**, *14* (10), 2894. https://doi.org/10.1039/c2gc36049g.
(86) *Selective Oxygenation of Ring-Substituted Toluenes with Electron-Donating and -Withdrawing Substituents by Molecular Oxygen via Photoinduced Electron Transfer*. https://doi.org/10.1021/ja036645r.
(87) Tada, N.; Hattori, K.; Nobuta, T.; Miura, T.; Itoh, A. Facile Aerobic Photooxidation of Methyl Group in the Aromatic Nucleus in the Presence of an Organocatalyst under VIS Irradiation. *Green Chem.* **2011**, *13* (7), 1669. https://doi.org/10.1039/c1gc15154a.
(88) Wen, G.; Gu, Q.; Liu, Y.; Schlögl, R.; Wang, C.; Tian, Z.; Su, D. S. Biomass-Derived Graphene-like Carbon: Efficient Metal-Free Carbocatalysts for Epoxidation. *Angewandte Chemie International Edition* **2018**, *57* (51), 16898–16902. https://doi.org/10.1002/anie.201809970.
(89) Wang, Y.; Li, H.; Yao, J.; Wang, X.; Antonietti, M. Synthesis of Boron Doped Polymeric Carbon Nitride Solids and Their Use as Metal-Free Catalysts for Aliphatic C–H Bond Oxidation. *Chem. Sci.* **2011**, *2* (3), 446–450. https://doi.org/10.1039/C0SC00475H.
(90) *Solvent-Free and Metal-Free Oxidation of Toluene Using O2 and g-C3N4 with Nanopores: Nanostructure Boosts the Catalytic Selectivity*. https://doi.org/10.1021/cs300413x.
(91) Li, X.-H.; Chen, J.-S.; Wang, X.; Sun, J.; Antonietti, M. Metal-Free Activation of Dioxygen by Graphene/g-C3N4 Nanocomposites: Functional Dyads for Selective Oxidation of Saturated Hydrocarbons. *J. Am. Chem. Soc.* **2011**, *133* (21), 8074–8077. https://doi.org/10.1021/ja200997a.
(92) Hu, X.; Zhou, Z.; Lin, Q.; Wu, Y.; Zhang, Z. High Reactivity of Metal-Free Nitrogen-Doped Carbon Nanotube for the C–H Activation. *Chemical Physics Letters* **2011**, *503* (4), 287–291. https://doi.org/10.1016/j.cplett.2011.01.045.
(93) Min, B.-H.; Ansari, M. B.; Mo, Y.-H.; Park, S.-E. Mesoporous Carbon Nitride Synthesized by Nanocasting with Urea/Formaldehyde and Metal-Free Catalytic Oxidation of Cyclic Olefins. *Catalysis Today* **2013**, *204*, 156–163. https://doi.org/10.1016/j.cattod.2012.07.027.
(94) Zhang, Y.; Schilling, W.; Riemer, D.; Das, S. Metal-Free Photocatalysts for the Oxidation of Non-Activated Alcohols and the Oxygenation of Tertiary Amines Performed in Air or Oxygen. *Nat Protoc* **2020**, *15* (3), 822–839. https://doi.org/10.1038/s41596-019-0268-x.
(95) Dunn, P. J. The Importance of Green Chemistry in Process Research and Development. *Chem. Soc. Rev.* **2012**, *41* (4), 1452–1461. https://doi.org/10.1039/C1CS15041C.
(96) *Superoxide Ion: Generation and Chemical Implications | Chemical Reviews*. https://pubs.acs.org/doi/10.1021/acs.chemrev.5b00407 (accessed 2023-08-28).
(97) *O2 Activation by Metal Surfaces: Implications for Bonding and Reactivity on Heterogeneous Catalysts | Chemical Reviews*. https://pubs.acs.org/doi/10.1021/acs.chemrev.7b00217 (accessed 2022-05-17).
(98) Ma, R.; Lin, G.; Zhou, Y.; Liu, Q.; Zhang, T.; Shan, G.; Yang, M.; Wang, J. A Review of Oxygen Reduction Mechanisms for Metal-Free Carbon-Based Electrocatalysts. *npj Comput Mater* **2019**, *5* (1), 1–15. https://doi.org/10.1038/s41524-019-0210-3.
(99) Abednatanzi, S.; Gohari Derakhshandeh, P.; Leus, K.; Vrielinck, H.; Callens, F.; Schmidt, J.; Savateev, A.; Van Der Voort, P. Metal-Free Activation of Molecular Oxygen by Covalent Triazine Frameworks for Selective Aerobic Oxidation. *Science Advances* **2020**, *6* (14), eaaz2310. https://doi.org/10.1126/sciadv.aaz2310.
(100) Kim, J. W.; Yamaguchi, K.; Mizuno, N. Heterogeneously Catalyzed Efficient Oxygenation of Primary Amines to Amides by a Supported Ruthenium Hydroxide Catalyst. *Angewandte Chemie International Edition* **2008**, *47* (48), 9249–9251. https://doi.org/10.1002/anie.200802464.
(101) Paquette, L. A. Comprehensive Organic Transformations. Von R. C. Larock. VCH Publishers, Inc., New York/VCH Verlagsgesellschaft, Weinheim 1989. XXXIV, 1160 S., Geb. $ 55.00. — ISBN 0-89573-710-8. *Angewandte Chemie* **1990**, *102* (8), 964–965. https://doi.org/10.1002/ange.19901020837.

(102) Acosta-Guzmán, P.; Ojeda-Porras, A.; Gamba-Sánchez, D. Contemporary Approaches for Amide Bond Formation. *Advanced Synthesis & Catalysis* **2023**, *365* (24), 4359–4391. https://doi.org/10.1002/adsc.202301018.
(103) Chan, L. C.; Cox, B. G. Kinetics of Amide Formation through Carbodiimide/N-Hydroxybenzotriazole (HOBt) Couplings. *J. Org. Chem.* **2007**, *72* (23), 8863–8869. https://doi.org/10.1021/jo701558y.
(104) Chan, T.-H.; Wong, L. T. L. Silicon Tetrachloride as a Coupling Reagent for Amide Formation. *J. Org. Chem.* **1969**, *34* (9), 2766–2767. https://doi.org/10.1021/jo01261a064.
(105) Ishihara, K.; Ohara, S.; Yamamoto, H. 3,4,5-Trifluorobenzeneboronic Acid as an Extremely Active Amidation Catalyst. *J. Org. Chem.* **1996**, *61* (13), 4196–4197. https://doi.org/10.1021/jo9606564.
(106) Taussat, A.; de Figueiredo, R. M.; Campagne, J.-M. Direct Catalytic Amidations from Carboxylic Acid and Ester Derivatives: A Review. *Catalysts* **2023**, *13* (2), 366. https://doi.org/10.3390/catal13020366.
(107) Mitsudome, T.; Mikami, Y.; Mori, H.; Arita, S.; Mizugaki, T.; Jitsukawa, K.; Kaneda, K. Supported Silver Nanoparticle Catalyst for Selective Hydration of Nitriles to Amides in Water. *Chem. Commun.* **2009**, No. 22, 3258. https://doi.org/10.1039/b902469g.
(108) Yamaguchi, K.; Matsushita, M.; Mizuno, N. Efficient Hydration of Nitriles to Amides in Water, Catalyzed by Ruthenium Hydroxide Supported on Alumina. *Angewandte Chemie International Edition* **2004**, *43* (12), 1576–1580. https://doi.org/10.1002/anie.200353461.
(109) Wu, X.-F.; Bheeter, C. B.; Neumann, H.; Dixneuf, P. H.; Beller, M. Lewis Acid-Catalyzed Oxidation of Benzylamines to Benzamides. *Chem. Commun.* **2012**, *48* (100), 12237–12239. https://doi.org/10.1039/C2CC37149A.
(110) Legacy, C. J.; Wang, A.; O'Day, B. J.; Emmert, M. H. Iron-Catalyzed Cα-H Oxidation of Tertiary, Aliphatic Amines to Amides under Mild Conditions. *Angew Chem Int Ed Engl* **2015**, *54* (49), 14907–14910. https://doi.org/10.1002/anie.201507738.
(111) Wang, Y.; Kobayashi, H.; Yamaguchi, K.; Mizuno, N. Manganese Oxide-Catalyzed Transformation of Primary Amines to Primary Amides through the Sequence of Oxidative Dehydrogenation and Successive Hydration. *Chem. Commun.* **2012**, *48* (20), 2642–2644. https://doi.org/10.1039/C2CC17499E.
(112) *Highly selective transition-metal-free transamidation of amides and amidation of esters at room temperature | Nature Communications*. https://www.nature.com/articles/s41467-018-06623-1 (accessed 2023-09-14).
(113) Ilangovan, A.; Satish, G. Copper-Mediated Selective C–H Activation and Cross-Dehydrogenative C–N Coupling of *2′*-Aminoacetophenones. *Org. Lett.* **2013**, *15* (22), 5726–5729. https://doi.org/10.1021/ol402750r.
(114) Poeschl, A.; M. Mountford, D. A Facile Manganese Dioxide Mediated Oxidation of Primary Benzylamines to Benzamides. *Organic & Biomolecular Chemistry* **2014**, *12* (36), 7150–7158. https://doi.org/10.1039/C4OB01166J.
(115) Jin, X.; Kataoka, K.; Yatabe, T.; Yamaguchi, K.; Mizuno, N. Supported Gold Nanoparticles for Efficient α-Oxygenation of Secondary and Tertiary Amines into Amides. *Angewandte Chemie International Edition* **2016**, *55* (25), 7212–7217. https://doi.org/10.1002/anie.201602695.
(116) Griffiths, R. J.; Burley, G. A.; Talbot, E. P. A. Transition-Metal-Free Amine Oxidation: A Chemoselective Strategy for the Late-Stage Formation of Lactams. *Org. Lett.* **2017**, *19* (4), 870–873. https://doi.org/10.1021/acs.orglett.7b00021.
(117) Meisl, G.; Kirkegaard, J. B.; Arosio, P.; Michaels, T. C. T.; Vendruscolo, M.; Dobson, C. M.; Linse, S.; Knowles, T. P. J. Molecular Mechanisms of Protein Aggregation from Global Fitting of Kinetic Models. *Nat Protoc* **2016**, *11* (2), 252–272. https://doi.org/10.1038/nprot.2016.010.
(118) *Ionic liquid catalysed aerobic oxidative amidation and thioamidation of benzylic amines under neat conditions - Green Chemistry (RSC Publishing)*. https://pubs.rsc.org/en/content/articlelanding/2019/gc/c8gc03726d (accessed 2023-09-14).
(119) Choudhury, S. S.; Mahapatra, S.; Biswal, H. S. Hydrogen Bond Mediated Conversion of Benzenenitriles and Arylacetonitriles to Amides: An "on/in-Water" Reaction Strategy. *Green Chem.* **2022**, *24* (12), 4981–4990. https://doi.org/10.1039/D2GC01341J.

(120) *Direct Synthesis of Amides from Alcohols and Amines with Liberation of H2*. https://doi.org/10.1126/science.1145295.
(121) *Iridium-Catalyzed Conversion of Alcohols into Amides via Oximes*. https://doi.org/10.1021/ol062549u.
(122) Fujita, K.; Takahashi, Y.; Owaki, M.; Yamamoto, K.; Yamaguchi, R. Synthesis of Five-, Six-, and Seven-Membered Ring Lactams by Cp*Rh Complex-Catalyzed Oxidative N-Heterocyclization of Amino Alcohols. *Org. Lett.* **2004**, *6* (16), 2785–2788. https://doi.org/10.1021/ol0489954.
(123) Tang, R.; Diamond, S. E.; Neary, N.; Mares, F. Homogeneous Catalytic Oxidation of Amines and Secondary Alcohols by Molecular Oxygen. *J. Chem. Soc., Chem. Commun.* **1978**, No. 13, 562–562. https://doi.org/10.1039/C39780000562.
(124) Plechkova, N. V.; Seddon, K. R. Applications of Ionic Liquids in the Chemical Industry. *Chem. Soc. Rev.* **2007**, *37* (1), 123–150. https://doi.org/10.1039/B006677J.
(125) Hulla, M.; Chamam, S. M. A.; Laurenczy, G.; Das, S.; Dyson, P. J. Delineating the Mechanism of Ionic Liquids in the Synthesis of Quinazoline-2,4(1H,3H)-Dione from 2-Aminobenzonitrile and CO2. *Angewandte Chemie* **2017**, *129* (35), 10695–10699. https://doi.org/10.1002/ange.201705438.
(126) *Use of Ionic Liquids as Phase-Transfer Catalysis for Deep Oxygenative Desulfurization | Energy & Fuels*. https://pubs.acs.org/doi/10.1021/ef700734x (accessed 2023-08-28).
(127) *Deep Eutectic Solvents (DESs) and Their Applications*. https://doi.org/10.1021/cr300162p.
(128) Wang, Y.; He, H.; Wang, C.; Lu, Y.; Dong, K.; Huo, F.; Zhang, S. Insights into Ionic Liquids: From Z-Bonds to Quasi-Liquids. *JACS Au* **2022**, *2* (3), 543–561. https://doi.org/10.1021/jacsau.1c00538.
(129) Tanwar, L.; Börgel, J.; Ritter, T. Synthesis of Benzylic Alcohols by C–H Oxidation. *J. Am. Chem. Soc.* **2019**, *141* (45), 17983–17988. https://doi.org/10.1021/jacs.9b09496.
(130) Mallat, T.; Baiker, A. Oxidation of Alcohols with Molecular Oxygen on Solid Catalysts. *Chem. Rev.* **2004**, *104* (6), 3037–3058. https://doi.org/10.1021/cr0200116.
(131) Cavani, F.; Teles, J. H. Sustainability in Catalytic Oxidation: An Alternative Approach or a Structural Evolution? *ChemSusChem* **2009**, *2* (6), 508–534. https://doi.org/10.1002/cssc.200900020.
(132) Besson, M.; Gallezot, P. Selective Oxidation of Alcohols and Aldehydes on Metal Catalysts. *Catalysis Today* **2000**, *57* (1), 127–141. https://doi.org/10.1016/S0920-5861(99)00315-6.
(133) Gan, T.; Yang, J.; Morris, D.; Chu, X.; Zhang, P.; Zhang, W.; Zou, Y.; Yan, W.; Wei, S.-H.; Liu, G. Electron Donation of Non-Oxide Supports Boosts O2 Activation on Nano-Platinum Catalysts. *Nat Commun* **2021**, *12* (1), 1–10. https://doi.org/10.1038/s41467-021-22946-y.
(134) Pan, C.; Wang, C.; Zhao, X.; Xu, P.; Mao, F.; Yang, J.; Zhu, Y.; Yu, R.; Xiao, S.; Fang, Y.; Deng, H.; Luo, Z.; Wu, J.; Li, J.; Liu, S.; Xiao, S.; Zhang, L.; Guo, Y. Neighboring Sp-Hybridized Carbon Participated Molecular Oxygen Activation on the Interface of Sub-Nanocluster CuO/Graphdiyne. *J. Am. Chem. Soc.* **2022**, *144* (11), 4942–4951. https://doi.org/10.1021/jacs.1c12772.
(135) Majumdar, S.; De, J.; Chakraborty, A.; Roy, D.; Maiti, D. K. A Protic Ionic Liquid Catalyzed Strategy for Selective Hydrolytic Cleavage of Tert-Butyloxycarbonyl Amine (N-Boc). *RSC Adv.* **2014**, *5* (5), 3200–3205. https://doi.org/10.1039/C4RA13419B.
(136) Bhawal, S. S.; Patil, R. A.; Armstrong, D. W. Rapid, Effective Deprotection of Tert-Butoxycarbonyl (Boc) Amino Acids and Peptides at High Temperatures Using a Thermally Stable Ionic Liquid. *RSC Adv.* **2015**, *5* (116), 95854–95856. https://doi.org/10.1039/C5RA21279K.
(137) Zhang, B.; Studer, A. Recent Advances in the Synthesis of Nitrogen Heterocycles via Radical Cascade Reactions Using Isonitriles as Radical Acceptors. *Chem. Soc. Rev.* **2015**, *44* (11), 3505–3521. https://doi.org/10.1039/C5CS00083A.
(138) Vitaku, E.; Smith, D. T.; Njardarson, J. T. Analysis of the Structural Diversity, Substitution Patterns, and Frequency of Nitrogen Heterocycles among U.S. FDA Approved Pharmaceuticals. *J. Med. Chem.* **2014**, *57* (24), 10257–10274. https://doi.org/10.1021/jm501100b.

(139) Humphrey, J. M.; Liao, Y.; Ali, A.; Rein, T.; Wong, Y.-L.; Chen, H.-J.; Courtney, A. K.; Martin, S. F. Enantioselective Total Syntheses of Manzamine A and Related Alkaloids. *J. Am. Chem. Soc.* **2002**, *124* (29), 8584–8592. https://doi.org/10.1021/ja0202964.
(140) Nicolaou, K. C.; Mathison, C. J. N.; Montagnon, T. O-Iodoxybenzoic Acid (IBX) as a Viable Reagent in the Manipulation of Nitrogen- and Sulfur-Containing Substrates: Scope, Generality, and Mechanism of IBX-Mediated Amine Oxidations and Dithiane Deprotections. *J. Am. Chem. Soc.* **2004**, *126* (16), 5192–5201. https://doi.org/10.1021/ja0400382.
(141) Zhao, M.; Bi, L.; Wang, W.; Wang, C.; Baudy-Floc'h, M.; Ju, J.; Peng, S. Synthesis and Cytotoxic Activities of β-Carboline Amino Acid Ester Conjugates. *Bioorganic & Medicinal Chemistry* **2006**, *14* (20), 6998–7010. https://doi.org/10.1016/j.bmc.2006.06.021.
(142) Muthaiah, S.; Hong, S. H. Acceptorless and Base-Free Dehydrogenation of Alcohols and Amines Using Ruthenium-Hydride Complexes. *Advanced Synthesis & Catalysis* **2012**, *354* (16), 3045–3053. https://doi.org/10.1002/adsc.201200532.
(143) So, M.-H.; Liu, Y.; Ho, C.-M.; Che, C.-M. Graphite-Supported Gold Nanoparticles as Efficient Catalyst for Aerobic Oxidation of Benzylic Amines to Imines and N-Substituted 1,2,3,4-Tetrahydroisoquinolines to Amides: Synthetic Applications and Mechanistic Study. *Chemistry – An Asian Journal* **2009**, *4* (10), 1551–1561. https://doi.org/10.1002/asia.200900261.
(144) Hurst, T. E.; Taylor, R. J. K. A Cu-Catalysed Radical Cross-Dehydrogenative Coupling Approach to Acridanes and Related Heterocycles. *European Journal of Organic Chemistry* **2017**, *2017* (1), 203–207. https://doi.org/10.1002/ejoc.201601336.
(145) Yamaguchi, R.; Ikeda, C.; Takahashi, Y.; Fujita, K. Homogeneous Catalytic System for Reversible Dehydrogenation−Hydrogenation Reactions of Nitrogen Heterocycles with Reversible Interconversion of Catalytic Species. *J. Am. Chem. Soc.* **2009**, *131* (24), 8410–8412. https://doi.org/10.1021/ja9022623.
(146) Wu, J.; Talwar, D.; Johnston, S.; Yan, M.; Xiao, J. Acceptorless Dehydrogenation of Nitrogen Heterocycles with a Versatile Iridium Catalyst. *Angewandte Chemie* **2013**, *125* (27), 7121–7125. https://doi.org/10.1002/ange.201300292.
(147) Chakraborty, S.; Brennessel, W. W.; Jones, W. D. A Molecular Iron Catalyst for the Acceptorless Dehydrogenation and Hydrogenation of N-Heterocycles. *J. Am. Chem. Soc.* **2014**, *136* (24), 8564–8567. https://doi.org/10.1021/ja504523b.
(148) Ghahremani, M.; Ciriminna, R.; Pandarus, V.; Scurria, A.; La Parola, V.; Giordano, F.; Avellone, G.; Béland, F.; Karimi, B.; Pagliaro, M. Green and Direct Synthesis of Benzaldehyde and Benzyl Benzoate in One Pot. *ACS Sustainable Chem. Eng.* **2018**, *6* (11), 15441–15446. https://doi.org/10.1021/acssuschemeng.8b03893.
(149) Crombie, C. M.; Lewis, R. J.; Taylor, R. L.; Morgan, D. J.; Davies, T. E.; Folli, A.; Murphy, D. M.; Edwards, J. K.; Qi, J.; Jiang, H.; Kiely, C. J.; Liu, X.; Skjøth-Rasmussen, M. S.; Hutchings, G. J. Enhanced Selective Oxidation of Benzyl Alcohol via In Situ H2O2 Production over Supported Pd-Based Catalysts. *ACS Catal.* **2021**, *11* (5), 2701–2714. https://doi.org/10.1021/acscatal.0c04586.
(150) Naya, S.; Niwa, T.; Negishi, R.; Kobayashi, H.; Tada, H. Multi-Electron Oxygen Reduction by a Hybrid Visible-Light-Photocatalyst Consisting of Metal-Oxide Semiconductor and Self-Assembled Biomimetic Complex. *Angewandte Chemie International Edition* **2014**, *53* (50), 13894–13897. https://doi.org/10.1002/anie.201408352.
(151) Su, Y.; Li, B.; Xu, H.; Lu, C.; Wang, S.; Chen, B.; Wang, Z.; Wang, W.; Otake, K.; Kitagawa, S.; Huang, L.; Gu, C. Multi-Component Synthesis of a Buta-1,3-Diene-Linked Covalent Organic Framework. *J. Am. Chem. Soc.* **2022**, *144* (40), 18218–18222. https://doi.org/10.1021/jacs.2c05701.
(152) Sahana, T.; Mondal, A.; Anju, B. S.; Kundu, S. Metal-Free Transformations of Nitrogen-Oxyanions to Ammonia via Oxoammonium Salt. *Angewandte Chemie International Edition* **2021**, *60* (38), 20661–20665. https://doi.org/10.1002/anie.202105723.
(153) Sun, Z.; Sun, K.; Gao, M.; Metin, Ö.; Jiang, H. Optimizing Pt Electronic States through Formation of a Schottky Junction on Non-reducible Metal–Organic Frameworks for Enhanced Photocatalysis. *Angew Chem Int Ed* **2022**, *61* (32). https://doi.org/10.1002/anie.202206108.

(154) Sunil, K.; Narayana, B. Spectrophotometric Determination of Hydrogen Peroxide in Water and Cream Samples. *Bull Environ Contam Toxicol* **2008**, *81* (4), 422–426. https://doi.org/10.1007/s00128-008-9477-7.
(155) Nicolaou, K. C. Organic Synthesis: The Art and Science of Replicating the Molecules of Living Nature and Creating Others like Them in the Laboratory. *Proc. R. Soc. A.* **2014**, *470* (2163), 20130690. https://doi.org/10.1098/rspa.2013.0690.
(156) *Design, Synthesis, and SAR of Potent and Selective Dipeptide-Derived Inhibitors for Dipeptidyl Peptidases*. https://doi.org/10.1021/jm0308803.
(157) *A Brief Introduction to Chemical Reaction Optimization*. https://doi.org/10.1021/acs.chemrev.2c00798.
(158) Mishra, K.; Siwal, S. S.; Nayaka, S. C.; Guan, Z.; Thakur, V. K. Waste-to-Chemicals: Green Solutions for Bioeconomy Markets. *Science of The Total Environment* **2023**, *887*, 164006. https://doi.org/10.1016/j.scitotenv.2023.164006.
(159) *Exploration of Reaction Pathways and Chemical Transformation Networks*. https://doi.org/10.1021/acs.jpca.8b10007.
(160) *Molecules | Free Full-Text | Applications of the Conceptual Density Functional Theory Indices to Organic Chemistry Reactivity*. https://www.mdpi.com/1420-3049/21/6/748 (accessed 2023-08-30).
(161) Grambow, C. A.; Pattanaik, L.; Green, W. H. Reactants, Products, and Transition States of Elementary Chemical Reactions Based on Quantum Chemistry. *Sci Data* **2020**, *7* (1), 137. https://doi.org/10.1038/s41597-020-0460-4.
(162) Uematsu, R.; Maeda, S.; Taketsugu, T. Multiple Reaction Pathways Operating in the Mechanism of Vinylogous Mannich-Type Reaction Activated by a Water Molecule. *Chemistry – An Asian Journal* **2014**, *9* (1), 305–312. https://doi.org/10.1002/asia.201301065.
(163) Saleheen, M.; Mamun, O.; Mohan Verma, A.; Sahsah, D.; Heyden, A. Understanding the Influence of Solvents on the Pt-Catalyzed Hydrodeoxygenation of Guaiacol. *Journal of Catalysis* **2023**, *425*, 212–232. https://doi.org/10.1016/j.jcat.2023.06.009.
(164) Reid, J. P.; Betinol, I. O.; Kuang, Y. Mechanism to Model: A Physical Organic Chemistry Approach to Reaction Prediction. *Chem. Commun.* **2023**, 10.1039.D3CC03229A. https://doi.org/10.1039/D3CC03229A.
(165) Truhlar, D. G. Potential Energy Surfaces. In *Encyclopedia of Physical Science and Technology (Third Edition)*; Meyers, R. A., Ed.; Academic Press: New York, 2003; pp 9–17. https://doi.org/10.1016/B0-12-227410-5/00606-2.
(166) *Design and Optimization of Catalysts Based on Mechanistic Insights Derived from Quantum Chemical Reaction Modeling | Chemical Reviews*. https://pubs.acs.org/doi/full/10.1021/acs.chemrev.9b00073 (accessed 2023-08-31).
(167) Jensen, L.; van Duijnen, P. Th.; Snijders, J. G. A Discrete Solvent Reaction Field Model within Density Functional Theory. *The Journal of Chemical Physics* **2002**, *118* (2), 514–521. https://doi.org/10.1063/1.1527010.
(168) Gwee, E. S. H.; Seeger, Z. L.; Appadoo, D. R. T.; Wood, B. R.; Izgorodina, E. I. Influence of DFT Functionals and Solvation Models on the Prediction of Far-Infrared Spectra of Pt-Based Anticancer Drugs: Why Do Different Complexes Require Different Levels of Theory? *ACS Omega* **2019**, *4* (3), 5254–5269. https://doi.org/10.1021/acsomega.8b03455.
(169) Hospital, A.; Goñi, J. R.; Orozco, M.; Gelpí, J. L. Molecular Dynamics Simulations: Advances and Applications. *Adv Appl Bioinform Chem* **2015**, *8*, 37–47. https://doi.org/10.2147/AABC.S70333.
(170) Decherchi, S.; Cavalli, A. Thermodynamics and Kinetics of Drug-Target Binding by Molecular Simulation. *Chem. Rev.* **2020**, *120* (23), 12788–12833. https://doi.org/10.1021/acs.chemrev.0c00534.
(171) Bowers, K.; Chow, E.; Xu, H.; Dror, R.; Eastwood, M.; Gregersen, B.; Klepeis, J.; Kolossvary, I.; Moraes, M.; Sacerdoti, F.; Salmon, J.; Shan, Y.; Shaw, D. Scalable Algorithms for Molecular Dynamics Simulations on Commodity Clusters. In *ACM/IEEE SC 2006 Conference (SC'06)*. https://doi.org/10.1109/SC.2006.54.

(172) *OPLS3: A Force Field Providing Broad Coverage of Drug-like Small Molecules and Proteins | Journal of Chemical Theory and Computation*. https://pubs.acs.org/doi/10.1021/acs.jctc.5b00864 (accessed 2023-08-31).
(173) Shivakumar, D.; Williams, J.; Wu, Y.; Damm, W.; Shelley, J.; Sherman, W. Prediction of Absolute Solvation Free Energies Using Molecular Dynamics Free Energy Perturbation and the OPLS Force Field. *J. Chem. Theory Comput.* **2010**, *6* (5), 1509–1519. https://doi.org/10.1021/ct900587b.
(174) *A new molecular dynamics method combining the reference system propagator algorithm with a fast multipole method for simulating proteins and other complex systems | The Journal of Chemical Physics | AIP Publishing*. https://pubs.aip.org/aip/jcp/article-abstract/103/21/9444/481377/A-new-molecular-dynamics-method-combining-the?redirectedFrom=fulltext (accessed 2023-08-31).
(175) Tuckerman, M. E.; Berne, B. J. Molecular Dynamics in Systems with Multiple Time Scales: Systems with Stiff and Soft Degrees of Freedom and with Short and Long Range Forces. *The Journal of Chemical Physics* **1991**, *95* (11), 8362–8364. https://doi.org/10.1063/1.461263.
(176) Torres, E.; DiLabio, G. A. A (Nearly) Universally Applicable Method for Modeling Noncovalent Interactions Using B3LYP. *J. Phys. Chem. Lett.* **2012**, *3* (13), 1738–1744. https://doi.org/10.1021/jz300554y.
(177) Hugo, V.-V. V.; Alejandro, H.-S. M.; María, V.-S. A.; María, R.-H.; Antonio, L.-R. M.; Guadalupe, P.-O. M.; Antonio, M.-G. M.; Fernando, A.-H.; Víctor, A.; Diego, C.-A.; Enrique, Á. Molecular Modeling and Synthesis of Ethyl Benzyl Carbamates as Possible Ixodicide Activity. *CC* **2019**, *07* (01), 1–26. https://doi.org/10.4236/cc.2019.71001.
(178) Grimme, S.; Antony, J.; Ehrlich, S.; Krieg, H. A Consistent and Accurate Ab Initio Parametrization of Density Functional Dispersion Correction (DFT-D) for the 94 Elements H-Pu. *The Journal of Chemical Physics* **2010**, *132* (15), 154104. https://doi.org/10.1063/1.3382344.
(179) Harvey, J.; Aschi, M.; Schwarz, H.; Koch, W. The Singlet and Triplet States of Phenyl Cation. A Hybrid Approach for Locating Minimum Energy Crossing Points between Non-Interacting Potential Energy Surfaces. *Theoretical Chemistry Accounts* **1998**, *99*, 95–99. https://doi.org/10.1007/s002140050309.
(180) Woon, D. E.; Dunning, T. H., Jr. Gaussian Basis Sets for Use in Correlated Molecular Calculations. III. The Atoms Aluminum through Argon. *The Journal of Chemical Physics* **1993**, *98* (2), 1358–1371. https://doi.org/10.1063/1.464303.
(181) Schäfer, A.; Horn, H.; Ahlrichs, R. Fully Optimized Contracted Gaussian Basis Sets for Atoms Li to Kr. *The Journal of Chemical Physics* **1992**, *97* (4), 2571–2577. https://doi.org/10.1063/1.463096.
(182) Neese, F.; Hansen, A.; Wennmohs, F.; Grimme, S. Accurate Theoretical Chemistry with Coupled Pair Models. *Acc. Chem. Res.* **2009**, *42* (5), 641–648. https://doi.org/10.1021/ar800241t.
(183) Neese, F.; Hansen, A.; Liakos, D. G. Efficient and Accurate Approximations to the Local Coupled Cluster Singles Doubles Method Using a Truncated Pair Natural Orbital Basis. *The Journal of Chemical Physics* **2009**, *131* (6), 064103. https://doi.org/10.1063/1.3173827.
(184) Kitagawa, Y.; Saito, T.; Ito, M.; Shoji, M.; Koizumi, K.; Yamanaka, S.; Kawakami, T.; Okumura, M.; Yamaguchi, K. Approximately Spin-Projected Geometry Optimization Method and Its Application to Di-Chromium Systems. *Chemical Physics Letters* **2007**, *442* (4–6), 445–450. https://doi.org/10.1016/j.cplett.2007.05.082.
(185) Neese, F. The ORCA Program System. *WIREs Comput Mol Sci* **2012**, *2* (1), 73–78. https://doi.org/10.1002/wcms.81.
(186) Klamt, A.; Schüürmann, G. COSMO: A New Approach to Dielectric Screening in Solvents with Explicit Expressions for the Screening Energy and Its Gradient. *J. Chem. Soc., Perkin Trans. 2* **1993**, No. 5, 799–805. https://doi.org/10.1039/P29930000799.
(187) *Incorporation of solvent effects into density functional calculations of molecular energies and geometries | The Journal of Chemical Physics | AIP Publishing*. https://pubs.aip.org/aip/jcp/article-abstract/103/21/9312/481290/Incorporation-of-solvent-effects-into-density (accessed 2023-12-16).

(188) Barone, V.; Cossi, M. Quantum Calculation of Molecular Energies and Energy Gradients in Solution by a Conductor Solvent Model. *J. Phys. Chem. A* **1998**, *102* (11), 1995–2001. https://doi.org/10.1021/jp9716997.
(189) Cossi, M.; Rega, N.; Scalmani, G.; Barone, V. Energies, Structures, and Electronic Properties of Molecules in Solution with the C-PCM Solvation Model. *Journal of Computational Chemistry* **2003**, *24* (6), 669–681. https://doi.org/10.1002/jcc.10189.
(190) *A Case Study of the Mechanism of Alcohol-Mediated Morita Baylis–Hillman Reactions. The Importance of Experimental Observations | Journal of the American Chemical Society*. https://pubs.acs.org/doi/10.1021/ja5111392 (accessed 2023-09-17).
(191) Jorgensen, W. L.; Maxwell, D. S.; Tirado-Rives, J. Development and Testing of the OPLS All-Atom Force Field on Conformational Energetics and Properties of Organic Liquids. *J. Am. Chem. Soc.* **1996**, *118* (45), 11225–11236. https://doi.org/10.1021/ja9621760.
(192) Chen, C.; Tse, Y.-L. S.; Lindberg, G. E.; Knight, C.; Voth, G. A. Hydroxide Solvation and Transport in Anion Exchange Membranes. *J. Am. Chem. Soc.* **2016**, *138* (3), 991–1000. https://doi.org/10.1021/jacs.5b11951.
(193) *Aqueous Basic Solutions: Hydroxide Solvation, Structural Diffusion, and Comparison to the Hydrated Proton*. https://doi.org/10.1021/cr900233f.
(194) Mahmoud, M. A. M.; Shiroudi, A.; Abdel-Rahman, M. A.; Shibl, M. F.; Abdel-Azeim, S.; El-Nahas, A. M. Structures, Energetics, and Kinetics of H-Atom Abstraction from Methyl Propionate by Molecular Oxygen: Ab Initio and DFT Investigations. *Computational and Theoretical Chemistry* **2021**, *1196*, 113119. https://doi.org/10.1016/j.comptc.2020.113119.
(195) Korth, H.-G.; Mulder, P. Phenolic Hydrogen Transfer by Molecular Oxygen and Hydroperoxyl Radicals. Insights into the Mechanism of the Anthraquinone Process. *J. Org. Chem.* **2020**, *85* (4), 2560–2574. https://doi.org/10.1021/acs.joc.9b03286.
(196) Ramanan, R.; Dubey, K. D.; Wang, B.; Mandal, D.; Shaik, S. Emergence of Function in P450-Proteins: A Combined Quantum Mechanical/Molecular Mechanical and Molecular Dynamics Study of the Reactive Species in the H2O2-Dependent Cytochrome P450SPα and Its Regio- and Enantioselective Hydroxylation of Fatty Acids. *J. Am. Chem. Soc.* **2016**, *138* (21), 6786–6797. https://doi.org/10.1021/jacs.6b01716.
(197) Plata, R. E.; Singleton, D. A. A Case Study of the Mechanism of Alcohol-Mediated Morita Baylis–Hillman Reactions. The Importance of Experimental Observations. *J. Am. Chem. Soc.* **2015**, *137* (11), 3811–3826. https://doi.org/10.1021/ja5111392.
(198) Lonsdale, R.; Harvey, J. N.; Mulholland, A. J. Effects of Dispersion in Density Functional Based Quantum Mechanical/Molecular Mechanical Calculations on Cytochrome P450 Catalyzed Reactions. *J. Chem. Theory Comput.* **2012**, *8* (11), 4637–4645. https://doi.org/10.1021/ct300329h.
(199) Lonsdale, R.; Harvey, J. N.; Mulholland, A. J. Inclusion of Dispersion Effects Significantly Improves Accuracy of Calculated Reaction Barriers for Cytochrome P450 Catalyzed Reactions. *J. Phys. Chem. Lett.* **2010**, *1* (21), 3232–3237. https://doi.org/10.1021/jz101279n.
(200) Tantillo, D. J. Portable Models for Entropy Effects on Kinetic Selectivity. *J. Am. Chem. Soc.* **2022**, *144* (31), 13996–14004. https://doi.org/10.1021/jacs.2c04683.
(201) Robiette, R.; Aggarwal, V. K.; Harvey, J. N. Mechanism of the Morita−Baylis−Hillman Reaction: A Computational Investigation. *J. Am. Chem. Soc.* **2007**, *129* (50), 15513–15525. https://doi.org/10.1021/ja0717865.
(202) Finn, M.; Friedline, R.; Suleman, N. K.; Wohl, C. J.; Tanko, J. M. Chemistry of the *t* -Butoxyl Radical: Evidence That Most Hydrogen Abstractions from Carbon Are Entropy-Controlled. *J. Am. Chem. Soc.* **2004**, *126* (24), 7578–7584. https://doi.org/10.1021/ja0493493.
(203) Dutta Dubey, K.; Stuyver, T.; Kalita, S.; Shaik, S. Solvent Organization and Rate Regulation of a Menshutkin Reaction by Oriented External Electric Fields Are Revealed by Combined MD and QM/MM Calculations. *J. Am. Chem. Soc.* **2020**, *142* (22), 9955–9965. https://doi.org/10.1021/jacs.9b13029.
(204) Strajbl, M.; Sham, Y. Y.; Villà, J.; Chu, Z.-T.; Warshel, A. Calculations of Activation Entropies of Chemical Reactions in Solution. *J. Phys. Chem. B* **2000**, *104* (18), 4578–4584. https://doi.org/10.1021/jp0003095.

(205) Martin, R. L.; Hay, P. J.; Pratt, L. R. Hydrolysis of Ferric Ion in Water and Conformational Equilibrium. *J. Phys. Chem. A* **1998**, *102* (20), 3565–3573. https://doi.org/10.1021/jp980229p.
(206) Sieffert, N.; Bühl, M. Hydrogen Generation from Alcohols Catalyzed by Ruthenium−Triphenylphosphine Complexes: Multiple Reaction Pathways. *J. Am. Chem. Soc.* **2010**, *132* (23), 8056–8070. https://doi.org/10.1021/ja101044c.
(207) Schultz, K. M.; Goldberg, K. I.; Gusev, D. G.; Heinekey, D. M. Synthesis, Structure, and Reactivity of Iridium NHC Pincer Complexes. *Organometallics* **2011**, *30* (6), 1429–1437. https://doi.org/10.1021/om101024x.
(208) Gaggioli, C. A.; Belpassi, L.; Tarantelli, F.; Zuccaccia, D.; Harvey, J. N.; Belanzoni, P. Dioxygen Insertion into the Gold(I)–Hydride Bond: Spin Orbit Coupling Effects in the Spotlight for Oxidative Addition. *Chem. Sci.* **2016**, *7* (12), 7034–7039. https://doi.org/10.1039/C6SC02161A.
(209) Harvey, J. N. Understanding the Kinetics of Spin-Forbidden Chemical Reactions. *Phys. Chem. Chem. Phys.* **2007**, *9* (3), 331–343. https://doi.org/10.1039/B614390C.
(210) Anglada, J. M.; Martins-Costa, M. T. C.; Francisco, J. S.; Ruiz-López, M. F. Triplet State Promoted Reaction of SO2 with H2O by Competition between Proton Coupled Electron Transfer (Pcet) and Hydrogen Atom Transfer (Hat) Processes. *Phys. Chem. Chem. Phys.* **2019**, *21* (19), 9779–9784. https://doi.org/10.1039/C9CP01105F.
(211) Skone, J. H.; Soudackov, A. V.; Hammes-Schiffer, S. Calculation of Vibronic Couplings for Phenoxyl/Phenol and Benzyl/Toluene Self-Exchange Reactions: Implications for Proton-Coupled Electron Transfer Mechanisms. *J. Am. Chem. Soc.* **2006**, *128* (51), 16655–16663. https://doi.org/10.1021/ja0656548.
(212) Li, J.; Zhou, S.; Zhang, J.; Schlangen, M.; Usharani, D.; Shaik, S.; Schwarz, H. Mechanistic Variants in Gas-Phase Metal-Oxide Mediated Activation of Methane at Ambient Conditions. *J. Am. Chem. Soc.* **2016**, *138* (35), 11368–11377. https://doi.org/10.1021/jacs.6b07246.
(213) Geng, C.; Weiske, T.; Li, J.; Shaik, S.; Schwarz, H. Intrinsic Reactivity of Diatomic 3d Transition-Metal Carbides in the Thermal Activation of Methane: Striking Electronic Structure Effects. *J. Am. Chem. Soc.* **2019**, *141* (1), 599–610. https://doi.org/10.1021/jacs.8b11739.
(214) Sirjoosingh, A.; Hammes-Schiffer, S. Proton-Coupled Electron Transfer versus Hydrogen Atom Transfer: Generation of Charge-Localized Diabatic States. *J. Phys. Chem. A* **2011**, *115* (11), 2367–2377. https://doi.org/10.1021/jp111210c.
(215) Li, P.; Bi, J.; Liu, J.; Wang, Y.; Kang, X.; Sun, X.; Zhang, J.; Liu, Z.; Zhu, Q.; Han, B. P–d Orbital Hybridization Induced by p-Block Metal-Doped Cu Promotes the Formation of C2+ Products in Ampere-Level CO2 Electroreduction. *J. Am. Chem. Soc.* **2023**, *145* (8), 4675–4682. https://doi.org/10.1021/jacs.2c12743.
(216) Hutchison, P.; Rice, P. S.; Warburton, R. E.; Raugei, S.; Hammes-Schiffer, S. Multilevel Computational Studies Reveal the Importance of Axial Ligand for Oxygen Reduction Reaction on Fe–N–C Materials. *J. Am. Chem. Soc.* **2022**, *144* (36), 16524–16534. https://doi.org/10.1021/jacs.2c05779.